

Daytime thermospheric neutral wave dynamics over low- and equatorial-latitudes

A thesis submitted in partial fulfilment of the requirements
for the degree of

Doctor of Philosophy

by

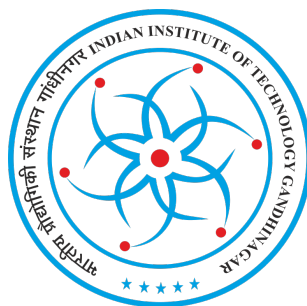
Subir Mandal

(Roll No. 15330013)

Under the guidance of

Prof. Duggirala Pallamraju

Space and Atmospheric Sciences Division
Physical Research Laboratory, Ahmedabad, India



Discipline of Physics
Indian Institute of Technology Gandhinagar, India
2020

Dedicated to all the special people in my life.

Declaration

I, Subir Mandal, declare that this written submission represents my ideas in my own words, and where others' ideas or words have been included, I have adequately cited and referenced the original sources. I also declare that I have adhered to all principles of academic honesty and integrity and have not misrepresented or fabricated or falsified any idea/data/fact/source in my submission. I understand that any violation of the above can cause disciplinary action by the Institute and can also evoke penal action from the sources which have thus not been properly cited or from whom proper permission has not been taken when needed.

Subir Mandal
(Roll no. 15330013)

Date: 24 December 2020

Certificate

It is certified that the work contained in the thesis entitled “*Daytime thermospheric neutral wave dynamics over low- and equatorial-latitudes*” by Mr. Subir Mandal (Roll no. 15330013), has been carried out under my supervision and this work has not been submitted elsewhere for any degree or diploma.

(Prof. Duggirala Pallamraju)

Thesis Supervisor

Space and Atmospheric Sciences Division

Physical Research Laboratory

Unit of Department of Space, Government of India

Ahmedabad-380009, Gujarat, India.

Date: 24 December 2020

Acknowledgments

It has always been a dream to get a Ph.D. This doctoral thesis, a journey of five years at Physical Research Laboratory (PRL), would not have been possible without the support, guidance, and blessings from my supervisor, teachers, friends, and family. I take this opportunity to express my gratitude to all of you for being there for me all the time.

First and foremost, I would like to express my heartfelt thanks and gratitude to my thesis supervisor Prof. Duggirala Pallamraju for his guidance and patience towards my progress from a Master of Science (MSc) student to a researcher. I am grateful to him for introducing me to this subject, and his unique way of visualizing the different scientific aspects of the subject has always inspired me. The discussions and interactions with him during the Ph.D. course work and project work have motivated me to carry out my research work under his supervision. Thank you, Sir, for having faith in me. I had the luxury to walk into his office at any time to clear my doubts about the research problems. His enormous patience and experiences had made my life easier during experimental observations and data analyses. His extensive knowledge with expertise in different areas in the field of upper atmospheric physics has immensely helped me to get more clarity in my understanding of this subject. I got the unique opportunity to have hands-on experience in the development of different instruments in his Optical Astronomy laboratory. A quick conversation with him has always motivated me and would bring my focus back to the research at the times when I felt confused and low. I am indebted to him for all his support. I am thankful for the love and affection I have got from Bhuvaneswari Ma'am, Ananth, and Samba. It brings me great joy when I recall the moments like Ananth playing the keyboard, playing table tennis with Ananth and Samba. And, special thanks to Ma'am and Sir for home-made sweets on Diwali and those tasty dishes at their place.

I would like to extend my gratitude to my Doctoral Studies Committee (DSC) members, Dr. D. Chakrabarty and Dr. A. Guharay. Their comments and suggestions in DSC seminars and reports in all the semesters, have been immensely helpful. I thank them for their constructive inputs in the thesis. Discussions with them have improved my understanding and interpretations of the results. I thank Prof. R. Sekar for his critical comments during my seminars and lectures on ionospheric physics, which have helped me to improve my understanding of the subject. I will always cherish the memories of discussions with them on different academic and non-academic topics during lunch and tea times. I also thank the Academic Committee members of PRL. Their inputs during annual reviews have helped to improve my presentation skills in conveying my scientific results to the experts of different fields. My sincere thanks to Prof. J Banerji for his lectures on improving scientific writing, poster, and oral presentation during the Research Communication course.

I am obliged to the Department of Space, Government of India for the research grant

offered to me during my tenure at PRL. I sincerely acknowledge the support and guidance of the Director of PRL, Dr. Anil Bhardwaj regarding my international travel to attend different scientific meetings. I also thank the former directors of PRL, Prof. Utpal Sarkar & Shri Tapan Mishra for their support. I thank the Director of IIT Gandhinagar, Prof. Sudhir K. Jain, and all the academic staff of IIT, Gandhinagar. I thank the former Dean of PRL, Prof. P. Janardhan, and former Chairperson of Space and Atmospheric Sciences Division (SPASC), S. Ramachandran for giving me the opportunity to work in this division of PRL. I am thankful to Prof. D. Pallamraju, present Dean of PRL for his continuous support towards the well-fare of the students. I express my sincere thanks to Dr. Bhushit Vaishnav, Head Academic Services, for his support regarding academic matters in PRL.

I thank the Registrar of PRL, Director office, Registrar office, and Dean office for the approvals of different applications. I thank the administration department of PRL for the allotment of different office orders. My heartfelt thanks to Richa Ma'am for her continuous support. I sincerely acknowledge the support of the Computer Centre, PRL for providing us with uninterrupted internet services and software support throughout my tenure. I express my deep gratitude to Nishtha Ma'am, Dr. Pragya, Dr. Nurul of PRL library for their continuous effort regarding ordering books, processing book grants, managing the library, organizing book fairs, and managing journal subscriptions. I also appreciate the co-operation by other library staff members. I thank the construction and maintenance group of PRL for their help regarding any kinds of repairing work in the office or hostel room. I am extremely thankful to the house keeping and canteen staffs for their continuous hospitality to us.

I extend my thanks to the Chairperson of the SPASC division, Prof. D. Pallamraju, for approving my field campaigns and recommending my applications for financial support to attend national/international conferences and workshops. I am grateful to all the colleagues of this division, Prof. H. Chandra, Prof. S. Ramachandran, Dr. L. K. Sahoo, Dr. S. K. Sharma, Dr. H. Gadhi, Dr. Narendra Ojha, Dr. T. A. Rajesh, Mr. S. Venkataramani, Mr. A. A. Manke, Mr. M. B. Bhavsar, Mr. T. K. S. Kumar, Anil, Aditya, Rahul, and Vishnu for the delightful work environment in the office. We used to participate in PRL's volleyball and football tournament. Winning the football tournament in 2019 was an incredible feeling and for that, I thank the division colleagues. I would like to thank the juniors of our division, Yogesh, Meghna, Kshitiz, Bijoy, and Gourav for their jolly company during lunch times or during playing games. My special thanks to Sneha'di for the constant support that she provides in the division office and definitely for sharing her yummy lunch on multiple occasions.

I am deeply grateful to my senior office mates, Deepak and Kedar. They both had welcomed me as a younger brother when I joined the group. I am extremely thankful to Kedar for helping me to understand the digisonde data and preliminary analysis of

such data. We three used to play table tennis and often go for lunch/dinners. Deepak is a big brother to me and the savior in the time of troubles. His critical evaluations of my results have been immensely helpful. I have learned the IDL with the help of Deepak and Kedar. Both me and Deepak, being a foodie, used to randomly plan of going out for lunch, and later on, Pradip also joined us. I am thankful to Pradip for helping me out with the manual scaling of ionograms. Field campaigns to Hyderabad with Kedar, Deepak, and Pradip have been wonderful times. I would like to extend my heartfelt thanks to my juniors Sovan and Sunil. Discussing different science topics and listening to their explanations have helped me to gain more insights into the subject. I am thankful to Dr. R. P. Singh, for his critical comments during discussions, division seminars have been very useful. I also thank my other group members Pankaj, Shashank, Mohit, and Chithra. I am extremely thankful to all of you for keeping a happening environment in the group. Playing table tennis with Sovan, Shashank, Pradip, and Pankaj has always been an enjoyable experience. I would like to express my sincere thanks to Kuldeep. He has always been the go to person for discussing science and clarifying doubts. I have learned a lot (patience and scientific writing) from him. Another special junior is Ankit, who is unique in his own way. I thank him for being jolly and helpful to me all the time. I thank Sandeep for his wonderful company and parties. I also thank Suman'da for the fun times and discussion on cooking.

I would also like to thank Dr. T. Vijayalakshmi, Samba bhai, Moid, and Abhilash of Jawaharlal Nehru Technological University, Hyderabad (JNTUH) for the logistic support during my field trips to JNTUH. I am grateful to the Indian Institute of Geomagnetism, Navi Mumbai; Coordinated Data Analysis Web, NASA; World Data Center for Geomagnetism, Kyoto, and several others for providing the data sets in open source.

I am thankful to the organizers of ISR Summer School-2018 for supporting my travel and local hospitality for attending the school at UML, Boston. I am extremely grateful to Dr. Nozomu Nishitani, Nagoya University, for providing me with the travel support to present my work at SuperDARN Workshop-2019 in Fujiyoshida, Japan. I sincerely acknowledge the travel grant received from the Council of Scientific & Industrial Research (India) to present my research works at Beacon Satellite Symposium-2019 held in Olsztyn, Poland.

The last five years in PRL have been my longest stay in a hostel. It has been a wonderful experience and one of the best times of my life, because of the friends I got here. The most special and close one is Archita. She is an amazing person and has been always there for me. She has always listened to me (no matter how much wrong I was) with a smile and always tried to understand me in my most troubled times. Being a good friend to Archita means you will always smile and listen to her endless collection of stories with each and every detail. I thank her for the times when she took care of me after I had an eye surgery and dengue. Memories of dinner parties, cooking parties at room number 11 of

Thaltej hostel, fun times during hostel functions, and celebrating each other success, will always be treasured. Thank you for helping me in writing in Latex. Shweta'di has been the elder sister to me that I never had. Hanging out at her place and cooking or cooked foods used to be the much-needed breaks from the daily routine. Time spent with these two people has helped me to become a better person in life. When I joined PRL, we were introduced to Aarthy, who later become a very close friend of mine. Aarthy taught me to avoid using the word 'South-Indian' while describing foods and persons, instead, I should use names of the different states. In the initial days, I used to get scared talking to her as she used to speak in English. I, Archita, and Aarthy had a lot of good memories during our stay at the Thaltej hostel. I have enjoyed playing football, volleyball, badminton, table tennis alongside my batchmates, Kaustav, Rahul, and Varun, and those good old times when we used to go out for coffee in the late night on many occasions. I consider myself to be very lucky to join PRL with Shefali, Nidhi, Akanksha, Shivangi, Richa, Ranadeep, Raju, Ashish, Harsh Oza, Harsh Raj, Balbeer, Naman, Arvind, Siddharth, Ritika & Prashant bhaiya. We used to have a lot of fun during our course work classes. We had amazing times during our course work days in Udaipur Solar Observatory, visit to Mt. Abu observatory of PRL, and celebrating all festivals in the hostel, playing antakshari, and dumb charades.

I had a great time with then seniors, Arko'da, Priyanka'di, Tanmoy'da, Monojit'da, Naveen bhaiya, Avdesh bhaiya, Girish bhaiya, Gaurav bhaiya, Manu, Deepak, Dipti, Apurv, Adi, and Bivin. Cooking home-style foods with Arko'da and Deepak were lots of fun. I thank Arko'da for being a mentor to me always. Priyanka'di, Arko'da, and Tanmoy'da had motivated us to organize Thaltej Students' Scientific meet. Playing a role in drama every year with them and others in the hostel was amazing. I thank Navpreet'di, Rupa'di, Kumar, Satish, & Prahlad for the wonderful memories. The company of these amazing people has made the Thaltej Hostel a home away from home for me. I used to be so fond of these seniors, that during the weekends our long chats used to go on from breakfast time to lunch time. Often I used to go out with Bivin and Kaustav for eating outside. Bivin, Apurva, Ali, Jabir had included me in their weekend football sessions at Thaltej. We have organized PRL's football tournaments, and matches between the students and staff. I thank Chandan Hati, Chandan Gupta, Niharika'di, Sharddha'di, Ikshu'di, Anil, Aman, Vishnu, Nijil, Kiran, and Anirban'da for their help. I had wonderful times with Sudip'da, Ujjwal'da and Nabyendu'da.

I am thankful to Goutam Sir and Moumita Ma'am for being the host of Bengali foods. We have been invited on countless occasions for lunch, dinners in their home. And, I have enjoyed a lot in help cooking (or cooking) different kinds of foods at their place along with Partha'Sir, Aveek' Sir, Kinsuk' Sir. I also thank Arvind bhaiya for inviting us to his place. I had great times playing football with Goutam Sir and volleyball with Arvind Sir. I have learned to play football, table tennis, volleyball, and badminton in Thaltej hostel and for that credits goes to Deepak, Arko'da, Tanmoy'da, Kaustav, Sandeep, Priyank, Sandeep,

Abdur, Surendra, Harish, Madhu, Ankit, Hrushi, Atif, Aravind, Sushant, Partha, Abhay, Naval, Yash, and Soumya. I would also like to thank Deepika, Nisha, Ritu, Sana, Shivani, Namita, and Monica for occasional sweet dishes and tasty foods. I thank all the Thaltej hostellers for helping each other in the very difficult times of lockdowns due to the Covid-19 outbreak.

I am thankful to my teachers Sajalbabu, Sanjay'da, Manobesh Sir, Basir sir, Krishnakali Ma'am, and Sourav'da, who has always motivated me for higher studies. It is their faith and dedication that instilled the confidence I needed to come this far. I take this opportunity to express my deep gratitude to my special friends whom I met during my college times and life has never been the same as before. I am extremely thankful to Samiran, Soumik, Kalyan, Tarun, Newton, Banibrata, Toton, and Tuli. They have always motivated and supported me in every step I have taken towards higher studies. Every year I wait for Durga Puja, so that we all can spend time together. Samiran has always inspired me in his own style to understand the details of everything; Soumik has taught me to work hard. Memories of the trip to Gangtok will always remain very close to my heart. Kalyan and Tarun have always put faith and confidence in me. And Newton, Toton, and Banibrata are the doses of stress reliever. Thank you, guys. My heartfelt thanks to the special person, Tuli, who has tolerated me in my bad times. I am extremely grateful for her wholehearted support in the most difficult times. She had to go through a lot of troubles and tough choices for me. She has always encouraged me to chase my dream and taught me to remain connected to my roots. She had made me a very kind person; thank you, Talkani! I thank Monalisa and Suchorita for the good times with full of positive energy. I am thankful to the people I have met during my MSc days, Falguni, Dilruba, Rinku, Suman, Rafikul, Nur'da, Wahida'di, Kanka, Titas, Saurav, Sudip, Deborshi, Subhrojyoti'da, and Sumit'da for the wonderful times. I would like to express my deepest gratitude to Madhumita, for being a true friend in tough times.

I am forever indebted to my Baba, Ma, Dadu, & Thamma. Since the time I can recall, I have only seen them sacrificing their wishes for me. Their love, blessings and unconditional support is the reason that I am at a stage of writing my doctoral thesis. Staying away from them is the toughest part. I thank Pisi, Priyanka, and all other relatives for their endless love and affection. I am extremely grateful to Chhanda'di, Jay'da, Jethima, Jethu, Mama, and Mamoni for their encouragement, love, and blessings. I am also thankful to Pom and Rukkai for the wonderful times.

Subir Mandal

Abstract

Earth's ionosphere-thermosphere system is driven by forcing from the top (radiation & high energy particles of solar origin) and the bottom (atmospheric waves). In addition, over low- and equatorial-latitudes, these upper atmospheric regions are affected by several phenomena driven by the equatorial electrodynamic. Further, during geomagnetic storms, high-latitude processes influence the dynamics of these regions. As a result of all these processes, the upper atmospheric dynamics over the low- and equatorial-latitudes is highly inter-coupled in nature. Systematic information on the gravity wave propagation characteristics in different geophysical conditions at thermospheric altitudes is crucial to gain a comprehensive understanding of the atmospheric coupling and dynamics.

This doctoral thesis presents new results on the daytime thermospheric wave dynamics obtained from low- and equatorial-latitude locations over different seasons and geomagnetic conditions. These results have been made possible by using an innovative approach to derive propagation characteristics of gravity waves in the daytime thermosphere, which has been arrived at as a part of the thesis work. This method has opened up new possibilities for investigations of daytime thermospheric wave dynamics on a continuous basis. Furthermore, the gravity wave characteristics, such as the time periods, vertical phase speeds, and scale sizes, obtained using this approach correspond to the highest possible altitude region reported so far in the literature.

The prediction of the occurrence of one of the equatorial phenomena, the equatorial spread F (ESF), which refers to the generation of plasma irregularities in the nighttime, has been one of the missing elements in the understanding of the equatorial upper atmosphere. Some of the earlier works had suggested that the daytime thermospheric dynamics makes the conditions, conducive or otherwise, for the occurrence of plasma irregularities in the nighttime equatorial ionosphere. In the recent past, the possibility of gravity waves offering the seed perturbation has been proposed, and investigations are underway around

the globe. In this context, as now an effective method is available to estimate the vertical propagation activity of gravity waves in the daytime, this aspect has been investigated further. It has been found that the vertical propagation activity is present on 85% of ESF days as compared to around 50% of non-ESF days. Also, the vertical propagation speeds of gravity waves on ESF days are higher compared to non-ESF days. ESF has been found to occur on 100% of occasions whenever the vertical phase speeds of daytime gravity waves were greater than 80 ms^{-1} . This threshold value of vertical propagation speeds of gravity waves can be used to predict the occurrence of ESF as early as 16 LT. The analysis shows that the time periods associated with these upward propagating gravity waves that are present in the afternoon persists until late in the evening of ESF occurrence, thereby offering a plausible connection of gravity wave seeding of ESF bubbles in the daytime.

The gravity wave propagation characteristics were studied to investigate the seasonal behavior. It has been found that the magnitudes of vertical propagation speeds and wavelengths of gravity waves in the daytime thermosphere over low-latitudes are maximum during equinoxes and minimum in the summers. The comparison between the gravity wave characteristics and model-derived winds indicates that these gravity waves propagate mostly in the westward direction. During geomagnetic storms, the values of wave speeds and vertical scale sizes are significantly different than those seen on geomagnetically quiet days. These differences are very similar to the variation in energy inputs at the high-latitudes, as characterized by the strength of the auroral electrojet index. This result presented direct evidence of high-to-low latitude coupling in the neutral wave dynamics during geomagnetically disturbed times. Numerical relations have been arrived at to represent variations in the vertical propagation speeds of gravity waves during both geomagnetic quiet and disturbed conditions.

Even though the gravity waves in the thermosphere are considered to be omnipresent, their vertical propagation in the daytime upper atmosphere is observed on only around 40% of the days. Nevertheless, the days in which vertical propagation exists, it is seen that the vertical propagation activity increases with increasing solar flux. This is inferred to be due to an increase in the scale height and decrease in the Brunt-Väisälä period of the upper atmosphere with increasing solar flux. Further, the number of gravity waves in the daytime thermosphere increases due to the weakening in wave dissipations during the period of higher solar flux. These influences of solar flux on the gravity wave characteristics

have been quantified, and empirical relations have been obtained.

Results obtained in this thesis work have provided new insights, which have significantly enhanced our understanding of the daytime neutral wave dynamics. The empirical relations established in this thesis work can form inputs to global-scale models of thermospheric dynamics. Furthermore, the innovative approach of using radio wave technique to derive neutral gravity waves, as demonstrated in this thesis, has opened up a new dimension in the investigations of Earth's upper atmospheric dynamics.

Contents

Abstract	i
List of Tables	ix
List of Figures	xi
List of Abbreviations	xv
1 Introduction	1
1.1 Background	1
1.2 Atmospheric structure	2
1.3 Upper atmospheric dynamics	4
1.3.1 Different phenomena of the ionosphere-thermosphere system over the low- and equatorial-latitudes	5
1.3.2 Influence of solar flux variation on the ionosphere-thermosphere system	14
1.3.3 Thermospheric Winds	16
1.3.4 Atmospheric waves	17
1.3.5 Geomagnetic storms	22
1.4 Summary	26
1.5 The objective of the thesis	28
1.6 Overview of the thesis	29
2 Data sets and analyses techniques	31
2.1 Background	31
2.2 Introduction	31
2.3 Measurement techniques and data sets	33

2.3.1	Digisonde	33
2.3.2	Dayglow measurement	39
2.3.3	EEJ Data	42
2.3.4	Solar $F_{10.7cm}$ flux	43
2.3.5	Disturbance storm time (Dst) index	44
2.3.6	Auroral electrojet (AE) index	45
2.3.7	HWM14 wind and NRLMSISE temperature	46
2.4	Analyses techniques	46
2.4.1	Fourier Transform (FT)	47
2.4.2	Lomb Scargle Fourier transformation (LSFT)	49
2.4.3	Wavelet analysis	52
2.5	Summary	55
3	Deriving thermospheric gravity wave characteristics using digisonde	57
3.1	Background	57
3.2	Introduction	58
3.3	Data sets used	59
3.4	Results and Discussions	60
3.4.1	Gravity wave time periods (τ) from optical data	60
3.4.2	Gravity waves from digisonde data	62
3.4.3	Estimation of vertical propagation speeds (c_z) of gravity waves	66
3.4.4	Estimation of vertical scale sizes (λ_z) of gravity waves	68
3.4.5	Comparison of gravity wave periods from simultaneous radio and optical measurements	70
3.4.6	Estimation of horizontal scale sizes (λ_H) of gravity waves	73
3.5	Summary	76
4	Vertical propagation of gravity waves as precursors to onset of ESF	77
4.1	Background	77
4.2	Introduction	78
4.3	Data sets used	81
4.4	Results and discussions	81
4.4.1	Variation in the EEJ strength	82

4.4.2	Variation in the ionospheric height in the evening hours	83
4.4.3	Variation in the strength of PRE	85
4.4.4	Time period and amplitudes of gravity waves in the daytime ther- mosphere	87
4.4.5	Vertical propagation of daytime thermospheric gravity waves	88
4.5	Summary	94
5	Vertical propagation of gravity waves in the daytime thermosphere	97
5.1	Background	97
5.2	Introduction	98
5.3	Data sets used	99
5.4	Analyses and Results	99
5.4.1	The occurrence of vertical propagation of gravity waves	100
5.4.2	Vertical propagation characteristics of gravity waves during geomag- netically quiet days	102
5.4.3	Vertical propagation characteristics of gravity waves during geomag- netically disturbed days	111
5.5	Summary	118
6	Effect of solar flux variation on the thermospheric gravity waves	121
6.1	Background	121
6.2	Introduction	121
6.3	Data sets used	122
6.4	Data analysis and results	123
6.4.1	Ionospheric variations	123
6.4.2	Influence of solar flux variation on the vertical propagation charac- teristics of gravity waves	126
6.4.3	Solar flux influence on gravity wave activity	131
6.5	Summary	138
7	Summary and Future scope	141
7.1	Summary	141
7.2	Future scope	145

References	149
List of Publications	189
Presentations at Conferences	191
Publications attached with the thesis	193

List of Tables

3.1	<i>The derived values of time period (τ), vertical propagation speeds (c_z), uncertainty in vertical propagation speeds (Δc_z), vertical wavelengths (λ_z), and uncertainty in vertical wavelengths ($\Delta \lambda_z$) of gravity waves in the daytime thermosphere for 16-21 May 2015.</i>	69
5.1	<i>Summary of analysis of thermospheric gravity wave characteristics for geomagnetic quiet days selected as per the criteria case-1 and case-2</i>	110
5.2	<i>Values of $\langle c_z \rangle_d$, $\langle \lambda_z \rangle_d$ over Ahmedabad and the integrated AE index during geomagnetic disturbed days. The days when $\langle c_z \rangle_d$ and the integrated AE index value do not show any similarity are shown in bold.</i>	115

List of Figures

1.1	Structure of the Earth's atmosphere.	4
1.2	EEJ strength at different latitudes	6
1.3	Schematic of equatorial ionization anomaly	7
1.4	Average vertical drift of F-region over Jicamarca in different seasons	9
1.5	Neutral anomaly as observed in N_2 measurements from OGO-6 satellite	10
1.6	Equatorial temperature and Wind anomaly and associated vertical winds	11
1.7	Signature of ESF in the ionogram	13
1.8	Upper atmospheric variability with solar cycle	15
1.9	Different types of waves present in the Earth's atmosphere	17
1.10	The different regimes of acoustic-gravity waves	20
1.11	Downward phase and upward wave propagation	21
1.12	Schematic diagram of the geomagnetic storm driven changes	24
1.13	Thermospheric wind patterns for equinox and solstice times during different geomagnetic activity level	25
2.1	Different locations in India from where the ground-based measurements are used in the thesis	32
2.2	A typical ionogram obtained from digisonde, Ahmedabad	34
2.3	Different modules of digisonde at Ahmedabad, India	35
2.4	Auto-scaling of ionogram	36
2.5	Comparison of electron density profile obtained from auto-scaling and manual scaling of ionogram.	37
2.6	Comparison of noon-time values of few standard ionospheric parameters obtained from manual and auto-scaling of ionograms of Ahmedabad station.	38
2.7	Schematic of MISE instrument	40

2.8	Method of extraction of dayglow emission rate at 630.0 nm wavelength. . . .	41
2.9	Variation in daily sunspot numbers and daily solar $F_{10.7cm}$ flux values	43
2.10	Variation in Dst and AE indices during 17/03/2015 - 26/03/2015	45
2.11	An example showing the effects of finite sampling of a continuous function in the Fourier transform	48
2.12	Performance of FFT and LSFT for data sampled at even and uneven rates	51
2.13	An example comparing wavelet analysis and FFT periodogram using syn- thetically generated signals	53
3.1	Deriving gravity wave time periods from OI 630.0 nm dayglow data	61
3.2	Diurnal variation in IEC , hmF_2 , and foF_2 & their time-series analyses	63
3.3	Comparison of isoelectron density contours obtained from auto-scaling, manual scaling, and virtual heights of ionogram	65
3.4	(a) Deriving c_z & λ_z from isoelectron density contours. (b) Their values resulted from analyses of one week of data. (c) Comparison of estimated λ_z values with earlier reported values from MU radar measurements.	68
3.5	(a) Comparison of gravity wave periods obtained from radio and optical techniques. (b) & (c) Phase evolution of the common periods observed between them.	72
3.6	Estimation of horizontal scale sizes from the measured vertical propagation parameters of gravity waves using dispersion relation.	75
4.1	Meridional winds and the $h'F$ values for ESF days over Trivandrum.	79
4.2	Variation in the strength of EEJ on ESF and non-ESF days.	83
4.3	Variation in the base height of the ionosphere in the evening hours in rela- tion to the occurrence of ESF.	84
4.4	The values of peak vertical drift of F-layer in the post-sunset hours for ESF and non-ESF days.	86
4.5	The time periods and amplitudes of gravity waves propagating in the ver- tical direction in the daytime thermosphere on ESF and non-ESf days. . . .	87
4.6	Daytime thermospheric gravity wave propagation speeds in the vertical direction on ESF and non-ESF days.	89

4.7	Wavelet analysis to find the duration of gravity wave activity in the daytime thermosphere.	90
4.8	Average vertical propagation speeds of gravity waves during 10-16 LT on ESF and non-ESF days.	91
4.9	(a) A barplot showing that higher values of $\langle c_z \rangle_{10-16LT}$ are more conducive for ESF occurrence. (b) Combined behavior of $\langle c_z \rangle_{10-16LT}$ and $V_{d_{max}}$ with regard to the occurrence or non-occurrence of ESF.	93
5.1	Variation in the vertical propagation activity of gravity waves in the daytime thermosphere	100
5.2	Seasonal variation in the occurrence percentage of vertical propagation of gravity waves	101
5.3	Vertical phase speeds and vertical wavelengths of gravity waves during geomagnetically quiet days ($Dst > -10$ nT)	103
5.4	Vertical phase speeds and vertical wavelengths of gravity waves during geomagnetically quiet days ($Dst > -15$ nT)	105
5.5	HWM14 model-derived noon-time thermospheric winds over Ahmedabad along with their time-series analyses using the Lomb-Scargle periodogram.	106
5.6	Vertical phase speeds and vertical wavelengths of gravity waves during geomagnetically quiet days ($Dst > -10$ nT) along with the variation in resultant horizontal winds at thermospheric altitudes	108
5.7	Vertical phase speeds and vertical wavelengths of gravity waves during geomagnetically quiet days ($Dst > -15$ nT) along with the variation in resultant horizontal winds at thermospheric altitudes.	109
5.8	(a) Vertical phase speeds of gravity waves for geomagnetically disturbed days. (b) Changes in phase speeds during geomagnetic storms as compared to their quiet time values. (c) Same as in (a) but for vertical wavelengths, and (d) same as in (b) but for vertical wavelengths.	112
5.9	Changes in vertical phase speeds and vertical wavelengths of gravity waves during geomagnetically disturbed times along with variation in the integrated values of the AE index	114
5.10	Correlation coefficients between changes in c_z and integrated AE index considered for different lags	116

5.11	(a) $\langle c_z \rangle_d$ values along with the integrated AE index of past 28 h. (b) $\langle c_z \rangle_d$ as a function of the integrated AE index values.	117
6.1	Variation in the NmF_2 , hmF_2 , IEC , and hmF_2	124
6.2	Variation in the NmF_2 as a functions of (a) $F_{10.7cm}$ and (b) $\langle F_{10.7cm} \rangle P$	125
6.3	Variation in the vertical propagation characteristics of gravity waves along with solar $F_{10.7cm}$ flux.	127
6.4	Variation in solar flux during 01/01/2007-31/12/2017, which includes the two-year period considered in the present investigation.	129
6.5	Variation in the maximum values of gravity waves vertical phase speeds in 20 day window and 20-day averaged solar flux values.	130
6.6	Variation in the vertical propagation activity of gravity waves in the daytime thermosphere and NRLMSISE model-derived neutral temperature.	132
6.7	Variation in the total number of gravity waves present in the daytime thermosphere and variation in solar $F_{10.7cm}$ flux.	134
6.8	Variation in solar $F_{10.7cm}$ flux and the average number of gravity waves present in the daytime thermosphere.	136
6.9	The variation in gravity wave drag (a measure of momentum deposition due to breaking of gravity waves) in different solar flux conditions.	138

List of Abbreviations

AE	Auroral electrojet
CEJ	Counter electrojet
CHAMP	Challenging minisatellite payload
CME	Coronal mass ejection
DE	Dynamics explorer
Dst	Disturbance storm time
EEJ	Equatorial electrojet
EIA	Equatorial ionization anomaly
EMF	Electromotive force
ESF	Equatorial spread-F
ETWA	Equatorial temperature and wind anomaly
FAL	False alarm limit
foF₂	Critical frequency of the F_2 -layer
GOLD	Global-scale observations of the limb and disk
GPS	Global positioning system
GW	Gravity wave
h'F	Base height of the F-layer
HF	High frequency
hmF₂	Peak height of the F_2 -layer
HWM	Horizontal wind model
ICON	Ionospheric connection explorer

IEC	Integrated electron content
IMF	Interplanetary magnetic field
ISR	Incoherent scatter radar
LIDAR	Light detection and ranging
MISE	Multi-wavelength imaging spectrograph using echelle grating
MLT	Mesosphere and lower thermosphere
MLAT	Magnetic latitude
NmF₂	Peak electron density of the <i>F</i> ₂ -layer
OGO	Orbiting geophysical observatory
PRE	Pre-reversal enhancement of electric field
PSD	Power spectral density
RADAR	Radio detection and ranging
TEC	Total electron content
TID	Traveling ionospheric disturbance

Chapter 1

Introduction

1.1 Background

Earth is the only planet known so far where life exists. The ozone layer, the upper atmosphere, and the geomagnetic field lines around the Earth form a shield from the harmful radiation and energetic particles of solar origin from reaching the surface. Earth's upper atmospheric species interact with the incoming radiation from the nearest star, the Sun, whereby charged particles are generated due to ionization. However, the density of charged particles is three orders of magnitude less than the neutral density in the upper atmosphere. Therefore, both the neutral and electrodynamic processes affect the dynamics of the Earth's upper atmosphere. These dynamics are not similar at all latitudes as different latitudinal and longitudinal regions receive different amounts of solar radiation at any given time. This differential nature in the amounts of absorption of the solar radiation engenders wind motions of varying magnitudes. Further, the curvature of the geomagnetic field lines leads to an anisotropic movement of plasma in the upper atmosphere. The horizontal nature of the geomagnetic field lines over the dip-equator in combination with the altitude-dependent differential responses of ions and electrons to neutral winds, gives rise to several electrodynamic phenomena. These processes control the distribution of plasma and neutral density over the low- and equatorial-latitudes. Also, the energy budget of the upper atmosphere is significantly influenced by the lower atmospheric waves, which can have different spatial and temporal characteristics in different parts of the Earth. In addition to these, during geomagnetic storms, the upper

atmosphere over low- and equatorial-latitudes get affected by the high-latitude processes. The effects of all these drivers on the upper atmosphere can be direct, indirect, and mixed. The highly unpredictable nature of occurrence of the nighttime plasma irregularities in the equatorial ionosphere, which depend on the prevailing neutral and plasma dynamics, adds further complications as they adversely affect the trans-ionospheric GPS and satellite communications. Therefore, a comprehensive understanding of the upper atmospheric dynamics over low- and equatorial-latitudes is essential for gaining insights into not only the fundamental aspects of space physics, but also possible space applications. The investigations of the upper atmospheric dynamics in the daytime gain importance as there are several dynamic and inter-coupled phenomena that occur in the daytime (discussed in section 1.3.1). Further, information on the wave dynamics in the daytime is quite sparse. This thesis aims to address some of these aspects. The work reported in this thesis has significantly enhanced our knowledge on the wave dynamical behavior over low- and equatorial-latitudes in the daytime.

In this chapter, we briefly discuss the structure of the Earth's atmosphere and various manifestations of upper atmospheric phenomena. The ionosphere-thermosphere system over the low- and equatorial-latitudes is replete with several electrodynamical processes. We have briefly outlined these forces that dominate the morphology, structure, and dynamics of these regions. Other drivers, such as the winds and the solar radiation that significantly alter the thermospheric composition and energy budget, are also discussed. Short descriptions are provided on different atmospheric waves in terms of their spatial and temporal scales, in general, and gravity waves, in particular. The effects of geomagnetic storms on the thermospheric dynamics over low- and equatorial-latitudes are also described in this chapter.

1.2 Atmospheric structure

The atmosphere refers to the thin gaseous layer that co-rotates with the Earth under the action of gravity. In terms of neutral constituents, our atmosphere consists of 78% N_2 , 21% O_2 , and 1% of other species. The number density of these neutral species de-

creases exponentially with altitude. Based on the variation in the temperature gradient, the atmosphere is divided into the *troposphere* (0-15 km), the *stratosphere* (15-50 km), the *mesosphere* (50-90 km), and the *thermosphere* (above 90 km). In the *troposphere*, the temperature drops at a rate of around $6.5 \text{ K}\cdot\text{km}^{-1}$ as we go away from the Earth's surface. Then temperature increases in the *stratosphere* owing to the absorption of the solar ultraviolet (UV) radiation by ozone. Radiative cooling by CO_2 causes negative temperature gradient in the *mesosphere*, which is located above the *stratosphere*. *Mesopause*, the upper boundary of the *mesosphere*, is the coldest region of the Earth's atmosphere with a temperature of around 180 K. Above *mesopause*, the atmospheric temperature increases due to the absorption of solar X-ray and extreme ultraviolet (EUV) radiation. Eventually, the temperature at these altitudes becomes constant due to high thermal conductivity. In the region below 100 km, where all the atmospheric constituents are evenly mixed due to turbulence, and composition does not vary with altitude, is known as the *homosphere*. The region above 100 km is known as the *heterosphere*, wherein the atmospheric constituents are distributed based on their masses through molecular diffusion, hence the composition varies significantly with altitude. The boundary between the *homosphere* and *heterosphere* is called the *turbopause*. For example, below the *turbopause*, the atmospheric composition is dominated by N_2 and O_2 in the ratio of 4:1. In contrast, around 120 km, the amount of atomic oxygen becomes equivalent to that of O_2 , and at 250 km altitude, the atomic oxygen density is higher than that of N_2 . This happens due to photo-dissociation of O_2 by solar EUV radiation and molecular diffusion at altitudes above the *turbopause*. Hydrogen dominated region of the atmosphere is known as the *protonosphere*. The altitude region beyond 600 km is termed as the *exosphere*. The region of the atmosphere, where the plasma corotates with the Earth, is known as the *plasmasphere*, which over the equatorial plane can be extended up to 4-5 R_E (Earth's radius) depending on the magnetic activity level. The *magnetosphere* refers to the outermost region, where the motion of plasma is generally governed by the convective electric fields of solar wind origin. The partially ionized region of the atmosphere is known as the *ionosphere*, which has enough plasma densities to affect the propagation of radio waves. The *ionosphere* is embedded in the *mesosphere*, the *thermosphere*, and the *exosphere*. The *upper atmosphere* refers to the region above 60 km. Figure 1.1 summarizes the different classifications of the Earth's atmosphere. The different layers of the ionosphere are defined as D-region (60-90 km;

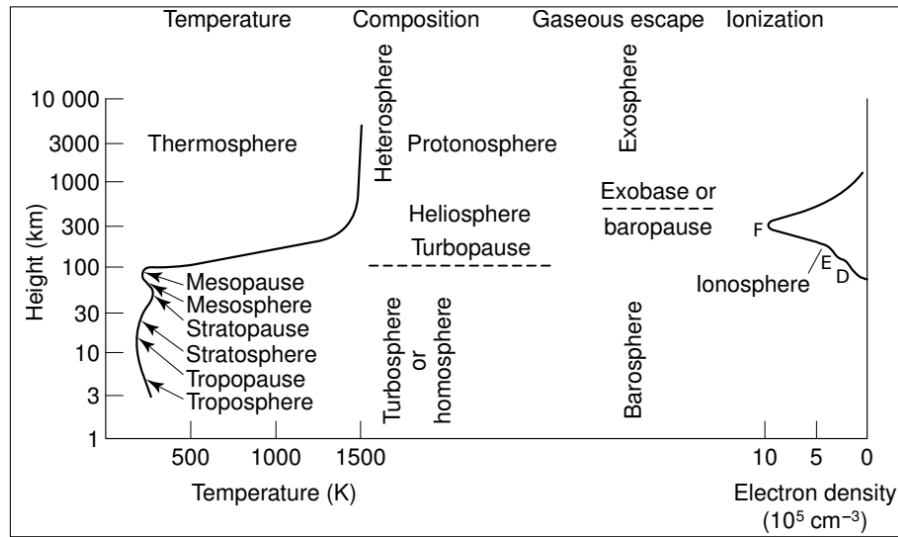


Figure 1.1: *Structure of the Earth's atmosphere. Different classifications based on temperature, composition, and ionization are shown.* [After [Hargreaves \(1992\)](#)]

electron density: 10^8 - 10^{10} m^{-3}), E-region (90-150 km; electron density: 10^{11} m^{-3}), and F-region (150 km and above; electron density: 10^{12} m^{-3} and higher). Depending on the seasons and locations, the F-region splits into two layers around the noon-time, namely F_1 and F_2 . During the nighttime, the D-layer vanishes due to the recombination of ions and electrons, and the E-layer remains present with lesser electron density than in the daytime. Over the high-latitude regions, in addition to the ionization of N_2 , O_2 , and O by incoming solar UV and X-rays, incoming energetic particles contribute significantly to the ionospheric plasma densities.

1.3 Upper atmospheric dynamics

The solar ionizing radiation that produces charged particles in the ionosphere varies with solar activity level. Also, the incoming charged particles from the Sun, deposit a significant amount of energy at the high-latitudes. The thermospheric temperature has been shown to vary by a factor of two, depending on the solar activity (e.g., [Roble and Dickinson, 1973](#); [Stolarski et al., 1975](#); [Hinteregger, 1976](#)). Waves generated in the lower altitudes can travel deep into the upper atmosphere under favorable background conditions (e.g., winds, temperature, and neutral density, etc.) and contribute to the energy budget of these

regions. Neutral winds varying with seasons cause compositional changes, variation in the ionospheric heights, and coupling between different parts of the atmosphere. All these different drivers that influence the upper atmosphere over low- and equatorial-latitudes are briefly discussed in the following sections.

1.3.1 Different phenomena of the ionosphere-thermosphere system over the low- and equatorial-latitudes

In the presence of the geomagnetic field, both ions and electrons gyrate along the geomagnetic field lines with gyro-frequencies Ω_i & Ω_e , respectively. Further, they undergo collisions with the neutrals (with collision frequencies ν_i & ν_e , respectively). These collision frequencies decrease with altitude as a result of an exponential reduction in the neutral densities. The motions of ions and electrons in the ionospheric D-region are controlled by the neutral winds as $\Omega_i \ll \nu_i$ and $\Omega_e < \nu_e$. In the F-region, both ions and electrons are bound to the geomagnetic field lines since their gyro-frequencies are higher than their collision frequencies with the neutrals. However, the ions and electrons in the E-region show differential behavior in their movements. Here, the motions of ions are governed by the neutral winds as $\Omega_i < \nu_i$, whereas, the geomagnetic field controls the movement of the electrons as $\Omega_e > \nu_e$.

1.3.1.1 Equatorial electrojet (EEJ)

Tidal forces due to solar heating and lunar gravitation pull set up horizontal wind motions in the ionosphere. In the E-region, due to the differential motion of ions and electrons under the influence of these neutral winds flowing across the magnetic field lines, an emf is generated. This results in an eastward electric field in E-region in the daytime. This process is akin to the dynamo action, and in the ionosphere, this is referred to as the E-region dynamo mechanism. This primary eastward electric field (\vec{E}_x), in combination with the horizontal field lines of the northward geomagnetic field (\vec{B}) over the dip-equatorial region, drives an ($\vec{E}_x \times \vec{B}$) drift in the vertical direction. As ions in the E-region are controlled by tidal winds, only electrons respond to this upward drift. A sharp reduction in the hall conductivity above 110 km restricts the upward drift of electrons, which results

in an upward polarization electric field (\vec{E}_z). This upward polarization electric field is nearly 30 times stronger than the primary electric field (e.g., [Anandarao, 1976](#); [Pandey et al., 2016](#)). Furthermore, a westward drift is generated as the aforementioned vertical polarization electric field crosses with the northward magnetic field lines. Again, only electrons experience a strong westward drift, as their gyrofrequency is higher than their collision frequency in the E-region. This leads to an enhanced eastward current in the E-region in the daytime, known as the equatorial electrojet (EEJ) ([Chapman, 1951](#)). The strength of this current maximizes over the dip-equator and drastically reduces at

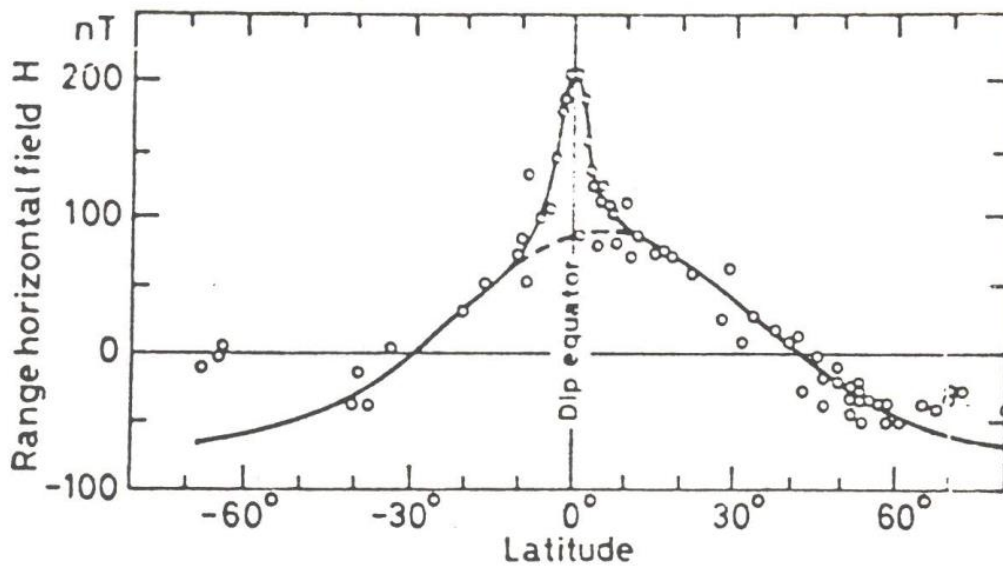


Figure 1.2: *Variation in the noon-time strength of horizontal component of the magnetic field at different latitudes as measured using ground-based magnetometers. [After Onwumechilli (1967)]*

higher latitudes (as depicted in figure 1.2). In-situ measurements of this current using magnetometers on-board sounding rockets revealed that this current maximizes around the altitude of 105 km (e.g., [Davis et al., 1967](#); [Sampath and Sastry, 1979](#)). Many models have been developed over the years to explain the features of the EEJ (e.g., [Baker and Martyn, 1953](#); [Sugiura and Cain, 1966](#); [Anandarao, 1976](#)). On some days, in the afternoon hours, this current flows in the westward direction for a brief period, which is known as the counter electrojet (CEJ). Different mechanisms have been proposed for the generation of CEJ (e.g., [Raghavarao and Anandarao, 1980](#); [Blanc and Richmond, 1980](#); [Somayajulu et al., 1993](#); [Stening et al., 1996](#); [Gurubaran, 2002](#); [Kikuchi et al., 2003](#); [Fejer et al., 2008](#); [Sridharan et al., 2009](#); [Pandey et al., 2018](#)).

1.3.1.2 Equatorial ionization anomaly (EIA)

The ionospheric electron density is expected to be higher over the equatorial-latitudes as it receives a major amount of incoming solar radiation. In contrast, an anomalous latitudinal distribution of plasma is observed with a density trough over the dip-equator and two crests at around $\pm 15^\circ$ dip-latitudes (*Namba and Maeda, 1939; Appleton, 1946; Mitra, 1946*), known as equatorial ionization anomaly (EIA). The E-region electric field from the off-equatorial locations maps to dip-equatorial F-region through the highly conducting magnetic field lines (*Farley, 1959, 1960*) (depicted in figure 1.3a). This mapped eastward electric field crosses with the northward magnetic field perpendicularly over the

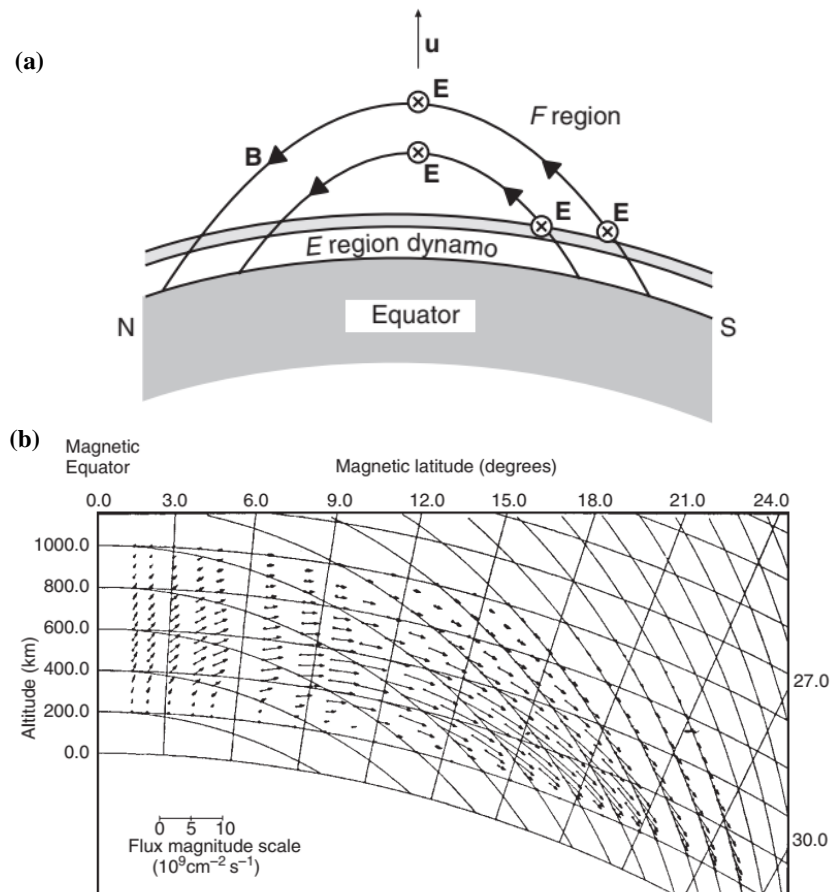


Figure 1.3: (a) Mapping of E-region dynamo electric field from the off-equatorial latitudes to equatorial F-region through geomagnetic field lines. [After *Schunk and Nagy (2009)*]. (b) Plasma movement over equatorial-latitudes due to $\vec{E} \times \vec{B}$ upward drift and their downward diffusion through magnetic field lines to low-latitudes. [After *Hanson and Moffett (1966)*]

dip-equator and pushes the plasma through the generation of ($\vec{E} \times \vec{B}$) drift in the upward direction (e.g., *Hanson and Moffett, 1966; Anderson, 1973*). In the F-region, as the gyrofrequencies of both ions and electrons are greater than their collision frequencies with neutrals, they move upward in response to this drift, V_d , which is independent of charge and mass. Owing to pressure gradient and gravity, this upward moving plasma in the equatorial F-region gets deposited over the low-latitudes on both sides of the equator similar to a fountain (as shown in figure 1.3b) and so this is also called the plasma fountain effect. Hence, the latitudinal distribution in F-region plasma shows an altitude dependent double-humped structure in the low-latitudes. The EIA structure is asymmetric about the geomagnetic equator due to season-dependent meridional winds (e.g., *Anderson, 1973; Raghavarao et al., 1988b; Balan et al., 1995*). The EIA strength has been shown to be remarkably correlated with the integrated EEJ strength (*Raghavarao et al., 1978*). The strength of the EIA, which controls the plasma distribution over low-latitudes, varies with local time, day-to-day, season, and solar activity (e.g., *Raghavarao et al., 1988b; Sastri, 1990; Pallam Raju et al., 1996; Balan et al., 2018*).

1.3.1.3 Pre-reversal enhancement of electric field (PRE)

Another unique electro-dynamical process of dip-equatorial latitudes is the pre-reversal enhancement of the zonal electric field (PRE). It refers to a significant increase in the strength of the daytime eastward electric field in the post-sunset hours for a brief period of time over the equatorial region. In the post-sunset hours, an increase in eastward zonal wind and sharp conductivity gradient at the day-night terminator are considered to be the cause of the PRE (*Heelis et al., 1974*). Because of this PRE, the F-layer plasma is often pushed to higher altitudes, where the recombinations are less due to infrequent collisions. Figure 1.4 showing the average vertical drift over Jicamarca as measured by incoherent scatter radar (ISR) during geomagnetically quiet times in different seasons for three different solar flux levels. The presence of PRE in all the seasons can be clearly seen as enhanced values of vertical drift near the evening times. Further, it can be noted that in the daytime $\vec{E} \times \vec{B}$ drift does not vary much with the solar flux, whereas, the PRE magnitude significantly changes with variation in the solar flux and seasons. This increase in the PRE is due to faster zonal winds over the equatorial region and an increase in E-

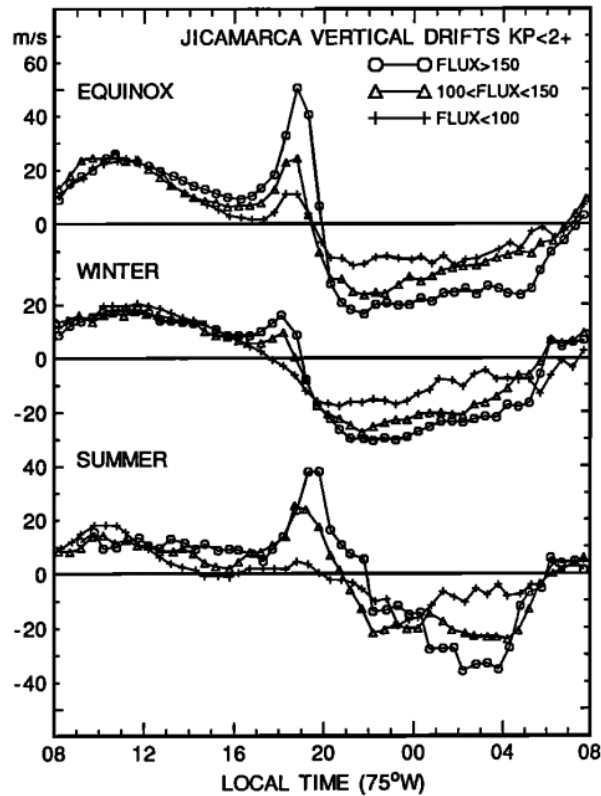


Figure 1.4: Average vertical plasma drift measured over Jicamarca during equinox (March-April, September-October), winter (May-August), and summer months (November-February) for three different solar flux levels. [After Fejer *et al.* (1991)]

layer conductivity gradient resulted from increasing solar flux (e.g., Farley *et al.*, 1986; Goel *et al.*, 1990; Fejer *et al.*, 1991).

1.3.1.4 Neutral anomaly (NA)

Equatorial electrodynamic not only controls the plasma distribution in the tropical latitudes but also affects the latitudinal distribution of neutral density. The off-equatorial EIA crest regions with higher plasma density offer greater resistance due to collision to the neutrals than those over the dip-equatorial region. As a result of such ion-neutral drag force, neutrals get accumulated at the crest regions, and lead to a double-humped structure in their latitudinal distribution with two peaks on both sides of the dip-equator, similar to the latitudinal distribution of plasma as in the case of EIA. This anomalous distribution of neutrals is known as the neutral anomaly (NA). The latitudinal distribution of N_2 and O obtained from the OGO-6 satellite measurements revealed that their

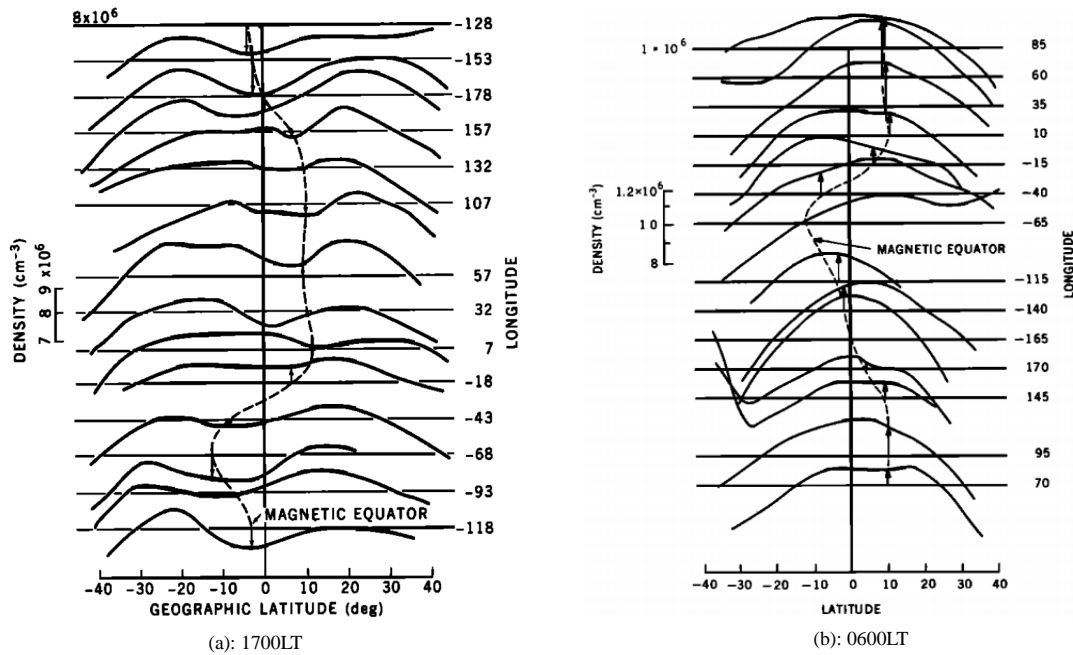


Figure 1.5: (a) The distribution of N_2 densities corresponding to 1700 LT as obtained from the OGO-6 satellite measurements showing minimum densities over the dip-equatorial region and two maxima on both sides of the equator. (b) Same as in (a) but with an increased density over the dip-equator at 0600 LT. [After [Hedin and Mayr \(1973\)](#)]

densities over the geomagnetic equator are 20% and 10% less, respectively, than those over the EIA crest locations ([Hedin and Mayr, 1973](#)). This satellite was instrumented for 26 experiments to understand the inter-relationships between different atmospheric parameters. Some of these experiments enabled measurements of airglow, auroral emissions, cosmic rays, electric fields, neutral compositions, solar radiation, etc. Figure 1.5a, shows the latitudinal distribution of N_2 density measured from the OGO-6 satellite corresponding to 1700 LT. But the N_2 distribution around 0600 LT, when the EIA strength is very weak, was found to be maximum over the geomagnetic equator (as depicted in figure 1.5b).

1.3.1.5 Equatorial temperature and wind anomaly (ETWA)

An anomalous distribution in the neutral temperature and zonal winds in the low- and equatorial-latitudes were first observed in the measurements from the DE-2 (Dynamics Explorer) satellite. As discussed above, the neutral wind motions experience more resistance over the EIA crest regions due to the ion-drag forces than the trough region.

Consequently, the zonal wind motions get slower over the crest locations than the EIA trough location. Higher ion-neutral collisions cause the temperature to rise over the crest regions that lead to an enhancement in temperature by ~ 50 - 100 K in the region of higher plasma densities, compared to those at the trough region. Such structure in the magnitudes of temperature and zonal winds in the low- and equatorial-latitudes, is known as the equatorial temperature and wind anomaly (ETWA) (*Raghavarao et al., 1991*). Variations

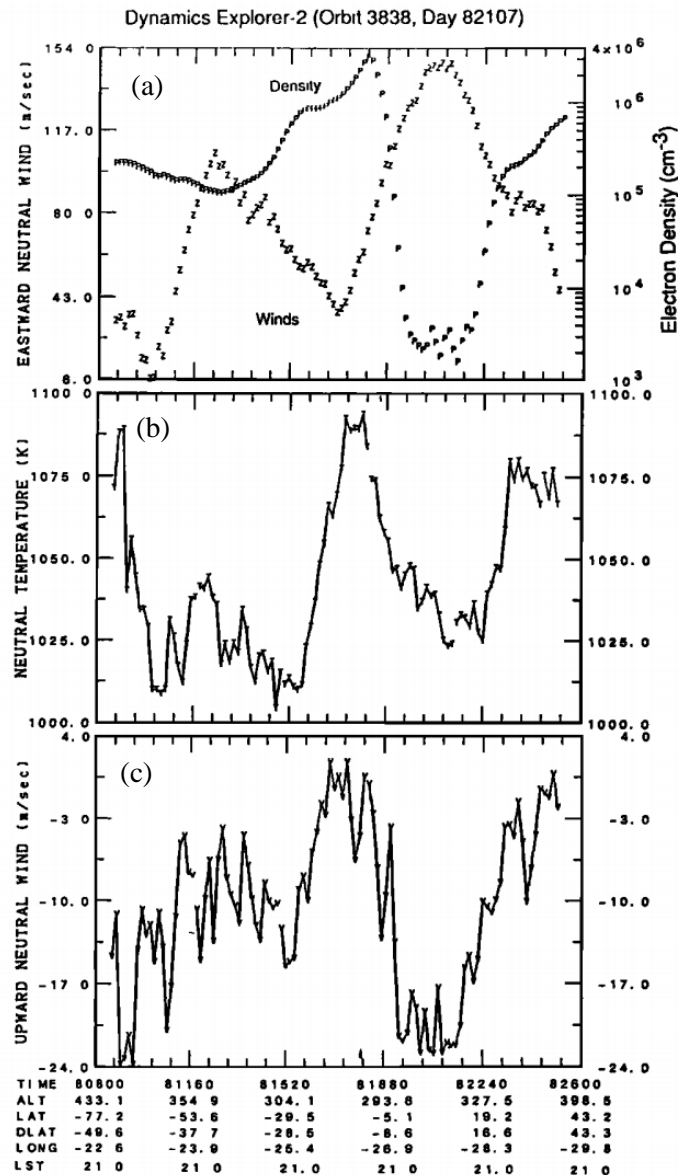


Figure 1.6: Latitudinal distribution of (a) electron density (symbols P) and zonal winds (symbols z), (b) neutral temperature (symbol T), and (d) vertical winds as obtained from Wind and Temperature Spectrometer (WATS) instrument on-board the DE-2 satellite. These values correspond to 2100 LT and 27° W longitude. [After *Raghavarao et al. (1993)*]

in them are depicted in figure 1.6 as obtained from the DE-2 satellite for 2100 LT. From the top panel of this figure, it can be seen that the zonal winds (curve with symbol z) magnitudes are smaller at the places of higher electron density (curve with symbol p) as compared to those over the equatorial region, where the electron densities are minimum. The middle panel of figure 1.6, depicts the latitudinal variation in temperature (curve with symbol T), with higher values at the crest locations and lower values at the dip-equatorial region. Therefore, the ETWA is clearly seen from figure 1.6a and 1.6b. The temperature gradient over the low- and equatorial-latitudes sets up meridional circulation, which leads to vertically upward wind over the crest, and downward wind over the trough regions. Variation in these vertical wind magnitudes can be seen in the bottom panel (figure 1.6c), wherein, the vertical wind magnitudes are showing similar latitudinal distribution to those observed in the temperature (figure 1.6b). Therefore, over the low- and equatorial latitudes, EIA is not only responsible for the redistribution of ionospheric plasma, but also for the latitudinal distribution of the neutrals.

1.3.1.6 Equatorial spread-F (ESF)

The various upper atmospheric phenomena discussed above briefly, not only make the ionosphere-thermosphere system of low- and equatorial-latitudes highly dynamic, but also influence the nighttime processes. One such example is the occurrence of equatorial spread-F (ESF) in the post-sunset hours over the dip-equatorial region. ESF refers to the large scale plasma irregularities in the nighttime F-region, one of whose manifestations is the range spread in the return echoes of ionograms obtained by ionosonde (as can be seen in figure 1.7). These plasma irregularities severely affect trans-ionospheric communication and navigation systems. In the post-sunset hours, a sharp vertical density gradient in plasma develops in the F-region, as during this time production of plasma stops, and the ionization in the bottom side of the ionosphere rapidly recombines. This configuration of heavier fluid (plasma) resting on a lighter fluid is an unstable condition, and on occasions, the Rayleigh-Taylor instability can get triggered. Even though such configuration of heavier fluid being balanced by lighter one is present in all the nights, there are only some nights when this Rayleigh-Taylor instability gets triggered. The published literature is rich with reports of several works, which address the pre-

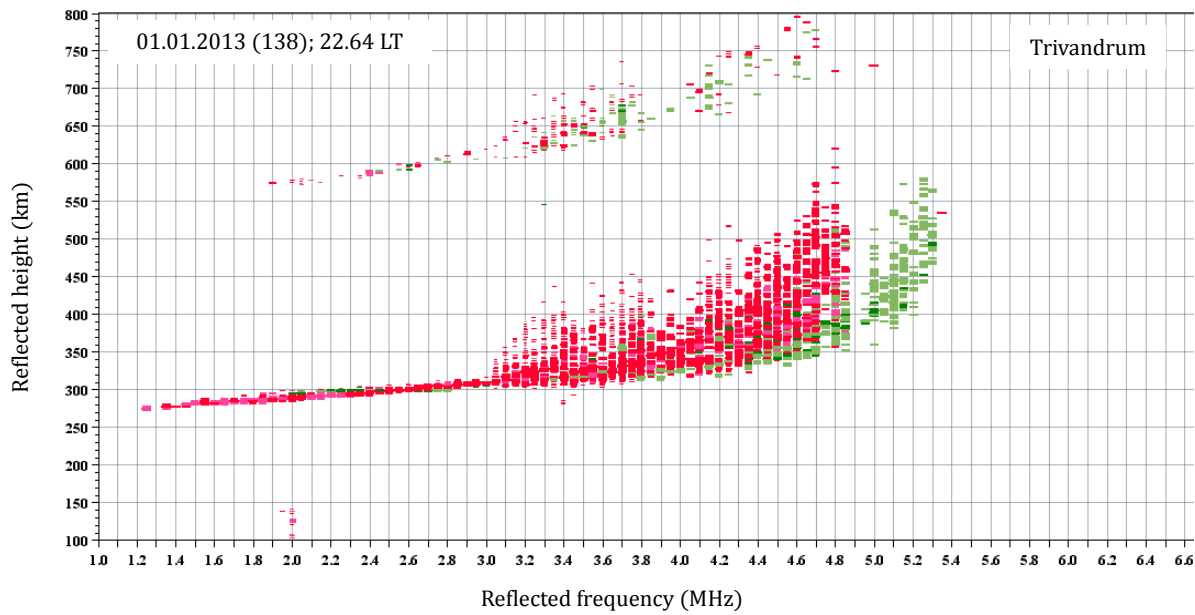


Figure 1.7: *ESF occurrence, as observed by the digisonde at Trivandrum, a magnetic equatorial location in India.*

conditions of the ionosphere-thermosphere system to enable triggering of Rayleigh-Taylor instability. Any density perturbations in the ionosphere caused by gravity waves (discussed in section 1.3.4) are thought to form the seeds that instigate the upward rise of lower density plasma. This leads to the generation of plasma irregularities through the Rayleigh-Taylor instability mechanism. Once generated, these irregularities grow nonlinearly and can have spatial scales ranging from a few centimeters to a few hundreds of kilometers. Variability in the occurrence of ESF with seasons, solar activity, and longitudes is relatively well-understood (e.g., [Chandra and Rastogi, 1970](#); [Rastogi, 1980](#); [Abdu et al., 1981a](#); [Maruyama and Matuura, 1984](#); [Tsunoda, 1985](#); [Raghavarao et al., 1988a](#); [Mendillo et al., 1992](#)), whereas the day-to-day variation in its occurrence still remains a mystery. As discussed earlier, the higher values of the PRE push the ionosphere to higher altitudes where the collisions are lesser, which helps these plasma irregularities to grow. Numerous results have been reported in the literature addressing the day-to-day variability in the ESF occurrence in the light of PRE strength (e.g., [Sekar and Kelley, 1998](#); [Sastri, 1996](#); [Fejer et al., 1999](#); [Anderson et al., 2004](#); [Ram et al., 2006](#); [Abdu et al., 2006b, 2009](#); [Prakash et al., 2009](#)). Strong EIA development in the daytime have been shown to be a necessary condition that makes the ionosphere-thermosphere region conducive for the occurrence of plasma irregularities in the nighttime over Indian longitudes

(e.g., *Raghavarao et al.*, 1988a; *Sridharan et al.*, 1994; *Jayachandran et al.*, 1997; *Prakash et al.*, 2009). Independent measurements were followed up by different research groups from other longitudes, which verified and confirmed these results (e.g., *Mendillo et al.*, 2001; *Valladares et al.*, 2001; *Pallamraju et al.*, 2004b). ETWA leads to the generation of vertically downward winds (*Raghavarao et al.*, 1993) over the dip-equator (shown in figure 1.6), and these downward vertical winds can play a crucial role in the growth rate of plasma irregularities in the nighttime ionosphere (*Sekar and Raghavarao*, 1987). These works suggest that the daytime thermosphere prepares the background conditions in this region, and make them conducive or otherwise for the occurrence of nighttime plasma irregularities in the ionosphere.

All these different upper atmospheric phenomena discussed so far (e.g., EEJ, EIA, NA, ETWA, and ESF) make the ionosphere-thermosphere system over low-and equatorial latitudes highly dynamic as their strength varies from day-to-day, day-to-night, seasons, solar activity, and geomagnetic activity.

1.3.2 Influence of solar flux variation on the ionosphere-thermosphere system

Solar radiation is the endless source of energy for the Earth's atmosphere. The activity level of the Sun changes with the 11-year cycle. The solar X-ray, EUV, and UV flux, which influence the upper atmospheric dynamics and plasma densities, change with the solar activity level. In addition to the 11-year cycle, solar radiation also shows an intrinsic 27-day periodicity, which is related to the solar rotation. There are several other periodicities as well that are displayed by the solar flux (*Willson*, 1982). Therefore, the upper atmospheric parameters show variability similar to those present in solar radiation (e.g., *Balan et al.*, 1994, 1996; *Pancheva et al.*, 2002; *Altadill and Apostolov*, 2003; *Pallamraju et al.*, 2010, 2020; *Kutiev et al.*, 2012; *Chakrabarty et al.*, 2012; *Mandal et al.*, 2020). As can be seen from figure 1.8, in the entire solar cycle, the upper atmospheric neutral temperatures changes by a factor of two, whereas the densities of neutrals and electrons can vary by a factor of ten (*Lean*, 1997). As the high-energy electromagnetic radiations from the Sun get absorbed in the Earth's upper atmosphere, they can not be measured from the

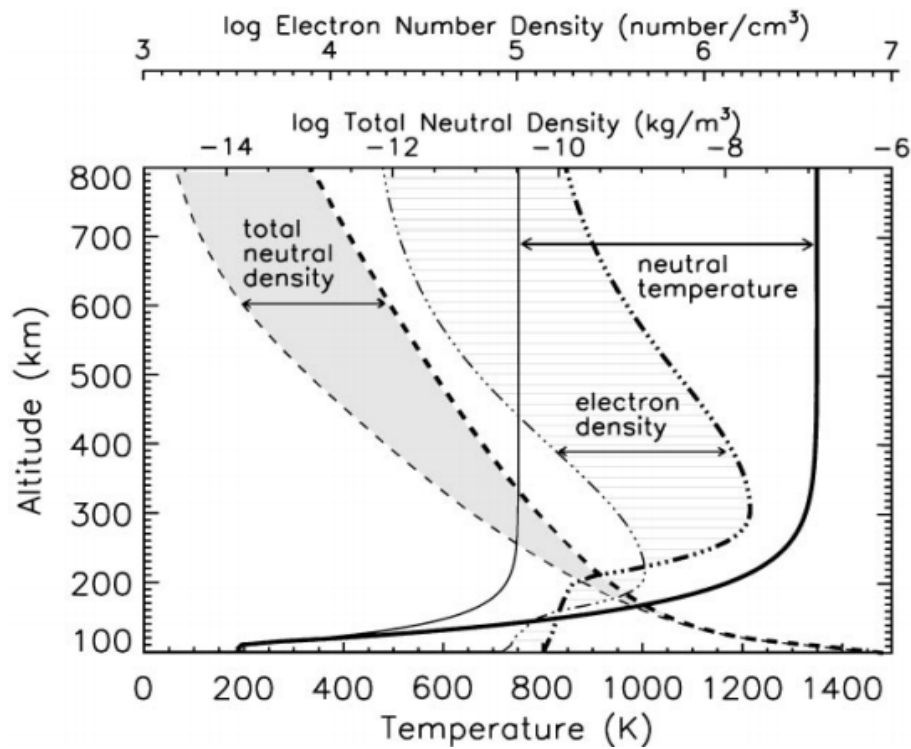


Figure 1.8: Variation in the Earth's upper atmospheric neutral temperature, electron and neutral density for low and high activity in a solar cycle is shown. Thick and thin lines in each case represent the values in high and low solar activity levels. [After [Lean \(1997\)](#)]

ground. One of the most commonly used indices for monitoring the solar activity level is $F_{10.7cm}$ flux ([Tapping, 2013](#)), whose variations are found to be similar to those in the solar EUV and X-ray radiation. These are discussed in chapter 2 of this thesis. High-speed energetic particles that are emitted from the active regions of the Sun during coronal mass ejections (CME) events, travel via the interplanetary magnetic fields (IMF) and interact with the Earth's magnetic field. On occasions, when the IMF is directed southward, the solar energetic particles can enter the upper atmosphere of the Earth over high-latitudes and produce what is called a geomagnetic storm. Geomagnetic storms can further modify the upper atmospheric dynamics over the low- and equatorial-latitudes as well through various transport mechanisms between high-to-low latitudes. Transient solar flare events lead to a surge in solar ionizing radiation and hence they significantly alter the background dynamics (e.g., [Mitra, 1974](#); [Mendillo et al., 1974](#); [Mendillo and Evans, 1974](#); [Immell et al., 2003](#); [Tsurutani et al., 2005](#); [Das et al., 2010](#); [Pallamraju et al., 2010](#); [Le et al., 2012, 2013, 2015](#); [Sumod et al., 2014](#)). Different amounts of absorption of solar radiation with latitudes generate wind motions of varying magnitudes in different directions. These winds

contribute significantly to the variability of the ionosphere-thermosphere system.

1.3.3 Thermospheric Winds

Primarily, the pressure gradient forces associated with temperature differences, drive winds in the upper atmosphere. These wind motions alter the compositions and bring in changes in neutral and plasma densities in different latitudes. In the thermosphere, winds flow in zonal, meridional, and vertical directions. The daytime zonal winds in the ionospheric E-region generates an electric field through the E-region dynamo (e.g., *Gouin and Mayaud, 1967; Onwumechilli, 1967; Anandarao and Raghavarao, 1987*). In the post-sunset hours, an enhanced eastward wind in the F-region causes PRE through the F-region dynamo (discussed in section 1.3.1.3). The meridional winds (equatorward or poleward) push the plasma (to higher or lower altitudes) along the magnetic field lines (*Rishbeth and Garriott, 1969; Rishbeth, 1979*). However, as the magnetic field lines are horizontal over the dip-equator, the meridional wind does not change the ionospheric heights over the dip-equator. Meridional and trans-equatorial winds have been shown to affect the evolution of plasma irregularities in the nighttime (e.g., *Maruyama and Matuura, 1984; Mendillo et al., 2001; Devasia et al., 2002; Abdu et al., 2006b*). Equatorward meridional winds, driven by Joule heating in the polar region during geomagnetic storms, change the neutral composition and electric field over the low- and equatorial-latitudes (e.g., *Richmond and Matsushita, 1975; Mayr et al., 1978; Richmond, 1978, 1979; Pallamraju et al., 2004b; Karan and Pallamraju, 2018*). Several reports are available in the literature on the thermospheric winds measured from satellites as well as ground (e.g., *Salah and Holt, 1974; Hernandez and Roble, 1976; Spencer et al., 1981; Forbes et al., 1987; Herrero et al., 1988; Meriwether et al., 1984, 1986; Gurubaran et al., 1995; Shiokawa et al., 2003; Shepherd et al., 2012*). Different empirical and physics based models also provide thermospheric neutral wind variation (e.g., *Hedin et al., 1988, 1996; Drob et al., 2008, 2015*). Thermospheric meridional and zonal winds vary with latitudes, longitudes, and seasons (e.g., *Gurubaran et al., 1995; Pant and Sridharan, 1998; Emmert et al., 2002*). Vertical winds in the thermosphere have been shown to contribute to the growth of plasma irregularities and at thermospheric altitudes, their effects can be comparable to the effect of gravity (e.g., *Sekar and Raghavarao, 1987; Sekar et al., 1994*). Measurement of vertical winds at

thermospheric altitudes are very limited (e.g., *Biondi and Sipler, 1985; Raghavarao et al., 1987, 1993; Herrero and Meriwether Jr, 1994; Smith, 1998*).

1.3.4 Atmospheric waves

Waves are motions induced by perturbations in the atmosphere due to internal or external sources. As the waves propagate away from the origin, they carry the energy from their source region. Hence, these waves play a crucial role in the atmosphere's energy budget. The Earth's atmosphere supports different kinds of wave motions. These waves can be categorized based on their spatial extents (planetary waves, tides, and gravity waves), excitation modes (free and forced waves), propagation in the atmosphere (stationary, evanescent, and traveling waves), and vertical displacement of the medium (longitudinal and transverse waves) (*Beer, 1974; Andrews, 1987*). Figure 1.9 depicts the direction of oscillations of the particles in the medium in the cases of acoustic waves (longitudinal), gravity waves (vertical transverse), and Rossby waves (horizontal transverse). Planetary

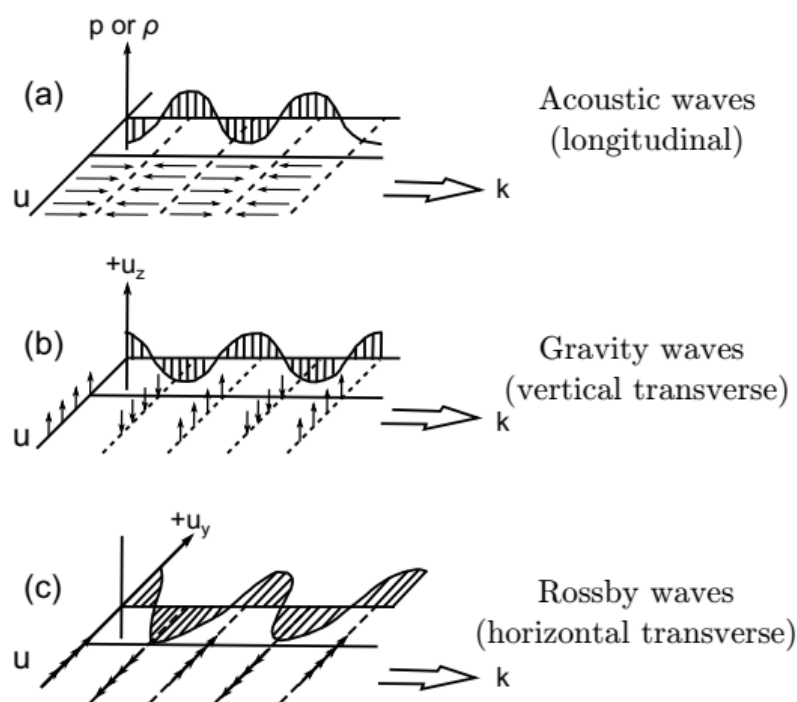


Figure 1.9: *Schematic of longitudinal, vertically transverse, and horizontally transverse wave motion and the direction of wave-induced motions of the medium. [After Beer (1974)]*

waves are large scale waves present in the atmosphere, whose motion is affected by Earth's rotation. These are global-scale waves and are mostly generated due to instability processes or dissimilar heating between land and ocean. These waves have periods of the order of 2-30 days and horizontal wavelengths of the order of Earth's radius. The sudden stratospheric warming (SSW) events, wherein the stratospheric temperature increases by tens of Kelvins, are considered to be caused by the interaction of planetary waves and zonal mean flow in the wintertime stratosphere of high-latitudes (e.g., [Matsuno, 1971](#); [Holton, 1980](#); [Chau and Woodman, 2005](#); [Chau et al., 2012](#)). Even though SSW is a high-latitude phenomenon, its effects have been observed in the different parameters of middle and lower thermosphere (MLT) regions of low- and equatorial-latitudes (e.g., [Liu and Roble, 2005](#); [Sridharan et al., 2009](#); [Chau et al., 2009](#); [Pedatella and Forbes, 2010](#); [Yue et al., 2010](#); [Pancheva and Mukhtarov, 2011b](#); [Fejer et al., 2010](#); [Guharay and Sekar, 2012](#); [Goncharenko et al., 2013](#); [Chandran et al., 2013](#); [Singh and Pallamraju, 2015](#); [Laskar et al., 2013, 2014, 2019](#); [Laskar and Pallamraju, 2014](#)). The planetary wave activity of quasi-16 day periodicity has been found to be enhanced during the SSW events (e.g., [Pancheva et al., 2008](#); [Laskar et al., 2013](#); [Laskar and Pallamraju, 2014](#)). Planetary waves do not directly propagate beyond 100-110 km ([Pogoreltsev et al., 2007](#)), but their effects are transferred to the mesosphere and thermosphere regions through interaction with gravity waves or tidal winds. These effects of planetary waves in the middle atmospheric dynamics and results on the vertical coupling have been reported in the literature (e.g., [Forbes, 1982](#); [Salby, 1984](#); [Parish et al., 1994](#); [Gurubaran et al., 2001](#); [Abdu et al., 2006a](#); [Pancheva et al., 2008](#); [Guharay et al., 2014](#); [Sassi et al., 2012](#)). The tidal wave motion in the upper atmosphere sets in due to differential heating by the solar radiation or lunar gravitational pull. These atmospheric tides play a major role in the general circulation of the MLT region, and their amplitude in the temperature and zonal winds can reach tens of Kelvin and ms^{-1} , respectively ([Chapman and Lindzen, 1970](#); [Miyoshi et al., 2017](#)). The tides can be both migrating (move westward with the Sun and are fixed in local time) or non-migrating (do not follow the apparent motion of Sun) in nature. The migrating diurnal and semi-diurnal modes are the atmospheric tides with the largest amplitudes. Non-migrating tides are generated due to a contrast in heating between land and ocean, and they cause a difference in the diurnal variation in the surface pressure between them ([Kato et al., 1982](#); [Miyoshi et al., 2017](#)). In the lower thermosphere, semi-diurnal tides

dominate due to the absorption of solar radiation in the Schumann-Runge band by atomic oxygen. In altitudes above 250 km, solar heating driven diurnal tides can be observed, whereas, in the altitude region 100-250 km, both diurnal and semi-diurnal components of tides are present. These large scale wave motions exhibit systematic behavior in both longitudes and latitudes (*Oberheide and Gusev, 2002; Oberheide et al., 2009*). The tidal wind motions in the ionospheric E-region generate an electric field through dynamo action. The longitudinal distribution of electron density in the ionospheric F-region has been shown to be affected by the non-migrating tides and communicated through the variation in the E-region electric field (e.g., *Immel et al., 2006; Hagan et al., 2007; Jin et al., 2008*). Atmospheric gravity waves refer to the smaller spatial scale waves, which are not affected by the Coriolis force, and gravity acts as the restoring force for these waves. The smallest spatial scale waves present in the atmosphere are the acoustic waves, which do not play any significant role in the upper atmospheric dynamics. In this thesis, we have studied the gravity wave activity in the daytime thermosphere using combined radio and optical measurements. In the following section, we present a brief discussion on the source, dissipation, and dispersion of gravity waves in the atmosphere. Generalized mathematical treatment of gravity waves can be found in the literature (e.g., *Hines, 1960; Beer, 1974; Holton, 1980; Lindzen, 1990*). Due to the presence of density gradients in the Earth's atmosphere, it acts as an anisotropic and dispersive medium to wave propagation. The spectrum of acoustic-gravity waves can be presented by the dispersion relation given by the equation 1.1.

$$m^2 = \left(1 - \frac{\omega_a^2}{\omega^2}\right) \frac{\omega^2}{s^2} - k^2 \left(1 - \frac{\omega_b^2}{\omega^2}\right) \quad (1.1)$$

where m is the vertical wave vector; k is the horizontal wave vector; ω_a is the acoustic cut-off frequency; ω_b is Brunt-Väisälä frequency, s is the speed of sound waves, and ω is the intrinsic frequency of the propagating wave.

The figure 1.10 depicts the different branches, namely, the acoustic waves ($\omega > \omega_a$), evanescent waves, and internal gravity waves ($\omega < \omega_b$) of the dispersion relation. For propagating waves, both m and k must be real and positive. This criterion is achieved for either $\omega > \omega_a$ or $\omega < \omega_b$, and these refer to waves of acoustic and internal gravity wave regimes. For complex values of m , the waves do not propagate vertically and they

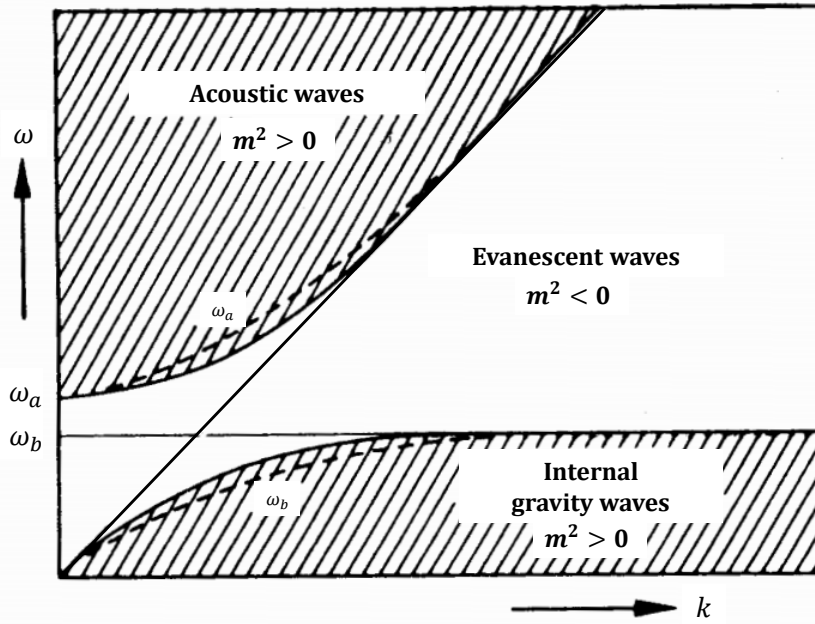


Figure 1.10: *The different regimes of acoustic-gravity waves. [After Hargreaves (1992)]*

are called evanescent waves ([Salby, 1996](#)). As the gravity waves do not get affected by the Earth's curvature, they refer to atmospheric oscillations of frequencies (ω), such that $\omega_b > \omega > f$ (where, $f = 2\Omega \sin \phi$, is the Coriolis parameter; Ω is the Earth's rotation rate, and ϕ is the latitude). The propagation direction (θ) of gravity waves can be estimated as $\theta = \tan^{-1}(\frac{m}{k})$. The linear theory of gravity waves in the Earth's atmosphere leads to the gravity wave dispersion relation of the form ([Fritts and Alexander, 2003](#)),

$$m^2 = \frac{k^2(\omega_b^2 - \omega^2)}{(\omega^2 - f^2)} - \frac{1}{4H^2} \quad (1.2)$$

where, H is the neutral scale height.

The group velocity of the waves determines the direction and rate of energy transport. As gravity wave periods are much smaller than the Earth's rotation period, we can neglect the parameter f in equation 1.2. Hence, the above equation reduces to equation 1.3.

$$\omega^2 = \frac{\omega_b^2 k^2}{(k^2 + m^2 + \frac{1}{4H^2})} \quad (1.3)$$

Therefore, the vertical phase speed of gravity waves (c_{pz}), is given by:

$$c_{pz} = \frac{\omega}{m} = \pm \frac{\omega_b k}{m(k^2 + m^2 + \frac{1}{4H^2})^{\frac{1}{2}}} \quad (1.4)$$

and, the vertical group velocity (c_{gz}) is given by:

$$c_{gz} = \frac{\partial \omega}{\partial m} = \mp \frac{\omega_b km}{(k^2 + m^2 + \frac{1}{4H^2})^{\frac{3}{2}}} \quad (1.5)$$

It can be noted from equations 1.4 and 1.5 that the direction of phase propagation and the wave propagation (i.e., direction of group velocity) are opposite to one another. Therefore, downward moving phases are always associated with upward propagating gravity waves (*Hines, 1960; Lindzen, 1990*). Pictorial representation of gravity wave propagation in the atmosphere is shown in figure 1.11a, wherein, variations in the background density are shown by nearly horizontal parallel lines. For downward phase propagation, an association of energy propagation in an obliquely vertical direction can also be seen here. As these waves propagate higher in altitudes, due to exponentially decreasing neutral density, the wave amplitude increases as a result of energy conservation. Such an increase in wave amplitude as the wave propagates to higher altitudes can be noted in figure 1.11a. *Djuth et al. (1997)* have shown the presence of gravity wave activity in the consecutive electron density profiles obtained from Arecibo radar (depicted in figure 1.11b). Here, gravity waves can be seen causing fluctuations of $\sim 4\%$ in the electron density at around 130 km.

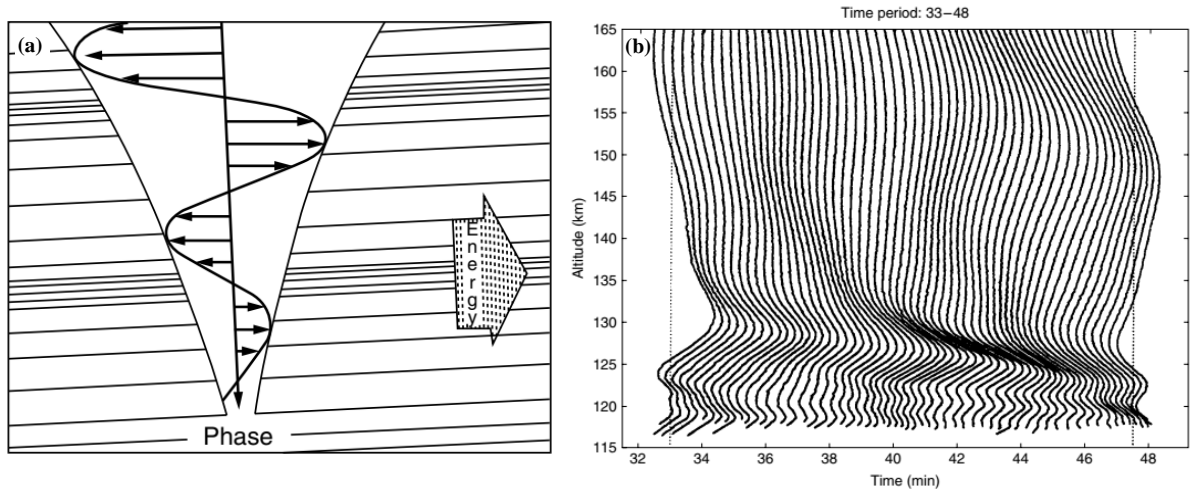


Figure 1.11: (a) Schematic representation of gravity wave propagation. Instantaneous neutral velocity vectors are shown by the arrows. Background density variations are shown by nearly horizontal parallel lines. [After (*Hines et al., 1974*)] (b) Electron density profiles measured by the Arecibo radar. The downward movement of the phase fronts can be clearly noticed here. [After *Djuth et al. (1997)*]

Clear downward phase movements with upward propagating gravity waves can be noted. But on this day, these waves are not seen in the region above about 130 km, which could be due to the dissipation of these waves with short vertical wavelength caused by viscous drag.

In the lower atmosphere, gravity waves can be generated due to changes in orography (e.g., *Long, 1955; Smith and Lyjak, 1985; Durran and Klemp, 1987; Alexander, 1996; Nance and Durran, 1998; Lott and Miller, 1997; Farmer and Armi, 1999*) or by the convective activities supported by the negative temperature gradient in this region (e.g., *Sato, 1993; Sato et al., 1995; Alexander and Pfister, 1995; Dewan et al., 1998; McLandress et al., 2000; Alexander et al., 2000; Singh and Pallamraju, 2016*). Gravity waves generated through topography have defined phase speed and frequency, whereas, convective activity excites a large spectrum of gravity waves (*Fritts and Alexander, 2003*). Generation of gravity waves from wind shears (e.g., *Davis and Peltier, 1979; Fritts, 1982, 1984; Scinocca and Ford, 2000; Pallamraju et al., 2014; Pramitha et al., 2015*), auroral processes over the high-latitudes (*Hocke, 1996; Pallamraju et al., 2001*), and equatorial electrojet over low-latitudes (*Raghavarao et al., 1988b; Pallamraju et al., 2010*) have also been reported. If the background conditions are favorable, these waves can propagate to higher altitudes and significantly contribute to the middle atmospheric dynamics (*Fritts and Alexander, 2003*). As the wave amplitudes increase with altitude, non-linear wave-wave interaction occurs in the MLT region, which leads to breaking of these waves. Energy deposition by the dissipation of waves accelerates the background mean flow at these altitudes. These further excite secondary waves in the MLT region (*Medvedev and Klaassen, 2000; Yigit et al., 2008*), which can reach thermospheric altitudes. Hence, a critical understanding of the gravity wave propagation activity in the thermospheric altitude is essential in order to address the coupling issues in the atmosphere.

1.3.5 Geomagnetic storms

So far we have discussed the effects of equatorial electrodynamics, different upper atmospheric phenomena, seasonally varying thermospheric wind structures, and neutral wave activity on the thermospheric dynamics. Furthermore, these drivers can get modified dur-

ing geomagnetically disturbed periods. The magnetosphere of the Earth is continuously bathed by the high-speed solar winds. The frozen-in magnetic fields in the high-speed solar winds drive geomagnetic disturbances in the Earth's magnetosphere. On occasions, when the IMF is directed southward, they merge with the northward directed geomagnetic field lines in the dayside, which is known as magnetic reconnection. After reconnection in the dayside, the geomagnetic field lines are dragged by the high-speed solar wind to the night side magnetotail region. Then the large-scale reconnections in the night side bring the plasma closer to the Earth. Eventually, these charged particles get trapped by the geomagnetic field lines. A resultant westward current gets developed due to the drifts of electrons and protons towards the east and west, respectively, when they encounter closed geomagnetic field lines. This westward current is known as the ring current, induces a southward magnetic field as measured by the magnetometers on the ground. Thus, an increase in the strength of the ring current indicates the onset of a geomagnetic storm. Different phases of a geomagnetic storm are characterized by measuring the induced southward magnetic field and represented by the disturbance storm time (Dst) index, which has been described in chapter 2. During geomagnetic storms, modifications in the ionospheric electric fields over the low- and equatorial-latitudes can be both prompt and delayed in nature. The convection electric field at the high-latitudes during geomagnetically disturbed periods promptly penetrate to the equatorial latitudes under favorable conditions, which is known as the prompt penetration electric field (e.g., *Nishida, 1968; Wolf, 1970; Senior and Blanc, 1984; Sastri et al., 2000; Kelley et al., 2003; Huba et al., 2005; Chakrabarty et al., 2005, 2015, 2017*). Auroral electrojet currents get intensified during the active phases of the geomagnetic storm as high energy particle precipitation takes place over high-latitude regions. Increased ionospheric currents generate Joule heating in the high-latitudes, which causes a rise in gas temperature (as shown in figure 1.12a) and drives meridional winds from the polar to the equatorial regions. These equatorward winds under the influence of Coriolis force generate an anti-Sq current vortex, that when encountered by the conductivity gradients, generates an electric field known as the disturbance dynamo field (e.g., *Blanc and Richmond, 1980; Scherliess and Fejer, 1997; Fejer et al., 2008; Yadav and Pallamraju, 2015; Yamazaki and Kosch, 2015; Fejer et al., 2017; Pandey et al., 2018*). In the equatorial region, the daytime disturbance dynamo electric field is in the westward direction and it is in the eastward direction during the

(*phase III* in figure 1.12b). Also, during these times, large scale wave features such as, the traveling ionospheric disturbances (TIDs) or the traveling atmospheric disturbances (TADs) are generated, which can bring the effect of the changes taking places at the high-latitudes to low- and equatorial-latitudes (Mayr *et al.*, 1978; Prolss, 1980). Storm time variation in the upper atmospheric composition has been observed in all the latitudes (e.g., Hedin *et al.*, 1977; Mayr *et al.*, 1978; Prolss *et al.*, 1988; Zhang and Shepherd, 2000; Zhang *et al.*, 2004, 2014). Figure 1.13 shows the results of the thermospheric circulation model (Roble, 1977), depicting changes in the thermospheric meridional wind pattern due to the Joule heating over high-latitudes. The top panel shows the thermospheric meridional wind patterns during geomagnetically quiet conditions. During equinoxes (figure 1.13a), the winds are poleward in both the hemisphere, whereas, during solstices (figure 1.13d), asymmetry in solar heating leads to the flow of the meridional winds from summer to winter hemisphere. The middle panel depicts the thermospheric wind pattern during equinox times (left side) and solstice times (right side) for moderate geomagnetic activity. The bottom panel depicts the thermospheric wind pattern during equinox times (left side) and solstice times (right side) for intense geomagnetic activity.

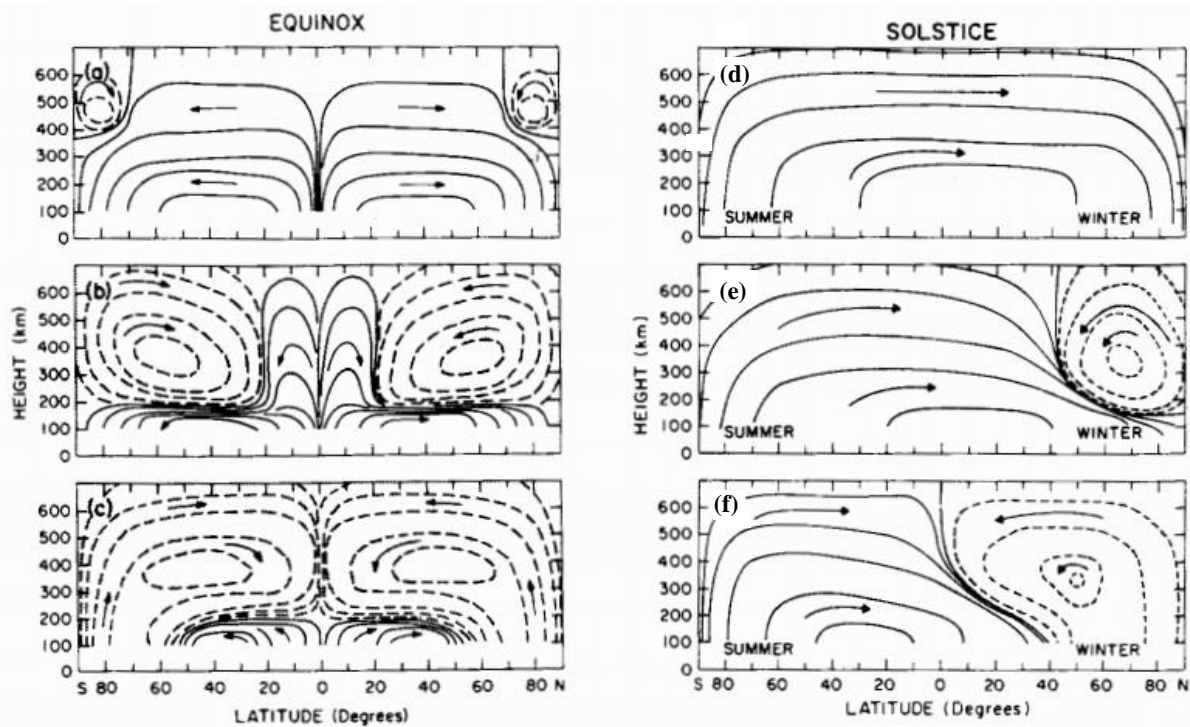


Figure 1.13: *Thermospheric meridional wind circulation pattern for equinoctial times during (a) quiet day, (b) average geomagnetic activity, and (c) in case of intense precipitation of energetic particles. (d), (e), and (f) are same as in (a), (b), and (c) but for solstice times. [After (Roble, 1977)]*

(10^{18} erg-s $^{-1}$). Due to heating at the high-latitudes, equatorward winds are set in, and they can reach up to 20° latitudes on both sides of the equator during equinoxes. But below 150 km, the winds remain poleward in all latitudes as a result of the absorption of solar UV radiation. In solstices, the equatorward winds generated from Joule heating at high-latitudes can reach 40° latitudes from the winter hemisphere, and below 150 km, the wind pattern remains unaltered. However, in the case of significant heating over the polar latitudes (10^{19} erg-s $^{-1}$) (bottom panel of figure 1.13), the equatorward meridional wind circulation increases drastically and alters the prevailing wind pattern above 150 km even till equatorial latitudes during equinoxes. Also, during solstices, high-latitude heating significantly modifies the thermospheric wind structure. These equatorward winds bring in the extra energy during geomagnetically active times from high-latitudes to low- and equatorial-latitudes. Therefore, during geomagnetic storms, the thermospheric dynamics of low- and equatorial-latitudes are coupled with the high-latitude processes.

1.4 Summary

Different drivers that control the morphology of the highly dynamic upper atmosphere of low- and equatorial-latitudes have been briefly discussed in this chapter. Their strengths are not the same every day but vary from day-to-day, day-to-night, seasons, solar activity, and geomagnetic activity. Energy transfer in the thermosphere through large-scale circulation has been shown to be comparable to the globally varying component of the solar EUV heating (*Dickinson et al.*, 1968; *Volland and Mayr*, 1970). Also, during geomagnetically active periods, the energy received in the high-latitudes through particle precipitation and electric fields is comparable to that from the absorption of solar EUV radiation (e.g., *Cole*, 1962, 1975; *Roble and Matsushita*, 1975; *Banks*, 1977). The morphological features of these different phenomena have been extensively studied. A negative temperature gradient in the troposphere supports convective activity, which generates wave motions of different spatial and temporal scales. These waves, while propagating, redistribute the energy and momentum in different parts of the atmosphere. Several dissipation factors, such as radiative damping, wave-induced diffusion, eddy diffusion, non-linear wave-wave interaction, thermal diffusion, kinematic molecular viscosity, and ion-drag affect the wave

propagation in the upper atmosphere (e.g., [Hines, 1960](#); [Pitteway and Hines, 1963](#); [Fritts, 1982, 1984](#); [Vadas and Fritts, 2005](#)). The first three parameters are effective in the region below the turbopause (~ 100 km altitude), whereas, the others are important for wave propagation in the altitudes above the turbopause. Large scale wave motions (planetary waves and tides) can be characterized by low temporal resolution measurements as these waves have higher time periods, whereas, in order to obtain information on gravity waves (of periods of few minutes to few hours), high-resolution measurements are needed. Numerous studies report the effects and morphology of planetary waves (e.g., [Gurubaran et al., 2001](#); [Sridharan et al., 2009](#); [Chau et al., 2009](#); [Pedatella and Forbes, 2010](#); [Sassi et al., 2012](#); [Guharay and Sekar, 2012](#); [Guharay et al., 2014, 2015](#); [Laskar et al., 2013, 2014, 2015](#); [Laskar and Pallamraju, 2014](#); [Singh and Pallamraju, 2015](#)) and tidal motions ([Talaat and Lieberman, 1999](#); [Oberheide and Gusev, 2002](#); [Forbes et al., 2002](#); [Hagan and Forbes, 2002](#); [Immel et al., 2006](#); [Forbes et al., 2008](#); [Pancheva et al., 2008, 2009](#); [Pancheva and Mukhtarov, 2011a](#); [Guharay et al., 2018, 2020](#); [Sridharan, 2017](#); [Sridharan and Meenakshi, 2020](#)) on the upper atmosphere. Conventionally, measurement of thermospheric airglow emissions using ground-based optical techniques have been used to understand the wave activity in the thermospheric altitudes. Gravity wave activity using nightglow measurements have been reported in many articles (e.g., [Shiokawa et al., 2009](#); [Taylor et al., 1995, 1998, 2007](#); [Lakshmi Narayanan et al., 2010](#); [Singh and Pallamraju, 2015, 2016, 2017, 2018](#)). But in the daytime, these optical measurements are sparse owing to the challenge of extracting faint dayglow from intense solar background radiation. Dayglow measurements using high-resolution photometers (e.g., [Narayanan et al., 1989](#); [Sridharan et al., 1991b, 1992b, 1993a, 1998](#); [Pallam Raju et al., 1996](#)) and imaging spectrographs (e.g., [Pallamraju et al., 2002, 2013](#); [Chakrabarti et al., 2001, 2012](#)) have opened up new avenues for understanding the thermospheric dynamics in the daytime. These developments have broadened our understanding of the daytime dynamics (e.g., [Sridharan et al., 1991a, 1992a, 1993b, 1994, 1995, 1999](#); [Pallam Raju et al., 1995, 1996](#); [Pallamraju et al., 2000, 2004b, 2010, 2011, 2020](#); [Pallamraju and Sridharan, 1998](#); [Pallamraju and Chakrabarti, 2005, 2006](#); [Das et al., 2010](#); [Laskar and Pallamraju, 2014](#); [Karan et al., 2016](#); [Karan and Pallamraju, 2017, 2018, 2020](#)). Such high-resolution dayglow measurements enable investigations on the coupling between the different atmosphere regions in the daytime through waves over low- and equatorial latitudes (e.g., [Laskar et al., 2013](#),

2014; *Pallamraju et al.*, 2014; *Laskar et al.*, 2015; *Pallamraju et al.*, 2016).

1.5 The objective of the thesis

As mentioned above, significant advancement has taken place in the understanding of daytime wave dynamics using optical measurements in the past two decades. However, the presence of clouds prevents the measurement of these optical emissions, and thereby hinders systematic investigations of gravity wave activity in the daytime thermosphere. Even when measurements are possible, photometric data provide information only on the gravity wave time periods. Specialized instruments of large field-of-view can yield information on spatial scale sizes in horizontal directions. Also, in the daytime, the emission layer thickness of three prominent thermospheric emissions (557.7, 630.0, & 777.4 nm) is very large. Therefore, from measurements of column-integrated dayglow, information on the vertical propagation of gravity waves, if any, can not be obtained unambiguously. In order to obtain information on the vertical propagation of gravity waves, measurements at close-by separated altitudes are needed. Knowledge of the vertically upward propagating gravity waves is extremely crucial as they alter the prevailing dynamics and energetic of the thermospheric altitude regions. The propagation of waves is affected by the background conditions (temperature, neutral density, winds, etc.). Therefore, any changes, such as solar flux and thermospheric winds, are expected to strongly influence the wave activity in the thermosphere. Also, gravity waves propagating in the vertical direction are considered to offer the seed perturbation for the generation of ESF irregularities in the evening hours, which adversely affects the trans-ionospheric radio wave communication. Based on the earlier works on the daytime dynamics, it is thought that the daytime thermosphere prepares the conditions, conducive or otherwise, for these plasma irregularities to occur in the nighttime ionosphere. In this background, this thesis aims to understand the following aspects of the daytime thermospheric dynamics of low- and equatorial-latitudes:

- I. Is it possible to obtain information on the vertical propagation characteristics of gravity waves in the daytime thermosphere?
- II. How do the changes in thermospheric background conditions (e.g., winds, tempera-

tures, and neutral densities) affect wave propagation in the daytime?

- III. Are the vertical propagation characteristics of gravity waves over low-and equatorial-latitudes influenced by the different energy inputs to the thermosphere (such as, solar radiation, particle precipitation at the high altitudes)? If they do, how can one quantify such variations?
- IV. Can the daytime gravity wave activity in thermospheric altitudes over the equatorial regions lead the way in the understanding of the day-to-day variation in ESF occurrences in the post-sunset hours?

1.6 Overview of the thesis

The different data sets used in the thesis work have been described in chapter 2. Spectral analysis techniques that are used to obtain wave characteristics, are discussed in this chapter. Chapter 3 describes an innovative approach to derive vertical propagation characteristics of gravity waves using digisonde derived electron densities. They have been compared with the wave properties obtained from the well-established optical measurements and earlier reported radar measurements. In chapter 4, daytime vertical propagation characteristics of gravity waves present in the equatorial thermosphere have been investigated to understand the day-to-day variability in the occurrence of ESF. Chapter 5 provides information on the variation in vertical propagation characteristics of gravity waves in geomagnetically quiet and disturbed conditions. Further, changes in them during disturbed days as compared to their quiet time values have been described in the light of high-to-low latitude coupling. Variation in solar activity level add additional variability in the incoming X-ray and EUV flux, which alter the thermospheric background conditions. The effect of these changes on the vertical propagation activity of gravity waves has been presented in chapter 6. Chapter 7 of the thesis summarizes all the findings presented in this thesis. Future scope for further investigation is also discussed in this chapter.

Chapter 2

Data sets and analyses techniques

2.1 Background

The Earth's upper atmosphere is a natural laboratory where different kinds of neutral and plasma processes occurring at all times. Critical understanding of these processes depends on how accurately we observe them and interpret the data that results from the measurements. Therefore, every researcher working in experimental/observational aspects needs to understand the data sets based on the existing knowledge in order to recognize the underlying processes. This thesis aims to understand the aspects of gravity wave activity in the daytime thermosphere over low- and equatorial-latitudes. Influences of different drivers on the thermospheric neutral wave dynamics have been investigated using independent measurements and observations along with some of the well-established empirical model outputs. In this chapter, we have briefly described these data sets and analyses techniques that have been used in this thesis.

2.2 Introduction

Measurements of different atmospheric parameters using both in-situ and remote sensing techniques, are used to derive information on the upper atmospheric dynamics. Measurements using satellites based platforms provide higher spatial resolution, whereas, ground-

based measurements yield high temporal resolution over a particular location. We have used ground-based experiments and observations to investigate the daytime thermospheric wave dynamics. Further, ground-based remote sensing can be both active and passive. For example, airglow measurement is a passive remote sensing method, wherein the naturally occurring emission rates are measured, and the medium is not disturbed during the course of observation. However, in the case of active remote sensing, such as digisonde/radars, radio waves are sent into the medium, and the reflected/scattered echo as a result of interactions between the radio waves and medium, is measured.

In this thesis, digisonde measurements from Ahmedabad (23°N , 72.5°E ; 14.9°N MLAT) and Trivandrum (8.5°N , 76.9°E ; 0.07°N MLAT); dayglow observation at OI 630.0 nm wavelength from Hyderabad (17.5°N , 78.5°E ; 8.9°N MLAT) have been used for the

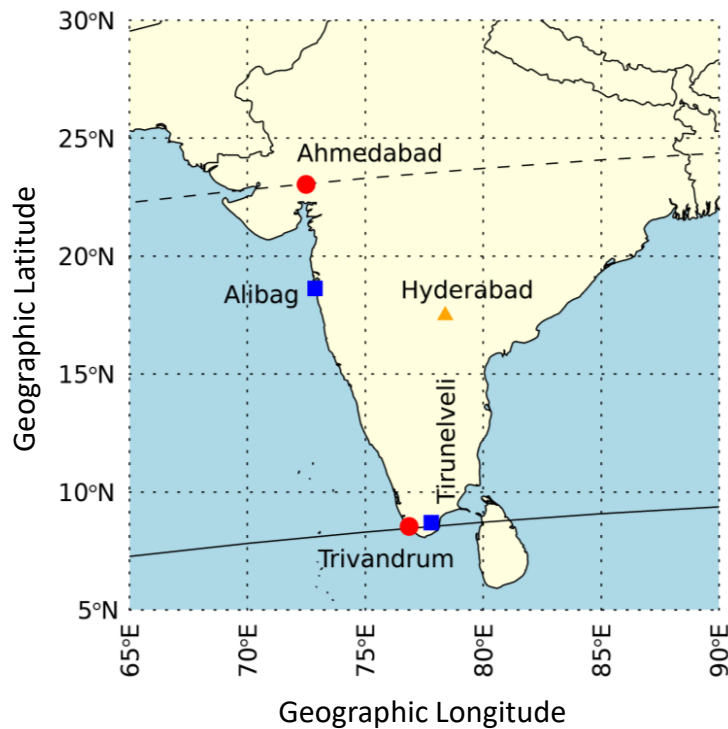


Figure 2.1: *The different locations of India from where the ground-based measurements have been obtained are shown. Digisonde measurements are taken from Ahmedabad and Trivandrum (red-colored circles). Dayglow observation at OI 630.0 nm emission data have been obtained from Hyderabad (orange-colored triangle). Magnetometer measurements used in the thesis are taken from Tirunelveli and Alibag stations (blue-colored squares). The solid and dashed lines represent the geomagnetic equator (obtained from IGRF-12; Emmert et al. 2010) and the typical location of the northern crest of EIA, respectively.*

investigation of daytime thermospheric neutral wave dynamics over low- and equatorial-latitudes. In addition, ground-based magnetometer measurements from Tirunelveli (8.7°N, 77.8°E; 0.15°N MLAT) and Alibag (18.6°N, 72.9°E; 10.5°N MLAT) have been used to calculate the strength of the EEJ over Indian longitudes. These locations over India are shown in figure 2.1.

2.3 Measurement techniques and data sets

2.3.1 Digisonde

Digisonde operates on the principle of radio wave reflection from the Earth's ionosphere. The height of reflection of these radio waves is calculated based on the time delay between transmitted and received signals. Information on the reflected frequency versus height of reflection is known as an ionogram (shown in figure 2.2). The reflection of radio waves from the ionosphere can be understood in the light of magneto-ionic theory. The Appleton-Hartree equation gives the refractive index (n) for radio waves propagating in the ionosphere (*Ratcliffe, 1959; Hargreaves, 1992*).

$$n^2 = 1 - \frac{X}{1 - jZ - \left[\frac{Y_T^2}{2(1-X-jZ)} \right] \pm \left[\frac{Y_T^4}{4(1-X-jZ)^2} + Y_L^2 \right]^{\frac{1}{2}}} \quad (2.1)$$

where, $X = \frac{\omega_N^2}{\omega^2}$, (ω_N and ω are the angular frequencies of plasma and radio waves, respectively); $Y_L = \frac{\omega_B \cos \theta}{\omega}$ and $Y_T = \frac{\omega_B \sin \theta}{\omega}$, (ω_B is the gyrofrequency of electrons; θ is the angle between radio wave propagation direction and geomagnetic field); and $Z = \frac{\nu}{\omega}$, (ν is the collision frequency of electrons) represents the absorption of radio waves in the medium. The angular frequency of electrons (ω_N) in the ionosphere is given by,

$$\omega_N = \sqrt{\frac{N_e e^2}{m \epsilon_0}} \quad (2.2)$$

where, N_e is the electron density; e is the electronic charge; m is the mass of the electron, and the permittivity of free space is denoted by ϵ_0 .

For simplification, if we neglect the absorption of radio waves (i.e., $Z = 0$) and effects of Earth's magnetic field ($Y_L = 0$ and $Y_T = 0$), then equation 2.1 reduces to,

$$n^2 = 1 - X = 1 - \left(\frac{\omega_N^2}{\omega^2}\right) \quad (2.3)$$

If the effects of the geomagnetic field are considered (i.e., $Y_L \neq 0$ and $Y_T \neq 0$), then equation 2.1 will give two values of refractive index. This is because, the presence of the magnetic field makes the ionosphere acts like a birefringent medium, and gives a double reflection of radio waves, i.e., ordinary and extraordinary (as shown in figure 2.2). The ionosphere does

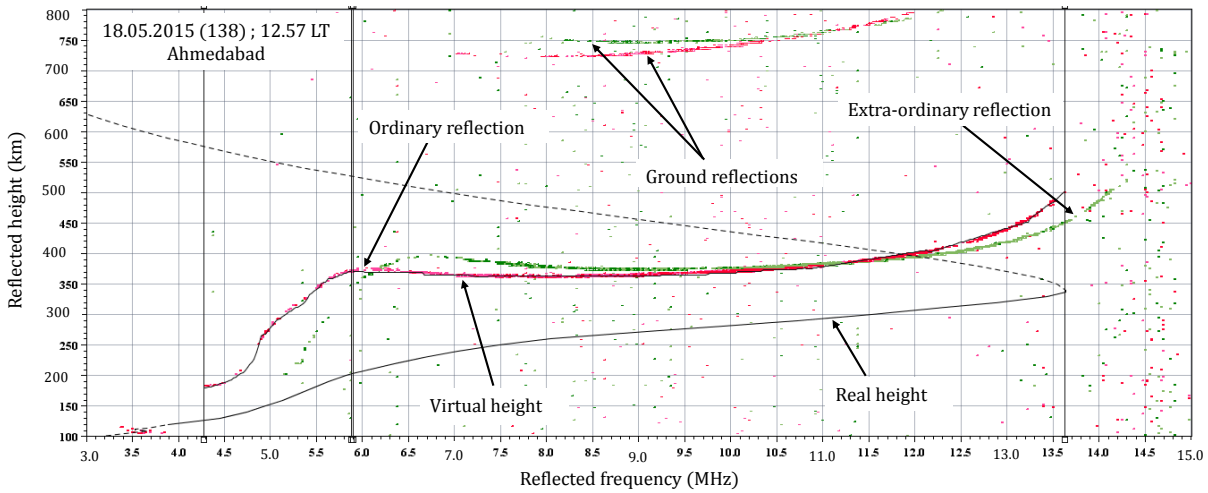


Figure 2.2: A typical ionogram obtained from digisonde at Ahmedabad, India on 18 May 2015 at 12.57 LT. Ordinary reflection (red-colored trace) and extraordinary reflection (green-colored trace) of radio waves in the ionosphere can be seen.

not change significantly within the distance of few wavelengths of radio waves (3-30 MHz of transmitted frequency corresponds to 100-10 m, respectively) with the assumption that the ionosphere is horizontally stratified. As the transmitted radio waves penetrate further into the ionosphere of increasing electron density (i.e., higher values of ω_N as per equation 2.2), the refractive index becomes smaller. Therefore, the ionosphere can be treated as slowly varying media of decreasing refractive indices with altitudes. The radio waves will bend more as they propagate deeper into the ionosphere and will get reflected at the critical level, where the frequency matches the plasma frequency ($\omega = \omega_N$). Digisonde, which uses the principle of radio wave reflection from the ionosphere, is one of the oldest, yet a very reliable technique to probe the ionosphere. Putting the values of the constants

in equation 2.2, the condition for radio wave reflection from the ionosphere becomes,

$$f_N = \sqrt{80.5N_e} \quad \& \quad N_e = 1.24 \times 10^{-2} \times f_N^2 \quad (2.4)$$

where, f_N is the frequency of the transmitted radio signal in Hz, and N_e is the electron density in m^{-3} .

Transmitted radio waves with frequencies higher than the frequency given by equation 2.4, will penetrate higher into the ionosphere and get lost in space. Therefore, ground-based digisonde measurements only provide information on the bottom side of the ionosphere. Similarly, topside profiles can be obtained from digisonde on-board satellites. The maximum value of the frequency reflected from the ionosphere is known as the critical frequency (f_oF_2). In the ionosphere, these radio pulses do not travel at the speed of light in free space but with the group velocity. The group speed of transmitted radio pulse is always less than the speed of light in free space, and hence, the true height of the plasma is always lower than the height of reflected echoes that appear in ionograms, which are known as virtual heights (as marked in figure 2.2). In this thesis work, the major portion of the data

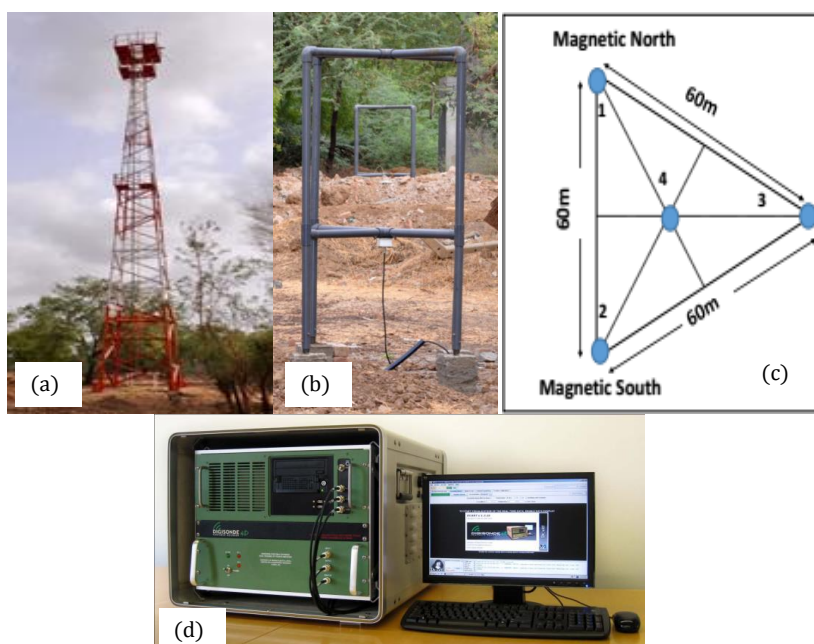


Figure 2.3: *Different components of digisonde of Ahmedabad, India. (a) Transmitter antenna, (b) Receiving antenna, (c) Layout of the four antennas, (d) Electronics and data acquisition system.*

sets used has been acquired from a digisonde portable sounder (DPS-4D) (*Reinisch et al., 2009*) that is in operation from Ahmedabad, India. Different components of the DPS-4D located at Ahmedabad are shown in figure 2.3. Digisonde has one antenna for transmitting radio waves, an array of four crossed loop receiver antennae, and an electronics unit. Typically, a digisonde is capable of transmitting radio waves in the frequency range of 0.1-30 MHz. For the digisonde located at Ahmedabad, ionograms are obtained every 7.5 minutes in continuous sounding mode with a sweep frequency in the range of 1-18 MHz in the daytime and 1-12 MHz in the nighttime. As Ahmedabad lies usually under the northern crest region of the EIA, the plasma parameters over this location are greatly affected by the varying strengths of the electrodynamics over the equatorial region (e.g., *Raghavarao et al., 1988b, 1991; Sastri, 1990*). These make the ionosphere highly dynamic, and therefore, the SAO software's auto-scaling feature (*Huang and Reinisch, 1996*) does not always accurately mark the traces of the reflected echoes (depicted in figure 2.4) in ionograms obtained from digisonde. Hence, all the ionograms are meticulously scaled

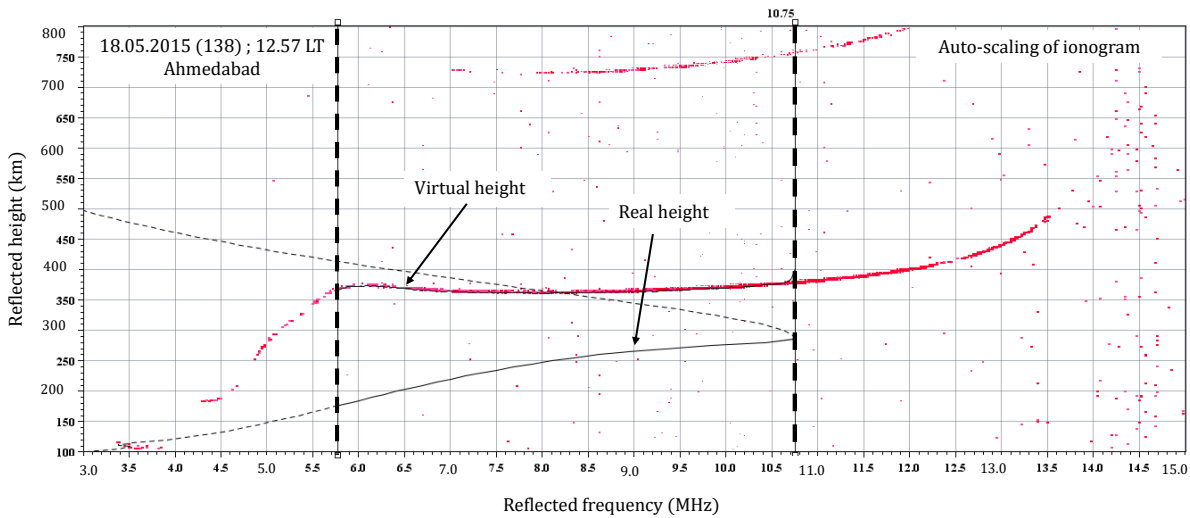


Figure 2.4: *Auto-scaling of the ionogram shown in figure 2.2. It can be noted here that even though the reflected echo ranges from 4.25 MHz to 13.5 MHz, the auto-scaling feature marked it incompletely (only from 5.75 MHz to 10.75 MHz; as can be seen by the black-colored vertical dashed lines).*

manually to avoid errors in the estimation of heights due to the auto-scaling. One can appreciate the need for manual scaling of ionograms when notices the bottom-side electron density profiles shown in figure 2.5. It can be clearly seen that the electron density profile obtained from auto-scaling (red-colored dashed line) is very different compared to that

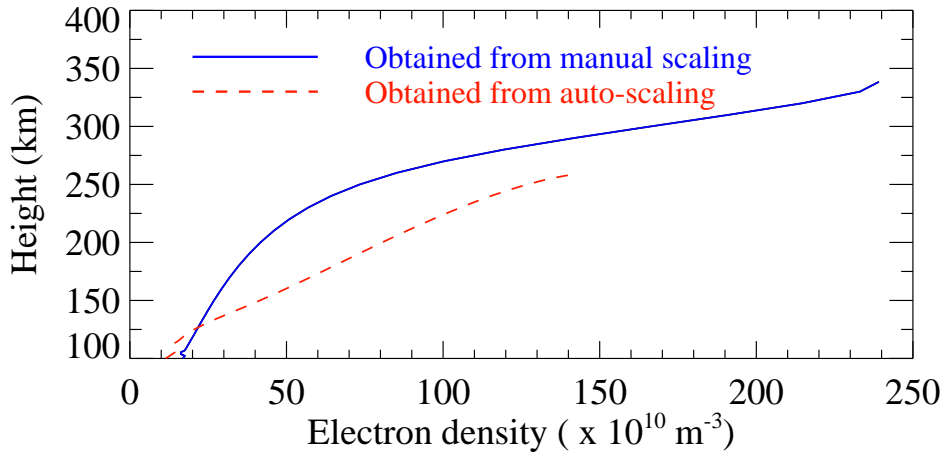


Figure 2.5: *Digisonde* derived bottom-side electron density profile for 18 May 2015 for auto-scaled (red-colored dashed line) and manually scaled ionogram (blue-colored solid line).

obtained from manual scaling (blue-colored line) of the ionogram. Therefore, in order to avoid any ambiguity in the inferences we draw or the results we would obtain from such analyses, in this thesis work we have only used manually scaled ionogram data. Further comparison between manual and auto-scaling is presented in figure 2.6. Here, variations in the daily noon-time values of the peak F_2 -layer frequency (foF_2), the peak F_2 -layer height (hmF_2), and the base height of F-layer ($h'F$) derived from auto-scaled and manually scaled ionograms are shown. The values of these ionospheric parameters obtained from manually scaled ionograms are significantly different compared to those obtained from auto-scaled ionograms. In the cases of foF_2 (figures 2.6a & 2.6b) and hmF_2 (figures 2.6c & 2.6d), auto-scaling of ionograms leads to underestimation of their values, whereas for the $h'F$ (figures 2.6e & 2.6f), the values are overestimated in auto-scaling when compared with those obtained from manual scaling of ionograms. Further, spectral analyses (figures 2.6g, 2.6h, and 2.6i) of these parameters reveal that variations in their auto-scaled and manually-scaled values show slightly different statistically significant periods.

We believe that as a result of these careful analyses, we have been able to obtain insightful results, hitherto not reported in the literature. These results are discussed in detail in chapters 3, 4, 5, and 6. Unlike the incoherent scatter radars, digisondes are low-cost instruments and are easy to install and operate. Also, being a radio technique, digisonde operations do not suffer from unfavorable weather conditions (such as clouds and rains), and thereby enabling uninterrupted measurements, which provide the much needed

continuous data to investigate the systemic behavior of the Earth's upper atmosphere.

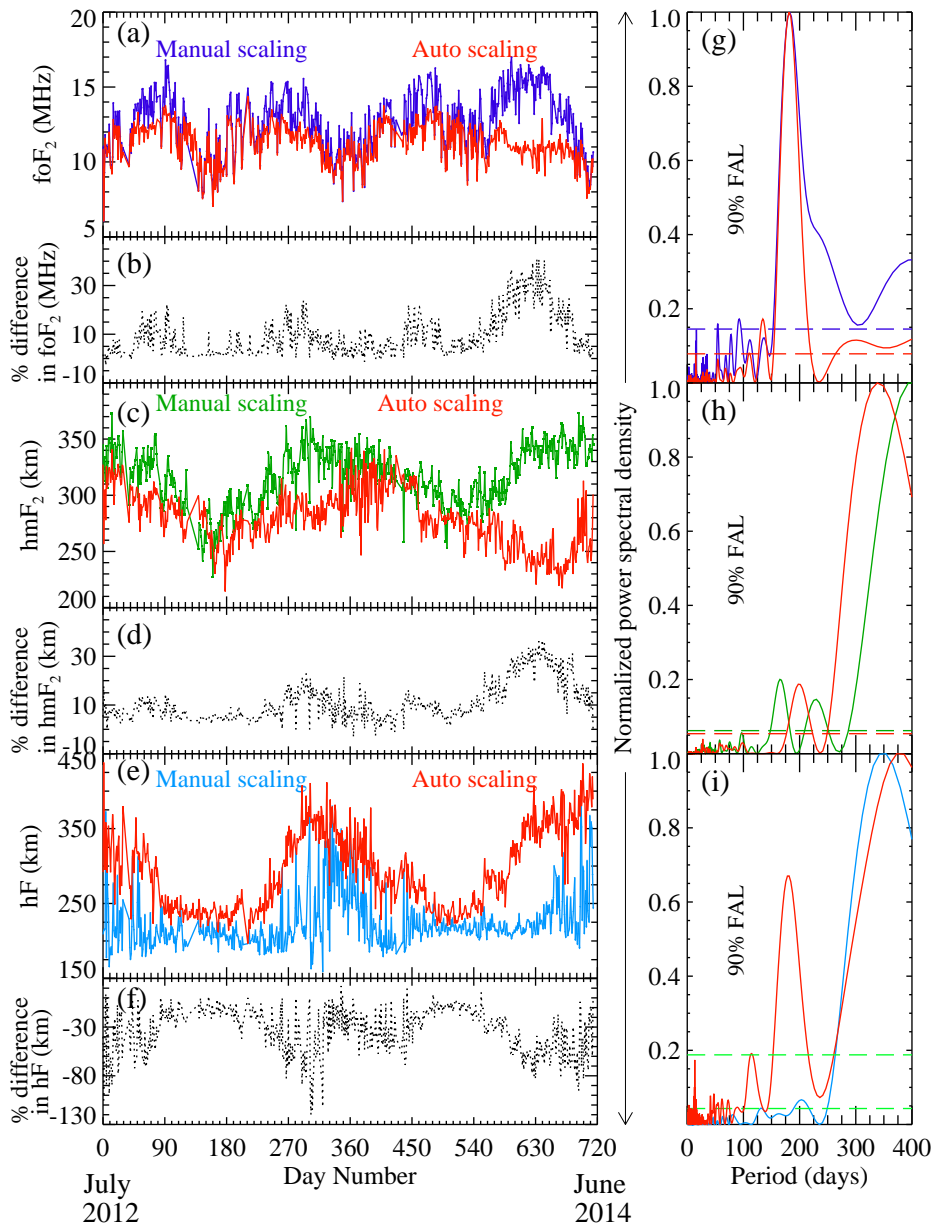


Figure 2.6: Variation in the local noon-time values of different ionospheric parameters for the duration of July 2012 - June 2014 as obtained from auto-scaled and manually scaled ionograms from Ahmedabad, India. (a) Variation in the daily noon-time values of foF_2 obtained from manually scaled (blue color) and auto-scaled (red) ionograms. (b) Percentage difference between the values obtained from auto-scaled and manually-scaled ionograms. (g) Periodogram analyses of the foF_2 values obtained from auto-scaled ionograms (blue color) and manually scaled ionograms (red color). Statistical significance levels of 90% are indicated by the dashed lines. (c), (d), and (h) are same as in (a), (b), and (g) but for the hmF_2 values. (e), (f), and (i) are same as in (a), (b), and (g) but for $h'F$ values.

2.3.2 Dayglow measurement

Naturally occurring emissions in the daytime upper atmosphere are known as dayglow, which are emitted as a result of the de-excitations of atmospheric species that are in the excited states. Dayglow emission rate depends on the concentration of the reactants and the background conditions. As a result, these emissions peak at different altitudes and they correspond to information on the dynamics that exist at the altitudes of their origin. These faint dayglow emissions are extremely difficult to measure as these are buried in the intense solar background continuum. However, measurements have become possible with the advent of new and innovative high spectral resolution optical techniques. These include those that use Fabry-Perot etalons (e.g., [Narayanan et al., 1989](#); [Sridharan et al., 1993a, 1998](#); [Pallam Raju et al., 1996](#)) and those that use high-resolution gratings ([Pallamraju et al., 2002, 2013, 2014](#); [Chakrabarti et al., 2012](#)). An overview of the past attempts made to detect dayglow has been explained in detail by [Pallam Raju et al. \(1996\)](#) and [Chakrabarti \(1998\)](#). Some of the results obtained by these high-resolution spectrographs are reviewed in [Pallamraju and Chakrabarti \(2006\)](#). In this thesis work, however, we have used the data obtained from the multi-wavelength imaging spectrograph using echelle grating (MISE). It is a high-resolution and large field-of-view spectrograph, capable of obtaining information on the emission rates at three different wavelengths (e.g., 557.7, 630.0, and 777.4 nm) simultaneously ([Pallamraju et al., 2013](#)). The schematic diagram of MISE is shown in figure 2.7, wherein, light from a large field-of-view is collected using an all-sky lens and then passed through a narrow slit. Further, this incoming light is collimated using an $f/11$ lens of focal length 1130 mm, and the parallel beams are then made to fall on an echelle grating. The diffracted beam from the grating (31.6 lines mm^{-1} , blaze angle = 63.5°) is imaged on a CCD through $f/6$ optics with an apochromatic lens of 600 mm focal length. In order to extract the dayglow from the strong solar background, high-resolution in MISE is achieved using an echelle grating operating at higher incident and diffraction angles. Mosaic filters are used at the image plane to avoid overlapping of multiple orders of different wavelengths. In this thesis, dayglow measurement at 630.0 nm wavelength using MISE from Hyderabad has been used. The OI 630.0 nm photons are emitted when the atomic oxygen de-excites from $\text{O}(^1\text{D})$ to $\text{O}(^3\text{P})$ energy state. Therefore, the variation in emission intensity of OI 630.0 nm depends on the production

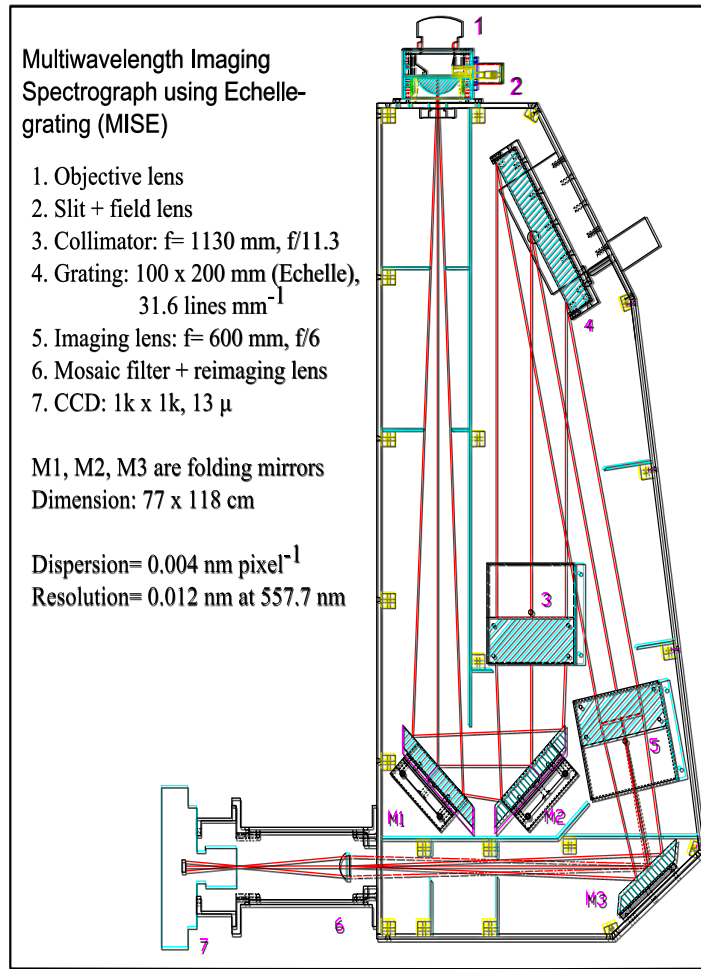


Figure 2.7: Schematic of the MISE that is used to obtain dayglow emission rates at three wavelengths, namely 557.7 nm , 630.0 nm , and 777.4 nm . Red-colored lines represent the ray diagram. [After Pallamraju et al. (2013)]

of $\text{O}(^1\text{D})$ state through various mechanisms, such as photoelectron impact excitation of atomic oxygen, photo-dissociation of molecular oxygen, dissociative recombination of O_2^+ , and cascading of $\text{O}(^1\text{S})$ (Solomon and Abreu, 1989; Witasse et al., 1999). Photoelectron impact excitation contributes maximum to the production of $\text{O}(^1\text{D})$, followed by photo-dissociation of molecular oxygen, whereas, dissociative recombination plays a significant role in causing the observed temporal variability in the emissions (Sridharan et al., 1992a; Pallam Raju et al., 1996). The OI 630.0 nm dayglow emission peaks at an altitude of around 230 km and has a layer thickness of about 100 km (Zhang and Shepherd, 2004; Shepherd and Cho, 2021). The daysky spectra obtained using MISE (shown in figure 2.8a) are compared with the normalized solar spectrum obtained from the BASS2000 Solar Survey Archive (http://bass2000.obspm.fr/solar_spect.php). The daysky spectra

are scaled to the continuum levels of the solar spectrum. The difference between the sky spectra and solar spectrum could be due to emissions (dayglow), absorption (telluric absorption), and scattering in the Earth's atmosphere. The filling-in of Fraunhofer lines due to atmospheric scattering is known as the Ring effect (*Grainger and Ring, 1962*). The magnitude of the Ring effect has been shown to be similar for nearby spectral lines with equivalent line strengths (normalized depth \times half-width) (*Pallamraju et al., 2000*). Here in figure 2.8c, the difference between the solar spectrum and sky spectra represents the atmospheric contribution. Filling-in at a wavelength of 630.03 nm is due to both dayglow emission and Ring effect, whereas, in the case of the 630.06 nm, it is only due to the Ring

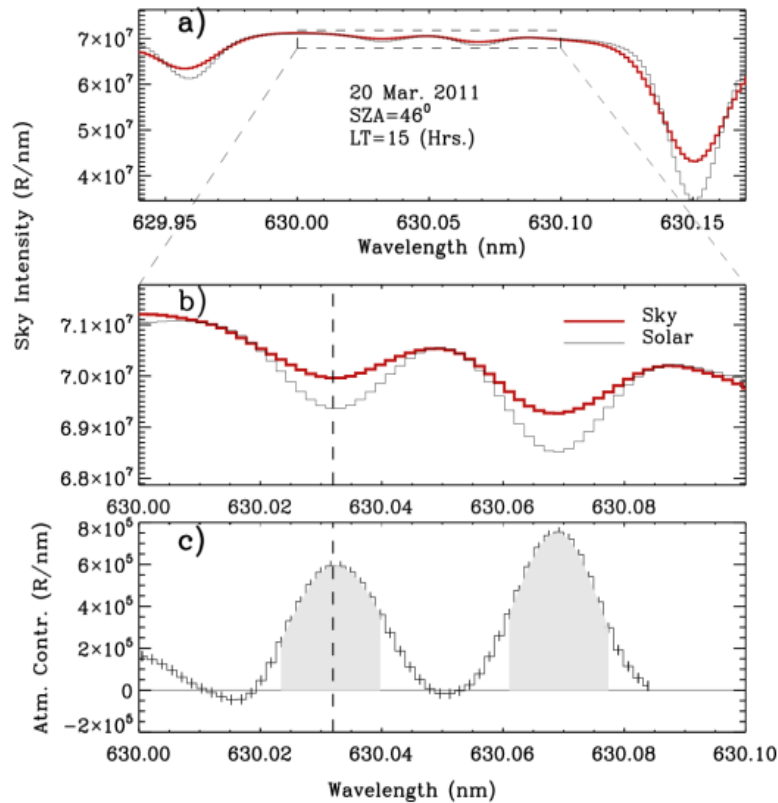


Figure 2.8: Method of extraction of dayglow emission rate at 630.0 nm wavelength. (a) Sky spectrum obtained from MISE are shown (red-colored curve) along with the standard solar spectrum (black-colored curve). The dotted rectangle refers to the emission region of interest around 630.0 nm. (b) Same as above but zoomed in around the emission region of OI 630.0 nm emission. It can be seen that the sky spectrum is filled-in as compared to the solar spectrum. (c) Difference between the sky and the solar spectrum showing the contribution of dayglow emission and atmospheric scattering (Ring effect). [After *Pallamraju et al. (2013)*]

effect. Further, as these two wavelengths are not of identical line strengths, in order to scale the scattering contribution at 630.06 nm for the dayglow emission line, factor f is calculated.

$$f = \frac{(I_{c_1} - I_{d_1}) \times \lambda_{\omega_1}}{(I_{c_2} - I_{d_2}) \times \lambda_{\omega_2}} \quad (2.5)$$

where, I_{c_1} is the normalized intensity at the continuum level, I_{d_1} is the depth of the Fraunhofer line where emission exists and λ_{ω_1} is the half-width of the Fraunhofer absorption line centered at 630.03 nm, and I_{c_2} , I_{d_2} , and λ_{ω_2} are the corresponding values at 630.06 nm.

Therefore, the dayglow emission intensity rate at 630.03 nm is given by,

$$Dayglow = (Area_{curve1} - Area_{curve2}) \times f \quad (2.6)$$

where, $Area_{curve1}$ is the area under the curve for the Fraunhofer line centered at 630.03 nm, and $Area_{curve2}$ is the area under the curve for the line centered at 630.06 nm. This retrieval method of dayglow is well-established and is described in great detail in the literature (*Pallamraju et al.*, 2002, 2013).

2.3.3 EEJ Data

EEJ refers to the intense eastward current in the daytime over the geomagnetic equatorial E-region, which is confined to a very narrow range of latitudes and altitudes. A brief description of the EEJ is given in chapter 1 (section 1.3.1.1). Conventionally, EEJ strength is derived from the observations of the horizontal component of the geomagnetic field (H) from equatorial and off-equatorial stations (*Cohen and Bowles*, 1963; *Rastogi and Iyer*, 1976; *Rastogi and Patil*, 1986). Over Indian longitudes, EEJ strength is calculated from the measurements of H from Tirunelveli (TIR), and Alibag (ABG). Alibag being a magnetically off-equatorial location, it is not influenced by the EEJ currents, whereas, Tirunelveli (TIR), a magnetic equatorial location with the maximum influence of currents induced due to the EEJ.

$$EEJ = \Delta H_{TIR} - \Delta H_{ABG} \quad (2.7)$$

Here, the ΔH values are obtained by subtracting the average nighttime values (23-03 LT) for each station to remove the effects of Earth's crustal magnetic fields. The off-equatorial ΔH values are finally subtracted from those of the equatorial station to remove the contribution of magnetospheric currents. Therefore, the difference between ΔH_{TIR} and ΔH_{ABG} provides the strength of the EEJ current. Hourly values of the horizontal component of the Earth's magnetic field are available at <http://wdciig.res.in/WebUI/ObservatoryDataahInfo.aspx>.

2.3.4 Solar $F_{10.7cm}$ flux

The solar EUV and X-ray radiation, which directly impact the thermospheric dynamics, significantly vary with the solar cycle of 11 years. As these high energy radiations can not be measured from the ground, solar $F_{10.7cm}$ flux is used as a proxy. Solar $F_{10.7cm}$ flux is the flux density measured in 100 MHz band centered at 2800 MHz and measured in solar flux units (sfu; $1 \text{ sfu} = 10^{-22} \text{ Wm}^{-2} \text{ Hz}^{-1}$). Solar $F_{10.7cm}$ flux is known to correlate extremely well with the sunspot number (*Floyd et al., 2005*). From figure 2.9, it can be seen that the variation in measured $F_{10.7cm}$ flux (bottom panel) for different solar cycles for

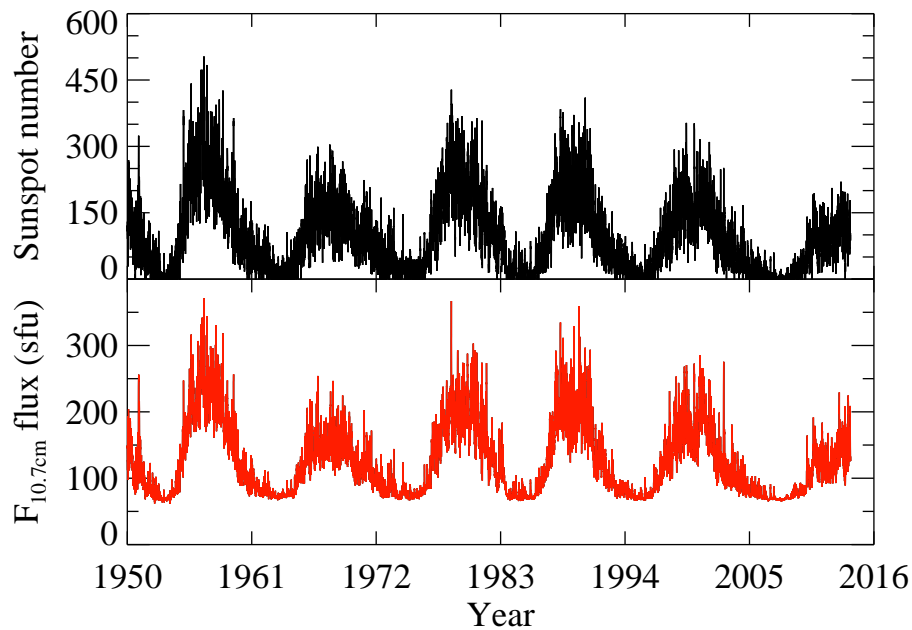


Figure 2.9: Top panel shows the variation in daily sunspot numbers for the duration 01/01/1950 to 31/12/2014. And the bottom panel shows the daily solar $F_{10.7cm}$ flux values measured in solar flux unit (sfu) for the same duration.

the duration of 01/01/1950 to 31/12/2014 are identical to the variation in solar activity level for the same period, as represented by the daily sunspot numbers (shown in the top panel). Further, the solar $F_{10.7cm}$ flux can be measured accurately from the ground in all weather conditions and hence can be used as a proxy to solar activity variation. Solar $F_{10.7cm}$ flux data have been obtained from http://lasp.colorado.edu/lisird/data/noaa_radio_flux/.

2.3.5 Disturbance storm time (Dst) index

Dst index is calculated as the average of horizontal magnetic fields, measured from four different locations, namely, Hermanus (34.4°S, 19.2°E), Kakioka (36.2°N, 140.2°E), Honolulu (21.3°N, 158.1°W) and Sanjuan (18.4°N, 66.1°W). These mid-latitude observatories are chosen as they are sufficiently away to be free from the effects of the auroral and equatorial electrojets and they are evenly distributed in longitudes. Due to particle precipitation over high-latitudes during geomagnetic storms, ring current (westward) gets enhanced, which leads to an increase in the induced magnetic field (southward). The Dst index represents the strength of this induced magnetic field and is used as an indicator of the occurrence of geomagnetic storms. In figure 2.10a, the variation in the Dst index for 17/03/2015 to 26/03/2015 is shown. For a typical geomagnetic storm, the Dst index first shows a sudden rise due to compression of the geomagnetic field lines by the incoming solar wind pressure. This rise in the Dst values refers to the storm sudden commencement (yellow-colored shaded region in figure 2.10a). The sharp decrease in the Dst values to a minimum due to increased ring current is known as the main phase of the storm (green-colored region of figure 2.10a). As the ring current decays, the Dst values start increasing and recovers to positive values. This phase is termed as the recovery phase of the storm (orange-colored shaded region of figure 2.10a). In the present thesis, we have obtained the Dst index from the ISGI website (<http://isgi.unistra.fr/index.php>) to identify the geomagnetic storms.

2.3.6 Auroral electrojet (AE) index

The AE indices are characterized as a measure of auroral electrojet currents over the high-latitude region (*Davis and Sugiura, 1966*). It is calculated using the measurement of the horizontal component of geomagnetic fields in the northern auroral region (60° - 70° N). Variations in the horizontal magnetic field values above quiet time level (average of five geomagnetically quiet days) corresponding to the same universal times for all the stations are superposed. The upper and lower envelopes of this superposition define the AU (amplitude upper) and the AL (amplitude lower) indices, respectively. In the absence of zonal currents in the auroral ionosphere or magnetosphere, AU and AL represent the maximum eastward and westward electrojet at any given time. Therefore, the difference between the two solely depends on the strength of auroral electrojet currents and is independent of other currents present in the ionosphere, if any. Hence, AE values are defined

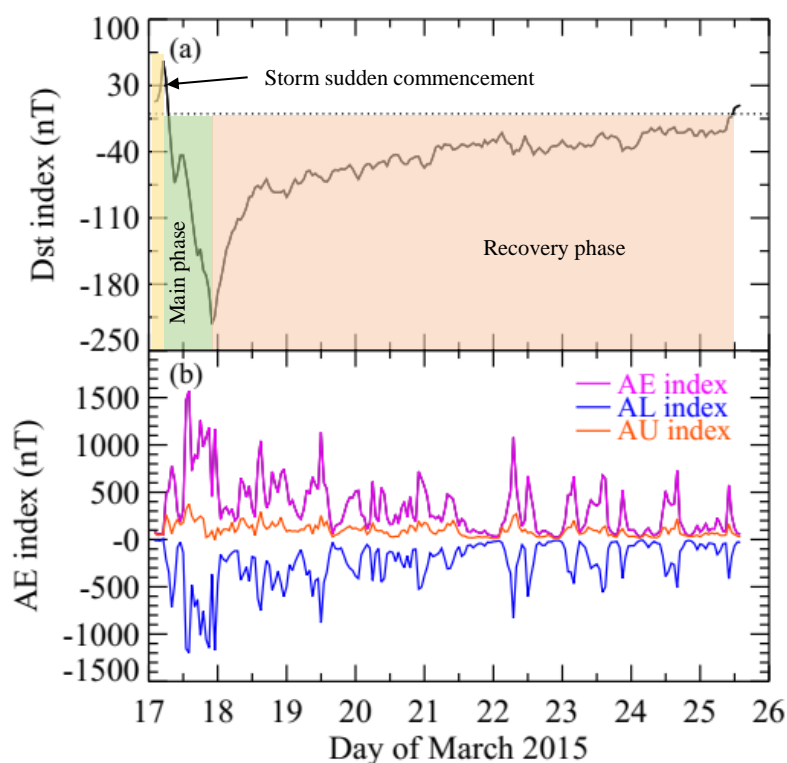


Figure 2.10: Variation in geomagnetic indices for the duration 17/03/2015 to 26/03/2015. (a) Hourly Dst index variation showing different phases of geomagnetic storms. (b) Variation in AE (pink-colored curve), AU (orange-colored curve), and AL (blue-colored curve) for the same duration.

as the separation between these two envelopes ($AE = AU - AL$). Variation in these indices during the St. Patrick's day storm of 2015 are shown in figure 2.10b. During geomagnetic storms, high energy particle precipitation causes an enhancement in auroral currents, which is seen in the auroral electrojet (AE) index. We have used the AE indices as a proxy of the energy deposition (*Akasofu, 1981*) over the high-latitude upper atmosphere during the times of geomagnetic storms. The AE index values have been obtained from <http://isgi.unistra.fr/index.php>.

2.3.7 HWM14 wind and NRLMSISE temperature

To investigate the effects of seasonally varying winds on the thermospheric neutral wave dynamics, we have used the HWM14 model-derived thermospheric winds (*Drob et al., 2015*) over Ahmedabad for geomagnetically quiet days. Also, the NRLMSISE model-derived parameters (*Picone et al., 2002*), such as, neutral temperatures and mass density of the thermosphere in the daytime have been used in the thesis.

2.4 Analyses techniques

As discussed in chapter 1 (section 1.3.4), waves perturb the atmospheric parameters during their course of propagation and manifest themselves as time-varying fluctuations in different parameters. Therefore, wave characteristics can be obtained from these fluctuations using time series analysis. Various methods have been used over the years to find the periodic signals present in the data, namely Fourier methods (*Schuster, 1898; Lomb, 1976; Scargle, 1982; VanderPlas, 2018*), phase-folding methods (*Stellingwerf, 1978; Dworetzky, 1983; Graham et al., 2013*), least-square methods (*Reimann, 1994*), Bayesian approaches (*Bretthorst, 2013; Gregory and Loredó, 1992*). In the thesis, we have carried out time series analysis using Fourier transform (FT) and Lomb-Scargle Fourier transform (LSFT), which are briefly discussed in the following sections.

2.4.1 Fourier Transform (FT)

The Fourier transform $G(f)$ of a continuous function $g(t)$ is given by,

$$G(f) = \int_{-\infty}^{+\infty} g(t)e^{-2\pi jft} dt \quad (2.8)$$

where, $j = \sqrt{-1}$.

The above equation suggests that $G(f)$ will have large non-zero values only if the function $g(t)$ has a periodic component of scale t . And, the inverse Fourier transform is given by,

$$g(t) = \int_{-\infty}^{+\infty} G(f)e^{2\pi jft} df \quad (2.9)$$

The power spectral density (PSD) is defined as the squared amplitude of the Fourier transform. PSD is a function of frequency (f) and represents the contribution of each frequency to the signal. It is given by,

$$P(f) = |G(f)|^2 \quad (2.10)$$

In Fourier transform, a function with characteristic scale T will transform to a scale of $1/T$. Therefore, a narrow function will transform into a broad function and vice-versa. So far, we have been discussing the Fourier transformation of continuous signals that are well defined for all the times, i.e., $-\infty < t < +\infty$. But in practice, measurement of any signal is always limited to finite time and with a particular sampling rate. Fourier transform of such measurement is known as discrete Fourier transform (DFT), and it will be of the form,

$$G(f) = \sum_{i=1}^{N_0} g(t_i)e^{-2\pi jft_i} \quad (2.11)$$

where, $g(t_i)$ corresponds to measurement at a time t_i , with $i = 1, 2, 3, \dots, N_0$. The corresponding power spectral density will be known as a periodogram ([Schuster, 1898](#);

Thompson, 1971; Deeming, 1975).

$$P(f) = \frac{1}{N_0} \left| \sum_{i=1}^{N_0} g(t_i) e^{-2\pi j f t_i} \right|^2 \quad (2.12)$$

The factor $1/N_0$ is the normalization factor of the transformation. For an illustration of the effects of measurements of a signal at particular sample rates, we have reproduced an example from *VanderPlas (2018)* and presented it in figure 2.11. The observation of any continuous signal, $g(t)$, at a uniform sampling rate, $W(t)$, for a finite span of time, can be represented as the product of the two.

$$g_{obs}(t) = g(t)W(t) \quad (2.13)$$

The uniform sampling can be thought of well-known Dirac-comb function as shown in the middle panel of figure 2.11. The Fourier transform of a Dirac-comb is also a Dirac-comb

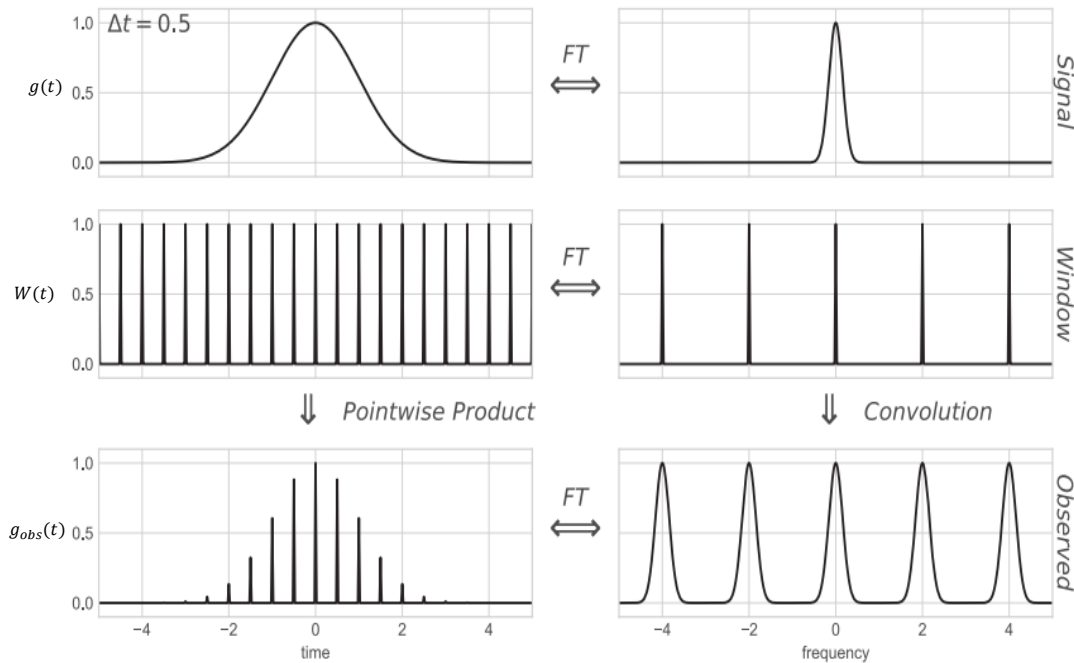


Figure 2.11: *In the top panel a signal $g(t)$ and its Fourier transform are shown. The middle panel represents an evenly spaced sampling, $W(t)$, which resembles the Dirac-comb function and the corresponding Fourier transform. The bottom panel shows the observation $g_{obs}(t)$. The Fourier transform of $g_{obs}(t)$ is given by the convolution of the Fourier transforms of $g(t)$ and $W(t)$. [After *VanderPlas (2018)*]*

with a characteristic scale inverse of the actual function (shown in the middle panel of figure 2.11). Therefore, the observations limited for a finite time lead to measurement of the signal as $g_{obs}(t)$ as shown in the bottom panel of figure 2.11. By virtue of its definition, the Fourier transform of the product of two functions is equal to the convolution of Fourier transforms of each function. Hence, the effects of the observing window lead to multiple identical frequencies that resulted in the transformation with spacing $1/T$. Therefore, evaluating the Fourier transform in the frequency range $0 \leq f < \frac{1}{T}$ is sufficient to ascertain all the frequency information of the signal. This implies that if we sample a signal at a rate of $1/T$, we can only retrieve information fully on the frequencies present in the signal, if the signal is band-limited between $\pm 1/2T$. This is the famous Nyquist criterion of data sampling. Therefore, for evenly spaced data at an interval of T , evaluation of DFT (given in equation 2.11) at a set of frequencies f_i is enough to retrieve information on the original data.

$$f_i = \frac{i}{T} \quad (2.14)$$

where $i = -\frac{N_0}{2}, \dots, +\frac{N_0}{2}$. The periodogram defined by equation 2.12 is an even function, therefore, all the information is present in the positive values of f_i .

2.4.2 Lomb Scargle Fourier transformation (LSFT)

In real-time experiments or observations, the sampling rate of measurements becomes non-uniform due to several practical considerations, such as, technical issues, unfavorable sky conditions, varying integration or exposure times, etc. In such cases of non-uniform sampling of a signal, the symmetry shown in the Dirac-comb structure (middle panel of figure 2.11) breaks and results in a very noisy Fourier transform. This makes it nearly impossible to recover the periodic information present in the actual signal. Also, these noises remain non-zero even with finer sampling. Another issue with this classical periodogram is the spectral leakage, which refers to non-zero finite values of periodogram (equation 2.12) in frequencies other than the signal frequency. Aliasing in frequencies is an example of spectral power leakage from high frequencies to low frequencies. In this background, Scargle derived a modified periodogram (equations 2.15 and 2.16) for spectral analysis of

a signal sampled at a non-uniform rate (*Scargle, 1982*).

$$P_{LSFT}(f) = \frac{1}{2} \left[\frac{(\sum_i g(t_i) \cos(2\pi f[t_i - \tau]))^2}{\sum_i \cos^2(2\pi f[t_i - \tau])} + \frac{(\sum_i g(t_i) \sin(2\pi f[t_i - \tau]))^2}{\sum_i \sin^2(2\pi f[t_i - \tau])} \right] \quad (2.15)$$

where,

$$\tau = \frac{1}{4\pi f} \tan^{-1} \left(\frac{\sum_i \sin(4\pi f t_i)}{\sum_i \cos(4\pi f t_i)} \right) \quad (2.16)$$

The difference between classical periodogram $P(f)$ (equation 2.12) and $P_{LSFT}(f)$ (equation 2.15) is that the denominators $\sum_i \cos^2(2\pi f[t_i - \tau])$ and $\sum_i \sin^2(2\pi f[t_i - \tau])$ are dissimilar than $\frac{N_0}{2}$, which is the expectation values of the two for the limit of evenly sampled case. The Scargle periodogram matches well with the model fitted frequencies constructed by χ^2 , the goodness of fit, as considered by *Lomb (1976)*. This similarity between the Fourier periodogram by Scargle (equation 2.15) and least square analysis (*Lomb, 1976*) has led to the name of the Lomb-Scargle periodogram for equation 2.15. The values of τ for each frequency ensure the invariance of the periodogram by time shifts. In the case of input data containing only noise, the $P_{LSFT}(f)$ shows an exponentially decaying nature, which helps to distinguish the spectral peaks due to signal and those due to noise. The significance of the derived frequencies using the Lomb-Scargle periodogram is quantified by the false alarm probability (FAP). The FAP value is related to spectral power (z) and the number of independent frequencies (N_i) by the following relation,

$$FAP = 1 - (1 - e^{-z})^{N_i} \quad (2.17)$$

$$N_i = -6.362 + 1.193 N_0 + 0.00098 N_0^2 \quad (2.18)$$

where, N_0 is the number of data points in the observation. Therefore, the frequencies with spectral peaks greater than or equal to z will be significant for a given FAP. For example, FAP=0.01 means that the significant level z will be calculated with 99% statistical significance (*Scargle, 1982; Horne and Baliunas, 1986*). The uncertainty in the frequencies estimated from the Lomb-Scargle periodogram is given by *Bretthorst (1988)*.

$$\delta f = \frac{1.1\sigma}{AT_{total}\sqrt{N_0}} \quad (2.19)$$

where, σ is the standard deviation of the data obtained after the signal has been subtracted (which corresponds to the noise), T_{total} is the total observation time, and N_0 is the number of data points in the observation. An example is shown in figure 2.12 to illustrate the advantage of the Lomb-Scargle periodogram over classical Fourier transformation. Variation in daily values of solar $F_{10.7cm}$ for 2012 is shown in figure 2.12a. Both the Fourier transform (figure 2.12b) and the Lomb-Scargle periodogram (figure 2.12c) show

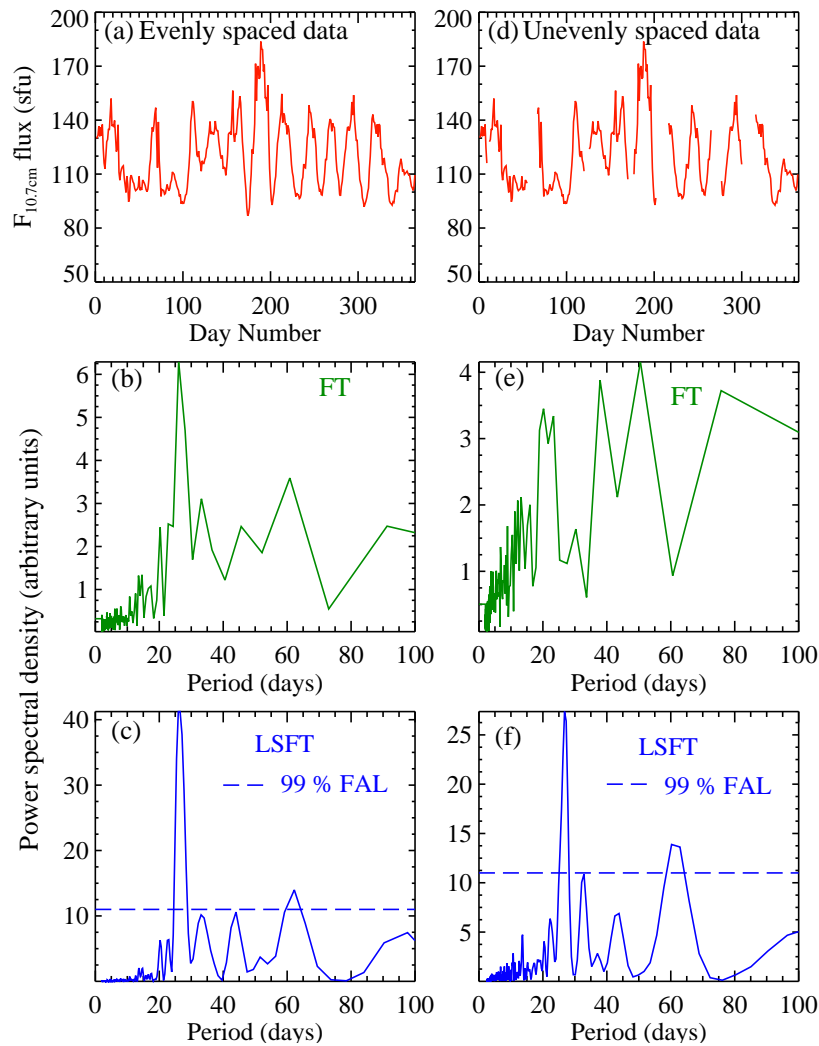


Figure 2.12: (a) Variation of the evenly spaced solar $F_{10.7cm}$ flux data for 2012. (d) Same as in (a) but unevenly spaced. (b) A periodogram obtained using the Fourier transform (FT). The presence of a well-known 27-day periodicity can be seen. (c) Same as in (b) but obtained using the Lomb-Scargle Fourier transform (LSFT). Here also 27-day period is significant. The dashed line represents the significance level of 99%. (e) Same as in (b), and (f) is same as shown in (c) but for the case of uneven spacing of solar $F_{10.7cm}$ flux as shown in (d).

the presence of the well-known 27-day period owing to solar rotation. Then the solar $F_{10.7cm}$ values for some random days are removed to make the data unevenly spaced and are shown in figure 2.12d. The Fourier transform of this unevenly spaced data becomes noisy with spectral powers showing higher values than those for the 27-day period (figure 2.12d). In contrast, the Lomb-Scargle periodogram still recovers the information on the 27-day periodicity that is present in the input data, even when the data are unevenly spaced.

The Lomb-Scargle periodogram is a unique and very popular technique to derive frequencies present in unevenly sampled data as it is based on Fourier analysis (*Scargle, 1982*), but can be understood as a least-square fitting method (*Lomb, 1976*), and can also be derived from the approach of Bayesian probability theory (*Jaynes, 2003; Smith and Erickson, 2012*).

2.4.3 Wavelet analysis

Both the classical Fourier transform and the Lomb-Scargle periodogram discussed in the previous sections, consider the signal to be stationary in time. Therefore, they do not provide information on the temporal evolution of the frequencies present in the signal. Assume a signal y_1 (shown in figure 2.13a) contains three different periods as given by equation 2.20.

$$y_1 = 3.0 \sin\left(\frac{2\pi}{40x}\right) + 2.5 \cos\left(\frac{2\pi}{90x}\right) + 3.5 \sin\left(\frac{2\pi}{180x}\right) \quad (2.20)$$

where, $x = 0, 1, \dots, 1000$.

Here, this synthetically generated signal has periods of 40, 90, and 180 days throughout the data range. The FFT periodogram confirms the presence of these periods in figure 2.13b. In contrast to figure 2.13a, the signal shown in figure 2.13d is created in such a way that these periods are present in the data for different time intervals. Also, in this case, the time series analysis indicates the presence of those periods in the signal (as depicted in figure 2.13e), albeit with smaller PSD values as these periods are not present all through the data range (as shown in figure 2.13d). Hence, it can be seen that the FFT brings out the periods that are present in the data. However, in almost

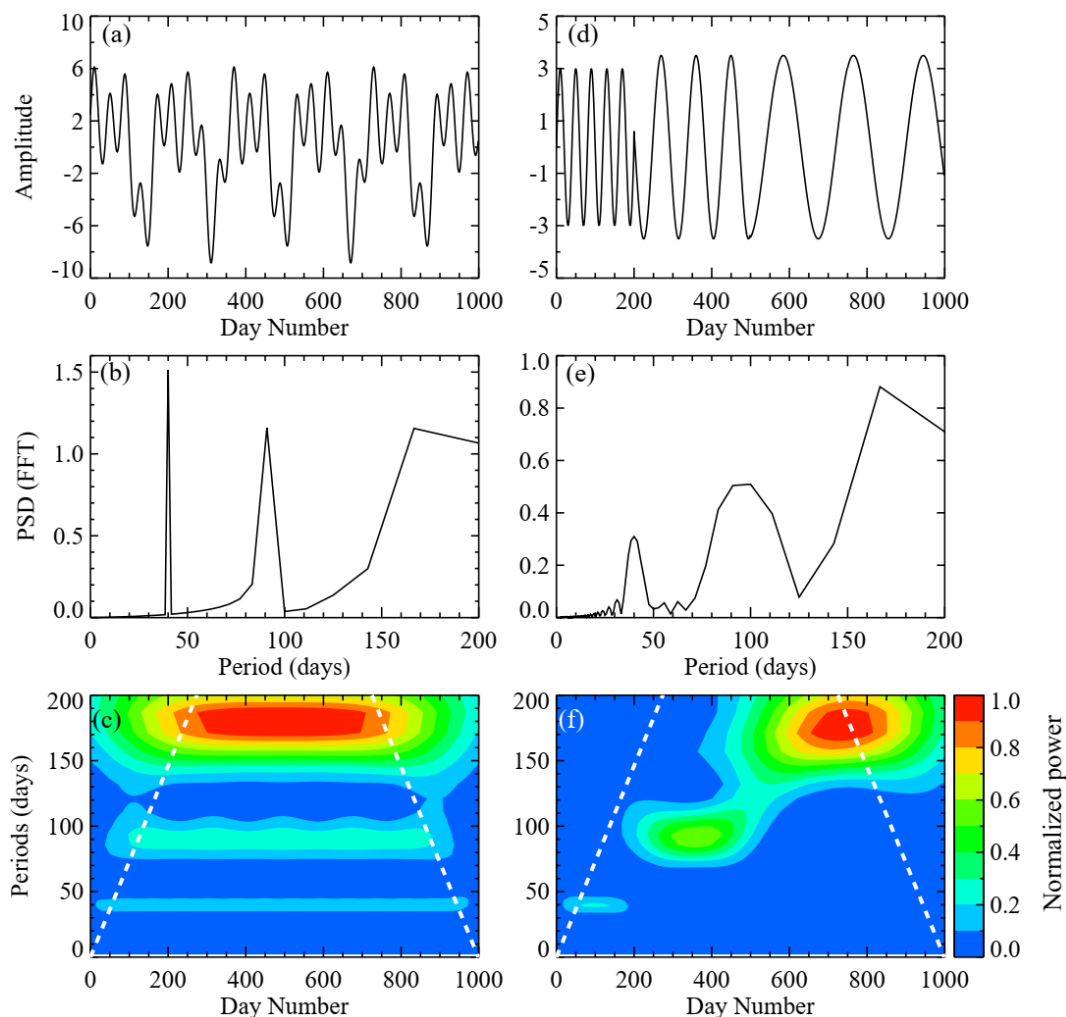


Figure 2.13: *Synthetically generated signals depicting the presence of periods of 40.0, 90.0, and 180.0 days (a) constant and (c) discrete in time. FFT periodogram of the data shown in (a & d) is shown in (b & e). Wavelet transforms of these signals are shown in figures (c) and (f). The white dashed lines correspond to the Cone of Influence (COI).*

all of the investigations of geophysical processes, it is extremely essential to know the duration of occurrence of a particular period in addition to information on the existence of that period. In order to obtain information on the spectral power localized in time for frequencies present in the dataset, we have used wavelet analysis in this thesis. Wavelet decomposes the one-dimensional time series to a two-dimensional time-frequency image. Detailed discussions of wavelet analysis are available in numerous numbers in the literature (*Morlet et al., 1982; Grossmann and Morlet, 1984; Goupillaud et al., 1984; Daubechies, 1988, 1990; Farge, 1992; Lau and Weng, 1995; Meyers et al., 1993; Liu, 1994*). We have used wavelet analysis using the Morlet technique (*Torrence and Compo, 1998*). A brief

description of the same is given below.

Consider a dataset, y_n , having values at equal time spacing with $n = 1, 2, \dots, N_0$ and $\psi(\eta)$ be a wavelet function that depends on dimensionless time parameter η . If $\psi(\eta)$ have zero mean and localized in both time and frequency space, then only it will be admissible as a wavelet function (*Farge, 1992*). For the Morlet technique, the wavelet function is given by,

$$\psi(\eta) = \pi^{-0.25} e^{(j\omega\eta - 0.5\eta^2)} \quad (2.21)$$

where, ω is the dimensionless frequency parameter. The continuous wavelet transformation (W_n) of discrete parameter y_n is the convolution of y_n with the translated $\psi(\eta)$ (*Torrence and Compo, 1998*).

$$W_n(s) = \sum_{m=1}^{N_0} x_m \psi^* \left[\frac{(m-n)\delta t}{s} \right] \quad (2.22)$$

where, s is the scale parameter; n is the translation parameter, and ψ^* represents the complex conjugate of ψ . Therefore, as per the convolution theorem of Fourier transform, the coefficients of wavelet transformation (given in equation 2.22) will be the product of Fourier transforms of x_m and $\psi^*(t/s)$.

$$W_n(s) = \sum_{k=1}^{N_0} x_k \psi^*(s\omega_k) e^{(j\omega_k n \delta t)} \quad (2.23)$$

where, x_k and $\psi^*(s\omega_k)$ are the Fourier transforms of x_m and $\psi^*(t/s)$, respectively.

The temporal evolution of the time periods for the signals shown in figures 2.13a and 2.13d can be seen in the wavelet spectra in figures 2.13e and 2.13f. Figure 2.13e confirms the presence of the periods throughout the data range. And for signal shown in 2.13d, wavelet spectra distinguishes the occurrence of these dominant periods at different time. In real-world measurements, we always deal with the finite length of the data. Therefore erroneous values will result in the beginning and at the end of the wavelet spectra. Zero paddings, i.e., putting zero values at the end, may solve the problem to some extent. Still, even in that case, wavelet amplitude will decrease near the edges due to zero values

in the data set. The Cone of influence (COI) of a wavelet spectra refers to the region, where these edge effects become significant. The COI is defined as the e-folding time of the auto-correlation of wavelet power. This e-folding time is chosen in such a way that the wavelet power for the discontinuity at the edges falls by a factor of e^{-2} (*Torrence and Compo, 1998*), which is $\sqrt{2}$ sec for the Morlet function. Therefore, it is difficult to ascertain whether the decrease in wavelet power in the COI (outer region beyond the white dashed lines shown in figures 2.13e and 2.13f) is due to the edge effect or a true reduction in the variance. Further, wavelet analysis is applicable to data of uniform intervals.

2.5 Summary

Digisonde measurements have been primarily used in this thesis work. In this chapter, the working principle, and importance of manual scaling of the raw ionograms obtained from digisonde have been briefly presented. We have also discussed other data sets and measurements, that have been used throughout the thesis work. Time series analysis of fluctuations in the measured atmospheric parameters provides information on the wave activity. Classical Fourier periodogram can retrieve the complete information on the frequencies present in the evenly spaced data, whereas, the Lomb-Scargle method is capable of spectral analysis of unevenly spaced data as well. Both of these techniques do not provide the temporal distribution of the frequencies present in the signal. Therefore, Morlet wavelet analysis becomes a useful tool for deriving the temporal evolution of frequencies present in the signal.

Chapter 3

Deriving thermospheric gravity wave characteristics using digisonde

3.1 Background

Different drivers affect the dynamics of the Earth's upper atmosphere. Perturbations from the lower atmosphere come in the form of waves. As described in section 1.3.4, waves of different spatial and temporal scales (planetary waves, tidal waves, and gravity waves) play a significant role in the redistribution of energy and momentum in the atmosphere as they propagate away from their source regions. Critical understanding of variation in their spatial or temporal scales is needed in addressing the issues of coupling in the atmosphere. Effects of gravity waves extend to relatively short distances from the place of their origin (a couple of thousands of kilometers), and they play important roles in modifying the atmospheric processes around the source regions. In general, gravity waves are characterized as those oscillations in the atmosphere whose time periods are smaller than the Coriolis period. In this chapter, we will discuss an innovative approach to derive vertical propagation characteristics of gravity waves present in the daytime thermosphere using digisonde measurements.

3.2 Introduction

After *Hines* (1960) postulated the existence of gravity waves in the atmosphere, there have been several experiments using optical, radio, and magnetic measurements from the ground (*Laskar et al.*, 2015), balloon (*Pallamraju et al.*, 2014), and space-borne (e.g., *Wu et al.*, 2006; *Park et al.*, 2014; *Ern et al.*, 2018) instruments to characterize them. As these waves propagate, they alter the density, pressure, and temperature of the atmosphere. Therefore, by monitoring fluctuations in these parameters, information on waves can be derived. The emission rates of airglow depend on the densities of the reactants that produce the excited atomic and molecular states, and also several of the reaction rates are temperature dependent. Therefore, by passively sensing the variations in airglow emissions as a function of time, information on waves can be obtained. Optical measurement techniques, being relatively inexpensive and easily portable, have been conventionally used to derive gravity wave characteristics (time periods, speeds, scale sizes, propagation directions, etc.) in the mesosphere and the thermosphere. Single point measurements provide information on the gravity wave periods (e.g., *Pallam Raju et al.*, 1996; *Chakrabarty et al.*, 2004), whereas measurement over a large field-of-view is needed to derive scale sizes and propagation directions (e.g., *Shiokawa et al.*, 2009; *Lakshmi Narayanan et al.*, 2010; *Karan and Pallamraju*, 2017; *Pallamraju et al.*, 2013, 2014, 2016). As discussed in section 1.4, information on gravity waves in the daytime is very sparse due to the technical difficulty of extracting faint airglow emissions buried in the bright solar background. As both the neutrals and plasma share the same volume of the upper atmosphere, these waves also alter the plasma parameters. By monitoring these fluctuations in plasma parameters using radar measurements, information on gravity waves has been derived in the daytime (*Oliver et al.*, 1997; *Djuth et al.*, 2004). Large scale motions, such as TIDs/TADs have been studied by monitoring variations of different ionospheric parameters using radio measurements (e.g., *Hunsucker*, 1982; *Rastogi and Klobuchar*, 1990; *Rao et al.*, 2006; *Mendillo*, 2006). Any changes in the electric fields, winds, temperature, and wave activity can cause the variations observed in ionospheric heights. Therefore, variations in the base height of the ionosphere ($h'F$) or the peak F₂-layer height (hmF_2) used for the investigations of wave-like phenomena may not give accurate information on

gravity waves. Also, integrated electron content (*IEC*) or total electron content (*TEC*) measurements, being column integrated parameters, do not yield information on the propagation of gravity waves. In addition, the prominent thermospheric airglow emissions in the daytime come from an altitude range, and consequently the gravity wave propagation features in the vertical direction, if any, get averaged out. Therefore, to obtain vertical propagation characteristics, simultaneous measurements at multiple nearby heights are needed, which is possible by monitoring the height variations at different fixed electron densities, as measured by digisonde. *Klausner et al. (2009)* have carried out one of the initial attempts in this regard, wherein variations in virtual heights for six fixed transmission frequencies were obtained, which showed quasi-periodic variations. However, being variations in virtual heights, ambiguity exists in the values of derived phase speeds, time periods, and vertical scale sizes of gravity waves.

In this chapter, we have presented a detailed methodology based on digisonde measurements to derive vertical propagation characteristics of gravity waves. Comparison is made between the gravity wave time periods obtained from the radio measurements and those from the well-established optical measurements of daytime airglow emissions to investigate the relation, if any. Also, simulations have been carried out using the gravity wave dispersion relation for estimation of the horizontal scale sizes as a function of the time period, vertical wavelength, and ambient winds. This method of deriving propagation characteristics of gravity waves opens up new possibilities of studying gravity waves globally at different locations as digisondes are available aplenty as compared to optical techniques. Investigations can be carried out around the year, including during the monsoon seasons, as radio measurements are not hindered by the opacity of clouds, as in optical measurements. Thus, this method fills in a much-needed gap in the investigations of neutral wave dynamics.

3.3 Data sets used

Data resulted from manual scaling of ionograms obtained by the digisonde of Ahmedabad, India, have been used in this work. Details of its working principle, measurements, and

output parameters have been discussed in the chapter 2 (section 2.3.1). Also, the thermospheric OI 630.0 nm dayglow measurements using MISE (figure 2.7) from a low-latitude location, Hyderabad, India, have been used. Specifications, observational capabilities of MISE, and dayglow extraction methodology have been described in section 2.3.2.

3.4 Results and Discussions

Spectral images obtained by MISE at varying times of integration are co-added for 5 minutes. As discussed in the chapter 2 (section 2.3.2), the daysky spectra obtained from MISE are compared with the solar spectra in both wavelength and continuum. Further, the scattering contribution is taken into account and dayglow emission rates are obtained. To compare the wave dynamics in the ionosphere as derived from the analysis of the digisonde data with those in the thermosphere as derived by optical measurement techniques, the height region from where optical OI 630.0 nm dayglow emission emanates (~ 230 km) is considered to be most optimal. The peak heights of the other two dayglow emissions measured by MISE are 130 km and peak F₂ layer altitude, which are either too low or too high when compared to the altitude region under consideration.

3.4.1 Gravity wave time periods (τ) from optical data

Diurnal variation of OI 630.0 nm emission rate in the daytime (dotted red-colored line) obtained for a sample day (18 May 2015), is shown in figure 3.1a. Such variation is governed by the three primary production mechanisms of daytime OI 630.0 nm airglow: photoelectron impact on atomic oxygen, photodissociation of molecular oxygen, and dissociative recombination of molecular oxygen ion (*Solomon and Abreu, 1989; Pallamraju et al., 2004b*). A broad solar zenith angle dependent variation is expected as these three production mechanisms are dependent on the solar flux. In addition to the solar zenith angle variation, other smaller fluctuations in the dayglow emissions can be seen as well. These fluctuations are known to be caused by gravity waves, which are convolved with those emissions engendered by the changes in the solar zenith angle. However, these smaller-scale waves (periods less than 3 h) can be submerged in the waves of larger time

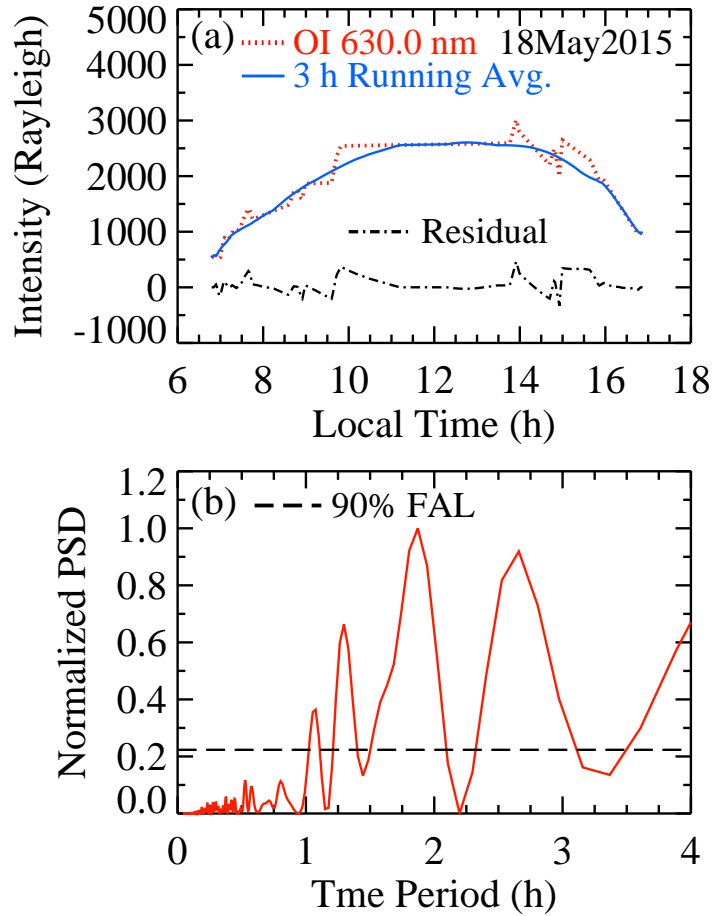


Figure 3.1: (a) Diurnal variation in OI 630.0 nm dayglow (dotted red-colored line) for 18 May 2015 along with the 3 h running average (solid blue-colored line) and the residual (dash-dotted black-colored line). (b) The Lomb-Scargle periodogram of the residual showing the presence of significant periods of 1.07, 1.30, 1.87, 2.66 h, which are of gravity wave regime.

periods. So their spectral power may not be above the statistical significance level on various occasions. Therefore, a 3 h running average (solid blue-colored line in figure 3.1a) is subtracted from the original data to obtain the residual (dashed-dotted black-colored line in figure 3.1a). The obtained residuals thus contain information on the fluctuations of wave periods smaller than 3 h, enabling comparison with the results on gravity waves reported in the literature. Spectral analysis of the residual obtained has been carried out (solid red-colored line and the 90% significance level is shown as dashed black-colored line in figure 3.1b) using the Lomb-Scargle periodogram analysis (*Lomb, 1976; Scargle, 1982*), which has been described in chapter 2 (section 2.4.2). Gravity waves of time periods of 1.07 ± 0.03 , 1.30 ± 0.02 , 1.87 ± 0.04 , and 2.66 ± 0.06 h are found to be present in the daytime

thermosphere on this day. The uncertainty in the values of time periods is estimated using the relation as given by [Bretthorst \(1988\)](#), which has been discussed in the chapter 2 (section 2.4.2). The uncertainty δf as given by equation 2.19, $\delta f = \frac{1.1\sigma}{AT_{total}\sqrt{N_0}}$; where, A is the amplitude of the signal, T_{total} is the total duration of observation, N_0 is the total number of observations, and σ is the standard deviation of the data obtained after the signal has been subtracted (which corresponds to the noise). Various aspects of neutral wave dynamics in low-latitudes, along with their dependence on the effects of equatorial processes and the solar activity, have been studied using such analyses for time periods of gravity waves (e.g., [Pallamraju et al., 2010](#); [Laskar et al., 2015](#)).

3.4.2 Gravity waves from digisonde data

Scaled ionograms yield information on the variation of electron density and ionospheric height as a function of time. We have considered variations in different ionospheric parameters (IEC , hmF_2 , & foF_2) on a sample day, which are conventionally used to infer gravity waves present in the ionosphere. To find out the periodic variations present in these ionospheric parameters, we have followed a similar analysis methodology, as described in section 3.4.1, for integrated dayglow data (figure 3.1). The IEC values provided by digisonde are calculated by approximating the topside profile to an α -Chapman function with a scale height that is estimated from the shape of electron density profile near the peak F₂-layer. Detailed descriptions can be found in [Huang and Reinisch \(2001\)](#), wherein it is shown that the digisonde derived IEC values agree well with those obtained from the radar measurements. The dotted (red-colored) line in figure 3.2a shows the IEC values in the units of 10^{16} electrons-m⁻² as provided by the digisonde of Ahmedabad. The 3 h running averaged values of the IEC data are shown by the blue-colored curve. The dash-dotted (black-colored) curve shows the residual obtained by subtracting the running averaged values from the IEC data. The Lomb-Scargle spectral analyses show (figure 3.2b) that no periods are significant in the variation of IEC in contrast to the dayglow emissions on the same day. This difference in the existence of gravity wave features in optical versus radio data is not surprising. It can be understood, if one considers the fact that the IEC from the radio data is averaged over a large height range (in this case 100-800 km) whereas, the daytime OI 630.0 nm emission layers semi-thickness is around

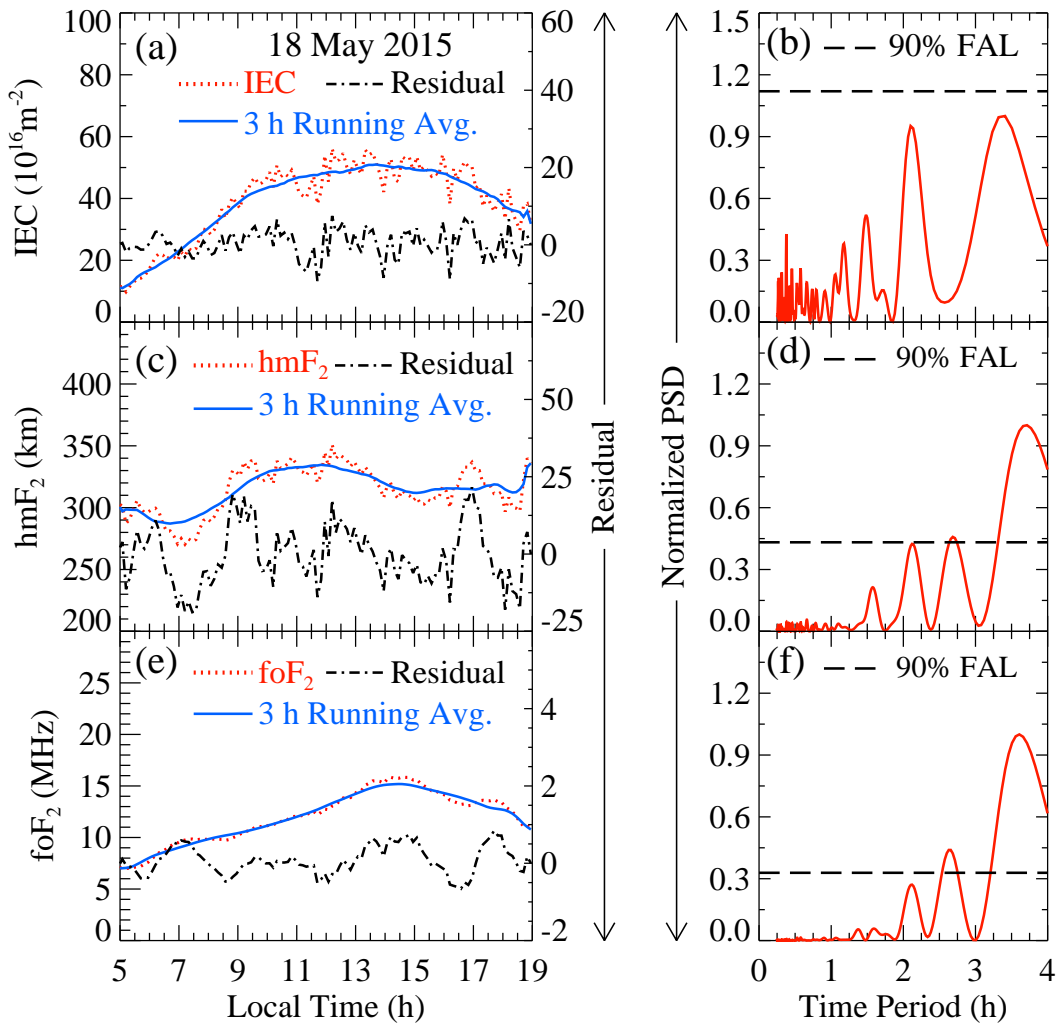


Figure 3.2: (a) Integrated electron content (IEC) (dotted red-colored line) from the digisonde along with 3 h running average (solid blue-colored line) and its residual (dash-dotted black-colored curve). (b) Normalized power spectral density of IEC , showing that there are no periods in the gravity wave domain that are significant (as their spectral power is lower than the FAL). (c & d) same as in (a & b) but for the height of peak F_2 layer, and (e & f) the same as in (a & b) but for the critical frequency of F_2 layer.

100 km. Thus, the dayglow emissions retain the information of fluctuations of smaller time scales as the reactants responsible for the airglow emissions do get affected by the passage of any wave-like fluctuations in the medium (e.g., [Pallamraju et al., 2010, 2014, 2016](#); [Laskar et al., 2015](#); [Karan and Pallamraju, 2017, 2018](#)). When modulations occur in the ionosphere as a whole, they reflect in the spectral analysis of IEC measurements. Therefore, large scale features, such as TIDs, have been conventionally investigated using data obtained from digisondes. However, as gravity waves do not perturb the ionosphere

at all the heights simultaneously with the same phase, it is impossible to unambiguously determine the gravity wave periods from the *IEC* variations. Similar analyses have been carried out for peak F₂-layer height (*hmF*₂) variation and peak frequency of the F₂ layer (*foF*₂) variation, the results of which are shown in figures 3.2c-e. Variations in *hmF*₂ and *foF*₂, when subjected to spectral analyses, confirm the presence of periodicities of 2.68 h and 2.63 h, respectively. Conventionally, these time periods in *hmF*₂ and *foF*₂ variation are attributed to gravity wave origin (*Rao et al.*, 2006; *Ram et al.*, 2012). But as discussed in section 3.2, these wave-like fluctuations can be caused by either one or combined effects of variations in the electric field, wind, temperature, and wave activity. Therefore, these time periods cannot be stated unambiguously to be of gravity wave origin. Also, any information in terms of propagation characteristics of gravity waves can not be estimated from these parameters as their variations refer to either integrated effect (in the case of *IEC*) or fluctuations at a particular height of the ionosphere (e.g., *hmF*₂ & *foF*₂). Depending on the strength of the source, gravity waves propagate both horizontally and vertically and alter the ionospheric densities at different heights at different times (phases). Therefore, independent investigations on height variations of different electron densities are required to gain more significant insights into the wave dynamics. Accordingly, all the individual ionograms have been meticulously scaled and analyzed for obtaining information on the true heights of the ionosphere at different frequencies of transmissions. The results of such analyses are shown in figure 3.3 for the same day, as in figure 3.2. Each of these fixed frequencies corresponds to particular values of electron density. And the variation in true heights of these fixed electron densities is known as isoelectron density contour. In figure 3.3a, the true height variations of isoelectron density contours from 8 to 12 MHz of operational frequencies of digisonde at an interval of 1 MHz are shown as a function of time. It may be noted that there exists a clear time difference in the modulations of ionospheric heights, which are earlier at greater transmission frequencies (and higher altitudes) as compared to the smaller ones (lower altitudes). To aid the eye, these are also shown as black dashed lines at different times in figure 3.3a. From *Hines* (1960) gravity wave theory, it is known that the downward phase movement is associated with upward propagation of gravity waves (discussed in section 1.3.4). If this downward phase movement is indeed caused by the upward propagation of a gravity wave, then it should be verifiable by spectral analyses, in terms of time periods present in the variations in the

heights of different isoelectron densities. Similar to the optical data shown above (figure 3.1), residuals have been obtained for the height variations of these isoelectron density contours by subtracting 3 h running averaged values. Such residuals for each of these isoelectron density contours have been subjected to the Lomb-Scargle spectral analysis and the results are shown in figure 3.3b. It may be noted that a common time period of 2.20 ± 0.08 h is present in the height variations of all the isoelectron density contours. The presence of a common period and downward phase propagation in the temporal variation of optical emissions from different altitudes have provided the signature of propagation of gravity waves from lower to higher altitudes in the MLT region (*Singh and Pallamraju, 2016*). Similarly, in the present case, the height variations of isoelectron density con-

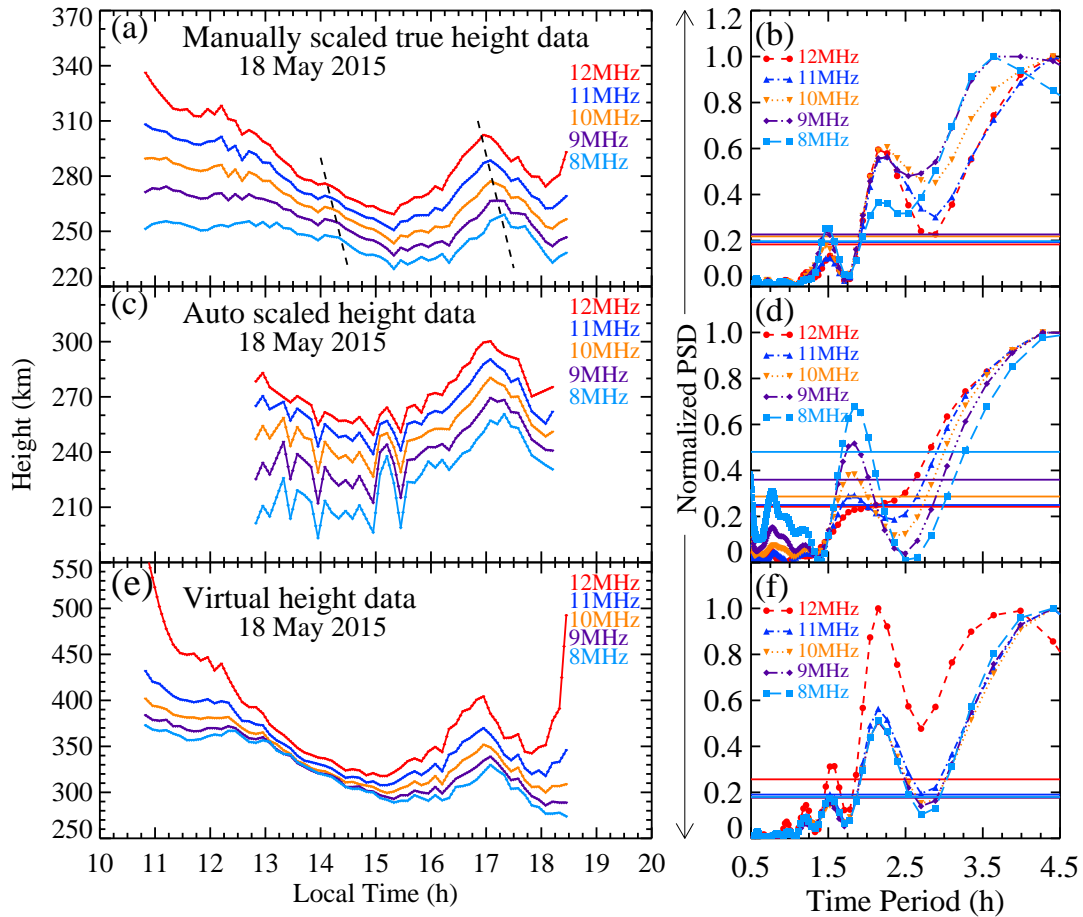


Figure 3.3: (a) True heights of isoelectron density variations at frequencies 8, 9, 10, 11, and 12 MHz on 18 May 2015. (b) The Lomb-Scargle periodogram showing the 1.54, 2.06, and 4.11 h periods to be significant for all the transmission frequencies. (c & d) Same as in (a & b) but obtained from auto-scaled ionograms. (e & f) same as in (a & b) but for variations in the virtual heights corresponding to fixed transmission frequencies.

tours show a common time period and downward phase movement (figure 3.3a), which confirm the propagation of gravity waves from lower to higher altitudes in the ionosphere-thermosphere region. The effect of diffusion on the thermosphere is non-linear in nature as it depends on temperature and neutral densities, which vary with altitude. As the magnitude of diffusion varies with altitude, its effect is not expected to produce any systematic phase offsets in the height variations of multiple isoelectron density contours (as seen in figure 3.3a). Further, fluctuations in multiple isoelectron density height variations may not show a common time period due to the effects of diffusion. Therefore, derivation of gravity wave propagation characteristics using the present approach is not expected to be affected by diffusion processes. The importance of manual scaling of the ionograms for estimating wave parameters through radio measurements, as discussed in this work, becomes obvious when one compares figures 3.3c & 3.3d with figures 3.3a & 3.3b. If one uses heights of isoelectron density variations obtained through auto-scaling software, the presence of several spurious fluctuations leads to common periods of around 1.80 h and 4.5 h in the Lomb-Scargle spectral analysis (figure 3.3d). They can be misunderstood to be the periods of gravity waves. Further, the virtual height variations of isoelectron densities are also analyzed (shown in figure 3.3e), and periodograms have been obtained (as shown in figure 3.3f). Although there exists a common period of around 2.1 h, the detailed analysis may not yield accurate information on the propagation of gravity waves as the height differences between different isoelectron density contours are very different than the case of manually scaled data (figure 3.3a). Hence, for reliable estimation of gravity waves characteristics, we have only used the data that resulted from manual scaling of these ionograms.

3.4.3 Estimation of vertical propagation speeds (c_z) of gravity waves

As seen in figure 3.3a & 3.3b for 18 May 2015, each of the isoelectron density contours shows the presence of periods other than the common time period, which will exhibit independent behavior. Therefore, the variations in the heights of isoelectron density contours are a superposition of fluctuations of different scales. In order to derive propagation characteristics of gravity wave of time period 2.2 h, one has to remove the effects of the others from the height variations of isoelectron density contours. For that, we have considered

one significant common time period at a time and removed the contributions of all other time periods in the Fourier domain. In this process, only the power corresponding to a particular dominant time period ($\text{PSD} > \text{FAL}$) is considered by using a bandpass filter with a width of $\text{peak period} \pm \text{Brunt-Väisälä period}$ ¹. The Brunt-Väisälä period is around 0.25 h for these altitudes. The powers of the rest of the spectra are equated to zero. While doing so, the imaginary part (which contains the phase information) of the power spectral density value corresponding to the particular time period is kept unchanged. Therefore, the phase of gravity wave before and after passing through this filter remains the same. Thus, by such a treatment (*Hocke and Kämpfer, 2009; Pallamraju et al., 2016*), the power of the common gravity wave period corresponding to the fluctuations in isoelectron density contour at a given transmission frequency is isolated in the Fourier frequency domain. The inverse Fourier transformation of this spectral series yields information of gravity wave fluctuations in the time domain. Such a method was successfully used in an earlier study to obtain the first three-dimensional gravity wave characteristics in the day-time through the optical measurement technique (*Pallamraju et al., 2016*). In the present case, the results obtained for the dominant time period of 2.2 h are shown in figure 3.4a. Here, an average height corresponding to each of the transmission frequencies is added to the relative variations in order to obtain information on temporal variations due to one gravity wave time period only. Clear wave-like fluctuations of a given time period are evident with troughs and crests at a given altitude. It can also be noted that the crests and troughs at lower heights occur at a slightly later time than those at higher altitudes showing a clear downward phase propagation in the height variations of isoelectron density contours, indicating the characteristic signature of upward propagating gravity waves (*Hines, 1960*). The vertical phase speed (c_z) of the gravity waves can be calculated with the information of the difference in heights (Δh) and the phase offset times (Δt), by using the relation, $c_z = \frac{\Delta h}{\Delta t}$. The time offsets between the crests/troughs of the height variations of consecutive isoelectron density contours have been linearly fitted to obtain a consolidated picture. On this day (figure 3.4a), vertical phase speeds vary from 37.74 ± 5.40 to $39.81 \pm 5.62 \text{ ms}^{-1}$ for the time period of 2.2h. However, these are not distinct as they are within the uncertainties associated with each of these values.

¹Brunt-Väisälä frequency, is estimated as, $N = \left(\frac{2g^*}{5H}\right)^{1/2}$ (*Shiokawa et al., 2009*); where, H is the neutral scale height ($\sim 50 \text{ km}$ for these altitude region), and g^* is the acceleration due to gravity at this altitude.

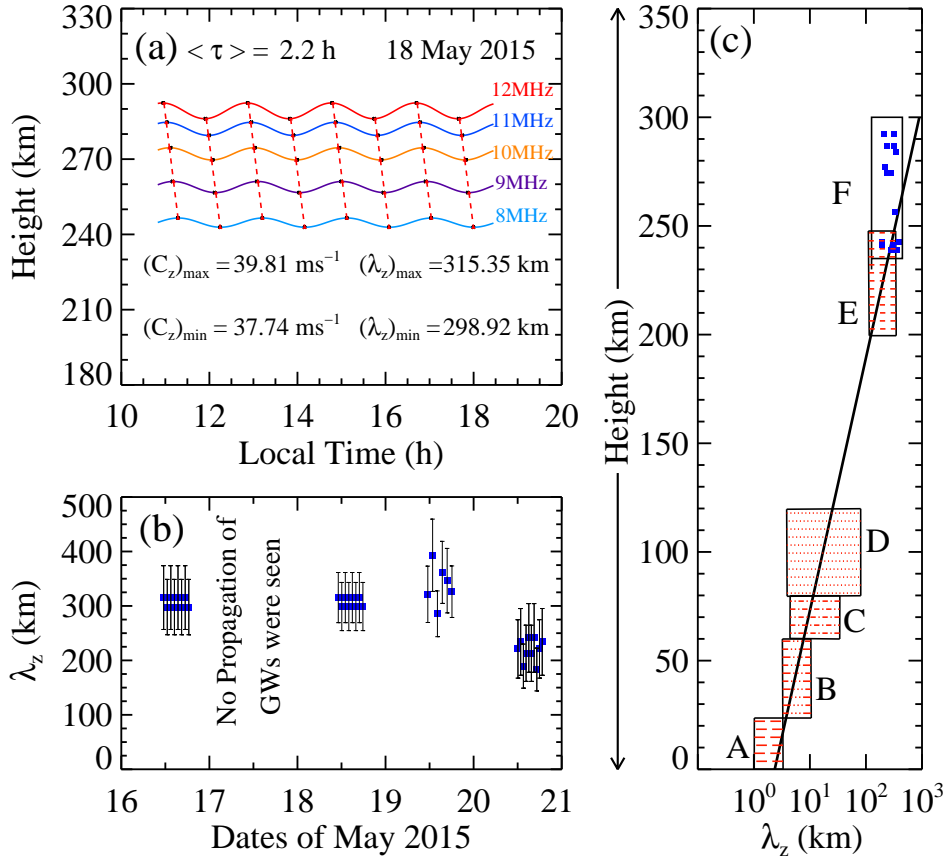


Figure 3.4: (a) Height variations of isoelectron density contours corresponding to transmission frequencies of 8, 9, 10, 11, and 12 MHz on 18 May 2015 for the gravity wave time period of 2.2 h. A clear downward phase movement can be seen. (b) The vertical scale sizes (blue-colored squares) obtained for the duration of 16–20 May 2015. (c) Variation in vertical wavelengths of gravity waves with altitude as observed from different measurements is shown. Here, boxes A, B, C, & D are taken from [Yamanaka and Fukao \(1994\)](#); box-E is from [Oliver et al. \(1997\)](#). And box-F is the results obtained from digisonde in the current method. Results shown in box-F are consistent with the earlier reported trend (as shown by the black-colored solid line).

3.4.4 Estimation of vertical scale sizes (λ_z) of gravity waves

In figure 3.4a, the phase variations correspond to the gravity wave period of 2.2 h have been shown. On such occasions, from the common period (τ) obtained and the derived phase speeds (c_z), the vertical scale sizes (λ_z) of gravity waves were estimated as $c_z \times \tau$, with an assumption that the phase speed does not change for the duration of the time period. On this day, the vertical scale sizes range from 298.92 ± 44.21 to 315.35 ± 46.07

Date	τ (h)	c_z (ms ⁻¹)	Δc_z (ms ⁻¹)	λ_z (km)	$\Delta \lambda_z$ (km)
16.05.2015	1.96	42.26 - 4.73	7.0-8.11	297.93 - 315.37	50.79 - 58.61
17.05.2015	No	vertical	propagation	of gravity	waves
18.05.2015	1.92	37.74 - 39.82	5.40 - 5.62	260.43 - 274.74	44.21 - 46.07
19.05.2015	2.64	30.06 - 41.38	4.90 - 6.89	285.58 - 393.03	47.36 - 66.38
20.05.2015	1.47	34.70 - 45.69	7.56 - 11.84	183.21 - 241.26	39.23 - 63.10

Table 3.1: *The derived values of time period (τ), vertical propagation speeds (c_z), uncertainty in vertical propagation speeds (Δc_z), vertical wavelengths (λ_z), and uncertainty in vertical wavelengths ($\Delta \lambda_z$) of gravity waves in the daytime thermosphere for 16-21 May 2015.*

km. Such analyses, as shown in figure 3.3a and figure 3.4a, have been carried out for the duration of 16-20 May 2015. The obtained time periods, vertical propagation speeds, and the vertical wavelengths of gravity waves are listed in table 3.1. On 17 May 2015, no signatures of vertical propagation of gravity waves are seen. The uncertainties in phase speeds, which turn out to be in the range of 14-26%, are estimated by considering the data cadence of digisonde and uncertainties in the values of heights. Similar analyses for deriving vertical propagation characteristics, as described above, have been successfully applied to nighttime airglow intensity variations originating at multiple altitudes in the MLT region to characterize the effect of lower atmospheric tropical cyclone generated gravity waves on the upper atmosphere (*Singh and Pallamraju, 2016*). Figure 3.4b shows all the vertical scale sizes (blue squares) of gravity waves obtained from digisonde for this duration. It can be clearly noted that the magnitudes of the vertical scale sizes of gravity waves vary from one day to another. Further, as there are waves of different periods that travel at different speeds, multiple vertical scale sizes of gravity waves can exist on the same day. In this duration, all the vertical scale sizes obtained in a day vary within the estimated uncertainties. During this observational window, the range of vertical scale sizes obtained is around 183.21 ± 39.23 to 393.07 ± 66.38 km. We have compared these values of vertical scale sizes that resulted from our analysis using digisonde data with the earlier reported systematic measurements of vertical scale sizes of gravity waves obtained from MU radar observations (*Yamanaka and Fukao, 1994; Oliver et al., 1997*). Figure 3.4c is adapted from *Oliver et al. (1997)* and updated with the values of vertical wavelengths that

resulted from the present work. The x- and y-axes of this figure represent the vertical scale sizes and the altitudes at which they are calculated, respectively. The boxes A, B, C, & D are as reported in *Yamanaka and Fukao (1994)*. The box-E depicts the results obtained from the MU radar observations by *Oliver et al. (1997)*. And the box-F presents the vertical scale sizes of gravity waves estimated from digisonde measurements as described in this work. Considering a scale height of 50 km in the numerical relation of vertical wavenumber m (in units of km^{-1}) of gravity waves as a function of height z as given by *Yamanaka and Fukao (1994)*, the resulting vertical scale sizes are plotted in figure 3.4c (solid black line).

$$m = \frac{2\pi}{1.5} \exp\left(\frac{-z}{50}\right) \quad (3.1)$$

It may be noted that the λ_z values obtained in the present work, as reported in box F, agree well with the numerical estimate given by equation 3.1 and they correspond to an altitude ~ 270 km. To the best of our knowledge, information on gravity wave propagation characteristics at heights ~ 270 km (box F as depicted in figure 3.4c) is being reported for the first time.

3.4.5 Comparison of gravity wave periods from simultaneous radio and optical measurements

In this section, we have compared the time periods of gravity waves obtained from the optical and radio measurements from two different locations to investigate if any similarities exist. The data available from optical measurements are for a duration of 7-17 h. In the case of digisonde measurements, the time duration of the echo corresponding to the transmission frequency of 12 MHz has been considered, which exists typically during 11-20 h. The data duration for other transmission frequencies has been truncated accordingly to keep the same data range for the sake of consistency in analysis. Nevertheless, there is a considerable overlap between these two data sets of around 6 h (from 11 h to 17 h) to enable inter-comparison. Spectral analyses have been carried out for optical measurements for all clear sky days during 16-20 May 2015. Figure 3.5a shows the comparison

of the time periods obtained from optical (red-colored triangles) and digisonde measurements (blue-colored circles). The data duration of each of the sets is ~ 10 h, which is much higher than the time periods that are being considered here (less than 3 h). In the case of periods obtained from digisonde data, each blue-colored circle corresponds to the common time period present at height variations of all the isoelectron density contours, which also show phase propagation features in the downward direction. In this way, it is ensured that they are of gravity wave origin. No gravity wave propagation features were seen on 17 May 2015 in the variation of isoelectron density contours. Optical measurements were not available on 16 May 2015 due to unfavorable sky conditions. It can be noted that the gravity wave periods present in the height variations of all the isoelectron densities match with the daytime optical data on 19 and 20 May 2015 (encircled values in figure 3.5a). The solid and dashed circles represent the matching of time periods corresponding to a similar/dissimilar phase evolution between the two, as described below. While matching, time periods within the limits of the Brunt-Väisälä period of around 0.25 h have been considered to be the same. Also, while there are similarities between the gravity wave time periods obtained by optical and radio measurements, not all of them match exactly with one another. This can be understood to be due to the fact that (i) the altitude regions of integration for optical emission and radio measurements are not exactly similar, and (ii) although the data are obtained simultaneously, the instruments are not collocated in the present study, therefore, depending on the ambient wind structures and thermospheric neutral temperatures, which could be different at different latitudes, these waves could evolve and propagate differently. These similar values of gravity wave time periods could be due to either the presence of the same wave structures at these two locations or a common source of fluctuations. To investigate the reason for the existence of similar gravity wave time periods measured from both the methods, the phase evolution obtained by these two measurements is compared. For such comparison, the height variation of isoelectron density contour corresponding to the transmission frequency of 8 MHz is chosen, since it is closest to the altitude of peak emission of OI 630.0 nm dayglow emission (~ 230 km). The times are shown in figures 3.5b and 3.5c corresponds to the local time for Ahmedabad. The same method to derive the variation in heights of isoelectron density contour for a particular period as described above (section 3.4.3 & figure 3.4a) has been applied to the optical OI 630.0 nm dayglow emission data analysis as well to

obtain the variation in emission intensity for a particular gravity wave time period. On 19 May 2015, the variation in them corresponding to periods of 2.52 h and 2.63 h for optical (dashed red-colored curve in figure 3.5b) and radio (solid black-colored curve in figure 3.5b) measurements, do match well with each other (within the limit of Brunt-Väisälä

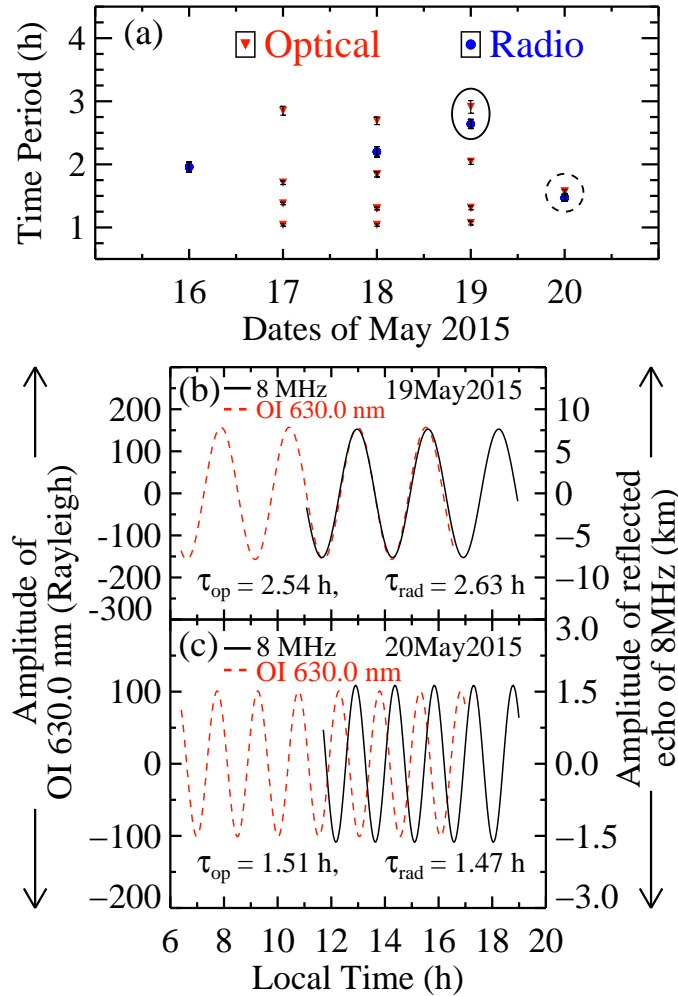


Figure 3.5: (a) Gravity wave periods obtained by optical (red-colored triangles) and radio (blue-colored circles) measurements during 16–20 May 2015. The dotted and solid circles around the time periods indicate a matching between the optical and radio measurements. The solid and dashed circles indicate that the gravity wave behavior from simultaneous dayglow and radio measurements are in phase (b), and out of phase (c), respectively. (b) Comparison of phase evolution of these periods from OI 630.0 nm dayglow and 8 MHz isoelectron density contour for 19 May 2015. (c) same as in (b) but for 20 May 2015. The OI 630.0 nm dayglow data are available from 7–17 h, and 8MHz isoelectron density contour data are typically available from 11 h onwards.

time period) (figure 3.5b). In spite of the large separation (~ 1000 km) between the two observational locations, such similarity is remarkable. Therefore, on days like 19 May 2015, when the gravity wave time period and their phase evolution match, it is possible that a similar broad source influences these two locations (e.g., equatorial electric field), which can simultaneously affect the spatially separated regions along the same longitude. On 20 May, however, the phase evolution corresponding to time periods of 1.51 h and 1.47 h obtained in a similar method do not match with each other (figure 3.5c). In such cases, the plausible causes for such observations are that these two locations are being influenced by independent sources/causes. Such a comparison between the gravity wave time period and phase at these two spatially separated locations provides a broader regional scale picture of the gravity wave characteristics in the daytime thermosphere over low-latitudes.

3.4.6 Estimation of horizontal scale sizes (λ_H) of gravity waves

So far, we have discussed the detailed analyses of digisonde data to derive time periods, vertical phase propagation speeds, and vertical scale sizes of gravity waves. Here, an attempt has been made to estimate the horizontal scale sizes of gravity waves using some of these derived parameters in the gravity wave dispersion relation. The gravity wave dispersion relation (*Fritts and Alexander, 2003*) is discussed in chapter 1 (section 1.3.4) and also given below:

$$m^2 = \frac{(k^2 + l^2)(N^2 - \bar{\omega}^2)}{(\bar{\omega}^2 - f^2)} - \frac{1}{4H^2} \quad (3.2)$$

Here, k , l , and m are the wavenumbers of gravity waves in X , Y (horizontal), and Z (vertical) directions, respectively; N is the Brunt-Väisälä frequency; H is the neutral scale height, and f is the Coriolis parameter.

The intrinsic frequency ($\bar{\omega}$) of gravity waves is related to the observed frequency (ω) by the following formula.

$$\bar{\omega} = \omega - \vec{k} \cdot \vec{u} - \vec{l} \cdot \vec{v} \quad (3.3)$$

where, \vec{u} and \vec{v} are the zonal and meridional components of the background wind.

The vertical scale size ($\lambda_z = \frac{2\pi}{m}$) values obtained from the analysis and the NRLMSISE model (Picone *et al.*, 2002) derived atmospheric neutral parameters have been used as inputs in equation 3.2 to calculate the horizontal scale sizes ($\lambda_H = \frac{2\pi}{k_H}$; $k_H = \sqrt{k^2 + l^2}$) of gravity waves. Here, we have carried out simulations to estimate the horizontal scale sizes (λ_H) for different vertical scale sizes (λ_z) with varying magnitudes (0-100 ms^{-1}) of horizontal winds (U_H). As the relative direction of winds to that of propagation of gravity waves ($\Delta\theta = \theta_{U_H} - \theta_c$; θ_{U_H} is the horizontal wind propagation direction, and θ_c is the direction of wave propagation) has a bearing on the gravity wave characteristics, several representative angles ($\Delta\theta$) of 0° , 45° , 90° , 145° , and 180° have been considered. The results for two different time periods (1.5 h and 2.5 h) of gravity waves are shown in the figure 3.6 as solid and dashed lines. If the ambient winds are in the direction of propagation of gravity wave (i.e., $\Delta\theta = 0^\circ$), then horizontal scale size grows at the expense of vertical scales. Conversely, if the wind is in the opposite direction to gravity wave propagation ($\Delta\theta = 180^\circ$), then the vertical scale increases as the ambient wind speed increases. Thus, as $\Delta\theta$ increases from 0° – 180° , the same value of horizontal scale size of 1000 km corresponds to higher values of vertical scale sizes. It may be noted that when the winds flow in the orthogonal direction ($\Delta\theta = 90^\circ$) to that of the wave propagation, the magnitudes of ambient wind speeds do not have any effect on the vertical and horizontal scale sizes of gravity waves. Therefore, in the absence of information on background winds and wave propagation direction, we have considered orthogonality in the wind flows to gravity wave propagation direction ($\Delta\theta = 90^\circ$) to get an estimate of λ_H values for the measured time periods, and λ_z values of gravity waves. It is important to understand that such assumption may not hold in reality, nevertheless, this simulation is essentially meant to provide a first-order estimate of λ_H of gravity waves for the values of λ_z obtained from digisonde data analysis. These results are shown in figure 3.6b. These are carried out for different gravity wave periods, such as 1.0 h (dotted red-colored line), 1.5 h (dashed yellow-colored line), 2.0 h (dash-dotted cyan-colored line), 2.5 h (dash-dot-dot-dot blue-colored line), and 3.0 h (solid purple-colored line). These simulation results given in the figure 3.6 can be used to estimate the horizontal scale sizes of a gravity wave, given the values of τ , and λ_z . For example, it can be seen from this figure that for $\tau \cong 2.0$ h, and λ_z of 300 km, λ_H turns out to be 2500 km; whereas, for $\tau \cong 1.5$ h and λ_z of 300 km, the value

of λ_H is 1400 km. These values are consistent with the earlier reported simulations (e.g., [Vadas, 2007](#); [Richmond, 1978](#); [Hocke, 1996](#)), which have considered the wave dissipation as a function of altitudes. As mentioned above, these estimated values of horizontal scale sizes of gravity waves are for no wind conditions; nevertheless, they provide a first-order estimate of the horizontal scale sizes of gravity waves for the observed duration. However,

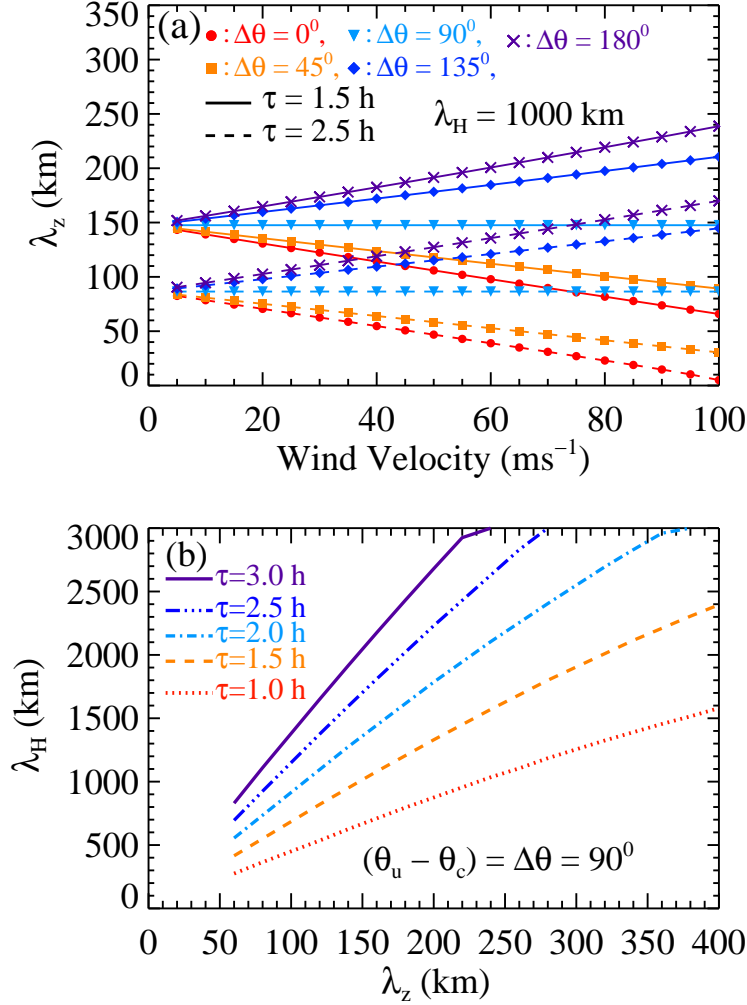


Figure 3.6: (a) Simulation of gravity wave vertical scale sizes (λ_z) for horizontal scale size (λ_H) of 1000 km using wind values ranging from 0-100 ms^{-1} and the relative angles ($\Delta\theta = \theta_{UH} - \theta_c$) of 0° , 45° , 90° , 145° , & 180° between the direction of wave propagation (θ_c) and wind (θ_{UH}) for gravity wave periods of 1.5 h (solid lines) and 2.5 h (dashed lines) obtained using the dispersion relation. (b) Simulation of λ_H , obtained for range of value of λ_z at $\Delta\theta = 90^\circ$ for gravity wave time periods of 1.0 (red), 1.5 (orange), 2.0 (cyan), 2.5 (blue), and 3.0 h (purple). This represents a first-order estimation of horizontal scale sizes of gravity waves in the absence of information on winds and wave propagation direction.

to remove ambiguity with respect to knowledge on the wave propagation direction, it is planned to carry out simultaneous and collocated radio and optical measurements in the near future, which will help to converge on more accurate estimates. Another aspect that emerges is that this technique is more reliable only for daytime conditions, when the thickness of the ionosphere is much larger than in the nighttime (typically, in the daytime, echoes can be obtained until 12 MHz for ~ 10 h duration, while in the nighttime it is 5 MHz for the same duration). This can be understood that for realistic estimates of vertical phase speeds and scale sizes, information on phase propagation from large spatial extents is required, which is possible in the daytime.

3.5 Summary

In this chapter, we have discussed the results from combined investigations of radio measurements and optical airglow emission data in the daytime. They are presented with a specific aim to extract information on the propagation characteristics of gravity waves. This work provides a detailed description of an approach for obtaining the propagation characteristics of gravity waves in the vertical direction using digisonde. Based on the vertical propagation speeds and time periods, vertical scale sizes of gravity waves are obtained (figure 3.4), which are well in agreement with earlier reported numerical estimates and measurements (figure 3.4). Therefore, the data obtained by the present radio method does reflect the behavior of neutral gravity waves as also confirmed by its comparison with the time period and phase of the simultaneous measurements of optical emissions in the daytime (figures 3.5b and 3.5c). The radio measurements can be interspersed between two optical observational locations to fill the much-needed gap in obtaining a larger scale picture of wave dynamical interactions in the thermosphere. Further, as the radio measurements are not affected by cloud cover; hence, using this approach systematic information on the daytime thermospheric wave dynamics can be understood.

Chapter 4

Vertical propagation of gravity waves as precursors to onset of ESF

4.1 Background

Plasma irregularities occur in the nighttime ionosphere on some occasions. These plasma irregularities severely affect trans-ionospheric radio wave communications, and their generation depends on both plasma and neutral processes. One of the manifestations of these plasma irregularities is the equatorial spread-F (ESF), which was discovered in 1938 by *Booker and Wells*. Even after decades of research since the discovery, variability in the day-to-day occurrence of ESF is still an enigmatic issue in the equatorial ionospheric physics. Gravity waves are considered to play the role of seed perturbation in initiating these irregularities in the equatorial ionosphere during evening hours. Some of the earlier works (e.g., *Raghavarao et al., 1988a*; *Sridharan et al., 1994*; *Pallamraju et al., 2004b, 2014*) had suggested that the daytime thermospheric dynamics makes the conditions, conducive or otherwise, for the occurrence of plasma irregularities in the nighttime equatorial ionosphere. In this context, as now an effective method is available to estimate the vertical propagation activity of gravity waves in the daytime thermosphere (as discussed in chapter 3), we have investigated day-to-day variation in the daytime thermospheric neutral wave dynamics over equatorial-latitudes in relation to the occurrence or non-occurrence of ESF in the post-sunset hours.

4.2 Introduction

Plasma irregularities span over seven orders of magnitudes in scale sizes and manifest in different forms in different measurements. For example, they are observed as spread in the reflected echoes in ionosondes, intensity depleted regions in airglow imagers, plasma bubbles, or backscatter plumes in incoherent radar measurement, scintillations in VHF and GPS signals. In the evening hours, the ionospheric F-layer gets lifted to higher altitudes due to the combined effects of the PRE and recombination in the bottom side of the ionosphere. Recombination of charged particles in the post-sunset hours leads to a sharp plasma density gradient in the bottom side of the ionosphere, which becomes unstable for perturbations and generates plasma irregularities through instability processes. The Rayleigh-Taylor instability is understood to be the primary cause of the generation of plasma bubbles (e.g., [Dungey, 1956](#); [Balsley et al., 1972](#); [Haerendel, 1973](#); [Ossakow et al., 1979](#)). The growth rate of the Rayleigh-Taylor instability in the F-region is given as, ([Sekar and Raghavarao, 1987](#))

$$\gamma = \frac{1}{L} \left[\frac{g}{v_{in}} + W_x \left(\frac{v_{in}}{\Omega_i} \right) - W_z \right] \quad (4.1)$$

where, L is the plasma scale length in the vertical direction ($L = \left[\frac{d}{dz} \{ \ln n \} \right]^{-1}$; n is the plasma density), g is the acceleration due to gravity, v_{in} is the ion-neutral collision frequency, W_x is the zonal wind (eastward), Ω_i is the gyro-frequency of ions, and W_z is the vertical wind.

As a result of the exponential decrease in neutral density with altitude, the ion-neutral collisions drastically reduce in the higher altitudes. Hence, the amplitudes of these plasma density perturbations in the bottom side of the equatorial ionosphere grow as they move upward. Over Trivandrum, ESF was observed, whenever the base of the F-layer height ($h'F$) reached altitudes of 300 km and beyond, and they were found to be absent if this height was below 260 km (as depicted in figure 4.1). It was also shown that the equatorward meridional wind is necessary for the occurrence of plasma irregularities on the days when $260 < h'F < 300$ km, ([Devasia et al., 2002](#)) as the equatorward winds assist in lifting the ionosphere to higher altitudes. Morphological characteristics of the ESF occurrences

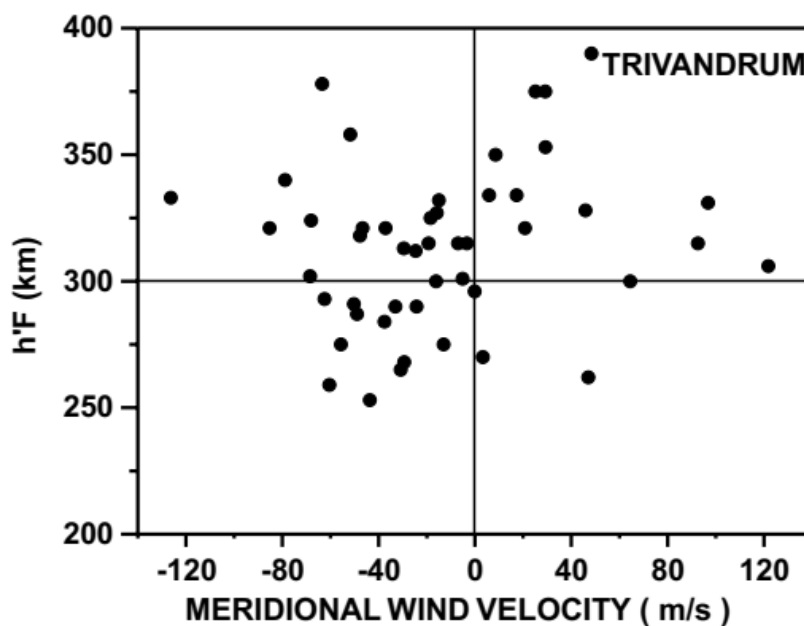


Figure 4.1: Scatter plot of the meridional wind values (positive poleward and negative equatorward) and the $h'F$ values over Trivandrum, on the ESF days during March–April, 1998. [After [Devasia et al. \(2002\)](#)]

in terms of local time, seasonal and solar cycle variability is relatively well understood (e.g., [Woodman and La Hoz, 1976](#); [Fejer and Kelley, 1980](#); [Abdu et al., 1981b](#); [Aarons, 1993](#); [Sastri et al., 1997](#); [Fejer et al., 1999](#); [Hysell and Burcham, 2002](#); [Burke et al., 2004](#)). For example, ESF occurrence has been found to be more during high solar activity periods (e.g., [Chandra and Rastogi, 1970](#); [Rastogi, 1980](#); [Jyoti et al., 2004](#)). Seasonal and longitudinal variability has been explained based on the trans-equatorial thermospheric winds, which suppress the plasma irregularities by lowering the ionospheric heights (e.g., [Maruyama and Matuura, 1984](#); [Mendillo et al., 2001](#)). The alignment of the solar terminator with the geomagnetic field lines has been shown to contribute to the longitudinal variability of ESF occurrence in the post-sunset hours ([Abdu et al., 1981b](#); [Tsunoda, 1985](#)). Such alignment leads to a decoupling of the ionospheric E and F-regions due to simultaneous sunsets in both the hemispheres, thereby help plasma irregularities to sustain, if generated on that night. Also, higher values of PRE favors ESF occurrence, as it pushes the ionosphere to higher heights. Therefore, several reports are available in the literature addressing the day-to-day variability in the ESF occurrence with PRE strength (e.g., [Sekar and Kelley, 1998](#); [Sastri et al., 1997](#); [Fejer et al., 1999](#); [Anderson et al., 2004](#); [Ram et al., 2006](#); [Abdu et al., 2006b](#); [Prakash et al., 2009](#)). [Raghavarao et al. \(1988a\)](#), using the

ratio of electron densities corresponding to heights of 270 and 300 km between an EIA crest location and an off-equatorial location, showed that ESF occurrences are most likely on the days when the EIA is stronger. The ratios of electron densities have been shown to shoot up by around 1730-1800 LT on the ESF days. A precursor to ESF occurrence has been shown to be present as early as 16 LT in the OI 630.0 nm dayglow emission using bidirectional measurements (*Sridharan et al., 1994*). Further, the strength of the EIA in relation to ESF occurrence has shown using critical F-layer frequencies (*Jayachandran et al., 1997*), TEC measurement (*Valladares et al., 2001*), and dayglow measurement over a large field-of-view (*Pallamraju et al., 2004b*). Vertical plasma drift magnitude in the evening hours with values greater than 20-30 ms^{-1} depending on the solar activity level has been shown to be necessary for the onset of ESF over Indian longitudes (*Ram et al., 2006*). Gravity waves are considered to play the role of seed perturbation in the generation of plasma irregularities. Case studies have been carried out using Jicamarca incoherent scatter radar data to study the gravity wave modulation observed in the irregularity plume formation (e.g., *Kelley and McClure, 1981*; *Hysell et al., 1990*). Effects of gravity wave activity on the onset of ESF occurrence have been discussed based on different measurements, such as LIDAR, radars, airglow imager, and ionosonde (e.g., *Tsunoda and White, 1981*; *Kelley et al., 1986*; *Nicolls and Kelley, 2005*; *Takahashi et al., 2009, 2018*; *Abdu et al., 2009*; *Taori et al., 2015*; *Sivakandan et al., 2019*). Theoretical works have been carried out to investigate the non-linear evolution of ESF by gravity wave seed perturbation (*Klostermeyer, 1978*; *Huang and Kelley, 1996*; *Krall et al., 2013*; *Yokoyama et al., 2019*). Over the Brazilian sector, using collocated backscatter radar and digisonde measurement, it has been shown that gravity wave-induced density fluctuations are necessary for ESF generation for vertical drift velocities $\leq 20 \text{ ms}^{-1}$ in the evening hours (*Abdu et al., 2009*). Earlier simulation studies have also suggested that vertically upward propagating gravity waves to ionospheric heights to be associated with the ESF occurrence (*Fritts and Vadas, 2008*). Signatures of gravity wave-induced electric fields observed in the evening hours in vertical drift measurements from Jicamarca Radio Observatory are suggested as the plausible contributory effect of gravity waves in initiating plasma irregularities (*Varney et al., 2009*). *Hysell et al. (2014)* have carried out numerical simulations to quantify the effects of gravity waves in the generation of ESF, wherein they have shown how gravity waves in the MLT and thermosphere can induce dynamo electric fields in

the equatorial F region ionosphere, deform it, drive currents, and deform the bottomside plasma configuration. Daytime wave dynamics in the MLT region in connection to the nighttime irregularities have been investigated using OI 297.2 nm dayglow measurements from a UV spectrograph on-board a high-altitude balloon. In this experiment, similar periodic behavior has been observed in the OI 297.2 nm dayglow, and simultaneous EEJ & ionospheric parameters over the dip equatorial region. This has provided one of the first clear experimental evidence that the nighttime ESF irregularities are due to gravity waves present in the daytime (*Pallamraju et al., 2014*). These findings indicate that a critical understanding of the daytime thermospheric neutral wave dynamics is important in addressing the enigmatic issue of day-to-day variability in the ESF occurrence.

4.3 Data sets used

Digisonde data of January, February, and March for 2013 and 2014 of Trivandrum, a dip-equatorial location over Indian longitudes, have been used to derive daytime thermospheric gravity wave propagation characteristics in the vertical direction. We have used digisonde derived base F-layer height ($h'F$) variation to assess the ionospheric conditions in the post-sunset hours. EEJ values have been obtained from magnetometer measurements of the horizontal component of the Earth's magnetic field from Tirunelveli and Alibag (described in section 2.3.3).

4.4 Results and discussions

Majority of the days in the given duration show signatures of ESF in the post-sunset hours. Therefore, in order to investigate the day-to-day variability in the occurrence or non-occurrence of ESF, we have chosen the days with no post-sunset ESF occurrence as control days against the backdrop of surrounding days, which showed the presence of post-sunset ESF. In this study, a day has been characterized as an ESF day if diffused traces in ionograms are observed for 30 minutes or more. To ensure that the observed

plasma irregularities are generated locally and are not traveling from a different source, we have not considered the days with ESF occurrences after 21 LT (*Saito and Maruyama, 2006; Manju et al., 2016*). Per these criteria, we have found 16 non-ESF days and 20 ESF days. As consecutive ESF and non-ESF days are considered, it allows us to study the behavior of different parameters from one day to another to arrive at a systematic picture. The role of various factors that were considered as important in the context of ESF occurrences has been investigated in detail and is discussed in the sections below.

4.4.1 Variation in the EEJ strength

Variation in the EEJ strength has been investigated for ESF and non-ESF days, as integrated values of EEJ correlate remarkably with EIA development (*Raghavarao et al., 1978; Karan et al., 2016*). As mentioned above, strengths of EIA have been shown to be conducive for the generation of post-sunset plasma irregularities. EEJ values over Indian longitudes have been calculated using the formula discussed in chapter 2 (section 2.3.3). In figure 4.2a, variation in hourly values of EEJ is shown for days with the occurrence of post-sunset ESF (blue-colored solid lines) and the days without post-sunset ESF (pink-colored dash-dotted lines). On some of the days, negative values of EEJ (CEJ) in the afternoon hours can be noticed. CEJ events are observed on 9 out of 16 non-ESF days, whereas, in the case of ESF days, CEJ has occurred on 9 out of 20 days. The CEJ has been shown to occur as a result of the westward solar quiet (Sq) electric field in the daytime (e.g., *Fejer et al., 2008; Pandey et al., 2018*). Also, the strength of the PRE, which is known to play an important role in ESF generation, is expected to be weaker on the days with CEJ in afternoon hours compared to days without CEJ events (*Haerendel and Eccles, 1992; Prakash et al., 2009*). Therefore, the occurrence of ESF in post-sunset hours on the days with CEJ events indicates to the influence of other factors. The average EEJ values for ESF and non-ESF days are overplotted as thick lines. Integrated EEJ values in the pre-sunset times have been shown to be higher for ESF days compared to non-ESF days over the Indonesian sector (*Uemoto et al., 2010*). Accordingly, in figure 4.2b, integrated values of EEJ (*IEEJ*) in the pre-sunset times (16-18 LT) for all the ESF (cross symbol) and non-ESF (filled rectangles) days are shown. However, *IEEJ* values do not show contrast in behavior and are not sufficient to explain the day-to-day variability

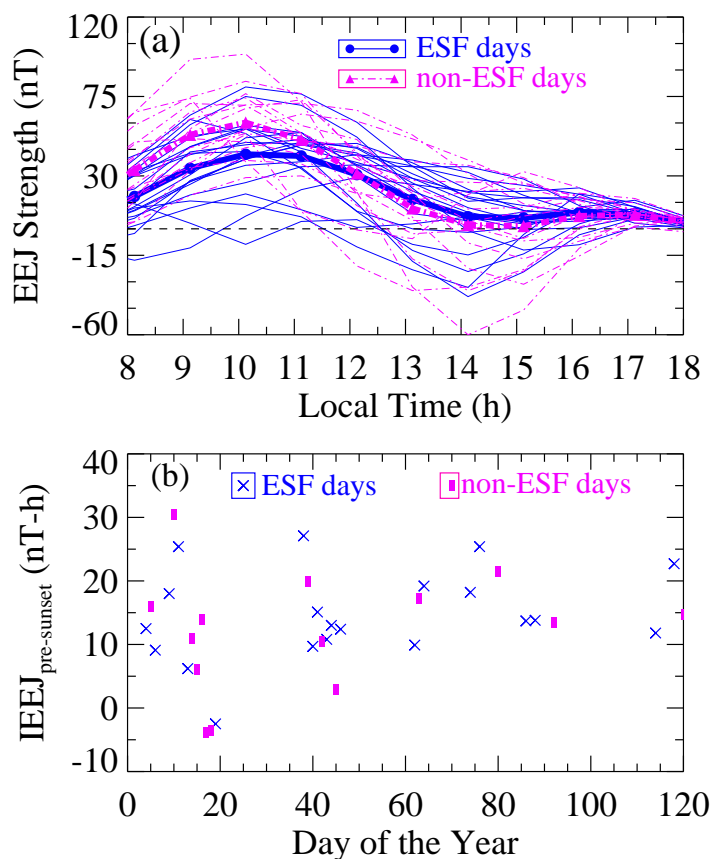


Figure 4.2: *a)* Hourly values of EEJ on ESF days (blue-colored lines) and on non-ESF days (pink-colored dash-dotted lines) during daytime (8-18 LT). The average behavior of EEJ on 20 days with post-sunset ESF and 16 non-ESF days are shown as a thick blue-colored line with circles and pink-colored dash-dotted lines with triangles, respectively. *(b)* Integrated values of EEJ (IEEJ) in the pre-sunset time are shown as a blue-colored cross for ESF days and pink-colored rectangles for non-ESF days.

in the occurrence of ESF over Indian longitudes.

4.4.2 Variation in the ionospheric height in the evening hours

Figure 4.3a shows the variation observed in the $h'F$ during the post-sunset time on ESF days (solid lines), and non-ESF (dotted lines) days. Here, $h'F$ values for ESF days are considered till the time of appearance of range spread in the ionograms, whereas, for non-ESF days, these values are plotted until 20 LT. Except for one day, $h'F$ values are greater than 300 km prior to the occurrence of ESF, whereas, for non-ESF days, only on 4 out of 16 days (25%), the height had reached up to an altitude of 300 km or beyond.

Thick lines represent their average behavior in the considered ESF and non-ESF days. As discussed earlier, higher ionospheric heights in the evening hours are conducive for the sustenance of plasma irregularities if generated, as ion-neutral collision frequency reduces with height. Therefore, the analyses presented in this section are consistent with the earlier proposition (*Rishbeth, 1981*) that the base height of F-layer reaching beyond 300 km in the evening hours is a necessary condition for ESF occurrence, but is not a sufficient one. However, on the ESF days, based on this criterion of $h'F > 300$ km, occurrence on post-sunset ESF can be stated only at or after 18.5 LT. Over Trivandrum,

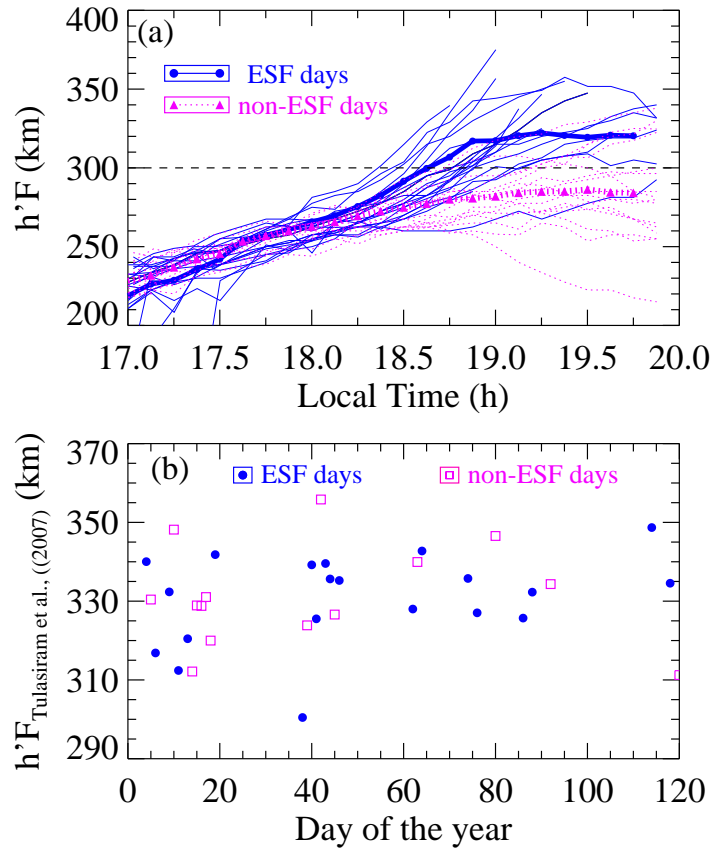


Figure 4.3: (a) Base height of F-layer ($h'F$) over Trivandrum in the evening hours are shown for ESF days (blue-colored lines) till the time of ionograms did not show any range spread in height, whereas for non-ESF days (pink-colored dotted lines) they are kept till 20 LT. Average values of $h'F$ for ESF (blue-colored line with triangles) and non-ESF days (pink-colored line with squares) in the evening hours are overplotted. (b) $h'F$ values calculated from the numerical relation given in *Tulasiram et al. (2007)*. These values for ESF days (blue-colored circles) and non-ESF days (pink-colored squares) do not show significant contrast.

using peak $h'F$ values before the ESF occurrence for March in different years of varying solar activity levels, *Tulasi Ram et al. (2007)* have suggested threshold values of peak $h'F$ for the ESF occurrence. For the solar activity level in the period of data considered in this work, this threshold value of $h'F$ is around 317 km. We have presented these numerically estimated values ($h'F_{Tulasiram et al., (2007)}$) in figure 4.3b as per the relation given in equation 4.2 (*Tulasi Ram et al., 2007*).

$$h'F_{Tulasiram et al., (2007)} = 317.0 + \frac{1}{2}(0.2IEEJ - 12.8K_p-avg) \quad (4.2)$$

where, $IEEJ$ is the integrated values of EEJ for 07-17 LT and K_p-avg is the average of K_p indices of 6 h before the sunset.

These values vary in the range of 290-350 km and they are not significantly different on ESF days as compared with the non-ESF days (as can be seen in 4.3b). This could be due to the fact that most of the data considered in the current study are for January and February, whereas, in *Tulasi Ram et al. (2007)*, the reported values are for the month of March. In the present study, there are hardly any non-ESF days in the month of March for making a more exact comparison. Further, based on the analyses of EEJ and $h'F$ data presented above, we had observed that ESF had also occurred on the days with CEJ events and remains absent on some days, when the base F-layer height had reached beyond 300 km. These indicate that some other factors are majorly influencing the day-to-day variability of ESF occurrence.

4.4.3 Variation in the strength of PRE

PRE is considered to be one of the most important factors for explaining the day-to-day variability in the occurrence of ESF in the nighttime. PRE refers to an enhancement of the electric field of the equatorial region for a brief period of time in the evening hours caused by F-region dynamo (discussed in section 1.3.1.3). As a result of such enhancement of the electric field, larger vertical electrodynamical drift uplifts the ionosphere to higher altitudes and helps the plasma irregularities to grow. *Bittencourt and Abdu (1981)* have shown that the drift values during evening hours obtained from the time rate of changes of ionospheric heights below or near F₂ layer, correspond to the electrodynamical drift

only when the ionospheric heights are above 300 km. Considering this factor, we have chosen the evening time height variation of isoelectron density contour corresponding to 8 MHz transmission frequency of digisonde to calculate the peak vertical drifts ($V_{d_{max}}$). For all the days, heights of reflected echo at 8 MHz are found to be beyond 300 km in the evening hours. Using the F-layer height variation over Trivandrum, PRE has been shown to occur after 18 LT (*Madhav Haridas et al., 2015*). Therefore, the maximum value of the rate of change of height of 8 MHz echoes over Trivandrum after 18 LT has been considered as the peak vertical drift ($V_{d_{max}}$), which is representative of the PRE strength on that particular day, and they are shown for ESF and non-ESF days in figure 4.4. For ESF days, $V_{d_{max}}$ values are found to vary from 9 to 51 ms^{-1} , whereas for

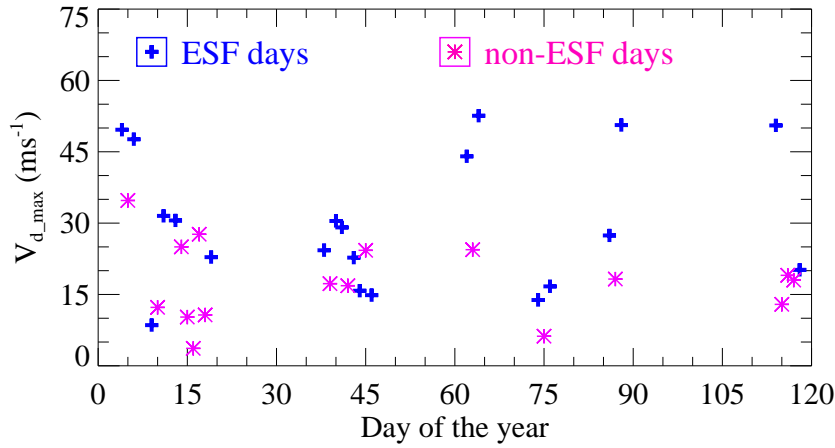


Figure 4.4: (a) Peak vertical drift derived from the height of 8 MHz echo in the post-sunset hours for ESF days (blue-colored plus symbol) and for non-ESF days (pink-colored asterisk).

non-ESF days, they are in the range of 4-35 ms^{-1} . It can be noticed from this figure that overall the $V_{d_{max}}$ values are higher on the ESF days than those for the non-ESF days. This is understandable because higher values of $V_{d_{max}}$ means stronger PRE, which is a known factor that favors the ESF occurrence. However, this information becomes available only after sunset. As it is also shown that the daytime thermosphere has a role to play in setting the background conditions conducive or otherwise for the generation of plasma irregularities in the nighttime, we have investigated the daytime neutral upper atmospheric behavior. In light of the above, daytime gravity wave characteristics present in the thermospheric altitudes for ESF and non-ESF days have been described in the following sections.

4.4.4 Time period and amplitudes of gravity waves in the daytime thermosphere

In order to derive vertical propagation characteristics of gravity waves in the daytime thermosphere, we have used variations in the heights of isoelectron density contours at discrete transmission frequencies (6.0, 6.5, 7.0, 7.5, and 8.0 MHz) of digisonde of Trivandrum. A detailed description of this methodology is given in chapter 3. These isoelectron density contours, due to the effect of different drivers such as electric field, winds, or temperature, will move in tandem with one another as all these drivers result in bulk movement of the ionosphere. Whereas, in the case of wave activity, these variations in heights of isoelectron density contours will show different phases at different heights (*Hines, 1960*). Therefore, to remove ambiguity in deriving gravity wave periods, we have considered the common period that is present in the variation of these isoelectron density contours, which shows downward phase propagation. These values of time periods of the gravity waves, which showed vertical propagation activity is depicted in figure 4.5a. Here, for the days of the year 2014, they are shifted by 65 days to separate them from those obtained in 2013. It

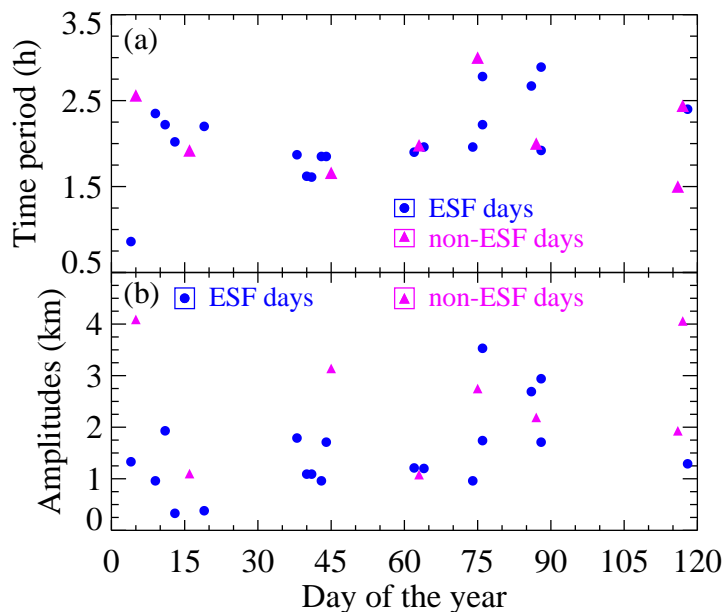


Figure 4.5: (a) Time periods of gravity waves, which are propagating in the vertical direction on ESF days (blue-colored circles) and days without ESF (red-colored triangles) in the post-sunset hours. (b) Same as in (a) but for the amplitudes of these gravity waves for ESF and non-ESF days.

can be seen that the time periods on the ESF days (blue-colored circles) and the non-ESF days (pink-colored triangles) do not show any distinct pattern. The amplitudes for these gravity waves have been obtained from the FFT periodogram and they are presented in figure 4.5b. On the ESF days, the gravity wave amplitudes range from 1 to 3.5 km, and those for the non-ESF days are 1-4 km. Similar to the case of time periods, amplitudes of these vertically propagating gravity waves in the daytime thermosphere on ESF days are also not significantly different than those obtained for non-ESF days. Growth in the gravity wave amplitudes on ESF days has been shown by several studies (e.g., [Sreeja et al., 2009](#); [Manju et al., 2016](#); [Aswathy and Manju, 2017](#)), however, these correspond to post-sunset times. As daytime information is discussed here, it seems that such behavior of gravity wave amplitude is not a definitive indicator of ESF occurrence.

4.4.5 Vertical propagation of daytime thermospheric gravity waves

Vertical phase speeds of gravity waves are calculated from the differences in heights and times observed in the fluctuations of the isoelectron density contours ([Singh and Pallamraju, 2016](#); [Mandal et al., 2019](#)). Gravity waves do not show vertical phase propagation every day in thermospheric altitudes. Different background conditions, such as the wind, temperature, and neutral densities affect their propagation (e.g., [Mandal et al., 2020](#); [Mandal and Pallamraju, 2020](#)) and they are discussed in greater detail in the following chapters. For the data used in this study, vertical propagation of gravity waves is observed on 17 out of 20 ESF days (85%) and 8 out of 16 non-ESF days (50%). Therefore, it is apparent that gravity wave propagation in the vertical direction is higher on the ESF days than those on the days without the ESF occurrence, which suggests an influence of daytime gravity waves on ESF occurrence. The daily average values of the vertical propagation speeds ($\langle c_z \rangle$) of these gravity waves for all the days are shown in figure 4.6. The vertical propagation speeds of gravity waves in the daytime thermosphere are clearly higher on the days with ESF in the post-sunset hours compared to those on the non-ESF days. This contrast in the vertical propagation speeds between the consecutive non-ESF and ESF days supports the proposition of gravity waves possibly offering the seed for the perturbation for the generation of plasma irregularities. Further, based on this study, it seems that the propagation speeds of gravity waves in the vertical direction

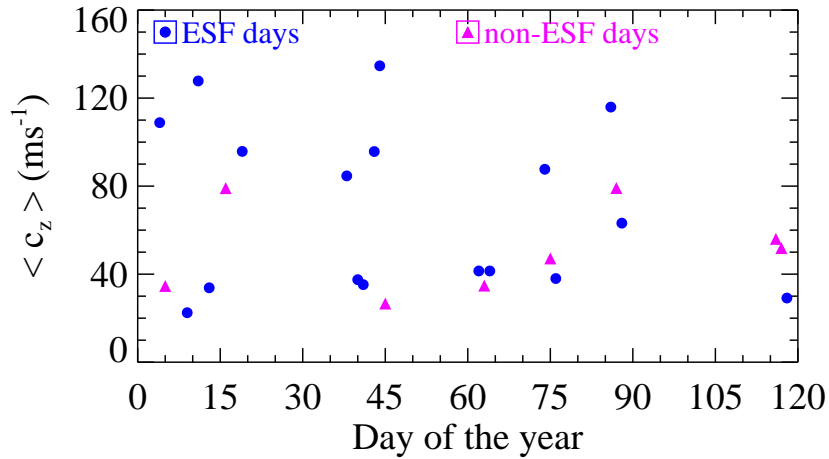


Figure 4.6: Daily averaged values of vertical phase speeds of gravity waves are shown for ESF days (blue-colored circles) and non-ESF days (red-colored triangles).

is a very important information to possibly explain the day-to-day variability in the occurrence of ESF. It is important to ascertain that the gravity waves, which show higher vertical phase speeds in the daytime, sustain well into the post-sunset hours/nighttime to serve as the much-needed trigger for the generation of plasma irregularities. Wavelet analysis, as described in the chapter 2 (section 2.4.3), has been performed on the height variation of isoelectron density contours corresponding to the transmission frequency of 6 MHz of digisonde. The transmission frequency of 6 MHz is chosen as it corresponds to altitude regions around the base of the F-layer. The normalized wavelet transformation for six sample days (four ESF days and two non-ESF days) is shown in figure 4.7a-f. It can be seen that the spectral powers corresponding to time periods presented in figure 4.5a on ESF days are present throughout the day and till the time of occurrence of ESF. Also in the case of two non-ESF days depicted in figures 4.7e and 4.7f, the gravity wave time periods (shown in figure 4.5a) remain present throughout the day. The situation is similar for other ESF and non-ESF days that are not shown in figures 4.7. Therefore, it is clear that the daytime gravity waves propagating in the vertical direction, as shown in figures 4.5 and 4.6, are present till evening hours and serve as possible seed perturbation in the generation of plasma irregularities. On a few days considered in this study, gravity waves have been found to be present from the afternoon to post-sunset times. Therefore, to bring all the days with vertical propagation activity of gravity waves on common footing, a time window of 10-16 LT has been chosen. And, during this time window gravity wave propagation activity is observed on all the ESF and the non-ESF days on which

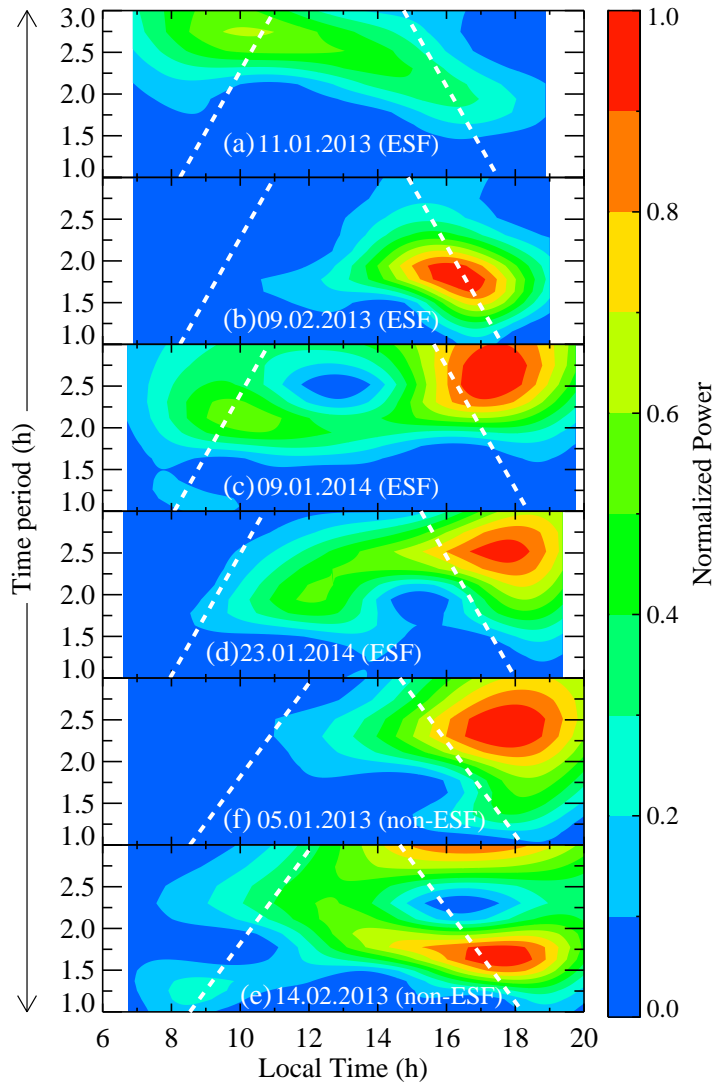


Figure 4.7: Temporal variation of spectral powers corresponding to different time periods of gravity waves are shown for four ESF days and two non-ESF days. (a) Normalized wavelet spectra resulted from the analysis of 6 MHz isoelectron density contour on an ESF day (11.01.2013). (b) Same as in (a) but for 09.02.2013, (c) 09.01.2014, (d) 23.01.2014, (e) 14.02.2013, (f) 05.01.2013. The white dashed lines correspond to the cone of influence (discussed in section 2.4.3).

vertical phase speeds are calculated. We have calculated the mean of values of vertical propagation speeds of gravity waves observed between 10 to 16 LT ($\langle c_z \rangle_{10-16LT}$) for all these days, and they are presented in figure 4.8. As discussed in chapter 3, on a given day, the range in the values of vertical propagation speed is within the limit of uncertainties, and thus, figure 4.8a looks similar to figure 4.6. The $\langle c_z \rangle_{10-16LT}$ values in figure 4.8a are shown as circles for the ESF days and represented as squares for the non-ESF days.

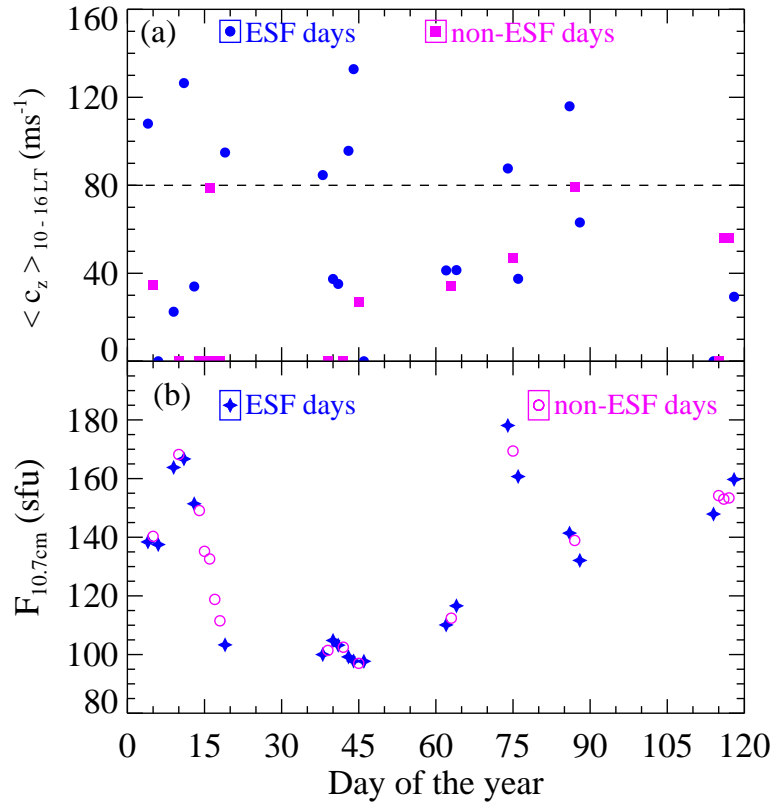


Figure 4.8: (a) Daily averaged values of c_z for the time window of 10-16 LT for ESF days (blue-colored circles) and non-ESF days (pink-colored triangles). (b) Daily solar $F_{10.7cm}$ flux values for all these ESF and non-ESF days are shown. These values for non-ESF days (pink-colored circle) are similar to their surrounding ESF days (blue-colored filled star).

The dashed line corresponds to propagation speeds of 80 ms^{-1} . Phase speeds values of 0 ms^{-1} refer to the days without vertical propagation activity in gravity waves. It can be seen that for the duration of data considered in this study, for all the non-ESF days, the values of $\langle c_z \rangle_{10-16LT}$ are less than around 80 ms^{-1} , whereas, for ESF days they are higher than 80 ms^{-1} for 8 out of 20 days. The vertical phase speeds of gravity waves in the daytime thermosphere have been shown to increase with increasing solar flux ([Mandal et al., 2020](#)) and are discussed in chapter 6. Therefore, to remove any ambiguity regarding solar flux being larger (coincidentally) on an ESF day, thereby contributing to higher speeds of vertical propagation, we have looked at the solar flux values on both the ESF and non-ESF days (figure 4.8b). It can be readily noticed that the solar $F_{10.7cm}$ values are not so different on non-ESF days (open circles) and their surrounding ESF days (filled stars). For example, (i) during day 35-45, the solar flux values are comparatively low for

both the ESF and non-ESF days (figure 4.8b), but vertical phase speeds are higher on the ESF days compared to the non-ESF days, and (ii) during doy 75-80, even though the solar flux value was high, the vertical phase speeds of gravity waves on the non-ESF day are lower. These observations add credence to the present interpretation that the variations observed in the vertical phase speeds of gravity waves in the daytime thermosphere on the ESF and the non-ESF days are clearly due to the local dynamics. Therefore, as discussed above, the vertical phase speeds of gravity waves are different on different days, and it has also been seen that higher values of vertical phase speeds of gravity waves during 10-16 LT are associated with the occurrence of ESF in the post-sunset hours. This aspect becomes much clearer when we categorize the number of days with the values of $\langle c_z \rangle_{10-16LT}$ observed on the days vis-à-vis ESF occurrence in the post-sunset hours. We have represented this in figure 4.9a as a barplot, wherein the ESF and non-ESF days are shown in blue and pink-colored bars, respectively. As shown in figure 4.9a, for phase speed values greater than 30 ms^{-1} , 30% of the total days are non-ESF, and 65% are ESF days. Progressively in this way as we go to the rightmost bar, it suggests that all the days with $\langle c_z \rangle_{10-16LT}$ greater than 80 ms^{-1} are ESF days. Therefore, there is a gradual decrease in the number of days from left to right in the non-ESF category (dash-dotted line). In contrast, one can note that higher values of vertical phase speeds are more conducive for the occurrence of ESF days (as depicted by the dotted line in figure 4.9a). As discussed above, daytime vertical propagation speeds of gravity waves seem to be one of the very important factors, which have not been reported earlier, for the generation of ESF irregularities in the post-sunset hours. Therefore, vertical propagation characteristics of gravity waves present in the daytime thermosphere can be used as an indicator to predict ESF occurrence as early as 16 LT. Further, to the best of our knowledge, such a clear indication of ESF occurrence based on gravity waves as presented in this work in the daytime thermosphere is reported for the first time.

Generation of ESF on the days when the vertical phase speeds of gravity waves are less than 80 ms^{-1} suggests the influence of other parameters along with the daytime wave dynamics. The relative strength of seed perturbation through gravity waves and the vertical drift in the post-sunset hours for the generation of plasma irregularities have been discussed in the literature (*Abdu et al., 2009*). In this duration, from figures 4.4 and 4.8, it can be noticed that for most of the ESF days when $V_{d,max}$ are smaller, corresponding

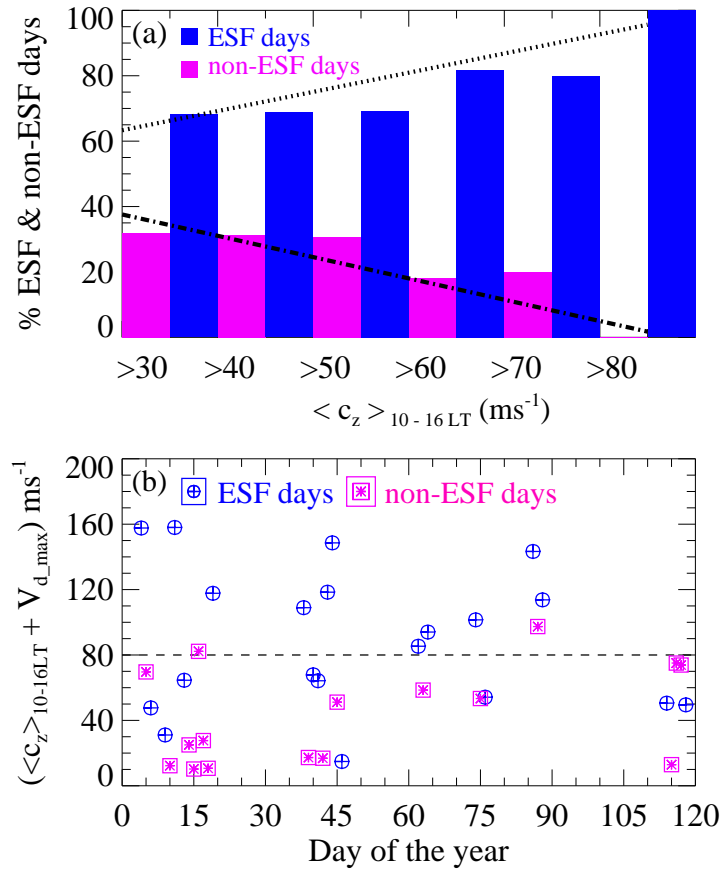


Figure 4.9: (a) Percentage of number of ESF and non-ESF days are categorized based on the values of vertical phase speeds of gravity waves in the daytime thermosphere. The leftmost pink-colored bar indicates that 30% of the days are non-ESF days when $\langle c_z \rangle_{10-16LT}$ are greater than 30 ms⁻¹, whereas, for ESF days it is 65% (leftmost pink-colored bar). Similarly, rightmost bars suggest that all the days are found to be ESF days if $\langle c_z \rangle_{10-16LT}$ is greater than 80 ms⁻¹. The dotted (for ESF days) and dash-dotted lines (for non-ESF days) represent the trend that days with higher $\langle c_z \rangle_{10-16LT}$ are more likely to be ESF days. (b) Sum of $\langle c_z \rangle_{10-16LT}$ and $V_{d,max}$ for ESF (blue-colored circles with plus symbols) and non-ESF days (pink-colored squares with asterisks). A Black dashed line is drawn for values of 80 ms⁻¹.

$\langle c_z \rangle_{10-16LT}$ values are large, and for ESF days when $\langle c_z \rangle_{10-16LT}$ values less than 80 ms⁻¹, mostly they have higher values of $V_{d,max}$. In this background, to understand their resultant behavior, we have calculated the sum of $\langle c_z \rangle_{10-16LT}$ and $V_{d,max}$, and they are presented in figure 4.9b for both the ESF (blue-colored circle with plus symbols) and non-ESF days (pink-colored squares with asterisk symbols). A clear contrast can be seen in summed values of these parameters, which is higher on the ESF days than on the non-

ESF days. In this case, if their sum is more than 80 ms^{-1} (as indicated by a dashed line in figure 4.9b), that day is found out to be an ESF day. But for the ESF days on which the summed values are less than 80 ms^{-1} , they are either the days with no vertical propagation activity of gravity waves in the daytime or both the values of vertical propagation speeds of gravity waves and peak vertical drift in the evening hours are smaller. Therefore, figure 4.9b brings in more contrast in the values of vertical propagation speeds between the occurrence or no-occurrence of ESF in the post-sunset time. And the threshold value of 80 ms^{-1} in the vertical phase propagation of gravity waves in the daytime (10-16 LT) still holds, which makes the vertical propagation speeds of gravity waves in the daytime thermosphere, a potential parameter for the prediction of ESF.

4.5 Summary

In this chapter, the daytime thermospheric wave dynamics have been investigated in connection with the occurrence and non-occurrence of the post-sunset plasma irregularities. Variation in the strength of the equatorial electrojet and base height of the F-layer have been found to be insufficient to comment on the day-to-day variation in ESF occurrence in the post-sunset hours. Periods and the amplitudes of vertically propagating gravity waves observed in the daytime do not show any different behavior on ESF days compared to non-ESF days. In contrast, the vertical propagation speeds of gravity waves in the daytime are found to be significantly larger on ESF days than those on non-ESF days. The gravity wave time periods were found to be present throughout the day until the time of ESF occurrence, thereby serving as possible seeds for the perturbation that lead to the formation of plasma irregularities. The following conclusions can be made based on this study: (a) 85% of the days with vertical propagation activity of gravity waves during daytime (10-16 LT) were followed up with the presence of plasma irregularities in the post-sunset time, irrespective of the height of F-region or the PRE values in the post-sunset time. This indicates the presence of vertically propagating gravity waves in the daytime is a necessary condition for ESF occurrence. (b) The magnitudes of vertical propagation speeds of gravity waves in the daytime (10-16 LT) are higher on the days of ESF occurrence compared to those with non-ESF days. (c) Whenever the vertical phase

propagation speeds of gravity waves during 10-16 LT are greater than 80 ms^{-1} , ESF occurrence has been observed in the nights. Per this criterion, ESF occurrence can be predicted as early as 16 LT. (d) The combined behavior of vertical propagation speeds of gravity waves and peak vertical drift of F-region in the evening hours, indicates that ESF has occurred even when the strength of PRE was weak but the daytime vertical phase speeds of gravity waves were higher. ESF remained absent on most of the nights when both of these parameters have smaller values. Thus, the results discussed in this chapter further strengthen the proposition of the role of daytime thermospheric dynamics in the day-to-day variability in the occurrence of nighttime plasma irregularities.

Chapter 5

Vertical propagation of gravity waves in the daytime thermosphere

5.1 Background

A new approach of deriving information on gravity waves present in the daytime thermosphere using digisonde measurement has been described in chapter 3. As digisonde measurements are available on a continuous basis, this approach provides the unique opportunity to investigate the seasonal variations, if any, in the vertical propagation activity of gravity waves in the daytime thermosphere. Background wind magnitudes and directions significantly affect the propagation characteristics of the gravity waves (discussed in section 3.4.6). These thermospheric winds change with seasons. Also, Joule heating at high-latitudes during geomagnetic storms due to enhanced auroral currents drives meridional winds toward the equator. If these heating magnitudes are significant, they can alter the prevailing wind pattern completely (depicted in figure 1.13). Therefore, on such occasions, thermospheric neutral wave dynamics over low-latitudes is expected to get affected. This chapter presents the variation in the vertical propagation characteristics of gravity waves present in the daytime thermosphere over low-latitudes during geomagnetically quiet and disturbed times.

5.2 Introduction

The low-latitude thermosphere gets energy from different sources. Solar forcing in terms of incoming radiation from the top changes the background conditions and composition of the thermosphere and hence alters the dynamics of this region (e.g., *Mayr et al., 1978; Prölss, 1993; Hocke, 1996*). During geomagnetic storms, intense Joule heating in the upper atmosphere of auroral regions drives the equatorward meridional winds that carry neutrals from high- to low-latitudes (e.g., *Richmond and Matsushita, 1975; Mayr et al., 1978; Richmond, 1978, 1979*) and also sets up large scale TIDs and TADs, which can reach up to equatorial regions and beyond (*Hunsucker, 1982; Prölss, 1980*). These motions redistribute the excess energy input in high-latitudes during geomagnetic storms to low-latitudes (*Hocke, 1996; Pallamraju et al., 2004b*). Further, the electric field of low- and equatorial-latitude regions get perturbed due to the effects of geomagnetic storms. These perturbations can be both instantaneous and delayed in nature. The solar wind-magnetosphere dynamo drives the instantaneous perturbation in the low-latitude electric field, and in general, their lifetime is less than an hour (*Kikuchi et al., 1996*). The delayed effect is caused by ionospheric disturbance dynamo, which is driven by meridional wind circulation due to Joule heating (*Blanc and Richmond, 1980*). The disturbance dynamo effects can take 1-28 h after the enhancement in current over high-latitudes during storms to reach the equatorial-latitudes. These effects are communicated through the fast traveling atmospheric disturbances and the changes in thermospheric circulation (e.g., *Mazaudier and Venkateswaran, 1990; Fejer and Scherliess, 1997; Fuller-Rowell et al., 2002; Fejer et al., 2017*). Dominant effects of disturbance dynamo have been observed during the recovery phases of geomagnetic storms (*Yamazaki and Kosch, 2015*). *Kakad et al. (2011)* have shown the effects of disturbance dynamo at two times, one at about 0.5-4 h and the other at 16-23 h after the geomagnetic activity enhancement. Over Indian longitudes, the strongest effects due to disturbance dynamo on the equatorial regions are observed during equinoctial times (*Pandey et al., 2018*).

Information on the effects of geomagnetic storms on the scales of gravity waves has been sparse. The zonal scale sizes of gravity waves in the daytime thermosphere over low-latitudes derived from large field-of-view dayglow measurements are found to be

distinctly different on geomagnetically disturbed days compared to quiet days. And the effects of geomagnetic storms over the low-latitudes are shown to be season-dependent (*Karan and Pallamraju, 2018*). Also, during geomagnetic storms, variation in the total electron content over high-latitudes shows similarity with the equatorial ring current, which indicates coupling between magnetosphere, thermosphere, and ionosphere (*Yadav and Pallamraju, 2015*). These have motivated us to investigate the vertical propagation characteristics of gravity waves in the daytime thermosphere over low-latitudes during geomagnetic quiet and disturbed times.

5.3 Data sets used

Two years of data (July 2012-June 2014) obtained from the digisonde located at Ahmedabad, India, have been used for this work. The description of the working principle and output parameters of digisonde are described in chapter 2 (section 2.3.1). We have used the Dst index (section 2.3.5) to identify the geomagnetic storms during this time. Also, the AE index (section 2.3.6) values have been used as a proxy of the energy deposition over the high-latitude upper atmosphere during geomagnetic storms. In addition, the HWM14 model (*Drob et al., 2015*) derived thermospheric winds and the NRLMSISE model (*Picone et al., 2002*) provided neutral temperatures for thermospheric altitudes over Ahmedabad have been used in this work. The description of these dataset is given in the chapter 2 (section 2.3.7).

5.4 Analyses and Results

Vertical propagation speeds (c_z) and vertical scale sizes (λ_z) of gravity waves in the thermosphere during daytime have been derived using digisonde data. These have been derived following the methodology discussed in chapter 3, by using the variations in the heights of isoelectron density contours at five discrete transmission frequencies of 8, 9, 10, 11, and 12 MHz of digisonde. In this duration, 661 days of digisonde data have been analyzed.

5.4.1 The occurrence of vertical propagation of gravity waves

In this duration vertical propagation of gravity waves has been observed only on 272 (41%) days. This could be due to the effects of the varying nature of ambient wind structures and various dissipation conditions (e.g., *Vadas and Fritts, 2005; Pallamraju et al., 2016; Mandal et al., 2019, 2020*). We have quantified the vertical propagation activity of gravity

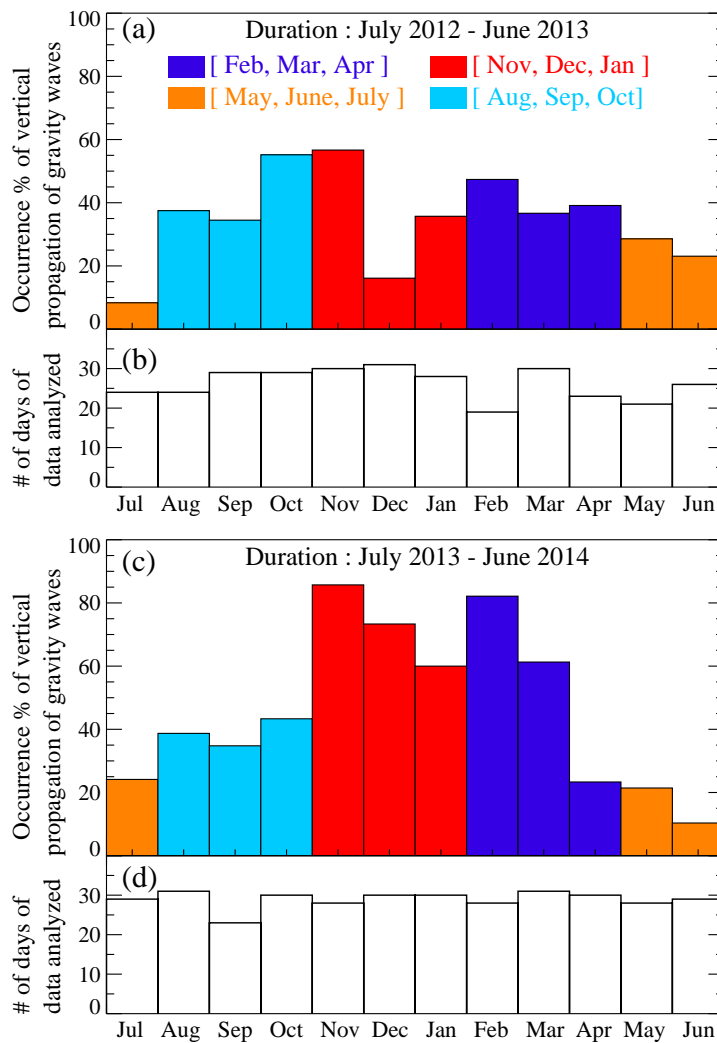


Figure 5.1: (a) Occurrence percentage of vertical propagation of gravity waves in the daytime thermosphere in different months during July 2012-June 2013. (b) The number of days of data analyzed in each month for investigation of vertical propagation activity of gravity waves for the duration July 2013-June 2014. (c) & (d) Same as shown in (a) & (b) but for the duration of July 2013-June 2014. A clear seasonal behavior in both years can be noted. Different colors represent different seasons of a year.

waves as a percentage of the ratio of days with vertical propagation to the number of days of data analyzed in a given month. In this way, the dissimilar number of days of data in a given month will not bias the values and the results are expected to get normalized. Figures 5.1a and 5.1c show bar plots depicting variations in the occurrence percentages of vertical propagation of gravity waves in different months from July to June for 2012-2013 and 2013-2014, respectively. The leftmost bar in each figure corresponds to the month of July, and the rightmost bar is for the month of June. On average, the vertical propagation activity of gravity waves in the daytime thermosphere is observed only 41% of the times. Figure 5.1b and 5.1d represent the number of days of data analyzed in each month for this duration. They clearly show that the data availability is consistent in each month for the entire duration of two years. This confirms that the variation in the vertical propagation activity of gravity waves in the daytime thermosphere is not biased by the data availability. Here, different seasons have been represented in different colors. One can readily notice from these figures that the gravity wave propagation in vertical

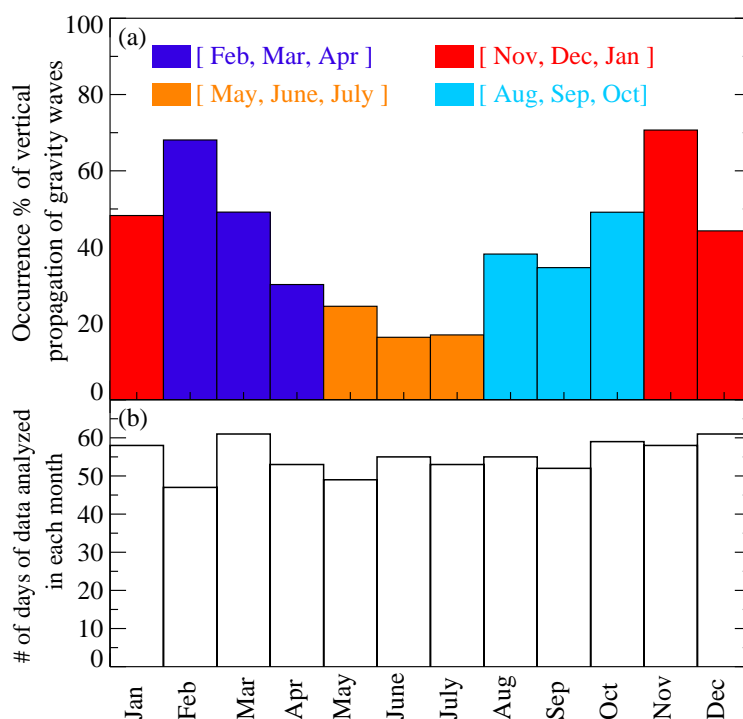


Figure 5.2: (a) Seasonal variation in the occurrence percentages of vertical propagation of gravity waves in the daytime thermosphere for the duration of July 2012-June 2014. (b) The number of days of data analyzed for each month. It can be noted that data are available for 79%-98% of the times.

direction varies significantly with seasons. They are significantly less during the months of May, June, and July in both the years with higher values in the year 2013-2014 compared to 2012-2013. But the overall variation in vertical propagation activity of gravity waves in these two years is very similar. Hence, data from the same month for the two years under consideration are added to get a comprehensive picture and are shown in figure 5.2. For the entire duration of data, $\sim 50\%$ or more number of days in January, February, March, October, November, and December show vertical propagation activity; and for April, May, June, and July it is 30% or lower. Therefore, on average, the occurrence percentage of vertical propagation activity of gravity waves shows a double-humped structure over low-latitudes in a given year and can be seen in figure 5.2.

5.4.2 Vertical propagation characteristics of gravity waves during geomagnetically quiet days

The days when vertical propagation of gravity waves has been observed are categorized into geomagnetically quiet and disturbed days based on the Dst index. Selection of geomagnetically quiet days are made in two ways, case-1: if the Dst index remains greater than -10 nT (i.e., $Dst > -10$ nT) for the period 00-18 LT on a given day and the entire previous day, and case-2: for $Dst > -15$ nT for the same duration as in case-1, then that given day has been considered to be a geomagnetically quiet day in our analysis. This eliminates any possibility of geomagnetic activity effects on the derived gravity wave characteristics. Thereby ensuring that gravity wave characteristics present on a quiet day to be purely due to ambient atmospheric variations. Per the criterion of case-1, 132 days, and 170 days as per the case-2 criterion, are found to be geomagnetically quiet days out of 272 days in which vertical propagation of gravity waves was observed. In figure 5.3a, the daily average values of phase speeds, $\langle c_z \rangle$, (inverted triangles) and their monthly averaged values, $\langle c_{z_monthly} \rangle$ (filled diamonds) during geomagnetic quiet days as per case-1 are shown. Variation in $\langle c_z \rangle$ shows two peaks during March-April and August-September. As the focus of this study is on the investigation of the systematic nature of the gravity wave characteristics on an annual time scale, we have considered the daily mean values of vertical propagation characteristics. In figure 5.3b, daily averaged values of vertical wavelengths $\langle \lambda_z \rangle$ (solid circles) and their monthly mean values, $\langle \lambda_{z_monthly} \rangle$ (filled

diamonds) for geomagnetic quiet times have been shown. Daily $\langle \lambda_z \rangle$ values also show a double-humped pattern with peaks around equinoctial months similar to those seen in daily $\langle c_z \rangle$. In figure 5.3c, the number of days of data available in each month for these

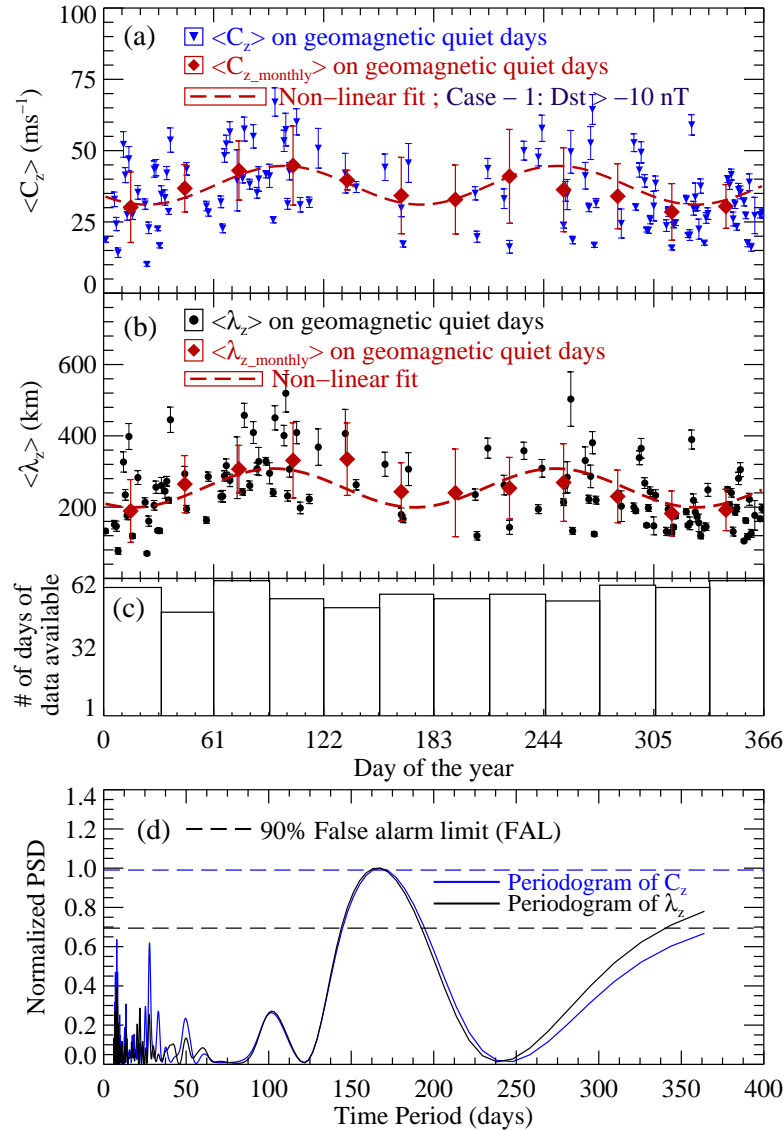


Figure 5.3: Vertical propagation characteristics of gravity waves during the geomagnetic quiet days as per case-1. (a) Daily vertical phase speeds ($\langle c_z \rangle$) of gravity waves are shown as filled inverted triangles. Filled diamonds represent their monthly averaged values ($\langle c_{z_monthly} \rangle$) along with their standard deviations. The dashed curve represents the non-linear fit (given by equation 5.1) representing the variations in their monthly averaged values. (b) Same as in (a) but for $\langle \lambda_z \rangle$. (c) Data availability for each month in these two years is shown. On average, data are available for around 89% of the days. (d) The Lomb-Scargle periodogram are shown for $\langle c_z \rangle$ (blue color), & $\langle \lambda_z \rangle$ (black color). Dashed lines represent 90% FAL.

two years is shown. As data of a given month from the two years considered are overlaid, the maximum number of days in a month is 62. It can be noted that data are available for 79%-98% of the time in a given month in this entire duration. All these data have been analyzed and on 41% of the days vertical propagation activity has been observed. Hence, the variation in vertical propagation speeds and wavelengths of gravity waves for geomagnetically quiet days (as presented in figures 5.3a and 5.3b), is clearly due to the seasonal effects. The Lomb-Scargle periodogram analysis has been carried out for both $\langle c_z \rangle$, and $\langle \lambda_z \rangle$, and the results are depicted in the figure 5.3d. Periodicity of around 165 days is found to be significant both in $\langle c_z \rangle$ and $\langle \lambda_z \rangle$. Variation in the daily $\langle \lambda_z \rangle$ values are similar to those of $\langle c_z \rangle$, because λ_z values are estimated from the c_z as described in chapter 3. This value of time period has been used to carry out a non-linear fit to the monthly averaged values $\langle c_{z_monthly} \rangle$, and $\langle \lambda_{z_monthly} \rangle$ (shown as filled diamonds in figures 5.3, to represent the geomagnetic quiet time variation as a function of day of the year. Here, the non-linear fit has been carried out using sinusoidal functions to characterize the oscillatory variation seen in the vertical phase speeds and wavelengths of gravity waves. In order to achieve the best fit, we have used the Levenberg-Marquardt technique, which gives the least-squares fit solution. Numerical relations of vertical propagation parameters of gravity waves as a function of day of the year resulted from such analysis is given below.

$$\langle c_z \rangle_q = 37.86 + 6.78 \sin\left[\left(\frac{2\pi}{152.12}\right)d + 3.73\right] \quad (5.1)$$

$$\langle \lambda_z \rangle_q = 253.82 - 54.37 \sin\left[\left(\frac{2\pi}{156.03}\right)d + 0.91\right] \quad (5.2)$$

where $\langle c_z \rangle_q$ and $\langle \lambda_z \rangle_q$, respectively, represent the annual variations in the gravity wave vertical phase speeds in units of ms^{-1} and vertical wavelengths in units of km, during geomagnetic quiet days, and d represents the day of the year.

Figure 5.4 describes the same parameters as shown in figure 5.3 but for 170 days of geomagnetically quiet conditions as per case-2. Variation in $\langle c_z \rangle$ and $\langle \lambda_z \rangle$ shows the presence of significant periods of ~ 170 & 165 days, respectively, when subjected to periodogram analyses (as shown in figure 5.4d). Similar to equations 5.1 and 5.2, seasonal variability in the values of $\langle c_z \rangle$ and $\langle \lambda_z \rangle$ for geomagnetically quiet days selected

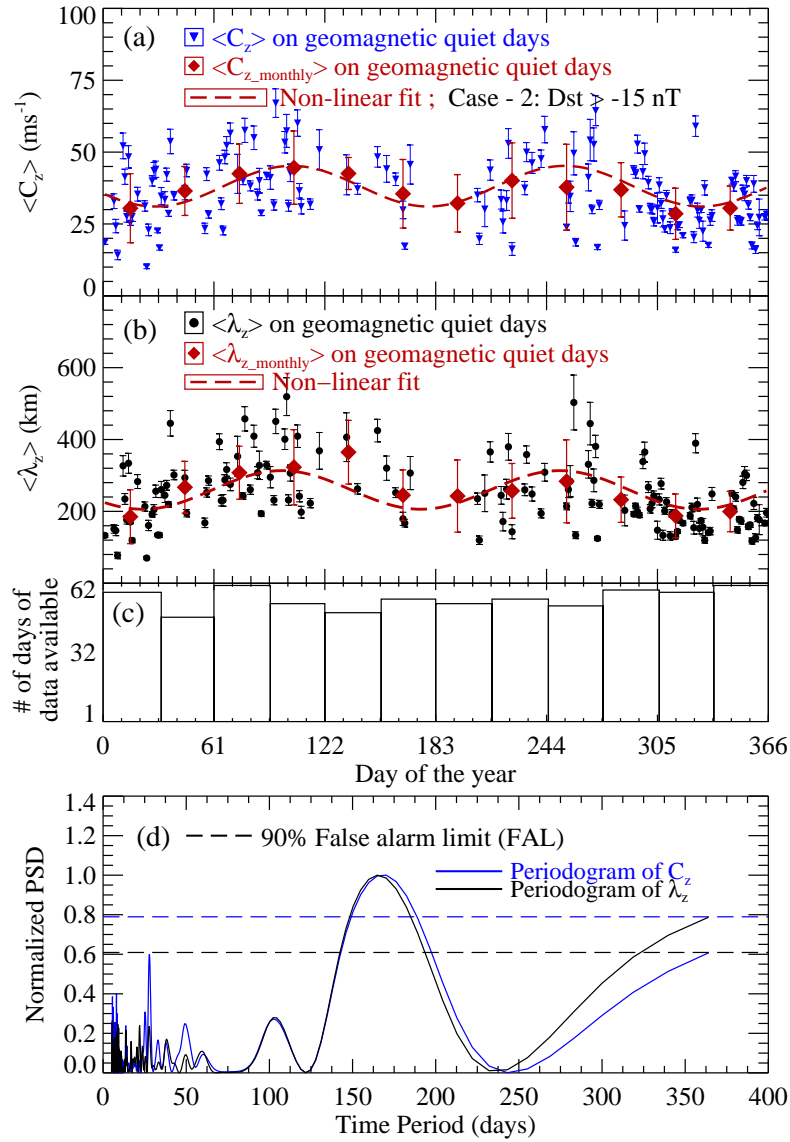


Figure 5.4: Same as shown in figures 5.3 but for geomagnetically quiet days as per the criterion of case-2 ($Dst > -15.0$ nT).

based on the criterion for case-2 have been carried out using similar non-linear fit analysis and are given by equations 5.3 and 5.4.

$$\langle c_z \rangle_q = 37.65 + 7.05 \sin\left[\left(\frac{2\pi}{150.55}\right) d + 3.47\right] \quad (5.3)$$

$$\langle \lambda_z \rangle_q = 269.11 - 67.32 \sin\left[\left(\frac{2\pi}{148.93}\right) d + 0.19\right] \quad (5.4)$$

These numerical relations (equations 5.1 to 5.4) can give the average behavior of gravity waves in the daytime thermosphere based on the day of year given as input for geomag-

netic quiet times. It is well-known that winds play an important role in wave propagation (*Pallamraju et al.*, 2014, 2016; *Mandal et al.*, 2019). If wind flows in opposite/same direction as that of the wave propagation, then the horizontal wavelength of the waves decreases/increases which is associated with an increase/decrease of the vertical wavelength. In section 3.4.6, we have discussed these effects of background wind structures on the scale sizes of gravity waves. In this work, variation in the HWM14 model (*Drob et al.*, 2015) derived winds have been investigated to understand the seasonal behavior observed in $\langle c_z \rangle$, and $\langle \lambda_z \rangle$ for geomagnetic quiet times. We have taken geomagnetic quiet time zonal (U_x), meridional (U_y), and the resultant horizontal (U_H), wind values for thermospheric altitudes over Ahmedabad for noon-time. As the gravity waves derived in the daytime thermosphere from the digisonde of Ahmedabad correspond to the altitude re-

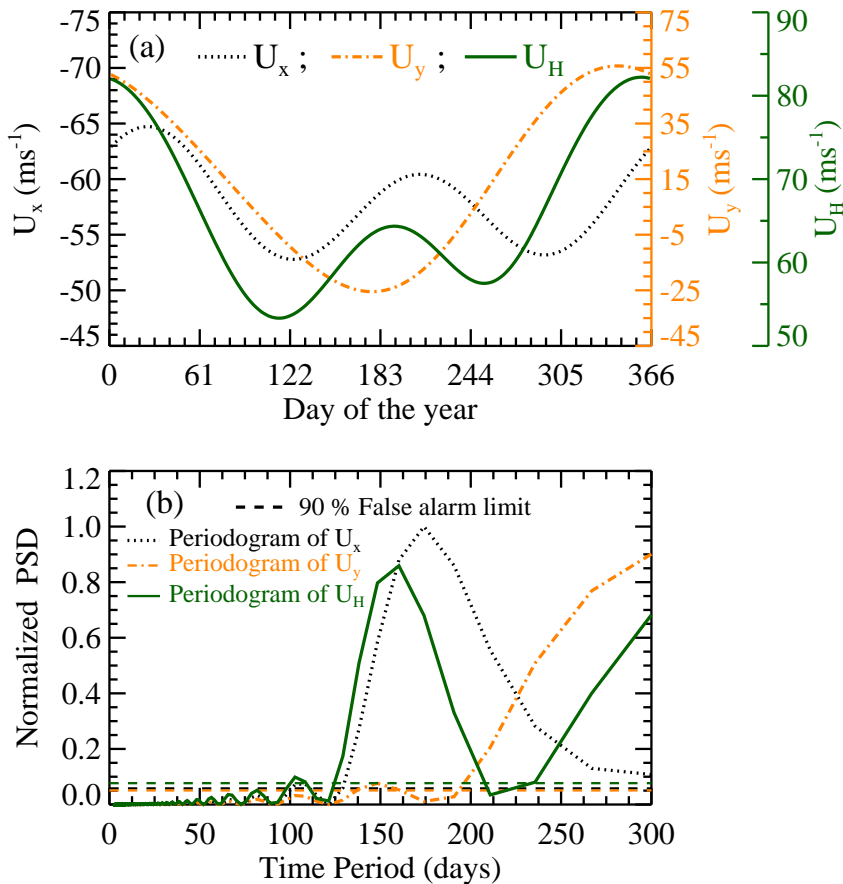


Figure 5.5: (a) The HWM14 model derived local noon-time zonal (U_x ; dotted curve; positive eastward), meridional (U_y ; dash-dotted curve; positive poleward), and the resultant horizontal winds (U_H ; solid curve) over Ahmedabad at an altitude of 270 km. (b) The Lomb-Scargle periodogram analyses of U_x , U_y , and U_H . The dashed lines represent the 90% FAL.

gion of ~ 270 km (described in chapter 3), we have averaged the wind values of an altitude of 270 km during 11-14 LT. Figure 5.5a shows variations of the HWM14 model derived noon-time zonal wind (U_x ; dotted curve), meridional wind (U_y ; dash-dotted curve), and horizontal wind (U_H ; solid curve) over Ahmedabad. In this duration, the zonal winds are westwards and vary between -53 to -65 ms^{-1} . Poleward/equatorward meridional winds are positive/negative, and their values are in the range of -25 to 55 ms^{-1} . Distribution of noon-time zonal wind shows two minima around the day of the year (doy) 111 and 255. Over Ahmedabad, noon-time meridional winds are equatorward during doys: 104-240 (around summer time), and are poleward for the rest of the year, as expected. Therefore, the daytime resultant horizontal winds over Ahmedabad flow either in the south-west direction (when meridional winds are equatorward), or in the north-west direction (when the winds are poleward) (depicted in figure 5.7c). The Lomb-Scargle periodogram analyses have been carried out on zonal, meridional, and total winds. Figure 5.5b shows the result of time series analysis of zonal (dotted curve), meridional (dash-dotted curve), and resultant horizontal winds (solid curve). Zonal winds show time periods (τ_{U_x}) of around 108 and 174 days. Time period (τ_{U_y}) of around 148 days is significant in the variation of meridional winds, and time periods (τ_{U_H}) of around 168 and 103 days are found in the resultant horizontal winds. Therefore, the time periods of around 165 days for case-1 and around 170 & 165 days for case-2 found in the variations of quiet time $\langle c_z \rangle$ and $\langle \lambda_z \rangle$, clearly seem to be an influence of τ_{U_H} of around 168 days. Variation in U_H shows two minima around the months of March-April (53 ms^{-1}) and August-September (58 ms^{-1}). Around the same time, we have also observed maxima in the values of vertical propagation characteristics of gravity waves. To facilitate an easy comparison, in figures 5.6a and 5.6b, we have shown the same information as in figures 5.3a and 5.3b in addition to the thermospheric resultant horizontal winds. The correlation coefficients between the monthly averaged values of winds with those of phase speeds and vertical wavelength are -0.80 and -0.85 , respectively. Therefore, such striking similarity in the time periods and anti-correlated behavior between these two gravity wave propagation parameters and U_H , suggest a strong influence of horizontal winds on the vertical propagation of gravity waves in the daytime thermosphere over low-latitudes. When the geomagnetic quiet days are chosen as per the criterion of case-2 (section 5.4.2), variations in $\langle c_z \rangle$ and $\langle \lambda_z \rangle$ for 170 quiet days are shown in figure 5.7 along with the values of noon-time resultant horizontal

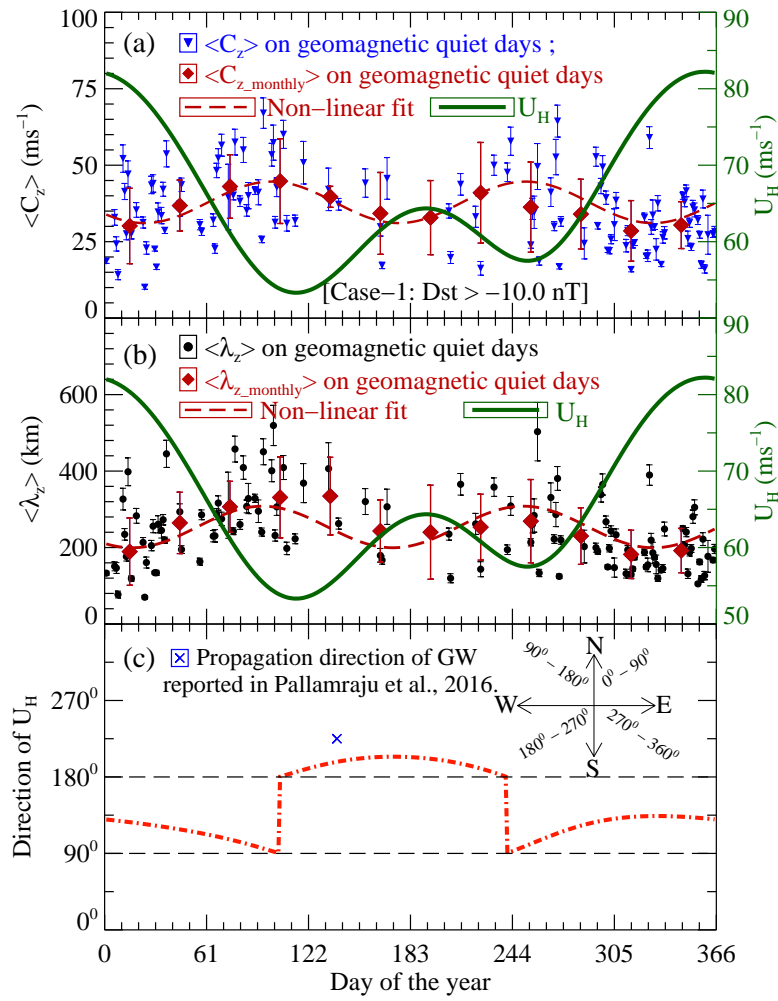


Figure 5.6: (a) $\langle c_z \rangle$ for geomagnetic quiet days as considered per the criterion of case-1 are shown as filled inverted triangle. Filled diamonds represent monthly averaged values ($\langle c_{z_monthly} \rangle$) along with their standard deviations. The dashed curve is the non-linear fit (equation 5.1). The solid curve represents noon-time resultant horizontal wind over Ahmedabad. (b) Same as in (a) but for the $\langle \lambda_z \rangle$. (c) Propagation directions of noon-time thermospheric horizontal winds (U_H) over Ahmedabad are shown as a dash-dotted curve. Horizontal dashed lines are drawn for angles of 90° and 180°. Winds are either north-westward or south-westward, depending on the direction of meridional winds. The blue-colored cross represents the earlier reported (Pallamraju et al., 2016) propagation direction of gravity waves in the daytime as obtained from large field-of-view optical measurements.

winds (U_H). Here, the values of c_z and λ_z as shown in figures 5.4a and 5.4b are shown again for easier comparison. For geomagnetically quiet days as per case-2, the correlation coefficients between the monthly averaged values of c_z and U_H is -0.85, and that for λ_z and U_H is -0.84. Hence, we see that the correlation coefficient between the vertical phase

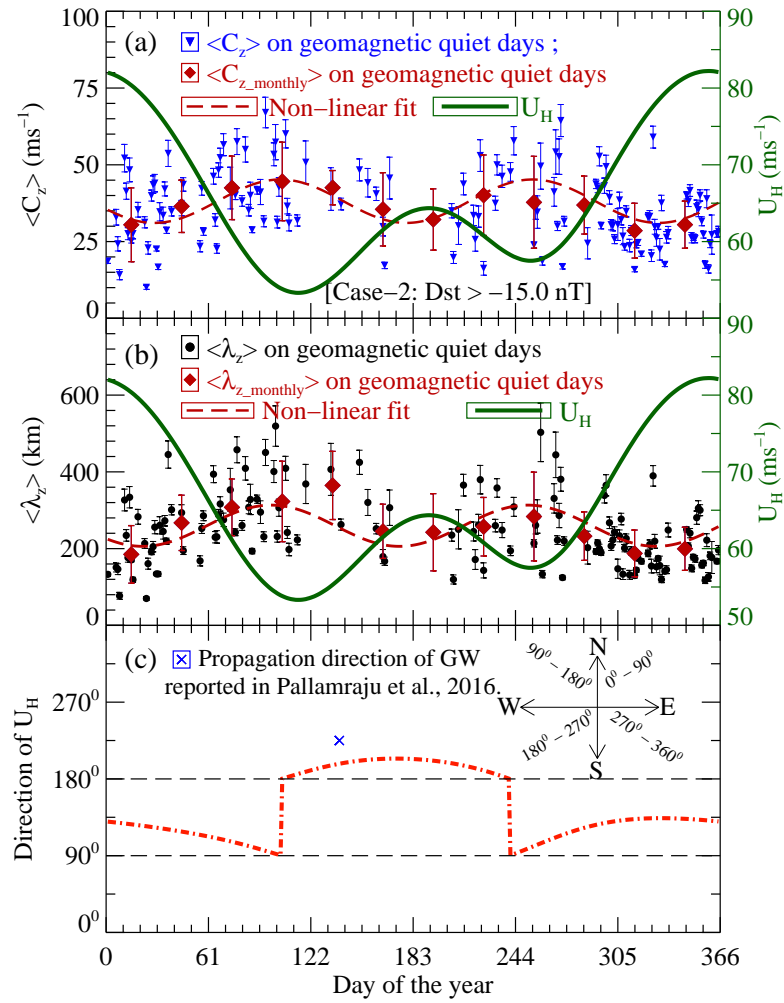


Figure 5.7: Same as shown in figures 5.6 but for 170 days of geomagnetically quiet condition based on the criterion mentioned in case-2.

speeds and resultant wind values in case-2 (170 days) shows a slight increase compared to case-1 (132 days). Figure 5.7c depicts the direction of wind propagation as derived from the HWM14 model. It can be seen that the daytime thermospheric horizontal winds over Ahmedabad flow in either north-west or south-west directions. The two maxima in the magnitudes of vertical propagation parameters of gravity waves nearly coinciding with the two minima in the horizontal winds, gives clues to the propagation direction of gravity waves. The increase in vertical phase speeds and scale sizes of gravity waves nearly concomitant with the weakening of westward horizontal winds suggests that in the daytime, gravity waves are propagating in the westward direction. Therefore, as the wind magnitudes in the north-west or south-west directions increase, the horizontal scale sizes of the gravity waves increase, and consequently, the vertical scale sizes of gravity waves decrease. Information on the propagation direction of gravity waves in the horizontal plane can be

obtained by carrying out dayglow emission measurements from over a large field-of-view. Using such measurements in zonal and meridional directions, in earlier work *Pallamraju et al.* (2016) have shown that gravity waves propagate in the south-west direction during the month of May (doy 139), with an angle of around 225° (shown as the blue-colored cross in figure 5.7c). It is reassuring to note that the sense of gravity wave propagation direction in the horizontal plane arrived at in the current work matches closely with that obtained from the independent optical measurements. To the best of our knowledge, this is a very new kind of information in the case of thermospheric gravity waves in the daytime over low-latitudes. It is striking that the results of the detailed analysis of digisonde data to obtain vertical propagation speeds and scale sizes of gravity waves and global scale empirical model winds over Ahmedabad, together yield a very clear synoptic picture of the possible direction of propagation of gravity waves in the daytime in the horizontal plane. Also, such information matches with the direction of propagation of gravity waves obtained by independent optical measurements. We have summarized the details of case-1 and case-2 of selecting geomagnetic quiet days in table 5.1, wherein correlation coefficients (R) between gravity wave propagation parameters and thermospheric horizontal wind have been listed. Correlation between the gravity wave propagation parameters and thermospheric winds is better when more quiet days are considered as per case-2 (170 days) compared to case-1 (132 days). Therefore, for further analysis, we have considered the non-linear fit for variation in vertical propagation characteristics of gravity waves for the case-2 as representative of their behavior during geomagnetic quiet times (equations 5.3 and 5.4).

Type	Criterion	Number of days	$R(c_z, U_H)$	$R(\lambda_z, U_H)$
Case-1	Dst > -10 nT	132	-0.80	-0.85
Case-2	Dst > -15 nT	170	-0.85	-0.84

Table 5.1: *Summary of analysis of thermospheric gravity wave characteristics for geomagnetic quiet days selected as per the criteria case-1 and case-2*

5.4.3 Vertical propagation characteristics of gravity waves during geomagnetically disturbed days

So far in section 5.4.2, we have seen that in the daytime thermosphere the vertical propagation speeds and wavelengths of gravity waves during geomagnetically quiet times show two peaks annually and they are strongly influenced by the thermospheric winds. During the events of geomagnetic storms, the thermospheric background wind pattern changes significantly as a result of equatorward meridional circulation due to heating at high-latitude (section 1.3.5 of chapter 1). To investigate the effects of these modified wind patterns, we have investigated the variation in the propagation characteristics of gravity waves during geomagnetically disturbed times. In this duration of two years of data, we have found 40 days of geomagnetically disturbed conditions ($Dst < -25$ nT), wherein vertical propagation characteristics of gravity waves exist. It is interesting to note that all these 40 days are in the recovery phases of geomagnetic storms of varying strengths. Following the methodology described in chapter 3, vertical phase speeds and vertical wavelengths of gravity waves for all these 40 days have been calculated. Figure 5.8a shows vertical phase speeds ($\langle c_z \rangle$; filled inverted triangles) derived on these days and a dashed curve representing the quiet time values ($\langle c_z \rangle_q$; as given in equation 5.3). The changes in the vertical phase speeds of gravity waves ($\langle c_z \rangle_d = \langle c_z \rangle - \langle c_z \rangle_q$) during geomagnetically disturbed times with respect to quiet time values ($\langle c_z \rangle_q$) are shown in figure 5.8b (dotted curve with filled inverted triangles). In this figure, positive/negative values indicate an increase/decrease in $\langle c_z \rangle$ during disturbed days as compared to geomagnetic quiet days. Figure 5.8c shows the vertical scale sizes ($\langle \lambda_z \rangle$; filled circles) of gravity waves derived for all 40 days of geomagnetic disturbed conditions and the dashed curve represents their quiet time behavior ($\langle \lambda_z \rangle_q$; represented by equation 5.4). Changes in vertical wavelengths ($\langle \lambda_z \rangle_d = \langle \lambda_z \rangle - \langle \lambda_z \rangle_q$) on disturbed days as compared to $\langle \lambda_z \rangle_q$ (equation 5.4) are shown in figure 5.8d (dotted curve with filled circles). The signs of $\langle c_z \rangle_d$, and $\langle \lambda_z \rangle_d$ are similar, but their variation and magnitudes are different. However, the changes in the $\langle c_z \rangle$ and $\langle \lambda_z \rangle$ values during geomagnetically disturbed times with respect to geomagnetic quiet times indicate response to the additional energy that becomes available to the ionosphere-thermosphere system during

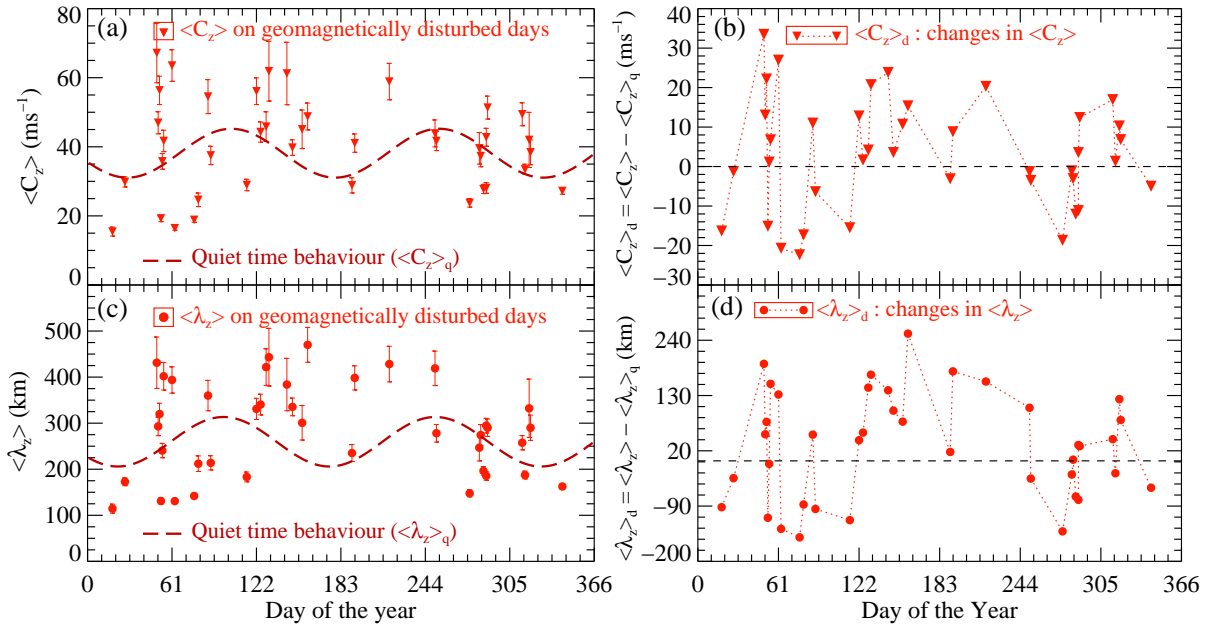


Figure 5.8: (a) Vertical phase speeds ($\langle c_z \rangle$) for geomagnetically disturbed days are shown as filled inverted triangles. And the dashed curve represents the averaged quiet time behavior of $\langle c_z \rangle_q$. (b) Changes in c_z values ($\langle c_z \rangle_d$) during geomagnetic storms as compared to their quiet time values are shown. (c) Same as in (a) but for vertical wavelengths (λ_z) of gravity waves during geomagnetically disturbed times, and (d) same as in (b) but for $\langle \lambda_z \rangle_d$.

geomagnetic storms. During these times, disturbances in the ionosphere-thermosphere system are created due to altered wind patterns in response to the differential heating in the thermosphere (e.g., [Richmond and Matsushita, 1975](#); [Mayr et al., 1978](#); [Pröls, 1993](#)). In section 5.4.2, we have seen that thermospheric wind structures govern the magnitudes of the vertical propagation characteristics of gravity waves. Therefore, one can expect that during geomagnetic storms, the additional energy inputs will result in altering the gravity wave propagation characteristics over low-latitudes, as the wind magnitudes and directions get modified. Here, we have made an attempt to quantify these changes in vertical propagation characteristics of gravity waves in terms of energy inputs at high-latitudes. During geomagnetically disturbed days, high energy particles precipitate in the upper atmosphere of high-latitudes, which increase the magnitudes of the ionospheric currents as characterized in the auroral electrojet (AE) values. An increase in currents causes intense Joule heating in the high-latitude regions during geomagnetic disturbed conditions. It has been shown that the values of the AE index are proportional to the

Joule heating that takes place in the high-latitudes ([Akasofu, 1981](#)). This Joule heating drives meridional circulation towards the equator, and their effects take time to reach the low- and equatorial-latitudes. We have taken 14 LT to be the representative time for daily values of $\langle c_z \rangle$, and $\langle \lambda_z \rangle$, as it is the mean of our observation duration. Therefore, we have considered the AE index values of the different time windows (6, 12, 18, 24, 28, 30, 36, 42, and 48 h) prior to 14 LT of a given day. High-latitude heating is considered to be significant during geomagnetic disturbed times when the AE index is greater than 300 nT ([Navarro et al., 2019](#)). Further, it is also known that the cumulative effect of this sustained heat energy received at high-latitudes has a role to play in bringing about redistribution in energies until low-latitudes. Therefore, we have integrated the values of the AE index for 4 h around the time of its peak value greater than 300 nT. In this way, it is expected that the integrated values of the AE index will fairly represent the magnitudes of Joule heating that took place in the high-latitudes for a given event of geomagnetic storms. The similarities between the integrated AE index values and changes in vertical propagation characteristics of gravity waves compared to their quiet time values are found to be significantly higher when the AE indices are chosen of 28 h and more (30, 36, 42, and 48 h) prior to 14 LT as seen in figure 5.10. As the geomagnetic storm events under consideration in this work are all in the recovery phases, it is required to limit to an optimum time delay while considering AE indices for the effects of geomagnetic storms are seen on the wave dynamics over the low-latitudes. Thus, we have used the shortest time lag of 28 h, which agrees with earlier findings reported in the literature ([Navarro et al., 2019](#)) for geomagnetic disturbed time effects to reach low-latitude regions, in order to restrict to the effects of the latest storm. In figure 5.9a, $\langle c_z \rangle_d$ i.e., changes in vertical phase speeds on geomagnetically disturbed days are shown (filled inverted triangles) along with the integrated values of the AE index (dashed line with asterisks). The same variation in $\langle \lambda_z \rangle_d$ along with the integrated values of AE index are shown in figure 5.9b. A considerable similarity is seen between these two gravity wave parameters derived from our measurements and the integrated values of the AE index. Joule heating at high-latitudes generates pressure gradient forces that drive the meridional circulation, which contributes to redistribution in the energy from high- to low-latitudes during geomagnetic disturbed times. Therefore, the similarities observed between the variations in the integrated values of AE index with $\langle c_z \rangle_d$ and $\langle \lambda_z \rangle_d$ is due to resultant disturbed time winds in the

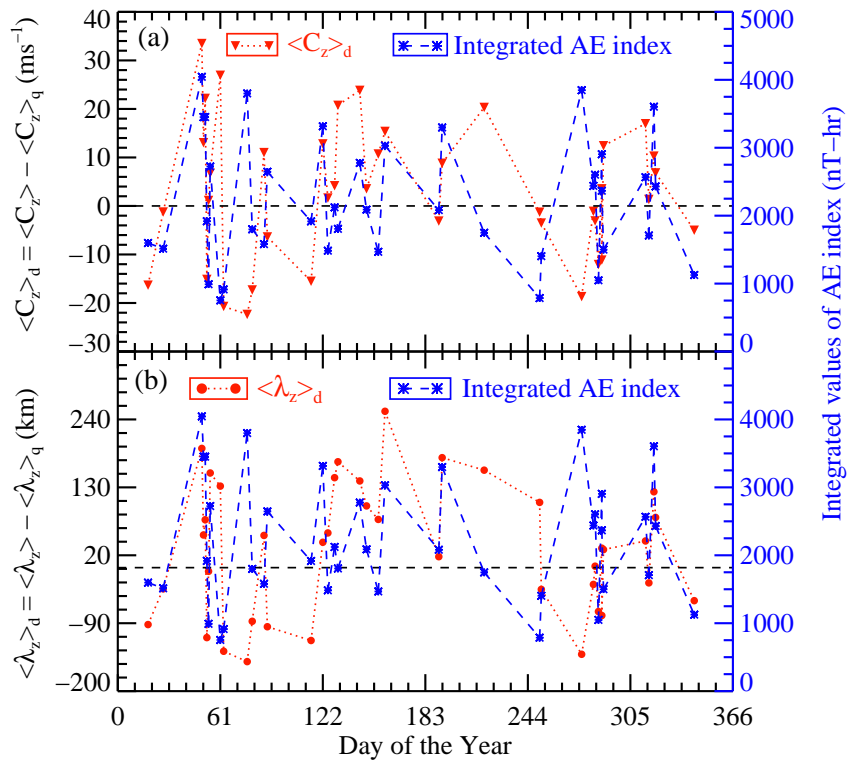


Figure 5.9: (a) Changes in vertical propagation speeds ($\langle c_z \rangle_d$) on disturbed days as compared to quiet times are shown as inverted filled triangles. Values of the AE index integrated over 4 h around the peak value of the AE index of the past 28h with respect to 14 LT on a given day are shown as asterisks. (b) Same as in (a) but for changes in the values of vertical wavelengths ($\langle \lambda_z \rangle_d$) during geomagnetic disturbed times.

low-latitudes caused by the modifications brought in during geomagnetic storms. Table 5.2 lists the integrated AE values and observed $\langle c_z \rangle_d$ and $\langle \lambda_z \rangle_d$ values on these geomagnetically disturbed days. In this table, data in bold represent the values on 9 days on which similarities in the behavior of these two parameters with the integrated AE indices have not been seen. It can be noted that these days, when the integrated values of AE index and changes in gravity wave parameters are not similar, happen to be mostly either with relatively lower values of integrated AE index or in equinoctial months. If the Joule heating magnitudes (which are characterized by integrated AE values in this work) are less, then their effects may not reach the low- and equatorial-latitudes or can get filtered out by different other thermospheric background conditions that affect the wave dynamics. During equinoxes both the hemispheres are expected to be heated up to nearly similar magnitudes, which, combined with the seasonal poleward directed winds in both the hemispheres from the equator, would weaken the meridional transport from

high- to low-latitudes. Thereby, the coupling between high-to-low latitudes via meridional winds may get weakened during these times. This is likely the cause that we do not see

Date	DOY	Integrated AE (nT-h)	$\langle c_z \rangle_d$ (ms ⁻¹)	$\langle \lambda_z \rangle_d$ (km)
18.01.2013	18	1597.50	-16.32	-92.18
27.01.2013	27	1513.50	-1.25	-34.37
19.02.2014	50	4044.50	33.48	193.08
20.02.2014	51	3452.00	13.04	52.85
21.02.2014	52	3452.00	22.18	77.51
22.02.2014	53	1918.00	-15.13	-113.32
23.02.2014	54	990.50	1.13	-5.98
24.02.2014	55	2724.50	6.78	153.28
02.03.2014	61	753.00	26.94	132.01
04.03.2013	63	913.50	-20.71	-135.41
18.03.2013	77	3799.00	-22.35	-152.19
21.03.2013	80	1799.00	-17.31	-86.88
28.03.2013	87	1580.50	11.00	52.19
30.03.2013	89	2646.50	-6.38	-95.71
25.04.2013	115	1916.00	-15.52	-118.01
02.05.2013	122	3316.00	12.80	41.08
05.05.2013	125	1484.00	1.64	56.19
09.05.2014	129	2122.50	4.17	145.69
11.05.2014	131	1805.50	20.74	171.45
24.05.2014	144	2776.50	23.83	140.39
28.05.2013	148	2088.50	3.54	99.95
04.06.2013	155	1467.50	10.71	78.07
08.06.2013	159	3030.50	15.37	253.21
09.07.2012	191	2081.50	-3.11	17.72
12.07.2013	193	3298.50	8.81	178.10
06.08.2013	218	1748.00	20.31	157.85
07.09.2012	251	787.00	-1.28	105.66
08.09.2012	252	1403.50	-3.52	-35.25
03.10.2013	276	3847.50	-18.69	-140.34
09.10.2012	283	2438.00	-1.10	-27.15
10.10.2012	284	2603.00	-3.08	2.33
12.10.2012	286	1048.50	-12.07	-71.11
15.10.2013	288	2904.50	3.54	31.52
14.10.2012	288	2367.00	-11.15	-77.54
15.10.2012	289	1500.00	12.41	29.21
10.11.2013	314	2566.50	16.95	43.17
12.11.2013	316	1707.50	1.34	-24.71
14.11.2012	319	3604.50	10.28	122.87
15.11.2012	320	2430.50	6.82	81.35
09.12.2013	343	1126.00	-5.00	-53.49

Table 5.2: Values of $\langle c_z \rangle_d$, $\langle \lambda_z \rangle_d$ over Ahmedabad and the integrated AE index during geomagnetic disturbed days. The days when $\langle c_z \rangle_d$ and the integrated AE index value do not show any similarity are shown in bold.

similarities between the integrated values of the AE index and changes in the gravity wave parameters for a few of the cases. This is also consistent with an earlier finding of [Karan and Pallamraju \(2018\)](#), wherein, using thermospheric dayglow measurements at multiple wavelengths, it was shown that during equinoctial months thermospheric dynamics over low-latitudes is majorly influenced by the equatorial electrodynamics rather than the geomagnetic disturbances (in terms of $[\frac{O}{N_2}]$ variation) from high-latitudes. For geomagnetic storms in other seasons energy inputs from high-latitudes are brought in through winds showed greater influences on the low-latitude thermospheric dynamics than the equatorial electrodynamics. Now, in order to quantify the similarities observed between $\langle c_z \rangle_d$ and integrated AE index values on the other 31 days, we have performed correlation analysis. Figure 5.10 depicts the variation in the correlation coefficient between $\langle c_z \rangle_d$ and the integrated AE values for different time lags prior to 14 LT of all these days (excluding the days shown in bold in table 5.2. It can be immediately noticed from this figure that

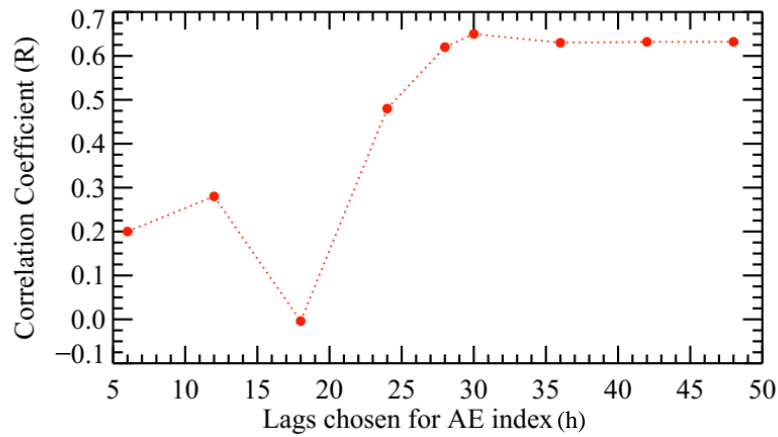


Figure 5.10: *Correlation coefficients between changes in c_z values with the integrated AE index considered for different lags during geomagnetically disturbed conditions.*

correlation coefficients are significantly higher when AE indices are considered with time lags of 28 h and beyond. Figure 5.11a shows $\langle c_z \rangle_d$ (inverted triangles) during disturbed times excluding the days shown in bold in table 5.2 along with the integrated values of AE index for these days (shown as asterisks). It is striking to note that the correlation coefficient is 0.64 between such clearly independent parameters. Vertical propagation speeds of gravity waves depend on various factors, such as prevailing wind magnitudes and their directions, background dissipation conditions, thermospheric temperatures, etc. Also, the thermosphere being a lethargic medium, takes time to respond to changes in

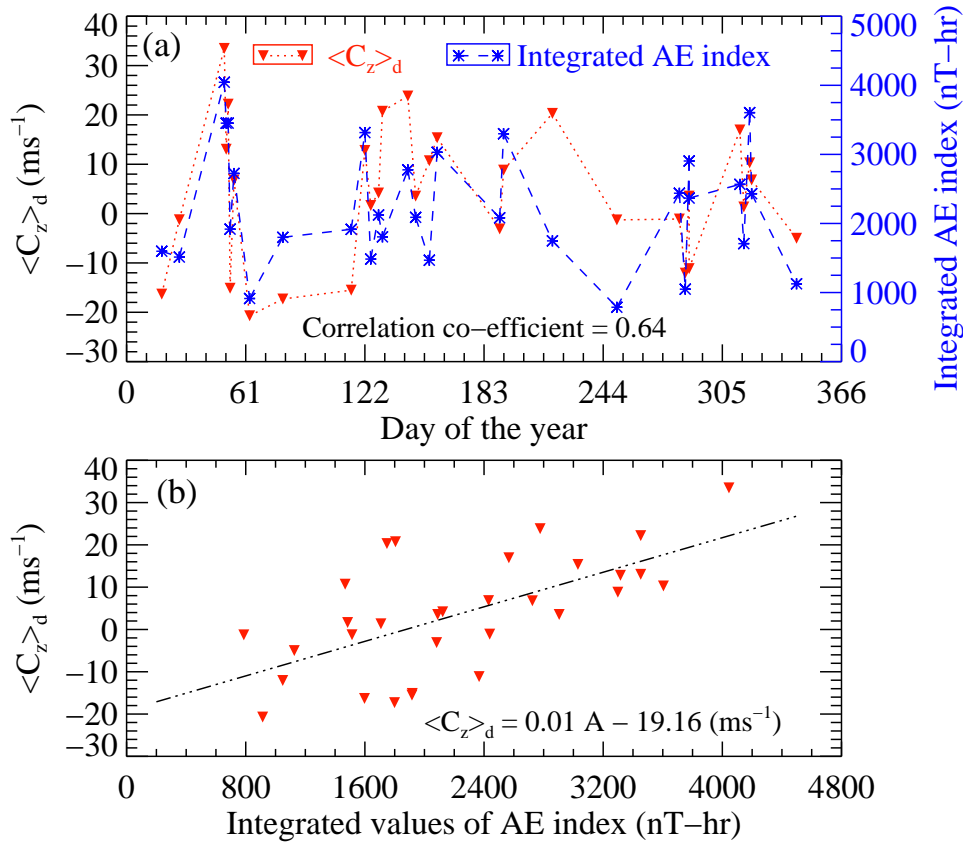


Figure 5.11: (a) $\langle c_z \rangle_d$ values of 31 days out of 40 days of geomagnetic disturbed conditions are shown (red-colored inverted triangles). Values of the AE index integrated over 4h around the peak value of the AE index of the past 28 hrs with respect to 14 LT on the day of observation for those days are shown (blue colored asterisks). (b) Scatter plot between $\langle c_z \rangle_d$ and integrated AE index values showing a linear relationship (dash-dotted line).

the system, and in the low-latitudes the thermosphere also gets influenced by equatorial electrodynamics. Considering all these factors, this correlation coefficient of 0.64 between the AE index and $\langle c_z \rangle_d$ is good. The apparently negative values of $\langle c_z \rangle_d$ can be understood to be a result of reversal in horizontal wind directions during geomagnetic storms. It can be seen from figure 5.11b that $\langle c_z \rangle_d$ linearly increases with increasing values of the integrated AE index. Linear relation (dash-dotted line) has been obtained between these two and given by equation 5.5. Using this relation with the knowledge of the AE index, disturbed time changes in vertical phase speeds of gravity waves can be estimated.

$$\langle c_z \rangle_d = 0.01 A - 19.16 \quad (5.5)$$

where, $\langle c_z \rangle_d$ represents changes in vertical phase speeds of gravity waves during geomagnetic disturbed times in the units of ms^{-1} ; A represents the integrated values of AE index.

As mentioned above, there are factors that filter out the responses of wave propagation effects from high- to low-latitudes, this relation gives estimates of the effect of geomagnetic storms on the low-latitude wave characteristic. This relation can also be used for equinoctial times but with caution. Equation 5.5, in addition to equation 5.3, can give information on the vertical phase speeds of gravity waves during geomagnetic disturbed times (equation 5.7).

$$\langle c_z \rangle = \langle c_z \rangle_q + \langle c_z \rangle_d \quad (5.6)$$

$$\langle c_z \rangle = 37.65 + 7.05 \sin\left[\left(\frac{2\pi}{150.55}\right)d + 3.47\right] + 0.01A - 19.16 \quad (5.7)$$

5.5 Summary

In this chapter, two years of digisonde data have been used innovatively to investigate the seasonal variability of the daytime thermospheric gravity wave dynamics over a low-latitude location, Ahmedabad, India. The vertical propagation of gravity waves is not seen every day (only on 41% of days), possibly due to the effect of dissipation conditions and winds. The phase speeds and wavelengths of gravity waves in the vertical direction on quiet days show semi-annual variations with two maxima during March-April and August-September. Daytime vertical propagation parameters of gravity waves over low-latitudes show anti-correlation with westward thermospheric horizontal winds, which suggests that gravity waves are propagating mostly in the westward direction over Ahmedabad. Equations 5.3 and 5.3 are represent seasonal variation in vertical propagation characteristics of gravity waves, which gives a synoptic picture of the daytime thermospheric wave dynamics during geomagnetic quiet times. Changes in gravity wave propagation parameters during geomagnetically disturbed times compared to quiet times show similar behavior with the variations in the integrated values of the AE index. The linear relation between the changes in vertical phase speeds of gravity waves and the integrated AE index values,

in combination with the non-linear empirical relationship, arrived at for geomagnetically quiet times, can be used to obtain a first-order estimate of gravity wave propagation speeds and their scale sizes in the vertical direction as a function of the day of the year. Such new information on the daytime propagation characteristics of gravity waves over low-latitudes can form definitive inputs to the modeling and simulation studies to understand the gravity wave dynamics in the daytime. This work provides strong and direct evidence of high- to low-latitude coupling in the times of geomagnetic storms.

Chapter 6

Effect of solar flux variation on the thermospheric gravity waves

6.1 Background

The prevailing background atmospheric conditions significantly influence the propagation activity of gravity waves. Effects of background wind structures on the propagation characteristics of the gravity waves have been discussed in detail in chapter 5. Other than the winds, variations in atmospheric density, and temperatures can modify the wave dissipation conditions. Changes in the solar flux directly or indirectly alter these parameters, thereby affecting the propagation of gravity waves. In this chapter, we discuss the influence of solar flux variation on the vertical propagation characteristics of gravity waves in the daytime thermosphere.

6.2 Introduction

Lower atmospheric waves in favorable background conditions, can propagate high up into the atmosphere and influence the energetics of those regions (e.g., *Fritts and Alexander, 2003*; *Laskar et al., 2013, 2014*). The amplitude of these waves increases as they propagate higher in the atmosphere of decreasing neutral density, which leads to non-linear

wave-wave interactions. Non-linear interactions maximize at the MLT region and cause most of these waves to break. This breaking of waves in the MLT region accelerates the mean flow, which again generates secondary waves (*Medvedev and Klaassen, 2000; Vadas et al., 2003; Yigit et al., 2008*). Numerous theoretical simulations and modeling studies have been carried out to understand the effects of lower atmospheric gravity waves on the dynamics of the thermosphere (e.g., *Vadas, 2007; Vadas and Liu, 2009; Yiğit and Medvedev, 2009*). Gravity waves have been shown to contribute to the heating or cooling of the thermosphere till peak F-layer altitude by up to 170 K-day^{-1} and these effects are found to be comparable to that of ion-drag (e.g., *Yiğit and Medvedev, 2009; Miyoshi et al., 2014*). The kinematic viscosity and molecular diffusion are shown to be the significant wave dissipation factors in the lower thermosphere region (*Vadas and Fritts, 2005; Yiğit et al., 2008*). These dissipation parameters are dependent on the neutral density and temperatures of the thermosphere, which are altered by the variation in the incoming solar radiation in EUV and X-ray wavelengths. Therefore, the gravity wave propagation activity gets significantly affected by the changes in solar flux (*Vadas and Fritts, 2005; Gavrilov et al., 2018*). Gravity wave activity in thermospheric altitudes derived using mass density measurements onboard CHAMP satellite has been shown to decrease with an increase in solar activity (*Park et al., 2014*). Whereas, using thermospheric dayglow measurements at different altitudes and EEJ measurements, *Laskar et al. (2015)* have shown that the gravity wave activity increases with an increase in solar activity.

In this chapter, the systematic variation in the vertical propagation occurrence and the propagation characteristics of gravity waves in the daytime thermosphere are discussed in relation to changes in the solar flux.

6.3 Data sets used

Manually scaled ionograms obtained from digisonde of Ahmedabad, India for two years (August 2012-June 2014) have been used in this study. Variation in other ionospheric parameters, such as the peak F₂-layer electron densities (NmF_2), the peak height of ionosphere (hmF_2), and the integrated electron content (IEC) has also been investigated to

understand the ionospheric behavior. Solar $F_{10.7cm}$ flux values for this duration have been used as a measure of solar flux variability. A detailed description of solar $F_{10.7cm}$ flux data is given in chapter 2 (section 2.3.4).

6.4 Data analysis and results

We have used the methodology described in chapter 3 to obtain the information on gravity waves. Height variations of the constant electron density values corresponding to fixed transmission frequencies of 8, 9, 10, 11, and 12 MHz of digisonde have been used for such analysis. Information on the phase offset has been utilized to derive vertical phase speeds and vertical wavelengths of gravity waves. Wave periods are obtained from spectral analyses of fluctuations in heights of isoelectron density contours.

6.4.1 Ionospheric variations

In this duration, variations in some of the standard ionospheric parameters, NmF_2 , hmF_2 , and IEC have been investigated. We have carried out spectral analyses of these ionospheric parameters to understand their dependencies with regard to different drivers. Variation in daily values of NmF_2 in the daytime (8-18 LT) for this entire duration is considered (shown in figure 6.1a). Here, on a few occasions, small gaps in the data exist. Therefore, spectral analysis has been carried out using the Lomb-Scargle technique ([Scargle, 1982](#)), which is suitable for periodogram analysis of unevenly spaced data, as described in chapter 2 (section 2.4.2). Periods of around 132.72 ± 0.41 , 180.71 ± 0.51 , and 290.89 ± 24.62 days are found to be significant (greater than 90% FAL) in NmF_2 , as depicted in figure 6.1b. Variations in hmF_2 corresponding to the daily maximum values of NmF_2 are shown in figure 6.1c. The Lomb-Scargle periodogram shows the presence of periods of around 190.97 ± 1.51 and 317.80 ± 5.10 days (figure 6.1d). Daily maximum of IEC as provided by digisonde ([Huang and Reinisch, 2001](#)) and their spectral analyses are shown in figures 6.1e and 6.1f, wherein periods of around 133.05 ± 0.40 , 181.11 ± 0.89 , and 299.71 ± 11.0 days are found to be significant. To understand the variations observed in the ionospheric parameters, we have investigated the variation in the solar EUV radiation, as it directly

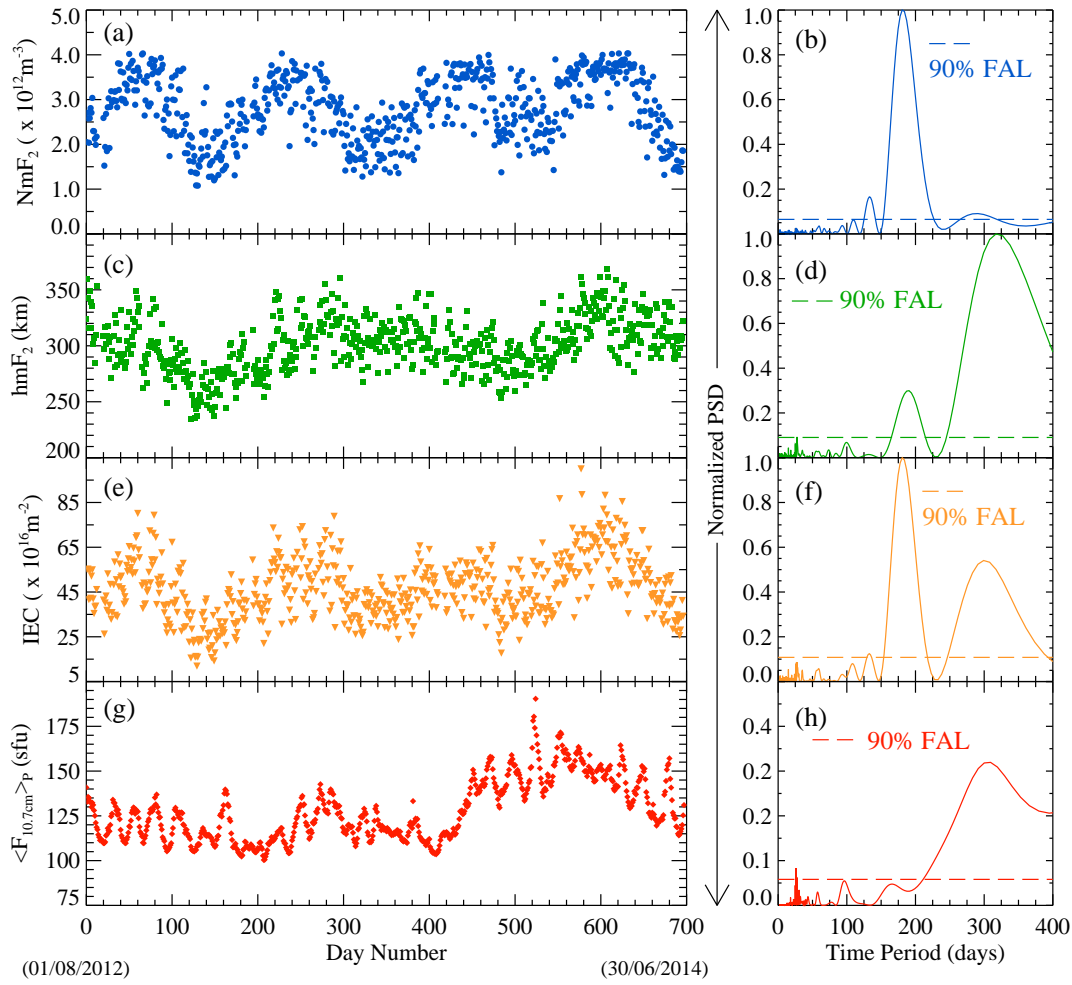


Figure 6.1: Variations in different ionospheric parameters from August 2012-June 2014 over Ahmedabad. (a) Variation in daily NmF_2 , and (b) The Lomb-Scargle periodogram analyses of NmF_2 , which show dominant periods of 132.72 ± 0.41 , 180.71 ± 0.51 , and 290.89 ± 24.62 days. The dotted line is the 90% significance level. (c) & (d) Same as in (a) & (b) but hmF_2 . Periodicities of 190.97 ± 1.51 , 317.80 ± 5.10 days are significant. (e) & (f) Same as in (a & b) but for IEC. Periods of 133.05 ± 0.40 , 181.11 ± 0.89 , 299.71 ± 11.0 days are present in IEC. (g) & (h) Same as in (a & b) but for $\langle F_{10.7cm} \rangle_P$. This parameter shows the significant periods of 27.18 ± 0.07 and 309.36 ± 2.79 days.

affects the ionospheric densities. It had been shown that the linear combination of the daily values and 81-day running averaged values of $F_{10.7cm}$ flux ($\langle F_{10.7cm} \rangle_P$), is a better proxy than $F_{10.7cm}$ flux values for solar cycle variation of EUV ionizing radiation (Richards *et al.*, 1994). Also, using long-term ISR and ionosonde observations over Millstone Hill Observatory, Lei *et al.* (2005) have shown that daily noon-time NmF_2 values increase linearly with an increase in $\langle F_{10.7cm} \rangle_P$ index instead of daily $F_{10.7cm}$ flux values (as

depicted in figures 6.2a and 6.2a). Therefore, to understand the variation in ionospheric parameters, we have considered $\langle F_{10.7cm} \rangle_P$ values. They are given by equation 6.1.

$$\langle F_{10.7cm} \rangle_P = \frac{1}{2}(F_{10.7cm} + \langle F_{10.7cm} \rangle_{81days}) \quad (6.1)$$

where, $F_{10.7cm}$ represents the daily values of solar $F_{10.7cm}$ flux, and $\langle F_{10.7cm} \rangle_{81days}$ is 81-day running averaged values of solar $F_{10.7cm}$ flux centered around the given day. Time periods of 27.18 ± 0.07 , and 309.36 ± 2.79 days (figure 6.1h) are found to be significant in the $\langle F_{10.7cm} \rangle_{81days}$ variation (shown in figure 6.1g). The F₂ layer electron density is directly related to the atomic/molecular ratio present in the thermosphere. Summer to winter hemisphere winds during solstices cause semi-annual variation in thermospheric compositions due to the upwelling in the summer hemisphere and a corresponding downwelling in the winter hemisphere. This semi-annual variation in compositions explains the strong oscillation of 180.71 ± 0.51 days observed in NmF_2 (Rishbeth et al., 2000b). Also, using spectral analyses of GPS derived TEC measurements over a low-latitude location in India, Chakrabarty et al. (2012) have shown that the semi-annual oscillations present in the TEC do not have their counterpart in solar EUV flux variation. Therefore, semi-annual

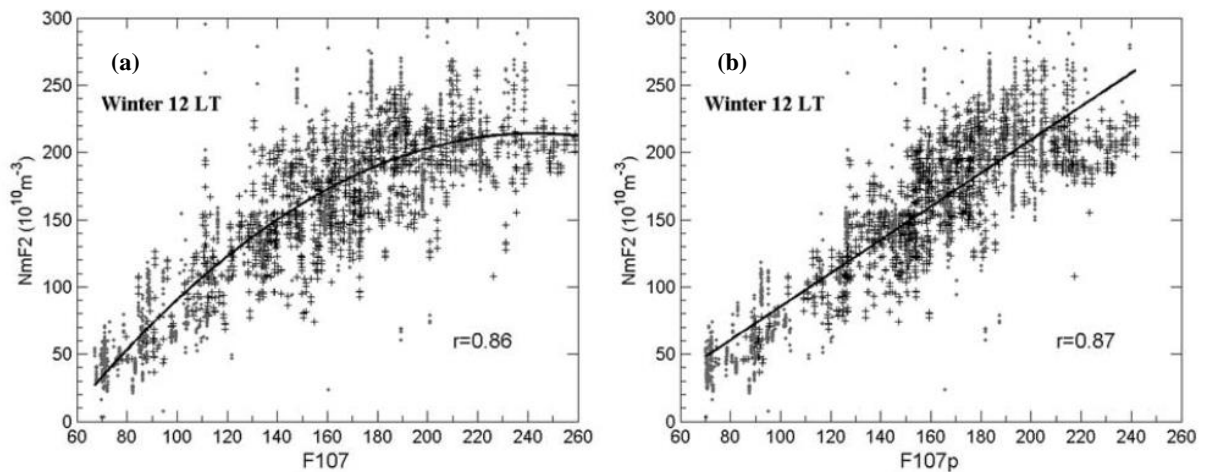


Figure 6.2: (a) The responses of the noontime NmF_2 to daily $F_{10.7cm}$ index; the observed data include ISR (points) and ionosonde (plus signs) measurements from Millstone Hill observatory. The solid line is the results of a 2^{nd} -degree polynomial fitting for both type data, and r represents the correlation coefficient. (b) Same as in (a), but for the responses of observed NmF_2 to $\langle F_{10.7cm} \rangle_P$ index, and the solid line is the results of a linear fitting. [After Lei et al. (2005)]

oscillations seen in a similar parameter, IEC (figures 6.1e and 6.1f), are due to compositional changes caused by large scale thermospheric dynamics. The semi-annual variation seen in hmF_2 has been attributed to the energy input from the lower atmosphere due to semi-annually varying waves and tides (*Rishbeth et al., 2000a*). Nevertheless, the variation in the solar flux changes the thermospheric neutral temperature, which has direct control over hmF_2 . This results in a strong periodicity of 317.80 ± 5.10 days observed in hmF_2 variations, which is around 309.36 ± 2.79 days present in the variation in $\langle F_{10.7cm} \rangle_P$. The periods of 290.89 ± 24.62 days found in NmF_2 and 299.71 ± 11.0 days in IEC are not as strong as those in the hmF_2 . This is possibly because, the amount of ionization present at a given location over low-latitudes, not only depends on the production due to incoming solar radiation but also on the transport due to highly active equatorial electrodynamics. This is more so in the present case as the current location, Ahmedabad, is generally under the northern crest region of the equatorial ionization anomaly, whose strengths show daily, seasonal, and solar flux variations (e.g., *Raghavarao et al., 1988b; Sastri, 1990*).

6.4.2 Influence of solar flux variation on the vertical propagation characteristics of gravity waves

As discussed in chapter 3, temporal variations of hmF_2 and IEC do not provide unambiguous information on neutral gravity wave activity and their propagation characteristics. Because they are affected by other parameters, such as electric fields, winds, and temperature, which vary with seasons, as noted in figures 6.1a-f with a strong semi-annual component. Therefore, in order to obtain information on the thermospheric neutral gravity wave dynamics, a different approach, as described in chapter 3, has been adopted. Whenever these height variations show phase offsets and the presence of a common time period(s) (τ), vertical phase propagation speeds (c_z) and vertical scale sizes (λ_z) of gravity waves have been calculated. Since our aim is to understand the systematic behavior of thermospheric wave dynamics with regard to the maximum effect that exists in the thermosphere due to different drivers that might be influencing them, we have considered the daily maximum values of λ_z (λ_{z-max}). These values, along with their uncertainties, are shown in figure 6.3a. The gaps correspond to days with no vertical propagation activity of gravity waves. Also, there are a few occasions when data are not available. In this

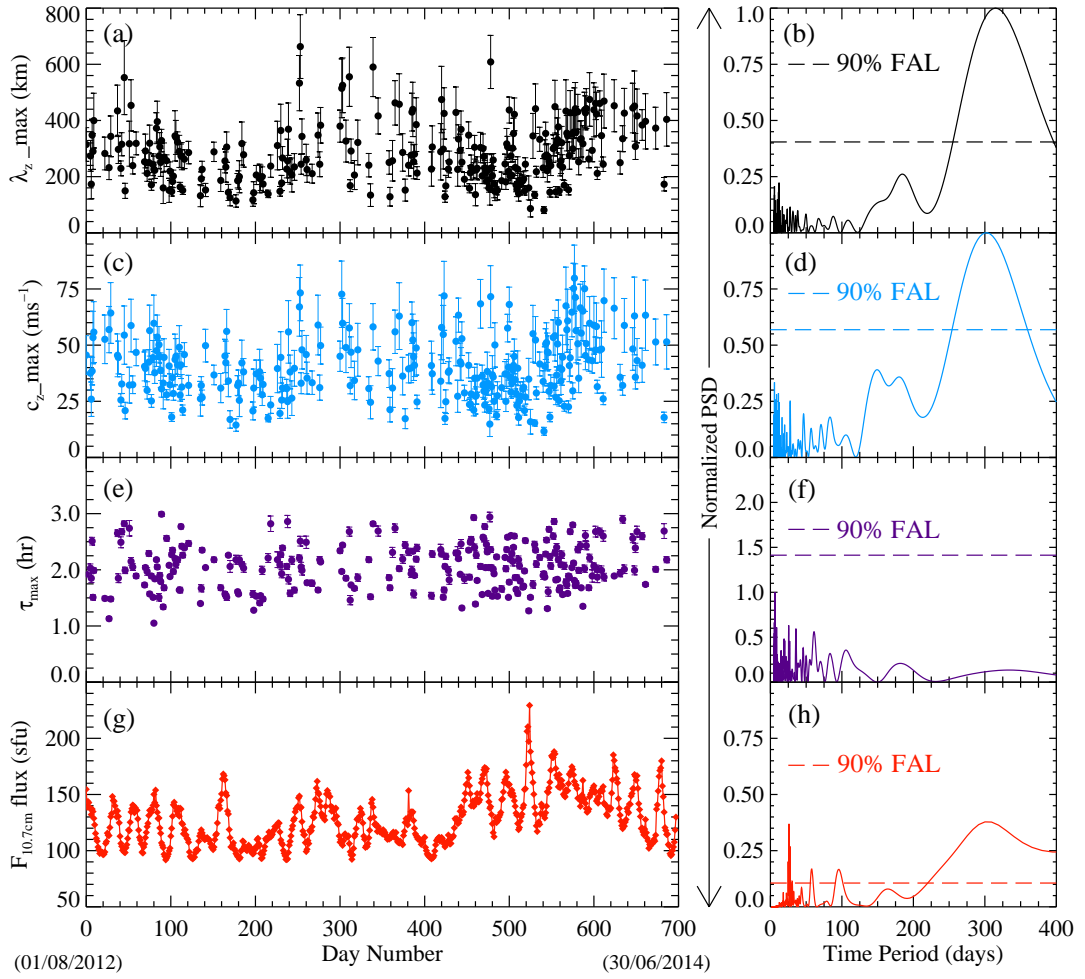


Figure 6.3: (a) Distribution of daily λ_{z_max} along with their uncertainties. (b) The Lomb-Scargle periodogram analysis of λ_{z_max} showing periodicity of 314.76 ± 7.28 days to be significant. (c) & (d) same as in (a & b) but for daily c_{z_max} . Periodicity of 303.56 ± 9.42 days is significant in the variations of c_{z_max} . (e) & (f) Same as in (a & b) but for daily values τ_{max} . It may be noted that there are no significant periods present. (g) & (h) Same as in (a & b) but for Solar $F_{10.7cm}$ flux. Periodogram analysis shows the presence of significant periods of 27.25 ± 0.02 , 57.75 ± 0.15 , 95.94 ± 0.69 , and 300.08 ± 7.96 days.

duration, we have found gravity wave propagation activity on 270 days out of 637 days ($\sim 41\%$). On the days when vertical propagation is not seen, it is possible that they could be propagating in the horizontal direction as a wave-like activity, which will manifest as in-phase variations in the height variations of different isoelectron density contours. As can be seen in figure 6.3a, variation in daily maximum values of λ_z shows an oscillatory pattern. Spectral analysis using the Lomb-Scargle technique has been carried out, wherein the periodicity of 314.76 ± 7.28 days is found to be significant (figure 6.3b). As the vertical

scale sizes (λ_z) depend on the vertical phase speeds and time periods of gravity waves, the variation in these parameters are also considered for detailed analyses. The distribution of the daily maximum of c_z (c_{z_max}) is shown in figure 6.3c. Similar to the distribution of λ_{z_max} , this also shows an oscillatory pattern, and spectral analysis shows the presence of a significant period of 303.56 ± 9.42 days (figure 6.3d), whereas, the distribution in the daily maximum values of time periods (τ_{max}), does not show any such significant period(s) (as can be seen in figures 6.3e and 6.3f). Since we are discussing the wave dynamics of the daytime thermosphere, which gets energy directly from the solar radiation, these propagation characteristics of gravity waves are compared with the variation in solar flux. We know that thermospheric background conditions, which affect the wave activity, vary significantly with changes in the thermospheric neutral temperature. Therefore, we have investigated the variation in solar $F_{10.7cm}$ flux, which is known to represent the overall variation in the solar radiation, whereas, $\langle F_{10.7cm} \rangle_P$ shown in figure 6.2g represents the variation in the solar EUV radiation. Solar $F_{10.7cm}$ flux values for this entire duration are shown along with the spectral analyses in figures 6.3g and 6.3h. Periodicities of 27.25 ± 0.02 , 57.75 ± 0.15 , 95.94 ± 0.69 , 300.08 ± 7.96 days are found to be significant. To confirm that the period of around 300 days observed in the variation in solar $F_{10.7cm}$ is not an artifact of the duration of data used in this study, we have carried out a spectral analysis of solar $F_{10.7cm}$ data for 2007-2017 (depicted in figure 6.4). The result of such analysis shows a periodicity of 297.14 ± 4.85 days to be significant, which suggests that this ~ 300 days periodicity present in our duration of study is indeed of solar origin. The striking similarity in the periods of λ_z (314.76 ± 7.28 days), c_z (303.56 ± 9.42 days), and solar $F_{10.7cm}$ flux (300.08 ± 7.96 days) indicate that the solar flux variation has a direct and significant effect on the daytime neutral wave dynamics in the thermosphere. It is striking to note that the time period of these gravity waves (figure 6.3c) do not show any such similarities with solar flux variation. This suggests that only the dynamical component of gravity waves i.e., their propagation speeds and scale sizes get affected by the changes in the thermospheric background conditions that result from solar flux variations. Therefore, measurements of wave periods alone may not provide complete information on the thermospheric dynamics. In this duration, the periodicity of about 180 days in c_z , and 185 days in λ_z (below the statistical significance level) hints to possible semi-annual oscillations due to seasonal effects similar to those seen in the cases of IEC and NmF_2

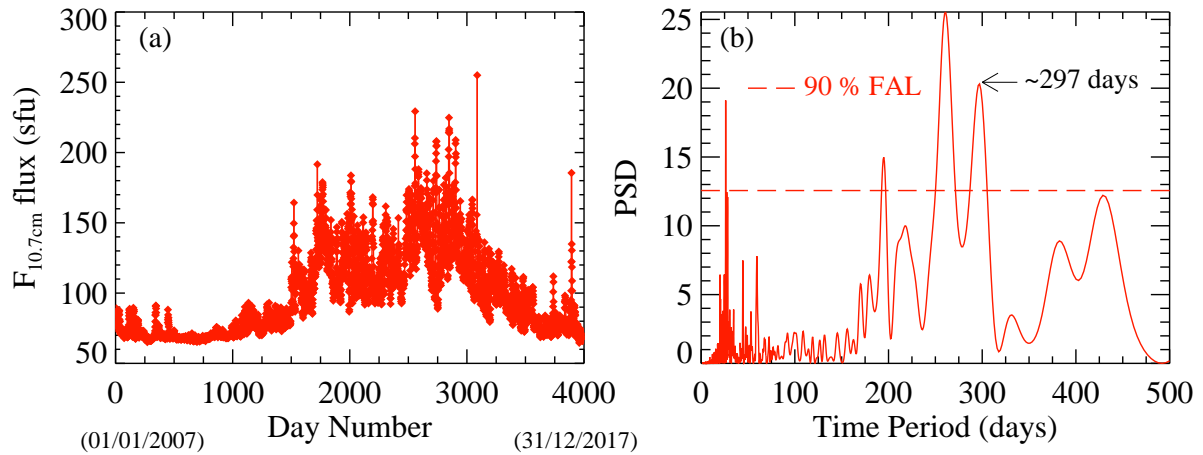


Figure 6.4: (a) Variation in solar flux during 01/01/2007-31/12/2017, which includes the two-year period considered in the present investigation. (b) Periodogram obtained using the Lomb-Scargle spectral analysis shows the presence of a significant period of ~ 297 days. This period is similar to that seen in the gravity wave phase speeds and wavelength in the vertical direction (figure 6.3).

(seen in figure 6.1), but not as strong. This indicates that the solar flux influence on the daytime thermospheric neutral gravity wave dynamics is quite stronger than the seasonal effects (discussed in the chapter 5) during this period. As the vertical wavelength of gravity waves are obtained from vertical phase speeds and time periods (discussed in chapter 3), the oscillations that are seen in λ_z are due to those present in c_z , as τ does not show any variation with solar flux. Therefore, in figure 6.5a, we show the distribution of c_z (cyan-colored circles) along with the variation in solar $F_{10.7cm}$ flux (red-colored diamonds) for the same duration. The variations in c_z are similar to those present in the solar $F_{10.7cm}$ flux. It is known that the thermosphere is a lethargic medium and effects due to systematic changes in solar irradiation take around 20 days to settle through thermospheric circulations (Rishbeth et al., 2000a). Keeping this time constant in consideration, we have selected the maximum values of c_z in each 20 day window of measurement to quantify the solar influence on thermospheric neutral wave dynamics (they are shown as cyan-colored circles in figure 6.5b). The solar $F_{10.7cm}$ flux variations show a strong periodicity of around 27 days owing to the solar rotation, which is not present in c_z (can be seen in figure 6.3d). Therefore, in order to make a fair comparison between the two, this intrinsic variability (of 27 days) present in solar $F_{10.7cm}$ flux has been suppressed by carrying out a 27-day moving average of the original data. Then, the averaged values of solar $F_{10.7cm}$ flux over 20

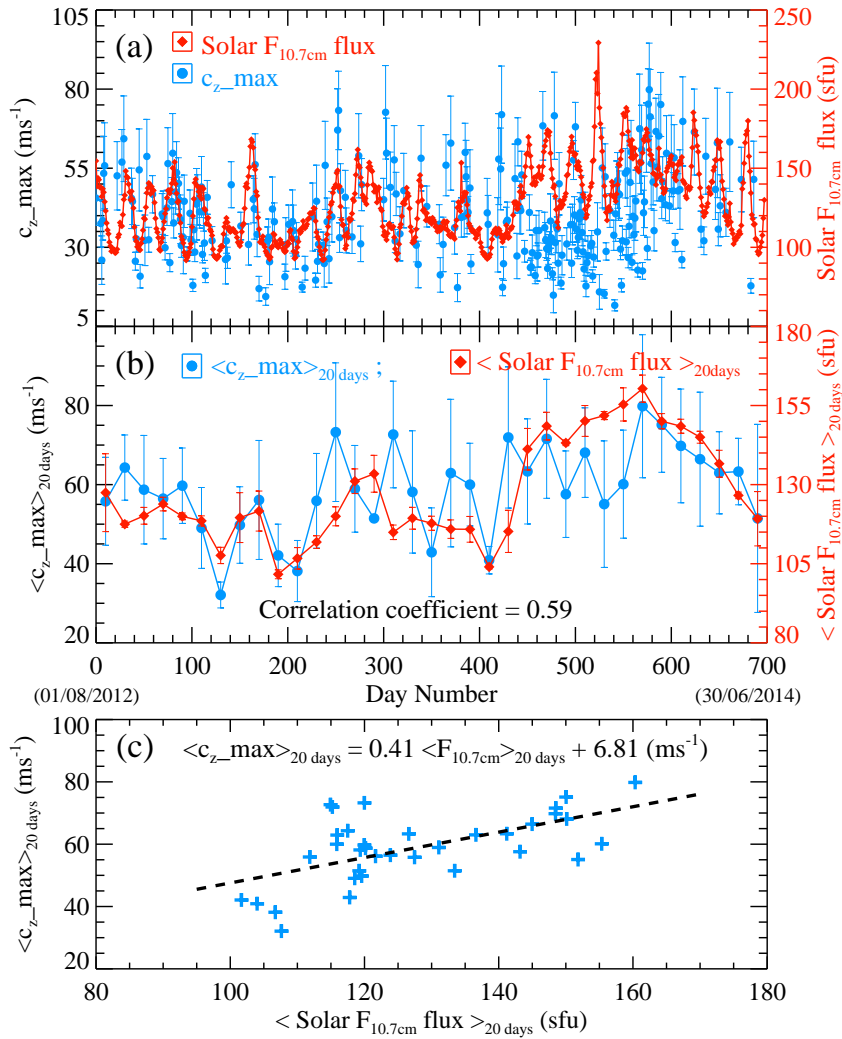


Figure 6.5: (a) The daily maximum values of vertical phase propagation speeds (cyan colored circles) along with variation in Solar $F_{10.7cm}$ flux (red colored diamonds). (b) Maximum values of c_z over 20 days window (cyan colored circles) and 20-day averaged values of the Solar $F_{10.7cm}$ flux (red-colored diamonds). (c) Maximum c_z in every 20-day window is plotted as a function of 20-day averaged values of Solar $F_{10.7cm}$ flux. The dashed line represents the linear fit between these two.

days are calculated and they are presented as red-colored diamonds in figure 6.5b. These values of c_z and solar $F_{10.7cm}$ flux show a good correlation (correlation coefficient of 0.59). Considering that the gravity wave propagation characteristics also depend on different background conditions, such as density, pressure, and winds, as discussed in chapter 5 as well, this correlation coefficient is quite good. In figure 6.5c, maximum c_z values over 20 days window are shown as a function of 20 days averaged values of solar $F_{10.7cm}$ flux. A linear relationship (equation 6.2) between the two has been obtained, and it may be noted

that the c_z shows an increasing trend with increasing solar $F_{10.7cm}$ flux values.

$$\langle c_{z_{max}} \rangle_{20 \text{ days}} = 0.41 \langle F_{10.7cm} \rangle_{20 \text{ days}} + 6.81 \quad (6.2)$$

where, $\langle c_{z_{max}} \rangle_{20 \text{ days}}$ represents the maximum values in ms^{-1} of vertical phase speeds of gravity waves over 20 days, and $\langle F_{10.7cm} \rangle_{20 \text{ days}}$ is 20-day averaged values of solar $F_{10.7cm}$ flux in sfu.

The influence of solar flux variation on the thermospheric neutral wave dynamics can be understood in the following manner. It is well known that with an increase in solar flux, there is a corresponding increase in the thermospheric neutral temperature. Such an increase in neutral temperature changes the static stability of the atmosphere as neutral scale height increases, and the Brunt-Väisälä frequency decreases (described in the footnote 1). As a result of these changes, for gravity waves of large periods (periods much greater than Brunt-Väisälä period), changes in the first term in the gravity wave dispersion relation (equation 3.2) dominates over the variation in scale height. And, as the vertical wavelength of gravity waves and the Brunt-Väisälä frequency are inversely proportional to each other, with an increase in neutral temperature resulted from rise in the solar flux values cause the local vertical wavelengths of gravity waves to shift to larger values (e.g., *Vadas and Fritts, 2005; Yiğit and Medvedev, 2010*). Hence, an increase in vertical wavelength and vertical phase speeds of gravity waves in the daytime thermosphere is observed with increasing solar flux.

6.4.3 Solar flux influence on gravity wave activity

In this section, we will discuss the variations observed in the number of gravity waves present in the daytime thermosphere and their vertical propagation activity in relation to changes in the solar flux.

6.4.3.1 The occurrence of vertical propagation of gravity waves

So far, we have discussed the effects of solar flux variation on the vertical propagation speeds and vertical scale sizes of gravity waves. It should be noted that vertical prop-

agation features of gravity waves do not exist on every day. For the duration of data analyzed, we have observed that vertical propagation of gravity waves exists only 41% of the times. Thermospheric background conditions, such as the varying nature of ambient wind magnitudes and their directions with respect to propagation directions of waves, and various dissipation parameters affect the vertical propagation of gravity waves (e.g., *Vadas and Fritts, 2005; Pallamraju et al., 2016; Mandal et al., 2020*). To quantify the variation

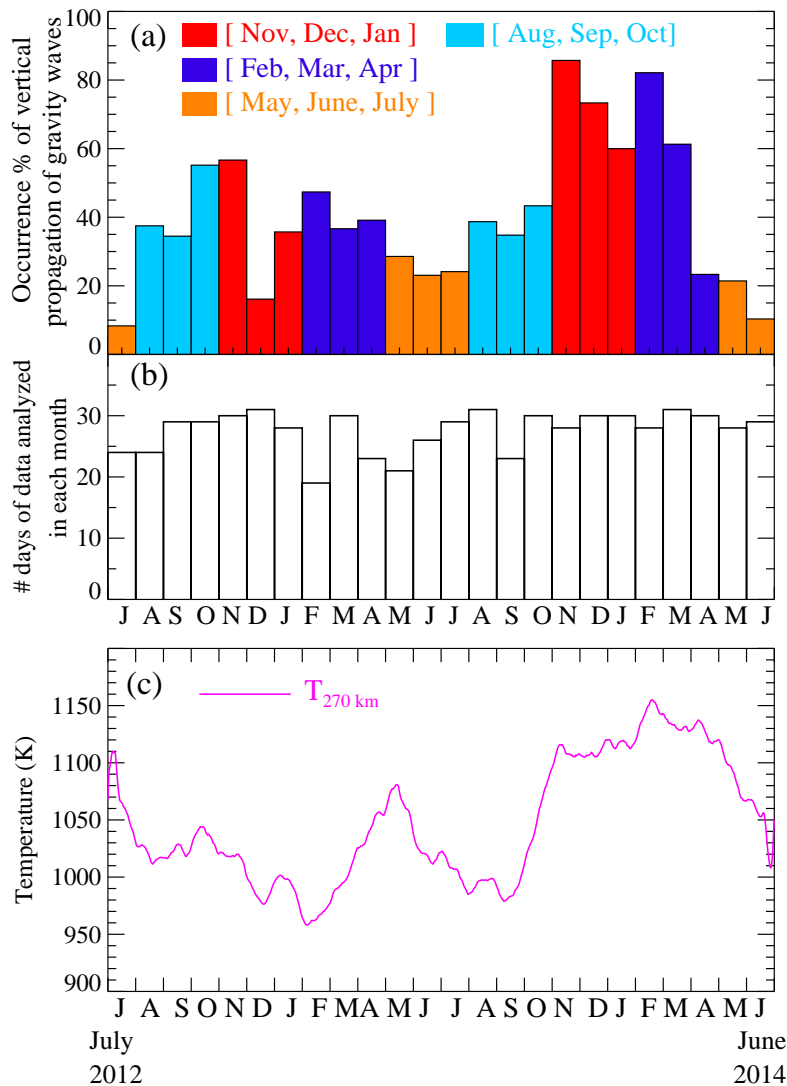


Figure 6.6: (a) Occurrence percentage of vertical propagation of gravity waves in the daytime thermosphere in different months for the duration July 2012-June 2014. Different colors are representative of different seasons. (b) Data availability for each month in these two years is shown. On average, data are available for around 89% of the days. (c) The NRLMSISE model-derived neutral temperatures at an altitude of 270 km over Ahmedabad, India, corresponding to 14 LT for the same duration.

in vertical propagation activity of gravity waves, we have defined it as the percentage of the ratio of the number of days with vertical propagation to the number of days of data analyzed in a given month. In figure 6.6a, we show a bar plot of the occurrence percentages of vertical propagation of gravity waves in different months over two years (leftmost bar corresponds to July 2012 and the rightmost bar for June 2014). We see that gravity wave propagation activity in the vertical direction varies significantly in different months and seasons. Vertical propagation activity is considerably less during May, June, and July months in both the years, but also shows a greater occurrence percentage in the year 2013-2014 than 2012-2013. The number of days of data analyzed in each month for investigation of gravity wave propagation activity is depicted in 6.6b. It can be clearly seen that data is available for 79%-98% of the times. Hence, variation in the vertical propagation activity of gravity waves in the daytime thermosphere as seen in figure 6.6a is independent of data availability. In figure 6.6c, the NRLMSISE model-derived neutral temperature, $T_{270\text{ km}}$ (Picone *et al.*, 2002) corresponding to an altitude of 270 km at 14 LT over Ahmedabad is shown. It can be noted that $T_{270\text{ km}}$ broadly shows a similar variation as that of occurrence percentage of vertical propagation of gravity waves, albeit with some phase offsets. As discussed in detail in chapter 5, these offsets arise due to seasonal effect as the vertical propagation characteristics of gravity waves are dependent on ambient wind directions, which show a seasonal variation at any given location.

6.4.3.2 Number of gravity waves in the daytime thermosphere

As mentioned above, gravity wave propagation in the vertical direction is seen only on some of the days. But to obtain a comprehensive picture of the gravity wave activity on a given day, we have carried out time period analyses for the entire duration. For this analysis, the height variation of isoelectron density contour corresponding to the transmission frequency of 10 MHz of digisonde has been chosen. As at this frequency (10 MHz), the data are continuously available throughout the two years of measurements considered in this study. Further, daily available data duration is suitable for spectral analysis for time periods of gravity wave domain, compared to data from higher frequencies (that correspond to higher altitudes), which may be limited depending on seasons. The number of distinct gravity wave time periods present in each day is considered as the measure of

the strength of the gravity wave activity on that day. Both, the days when gravity waves showed propagation features, and those that did not show any propagation are considered in the estimation of the number of gravity waves present in the thermospheric altitudes. On any given day, the time period values within 0.25 h (Brunt-Väisälä period) of each other have been considered to be the same. The number of independent gravity wave

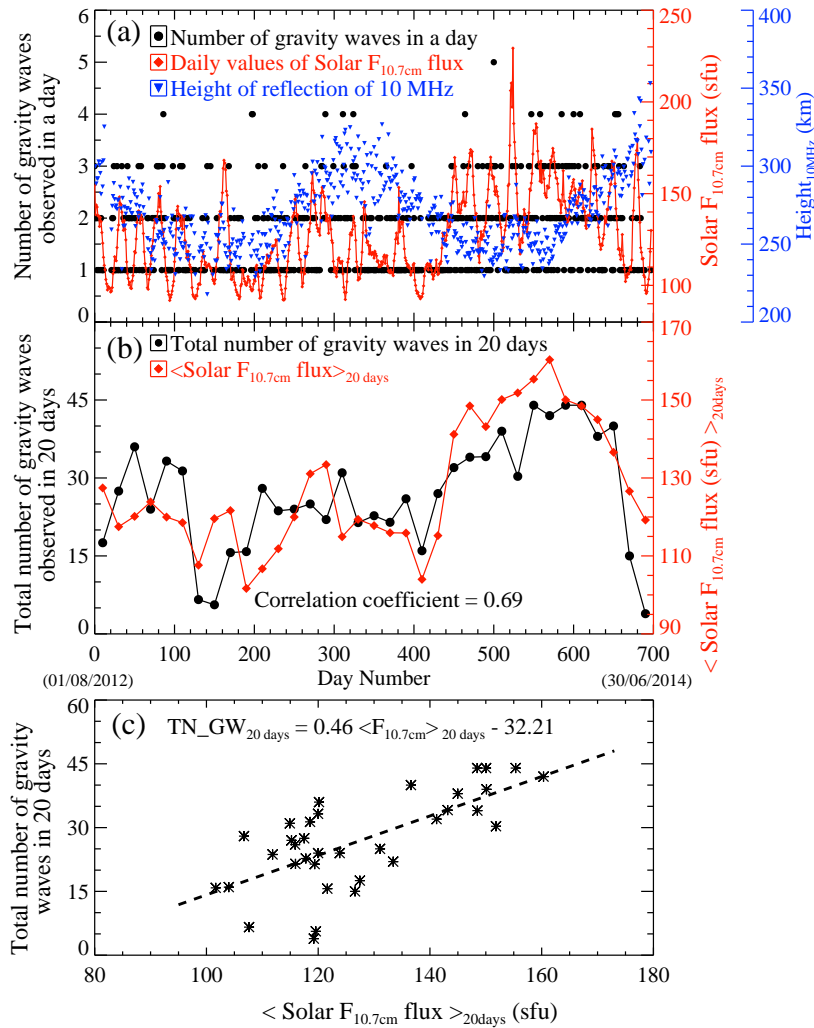


Figure 6.7: (a) Number of gravity waves (with distinct periods) observed in each day whenever they are present (shown as black-colored circles) along with the daily solar $F_{10.7\text{cm}}$ flux values (red-colored diamonds) and height of reflection of 10 MHz echo (blue colored triangles) for this entire duration. (b) The total number of gravity waves observed over 20 days are shown (black circles) along with the averaged Solar $F_{10.7\text{cm}}$ flux in that corresponding window (red-colored diamonds). (c) The total number of gravity waves observed over 20 days are plotted as a function of averaged values of solar $F_{10.7\text{cm}}$ flux over the same duration. The dashed line shows the linear least-square fit between them.

periods, i.e., the number of gravity waves present on a given day for this entire duration of the study, is shown in figure 6.7a (black-colored circles). It can be noted that gravity waves are nearly omnipresent in the thermosphere (around 91% of the days). Variation in the solar $F_{10.7cm}$ flux (red-colored curve with diamonds) for this entire duration is also shown in figure 6.7a. We see that the number of gravity waves (of independent periods) increases around the day numbers of 240-300, and around 440-620, during which the solar flux also increases. Variation in waves and tides in the lower atmosphere indirectly affect the height variations of the F_2 layer peak (hmF_2). To explore if these influences have any discernable effect on the number of gravity waves observed in the thermosphere, we have also shown the height variation of 10 MHz ($Height_{10MHz}$; blue-colored triangles) in figure 6.7a. It can be readily noted that these do not display any systematic variation with the number of gravity waves observed in the thermosphere. This again highlights the positive influence of the solar flux variation on the thermospheric gravity wave activity. In figure 6.7b, the total number of gravity waves observed over each 20 days window for this entire duration are shown along with the 20-day averaged values (taking into account the lethargy of the thermosphere as discussed above) of solar $F_{10.7cm}$ flux. As discussed earlier, 27 days running averaged values of the solar $F_{10.7cm}$ flux have been taken to suppress the intrinsic period of 27 days. Similar to the situation of phase speeds (figure 6.5b), the number of gravity waves present in the daytime thermosphere also shows very good semblance with the variation in solar flux. They show a good correlation coefficient of 0.69. The correlation coefficient of -0.29 between $Height_{10MHz}$ and gravity wave activity indicates that variation in gravity wave activity is mainly because of changes in the solar flux and is not due to variation in F-region heights ($Height_{10MHz}$) with seasons or solar flux. Figure 6.7c shows the increase in gravity wave activity in the daytime thermosphere as a function of the solar flux variation. A linear relation between the number of gravity waves present in the thermosphere in each period of 20 days, and the averaged solar flux values in that duration has been derived (equation 6.3).

$$TN_GW_{20\ days} = 0.41 \langle F_{10.7cm} \rangle_{20\ days} - 24.19 \quad (6.3)$$

where, $TN_GW_{20\ days}$ is the total number of gravity waves observed over 20 days, and $\langle F_{10.7cm} \rangle_{20\ days}$ represents the 20-day averaged values of the solar $F_{10.7cm}$ flux.

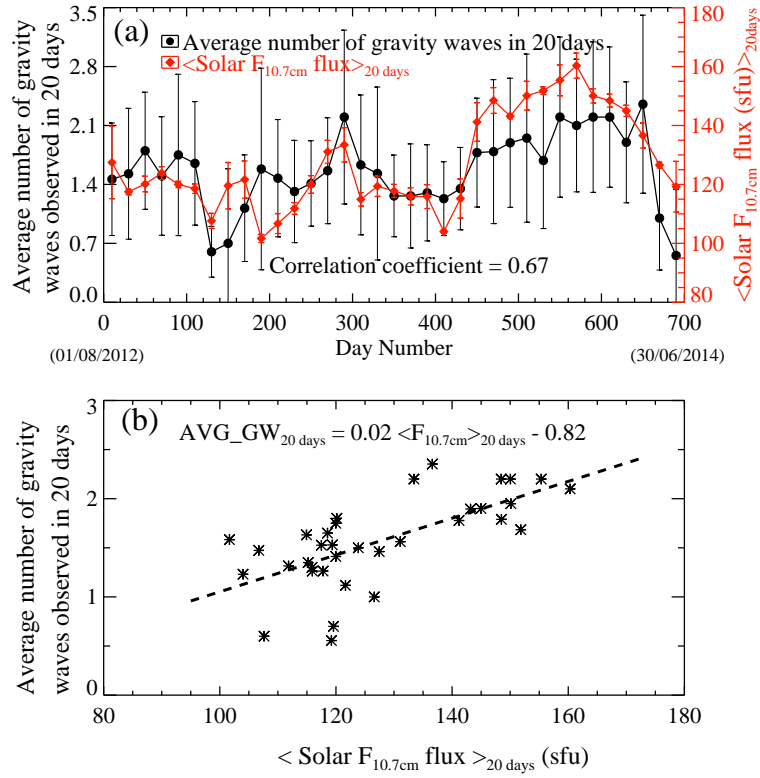


Figure 6.8: (a) The average number of gravity waves observed over 20 days window for this entire duration of two years are shown (black circles) along with their standard deviations. The 20-day averaged values of solar $F_{10.7cm}$ flux in that corresponding window (red-colored diamonds) are shown with their standard deviations. (b) The average number of gravity waves observed in every 20 days is shown as a function of 20 days averaged values of solar $F_{10.7cm}$ flux over the same duration. The dashed line shows the linear least-square fit between them.

Furthermore, the average number of gravity waves in each 20 days window for this entire duration also shows similar variation with solar flux values and they are presented in figure 6.8. They show a good correlation (correlation coefficient is 0.67). In order to quantify these similarities observed between them, the average number of gravity waves in every 20 days ($AVG_GW_{20\ days}$) are shown as a function of the 20 days averaged solar $F_{10.7cm}$ flux values ($\langle F_{10.7cm} \rangle_{20\ days}$) in figure 6.8. The linear relation arrived at between these two parameters is given by equation 6.4.

$$AVG_GW_{20\ days} = 0.02 \langle F_{10.7cm} \rangle_{20\ days} - 0.82 \quad (6.4)$$

These numerical relations (6.3 and 6.4) can give first-order estimates of gravity wave activity in the daytime thermosphere provided the values of solar $F_{10.7cm}$ flux.

The answer for the increase in the number of gravity waves in the daytime thermosphere with increasing solar flux lies in the variation of background wave dissipation conditions with changes in the solar flux. The molecular kinematic viscosity (ν_{mol}) and thermal diffusivity (α) are the two primary gravity wave dissipation parameters in the thermospheric altitudes (*Yiğit and Medvedev, 2010*). They are related to background temperature and neutral density as given in equations 6.5 and 6.6.

$$\nu_{mol} = \frac{3.563 \times 10^{-7} T^{0.69}}{\rho} \quad (6.5)$$

$$\alpha = \frac{K}{\rho c_p} \quad (6.6)$$

where, K is thermal conductivity, T is neutral temperature, ρ is number density, and c_p is the specific heat at constant pressure.

Both these dissipation factors are inversely proportional to the neutral density, and the molecular kinematic viscosity is weakly proportional to the temperature. As discussed in section 6.5, the thermosphere expands when the neutral temperature increases due to an increase in solar $F_{10.7cm}$ flux. This results in an increase in the neutral density at higher altitudes of the thermosphere (as opposed to the conditions when the thermospheric temperature is lower). This increase in neutral density leads to a weakening of the wave dissipation parameters, thermal diffusivity (equation 6.6). However, in the case of molecular viscosity (equation 6.5), an increase in neutral density and neutral temperature act in opposition to each other, nevertheless leading to slow growth of this dissipation with altitude in the upper thermosphere. Therefore, the dissipation of gravity waves decreases in the thermosphere when solar flux increases. *Yiğit and Medvedev (2010)* have shown that the gravity wave drag, which is considered a measure of momentum deposition due to wave dissipation, is smaller during the high solar flux period than during low solar flux conditions (shown in figure 6.9). Also, as discussed earlier, an increase in the vertical wavelengths of gravity waves with an increase in neutral temperature of the thermosphere favors vertical propagation (as seen in figures 6.6a and 6.6b) of these waves into higher

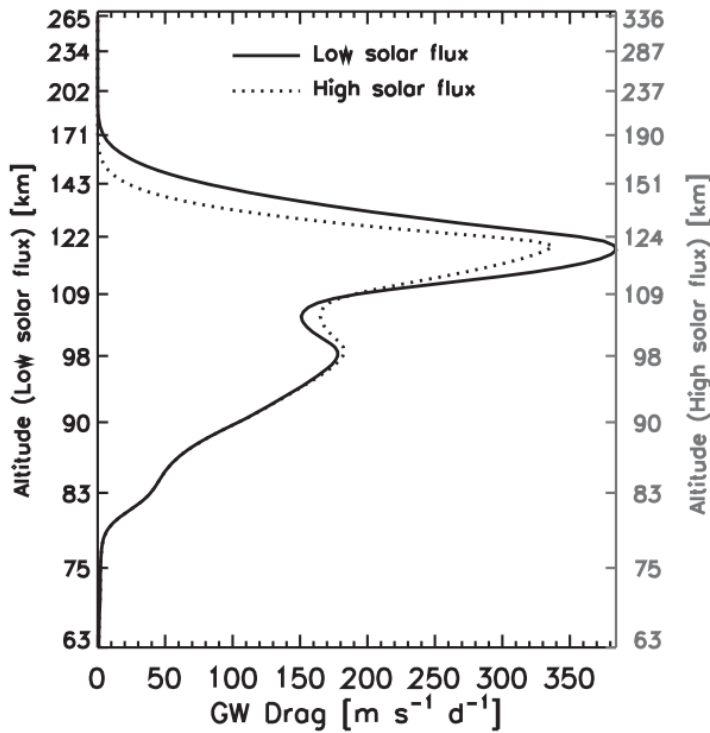


Figure 6.9: *The variation in gravity wave drag in different solar flux conditions. The gravity wave drag, a measure of momentum deposited due to the breaking of gravity waves as modeled by introducing the gravity wave parameterization into the global circulation model. [After Yigit and Medvedev (2010)].*

altitudes (*Vadas and Fritts, 2005*). Hence, we see an increase in gravity wave activity in the daytime thermosphere with increasing solar flux. This result is consistent with earlier works of *Laskar et al. (2015)* carried out by analyzing daytime optical airglow emission measurements from a low-latitude location at three wavelengths corresponding to three different altitudes in the thermosphere.

6.5 Summary

From the results and discussion presented above, it may be noted that, the low-latitude ionospheric behavior in terms of electron density variation (NmF_2 & IEC) shows semi-annual oscillations due to changes in the composition of the thermosphere. The effect of solar flux variation on the neutral gravity wave activity in the daytime thermosphere is dominant as compared to that of seasonal variations. Although the gravity waves are

nearly omnipresent, not all days do they show signatures of vertical propagation. Our data shows that upward propagating gravity waves exist in about 41% of the days. The vertical phase speeds and the vertical scale sizes of gravity waves show a clear influence of solar flux variation. As there are several factors that affect the propagation of gravity waves in the upward direction, on which day(s) vertical propagation exists is a study that needs to be carried out using simulations and will be taken up in the future. Nevertheless, this study brings out a systematic picture of the thermospheric wave dynamics with respect to variations in solar flux. Linear relationships (equations 6.2 and 6.3) have been obtained, which can be used in parameterized models to describe the neutral dynamics of the upper atmosphere. These results provide new insights into the thermospheric neutral gravity wave dynamics and advance our understanding of the influence of various drivers on the gravity wave behavior with respect to seasons and solar flux variations.

Chapter 7

Summary and Future scope

7.1 Summary

Waves of different spatial and temporal scales are present in the thermosphere, and the majority of these atmospheric waves are generated in the lower atmosphere through various processes. These waves carry the energy away from their source regions as they propagate in the medium. While propagating upward, their amplitudes increase, and these waves break below the turbopause region, resulting in the redistribution of energy. Further, secondary waves are generated at these altitudes, which can propagate up into the thermosphere. Gravity waves of in-situ generation also exist in the thermosphere. In this thesis, an innovative approach has been arrived at using radio wave measurements, which has opened up several new avenues to investigate daytime thermospheric wave dynamics on a continuous and systematic basis. Applying this approach, several new and insightful results have been obtained, which advance our understanding of the daytime gravity wave behavior as a system. These are (i) influence of solar flux variation on the daytime gravity wave characteristics, (ii) variation in the vertical propagation speeds and scale sizes of gravity waves over low-latitudes in response to the seasonally varying thermospheric winds, (iii) effect on gravity wave propagation characteristics over low-latitudes due to influences from high-latitudes during geomagnetic storms, and (iv) characteristics of the gravity waves in the daytime that form the seeds for the occurrence of nighttime equatorial plasma irregularities.

The highly dynamic thermosphere-ionosphere region over low- and equatorial latitudes have been described in chapter 1. Several electrodynamical phenomena of the dip-equatorial region (e.g., EEJ, EIA, ETWA, and ESF) affect the neutral and plasma distribution over the tropical latitudes. The strength of these phenomena varies from one day to another, day-to-night, seasons, and solar activity. Atmospheric waves and their effects have been briefly described in this chapter. Digisonde data from Ahmedabad and Trivandrum, low- and equatorial-latitude locations over Indian longitudes, have been the primary dataset used to characterize and investigate the systemic behavior of gravity waves in the daytime thermosphere. Working principle, data products, and manual scaling of the ionograms obtained every 7.5 minutes by these digisondes have been discussed in chapter 2. Furthermore, other datasets, such as OI 630.0 nm dayglow emission, magnetometer measurements, $F_{10.7cm}$ solar flux, Dst index, and AE index, have been summarized. To complement the lack of daytime measurements of thermospheric winds and atmospheric parameters (mass, neutral temperature), HWM14 and NRLMSISE model-derived values have been used. Different methods for obtaining periodograms, such as FFT, Lomb-Scargle periodogram technique, and wavelet analysis, are also described briefly.

We briefly summarize the findings of the thesis by answering the questions that have been put forth in section 1.5.

- I. Is it possible to obtain information on the vertical propagation characteristics of gravity waves in the daytime thermosphere?

Chapter 3 describes an innovative approach using digisonde data to derive information on the neutral gravity wave propagation characteristics in the vertical direction (*Mandal et al., 2019*). Height variations of constant electron densities are monitored for downward phase propagation, which indicates atmospheric gravity waves moving in the upward direction. The presence of downward phase propagation and a common period in the height variations of all the isoelectron density contours rule out ambiguities in identifying the gravity waves. The vertical propagation speeds of gravity waves are calculated using differences in height and time. Assuming that the phase speeds remain constant for the duration of the time period, vertical scale sizes of gravity waves are estimated. These

values agree very well with the earlier reported numerical trend of gravity wave scale sizes present at different altitudes, as derived from radar measurements (*Oliver et al., 1997*). Furthermore, the dispersion relation of gravity waves has been used to arrive at a first-order estimation of horizontal scale sizes of these gravity waves with the derived gravity wave parameters.

- II. How does the change in thermospheric background conditions (e.g., wind structures, temperatures, and neutral density) affect these wave propagation in the daytime?

Chapter 5 and chapter 6 discuss these aspects of gravity wave propagation in the daytime thermosphere. The vertical phase speeds and scale sizes of gravity waves during geomagnetically quiet days show two peaks annually with maximum values around the equinox times. These maximum values in the gravity wave parameters coincide with the minima of thermospheric horizontal wind magnitudes, indicating a strong influence of wind motions on the gravity wave propagation in the thermospheric regions. Gravity waves are considered to be omnipresent. However, no systemic information exists with regard to vertical propagation characteristics. In this thesis, propagation characteristics of gravity waves in the vertical direction have been quantified. It is found that not on all days vertical propagation exists. Variation in the vertical propagation activity is discussed in chapter 6, and they vary significantly from one month to another month. On average vertical propagation of gravity waves is found to exist only 41% of the time in thermospheric altitudes (*Mandal and Pallamraju, 2020*). The occurrence percentage of vertical propagation in gravity waves is found to increase with an increase in the solar flux values. Due to changes in solar flux values, thermospheric neutral temperature, and neutral density changes. As a result of these changes, wave dissipation gets weakened with increasing solar flux values, and a large number of waves are allowed to propagate in this region (*Mandal et al., 2020; Mandal and Pallamraju, 2020*).

- III. Do the vertical propagation parameters of gravity waves over low-and equatorial-latitudes get influenced by the different energy inputs in the thermosphere (solar radiation, particle precipitation at the high altitudes)? If they do, how to quantify those variations?

Chapter 6 describes the effects of solar flux variation on the daytime thermospheric gravity

waves over low-latitudes. Vertical propagation speeds and vertical scale sizes of these gravity waves show similar variation with solar flux. Thermospheric neutral temperature is correlated one-to-one with the variation in the solar flux. With increasing temperature, the background stability condition changes, more specifically, the neutral scale height increases, and the Brunt-Väisälä frequency at these altitudes decreases. The local vertical wavelength (inversely proportional to this frequency) of gravity waves shifts to higher values with an increase in the temperature as a result of changes in the background stability conditions. Not only do the magnitudes of vertical scale size increase, but the number of gravity waves present in the daytime thermosphere also increases with an increase in solar flux. This increase in the number of gravity waves is understood to be due to a weakening in wave dissipation in the thermosphere with increasing solar flux. These similarities have been quantified using thermospheric time constant of around 20 days to arrive at linear relations, wherein, first-order estimations of gravity wave activity (namely, vertical propagation speeds, their scale sizes, and their number) in thermospheric altitudes as a function of solar flux (*Mandal et al., 2020*).

The control of thermospheric winds on the gravity wave characteristics over the low-latitude thermosphere has been discussed in chapter 5. During geomagnetically disturbed times, the background thermospheric wind pattern gets modified due to heating at the high-latitudes. The gravity wave parameters during geomagnetically disturbed times are found to be different than the values at quiet times. Their differences on disturbed days show a very good correlation with the integrated values of the AE index, which is considered as a proxy of the energy inputs into high-latitudes. Such results provide direct evidence of the high-to-low latitude coupling in the neutral gravity waves during geomagnetic storm times (*Mandal and Pallamraju, 2020*).

- IV. Can the daytime gravity wave activity in thermospheric altitudes over the equatorial region lead the way in understanding the day-to-day variation in ESF occurrences in the post-sunset hours?

Chapter 4 of the thesis addresses this question. To understand the day-to-day variability in the ESF occurrences, we have chosen non-ESF days as control days to compare with the behavior around their surrounding ESF days. Earlier findings suggested that the EEJ strength, the base height of the ionosphere before the occurrence of ESF, and the strength

of the PRE are important factors to understand the predictability of the ESF occurrence. However, in our study, no significant contrast has been observed in the EEJ strength on the ESF and non-ESF days. Also, ESF has been found to occur on the days with CEJ events. Regarding the variation in the base height of the ionospheric F-region and the PRE prior to the ESF occurrence, to some extent, differences have been observed for ESF days compared to the non-ESF days. However, in all these cases, ESF occurrence can only be stated unambiguously after local sunset or just before the ESF onset. In contrast to these results, from the investigation of daytime thermospheric wave dynamics, it can be noted that vertical propagation activity of gravity waves is significantly higher on the ESF days as compared with the non-ESF days. Wavelet analyses confirmed the presence of these gravity waves until the time of ESF occurrence. Thus, they seem to play the role of seed perturbation for the generation of plasma irregularities. The average vertical phase speed of these gravity waves during 10-16 LT has been significantly higher on ESF days than those on non-ESF days. Whenever these values were higher than 80 ms^{-1} , they were found out to be ESF days, and as per this criterion, ESF occurrence can be predicted as early as 16 LT.

7.2 Future scope

This thesis has broadened our knowledge of the daytime thermospheric neutral wave dynamics, especially over low- and equatorial-latitudes. The focus of the thesis is on gaining a greater understanding of the systematic behavior of the neutral wave dynamics in the daytime thermosphere. These new insightful findings have opened up several new possibilities that can give rise to a comprehensive understanding of the daytime thermospheric wave dynamics. Thus, the future scope of this thesis is as follows:

- i. The basis of the thesis lies in laying the foundation in terms of an innovative approach to derive vertical propagation characteristics of gravity waves in the daytime thermosphere using digisonde measurements. As these are radio measurements, this approach can be applied during monsoon and cloudy sky conditions as well, to obtain a comprehensive global picture around the year. This has been accomplished

for a low-latitude location, Ahmedabad. As several digisondes are operating around the globe, such an analysis can be attempted at several other locations as well. Such an effort will enable one to get a global picture of neutral wave dynamics in the thermospheric altitudes, which will be a greatly valuable product.

- ii. From one digisonde vertical propagation characteristics of gravity waves can be obtained. In this thesis work, a simulation framework has been presented to obtain the horizontal scale sizes of the gravity waves. However, using phase offset information between the isoelectron density contours obtained from spatially separated digisondes, it is possible to empirically obtain the horizontal characteristics of the gravity waves in the thermospheric altitudes continuously along with their vertical propagation parameters.
- iii. Large field-of-view optical measurements provide horizontal speeds and scale sizes of gravity waves. Therefore, using collocated optical and digisonde measurements, a three-dimensional wave structure can be obtained. Thermospheric wind magnitudes in the direction of wave propagation can be estimated in the daytime from the dispersion relation using these measured horizontal and vertical propagation characteristics.
- iv. Different empirical relations are obtained in this thesis, which has quantified the effects of solar flux variations, heat input over the high-latitudes on the gravity wave propagation in the vertical direction in the thermospheric altitudes. These empirical formulations can form inputs to global-scale modeling of the thermospheric energy budget.
- v. As revealed in this thesis work, vertical propagation of gravity waves in the daytime thermosphere is found to be present only 41% of the time. This opens up a question as to what prevented its propagation during the majority 59% of the time. Different factors, such as wind shears, kinematic viscosity, and thermal diffusivity, can stop these waves from propagating vertically to thermospheric altitudes. Based on the satellite observations and empirical model-derived values, these conditions need to be further investigated to understand the absence of gravity waves' vertical propagation activity. It would also be interesting to see the relative importance

of the factors mentioned above using simulation studies on the days when other supporting/supplementary datasets are available.

- vi. Digisonde measurements along with collocated ISR observations will provide a unique opportunity to quantify the gravity wave propagation characteristics with different background conditions. Also, as the ISR gives the information on the topside of the ionosphere, the vertical propagating gravity wave characteristics can be traced to altitudes above the peak of the F-region, which is the inherent limitation of the digisonde technique.
- vii. Gravity waves are perturbation in the neutral motions, and these motions are communicated to plasma parameters through ion-neutral drag force. In earlier works, e.g., *Pallamraju et al. (2001)* showed that the wave activity was seen in the neutrals (dayglow emission variation) but not in the IEC measurements. It was inferred that once the wave disturbance is strong enough, these variations are communicated to the plasma parameters, and only then, variations in the IEC becomes perceptible. Simultaneous optical and digisonde measurements will enable characterizing these variations and quantifying the dependencies with respect to ion-neutral drag forces, so that a probable threshold value(s) of these forces that are required to experience the effect of neutral waves in the plasma parameters can be assessed.
- viii. Simultaneous operation of the digisonde and a Fabry-Perot Interferometer can provide information on neutral wind and temperature, which along with the vertical phase speeds and scale sizes can be considered as inputs into the gravity wave dispersion relation to estimating the horizontal scale sizes.
- ix. Satellite data sets of neutral parameters, such as those currently under operation by ICON and GOLD missions, can be used in conjunction with the the digisonde derived gravity wave characteristics to describe the nature and behavior of the upper atmosphere more accurately.

Several of the above mentioned future problems are being pursued/planned in the Space and Atmospheric Sciences Division of PRL, in the near future. Nevertheless, these are some of the future prospects that this thesis work has thrown open for any future re-

searcher interested in the understanding of the gravity wave dynamics of the upper atmosphere at any latitude on the globe.

=====

“The feeling is less like an ending than just another starting point.”

-Chuck Palahniuk.

References

- Aarons, J., The longitudinal morphology of equatorial f-layer irregularities relevant to their occurrence, *Space Science Reviews*, *63*, 209–243, 1993. [Cited on page 79.]
- Abdu, M., I. Batista, and J. Bittencourt, Some characteristics of spread f at the magnetic equatorial station fortaleza, *Journal of Geophysical Research: Space Physics*, *86*, 6836–6842, 1981a. [Cited on page 13.]
- Abdu, M., P. Batista, I. Batista, C. Brum, A. Carrasco, and B. Reinisch, Planetary wave oscillations in mesospheric winds, equatorial evening prereversal electric field and spread f, *Geophysical research letters*, *33*, 2006a. [Cited on page 18.]
- Abdu, M., K. N. Iyer, R. de Medeiros, I. S. Batista, and J. H. Sobral, Thermospheric meridional wind control of equatorial spread f and evening prereversal electric field, *Geophysical research letters*, *33*, 2006b. [Cited on pages 13, 16, and 79.]
- Abdu, M., E. A. Kherani, I. Batista, E. De Paula, D. Fritts, J. Sobral, et al., Gravity wave initiation of equatorial spread f/plasma bubble irregularities based on observational data from the spreadfex campaign, *Ann. Geophys*, *27*, 2607–2622, 2009. [Cited on pages 13, 80, and 92.]
- Abdu, M. A., J. A. Bittencourt, and I. S. Batista, Magnetic declination control of the equatorial F region dynamo electric field development and spread F, *J. Geophys. Res.*, *86*, 11,443–11,446, 1981b. [Cited on page 79.]
- Akasofu, S.-I., Energy coupling between the solar wind and the magnetosphere, *Space Science Reviews*, *28*, 121–190, 1981. [Cited on pages 46 and 113.]
- Alexander, M. J., A simulated spectrum of convectively generated gravity waves: Propagation from the tropopause to the mesopause and effects on the middle atmosphere, *Journal of Geophysical Research: Atmospheres*, *101*, 1571–1588, 1996. [Cited on page 22.]
- Alexander, M. J., and L. Pfister, Gravity wave momentum flux in the lower stratosphere over convection, *Geophysical Research Letters*, *22*, 2029–2032, 1995. [Cited on page 22.]

- Alexander, M. J., J. H. Beres, and L. Pfister, Tropical stratospheric gravity wave activity and relationships to clouds, *Journal of Geophysical Research: Atmospheres*, 105, 22,299–22,309, 2000. [Cited on page 22.]
- Altadill, D., and E. Apostolov, Time and scale size of planetary wave signatures in the ionospheric f region: Role of the geomagnetic activity and mesosphere/lower thermosphere winds, *Journal of Geophysical Research: Space Physics*, 108, 2003. [Cited on page 14.]
- Anandarao, B. G., Effects of gravity wave winds and wind shears on equatorial electrojet, *Geophys. Res. Lett.*, 3, 545–548, 1976. [Cited on page 6.]
- Anandarao, B. G., and R. Raghavarao, Structural changes in the currents and fields of the equatorial electrojet due to zonal and meridional winds, *J. Geophys. Res.*, 92, 2514–2526, 1987. [Cited on page 16.]
- Anderson, D., A. Anghel, J. Chau, and O. Veliz, Daytime vertical $E \times B$ drift velocities inferred from ground-based magnetometer observations at low latitudes, *Space Weather*, 2, 2004, <http://dx.doi.org/10.1029/2004SW000095>. [Cited on pages 13 and 79.]
- Anderson, D. N., A theoretical study of the ionospheric F region equatorial anomaly—I. Theory, *Planet. Space Sci.*, 21, 409–419, 1973. [Cited on page 8.]
- Andrews, D. G., *Middle Atmosphere Dynamics*, Academic Press, 1987. [Cited on page 17.]
- Appleton, E. V., Two anomalies in the ionosphere, *Nature*, 157, 691–691, 1946. [Cited on page 7.]
- Aswathy, R., and G. Manju, Gravity wave control on esf day-to-day variability: An empirical approach, *Journal of Geophysical Research: Space Physics*, 122, 6791–6798, 2017. [Cited on page 88.]
- Baker, W. G., and D. F. Martyn, Electric currents in the ionosphere - The conductivity, *Philosophical Transactions of the Royal Society of London A*, 246, 281–294, 1953, <http://dx.doi.org/10.1098/rsta.1953.0016>. [Cited on page 6.]

- Balan, N., G. Bailey, and R. Moffett, Modeling studies of ionospheric variations during an intense solar cycle, *Journal of Geophysical Research: Space Physics*, *99*, 17,467–17,475, 1994. [Cited on page 14.]
- Balan, N., G. J. Bailey, R. J. Moffett, Y. Z. Su, and J. E. Titheridge, Modelling studies of the conjugate-hemisphere differences in ionospheric ionization at equatorial anomaly latitudes, *J. Atmos. Terr. Phys.*, *57*, 279 – 292, 1995. [Cited on page 8.]
- Balan, N., G. Bailey, and Y. Su, Variations of the ionosphere and related solar fluxes during solar cycles 21 and 22, *Advances in Space Research*, *18*, 11–14, 1996. [Cited on page 14.]
- Balan, N., J. Souza, and G. J. Bailey, Recent developments in the understanding of equatorial ionization anomaly: A review, *Journal of Atmospheric and Solar-Terrestrial Physics*, *171*, 3–11, 2018, <https://doi.org/10.1016/j.jastp.2017.06.020>. [Cited on page 8.]
- Balsley, B., G. Haerendel, and R. Greenwald, Equatorial spread f: Recent observations and a new interpretation, *Journal of Geophysical Research*, *77*, 5625–5628, 1972. [Cited on page 78.]
- Banks, P., Observations of joule and particle heating in the auroral zone, *Journal of Atmospheric and Terrestrial Physics*, *39*, 179–193, 1977. [Cited on page 26.]
- Beer, T., *Atmospheric Waves*, Wiley, 1974. [Cited on pages 17 and 19.]
- Biondi, M. A., and D. P. Sipler, Horizontal and vertical winds and temperatures in the equatorial thermosphere: Measurements from Natal, Brazil during August-September, *Planet. Space Sci.*, *33*, 817–823, 1985. [Cited on page 17.]
- Bittencourt, J., and M. Abdu, A theoretical comparison between apparent and real vertical ionization drift velocities in the equatorial f region, *Journal of Geophysical Research: Space Physics*, *86*, 2451–2454, 1981. [Cited on page 85.]
- Blanc, M., and A. D. Richmond, The ionospheric disturbance dynamo, *J. Geophys. Res.*, *85*, 1669–1686, 1980. [Cited on pages 6, 23, and 98.]

- Bretthorst, G., Bayesian spectrum analysis and parameter estimation, lecture notes in statistics 48, springer-verlag, berlin, 1988. [Cited on pages 50 and 62.]
- Bretthorst, G. L., *Bayesian spectrum analysis and parameter estimation*, vol. 48, Springer Science & Business Media, 2013. [Cited on page 46.]
- Burke, W., L. Gentile, C. Huang, C. Valladares, and S. Su, Longitudinal variability of equatorial plasma bubbles observed by dmsp and rocsat-1, *Journal of Geophysical Research: Space Physics*, 109, 2004. [Cited on page 79.]
- Chakrabarti, S., Ground based spectroscopic studies of sunlit airglow and aurora, *J. Atmos. Sol. Terr. Phys.*, 60, 1403 – 1423, 1998. [Cited on page 39.]
- Chakrabarti, S., D. Pallamraju, and J. Baumgardner, HiTIES: A High Throughput Imaging Echelle Spectrograph for ground-based visible airglow and auroral studies, *J. Geophys. Res.*, 106, 30,337–30,348, 2001. [Cited on page 27.]
- Chakrabarti, S., O.-P. Jokiahho, J. L. Baumgardner, T. A. Cook, J. Martel, and M. Garland, High-throughput and multislit imaging spectrograph for extended sources, *Optical Engineering*, 51, 013,003, 2012. [Cited on pages 27 and 39.]
- Chakrabarty, D., R. Sekar, R. Narayanan, T. K. Pant, and K. Niranjana, Thermospheric gravity wave modes over low and equatorial latitudes during daytime, *J. Geophys. Res.*, 109, 2004. [Cited on page 58.]
- Chakrabarty, D., R. Sekar, R. Narayanan, C. V. Devasia, and B. M. Pathan, Evidence for the interplanetary electric field effect on the OI 630.0 nm airglow over low latitude, *J. Geophys. Res.*, 110, 2005. [Cited on page 23.]
- Chakrabarty, D., M. S. Bagiya, S. V. Thampi, and K. Iyer, Solar euv flux (0.1-50 nm), f10.7 cm flux, sunspot number and the total electron content in the crest region of equatorial ionization anomaly during the deep minimum between solar cycle 23 and 24, *94.20. dt; 96.60. qd; 96.60. tj*, 2012. [Cited on pages 14 and 125.]
- Chakrabarty, D., D. Rout, R. Sekar, R. Narayanan, G. D. Reeves, T. K. Pant, B. Veenadhari, and K. Shiokawa, Three different types of electric field disturbances affecting equatorial ionosphere during a long-duration prompt penetration event, *J. Geophys. Res.*, 120, 4993–5008, 2015. [Cited on page 23.]

- Chakrabarty, D., D. Hui, D. Rout, R. Sekar, A. Bhattacharyya, G. D. Reeves, and J. M. Ruohoniemi, Role of IMF by in the prompt electric field disturbances over equatorial ionosphere during a space weather event, *J. Geophys. Res.*, *122*, 2574–2588, 2017. [Cited on page 23.]
- Chandra, H., and R. Rastogi, Solar cycle and seasonal variation of spread-F near the magnetic equator, *Journal of Atmospheric and Terrestrial Physics*, *32*, 439–443, 1970. [Cited on pages 13 and 79.]
- Chandran, A., R. R. Garcia, R. L. Collins, and L. C. Chang, Secondary planetary waves in the middle and upper atmosphere following the stratospheric sudden warming event of January 2012, *Geophys. Res. Lett.*, *40*, 1861–1867, 2013. [Cited on page 18.]
- Chapman, S., The equatorial electrojet as detected from the abnormal electric current distribution above Huancayo, Peru, and elsewhere, *Archiv für Meteorologie, Geophysik und Bioklimatologie, Serie A*, *4*, 368–390, 1951, <https://doi.org/10.1007/BF02246814>. [Cited on page 6.]
- Chapman, S., and R. S. Lindzen, Atmospheric tides: Thermal and gravitational, 201 pp., ed. D. Reidel, Norwell, Mass, 1970. [Cited on page 18.]
- Chau, J. L., and R. F. Woodman, D and E region incoherent scatter radar density measurements over Jicamarca, *J. Geophys. Res.*, *110*, 2005. [Cited on page 18.]
- Chau, J. L., B. G. Fejer, and L. P. Goncharenko, Quiet variability of equatorial $E \times B$ drifts during a sudden stratospheric warming event, *Geophys. Res. Lett.*, *36*, 2009. [Cited on pages 18 and 27.]
- Chau, J. L., L. P. Goncharenko, B. G. Fejer, and H.-L. Liu, Equatorial and low latitude ionospheric effects during sudden stratospheric warming events, *Space Sci. Rev.*, *168*, 385–417, 2012. [Cited on page 18.]
- Cohen, R., and K. L. Bowles, The association of plane-wave electron density irregularities with the equatorial electrojet, *Journal of Geophysical Research*, *68*, 2503–2525, 1963, <http://dx.doi.org/10.1029/JZ068i009p02503>. [Cited on page 42.]
- Cole, K., Joule heating of the upper atmosphere, *Australian Journal of Physics*, *15*, 223, 1962. [Cited on page 26.]

- Cole, K., Energy deposition in the thermosphere caused by the solar wind, *Journal of Atmospheric and Terrestrial Physics*, *37*, 939–949, 1975. [Cited on page 26.]
- Das, U., D. Pallamraju, and S. Chakrabarti, Effect of an X-Class solar flare on the OI 630 nm dayglow emissions, *J. Geophys. Res.*, *115*, 2010. [Cited on pages 15 and 27.]
- Daubechies, I., Orthonormal bases of compactly supported wavelets, *Commun. Pure Appl. Math.*, *41*, 909–996, 1988. [Cited on page 53.]
- Daubechies, I., The wavelet transform, time-frequency localization and signal analysis, *IEEE transactions on information theory*, *36*, 961–1005, 1990. [Cited on page 53.]
- Davis, P., and W. Peltier, Some characteristics of the kelvin-helmholtz and resonant overreflection modes of shear flow instability and of their interaction through vortex pairing, *Journal of the Atmospheric Sciences*, *36*, 2394–2412, 1979. [Cited on page 22.]
- Davis, T. N., and M. Sugiura, Auroral electrojet activity index AE and its universal time variations, *Journal of Geophysical Research*, *71*, 785–801, 1966, <http://dx.doi.org/10.1029/JZ071i003p00785>. [Cited on page 45.]
- Davis, T. N., K. Burrows, and J. D. Stolarik, A latitude survey of the equatorial electrojet with rocket-borne magnetometers, *Journal of Geophysical Research*, *72*, 1845–1861, 1967, <http://dx.doi.org/10.1029/JZ072i007p01845>. [Cited on page 6.]
- Deeming, T. J., Fourier analysis with unequally-spaced data, *Astrophys. Space Sci.*, *36*, 137–158, 1975. [Cited on page 48.]
- Devasia, C., N. Jyoti, K. Subbarao, K. Viswanathan, D. Tiwari, and R. Sridharan, On the plausible linkage of thermospheric meridional winds with the equatorial spread f, *Journal of atmospheric and solar-terrestrial physics*, *64*, 1–12, 2002. [Cited on pages 16, 78, and 79.]
- Dewan, E. á., R. Picard, R. O’Neil, H. Gardiner, J. Gibson, J. Mill, E. Richards, M. Kendra, and W. Gallery, Msx satellite observations of thunderstorm-generated gravity waves in mid-wave infrared images of the upper stratosphere, *Geophysical Research Letters*, *25*, 939–942, 1998. [Cited on page 22.]

- Dickinson, R. E., C. P. Lagos, and R. E. Newell, Dynamics of the neutral gas in the thermosphere for small rossby number motions, *Journal of Geophysical Research*, *73*, 4299–4313, 1968. [Cited on page 26.]
- Djuth, F., M. Sulzer, J. Elder, and V. Wickwar, High-resolution studies of atmosphere-ionosphere coupling at arecibo observatory, puerto rico, *Radio Science*, *32*, 2321–2344, 1997. [Cited on page 21.]
- Djuth, F., M. Sulzer, S. Gonzales, J. D. Mathews, J. Elder, and R. Walterscheid, A continuum of gravity waves in the arecibo thermosphere?, *Geophysical Research Letters*, *31*, 2004. [Cited on page 58.]
- Drob, D. P., et al., An empirical model of the Earth’s horizontal wind fields: HWM07, *J. Geophys. Res.*, *113*, 2008. [Cited on page 16.]
- Drob, D. P., et al., An update to the Horizontal Wind Model (HWM): The quiet time thermosphere, *Earth and Space Science*, *2*, 301–319, 2015. [Cited on pages 16, 46, 99, and 106.]
- Dungey, J., Convective diffusion in the equatorial f region, *Journal of Atmospheric and Terrestrial Physics*, *9*, 304–310, 1956. [Cited on page 78.]
- Durrán, D. R., and J. B. Klemp, Another look at downslope winds. part ii: Nonlinear amplification beneath wave-overtaking layers, *Journal of the atmospheric sciences*, *44*, 3402–3412, 1987. [Cited on page 22.]
- Dworetzky, M., A period-finding method for sparse randomly spaced observations or “how long is a piece of string?”, *Monthly Notices of the Royal Astronomical Society*, *203*, 917–924, 1983. [Cited on page 46.]
- Emmert, J., B. G. Fejer, G. Shepherd, and B. Solheim, Altitude dependence of middle and low-latitude daytime thermospheric disturbance winds measured by windii, *Journal of Geophysical Research: Space Physics*, *107*, SIA–19, 2002. [Cited on page 16.]
- Emmert, J. T., A. D. Richmond, and D. P. Drob, A computationally compact representation of magnetic-apex and quasi-dipole coordinates with smooth base vectors, *Journal of Geophysical Research: Space Physics*, *115*, 2010. [Cited on page 32.]

- Ern, M., Q. T. Trinh, P. Preusse, J. C. Gille, M. G. Mlynczak, J. M. Russell III, and M. Riese, Gracile: A comprehensive climatology of atmospheric gravity wave parameters based on satellite limb soundings, *Earth System Science Data*, *10*, 857–892, 2018. [Cited on page 58.]
- Farge, M., Wavelet transforms and their applications to turbulence, *Annual review of fluid mechanics*, *24*, 395–458, 1992. [Cited on pages 53 and 54.]
- Farley, D., E. Bonelli, B. G. Fejer, and M. Larsen, The prereversal enhancement of the zonal electric field in the equatorial ionosphere, *Journal of Geophysical Research: Space Physics*, *91*, 13,723–13,728, 1986. [Cited on page 9.]
- Farley, D. T., A theory of electrostatic fields in a horizontally stratified ionosphere subject to a vertical magnetic field, *J. Geophys. Res.*, *64*, 1225–1233, 1959. [Cited on page 7.]
- Farley, D. T., A theory of electrostatic fields in the ionosphere at nonpolar geomagnetic latitudes, *J. Geophys. Res.*, *65*, 869–877, 1960. [Cited on page 7.]
- Farmer, D., and L. Armi, Stratified flow over topography: The role of small-scale entrainment and mixing in flow establishment, *Proceedings of the Royal Society of London. Series A: Mathematical, Physical and Engineering Sciences*, *455*, 3221–3258, 1999. [Cited on page 22.]
- Fejer, B., M. Blanc, and A. Richmond, Post-storm middle and low-latitude ionospheric electric fields effects, *Space Science Reviews*, *206*, 407–429, 2017. [Cited on page 98.]
- Fejer, B. G., and M. C. Kelley, Ionospheric irregularities, *Reviews of Geophysics*, *18*, 401–454, 1980, <http://dx.doi.org/10.1029/RG018i002p00401>. [Cited on page 79.]
- Fejer, B. G., and L. Scherliess, Empirical models of storm time equatorial zonal electric fields, *J. Geophys. Res.*, *102*, 24,047–24,056, 1997. [Cited on page 98.]
- Fejer, B. G., E. R. Paula, S. A. González, and R. F. Woodman, Average vertical and zonal F region plasma drifts over Jicamarca, *Journal of Geophysical Research: Space Physics*, *96*, 13,901–13,906, 1991, <https://doi.org/10.1029/91JA01171>. [Cited on page 9.]

- Fejer, B. G., L. Scherliess, and E. De Paula, Effects of the vertical plasma drift velocity on the generation and evolution of equatorial spread f, *Journal of Geophysical Research: Space Physics*, *104*, 19,859–19,869, 1999. [Cited on pages 13 and 79.]
- Fejer, B. G., J. W. Jensen, and S.-Y. Su, Seasonal and longitudinal dependence of equatorial disturbance vertical plasma drifts, *Geophysical Research Letters*, *35*, L20,106, 2008, <http://dx.doi.org/10.1029/2008GL035584>. [Cited on pages 6, 23, and 82.]
- Fejer, B. G., M. E. Olson, J. L. Chau, C. Stolle, H. Lühr, L. P. Goncharenko, K. Yumoto, and T. Nagatsuma, Lunar-dependent equatorial ionospheric electrodynamic effects during sudden stratospheric warmings, *Journal of Geophysical Research*, *115*, 2010, <http://dx.doi.org/10.1029/2010JA015273>. [Cited on page 18.]
- Fejer, B. G., M. Blanc, and A. D. Richmond, Post-storm middle and low-latitude ionospheric electric fields effects, *Space Science Reviews*, *206*, 407–429, 2017, <https://doi.org/10.1007/s11214-016-0320-x>. [Cited on page 23.]
- Floyd, L., J. Newmark, J. Cook, L. Herring, and D. McMullin, Solar EUV and UV spectral irradiances and solar indices, *J. Atmos. Sol. Terr. Phys.*, *67*, 3–15, 2005. [Cited on page 43.]
- Forbes, J. M., Atmospheric tides: 1. Model description and results for the solar diurnal component, *J. Geophys. Res.*, *87*, 5222–5240, 1982. [Cited on page 18.]
- Forbes, J. M., R. G. Roble, and F. A. Marcos, Thermospheric dynamics during the March 22, 1979, magnetic storm: 2. Comparisons of model predictions with observations, *J. Geophys. Res.*, *92*, 6069–6081, 1987. [Cited on page 16.]
- Forbes, J. M., X. Zhang, W. Ward, and E. R. Talaat, Climatological features of mesosphere and lower thermosphere stationary planetary waves within $\pm 40^\circ$ latitude, *J. Geophys. Res.*, *107*, 4322, 2002. [Cited on page 27.]
- Forbes, J. M., S. L. Bruinsma, Y. Miyoshi, and H. Fujiwara, A solar terminator wave in thermosphere neutral densities measured by the CHAMP satellite, *Geophys. Res. Lett.*, *35*, 2008. [Cited on page 27.]

- Fritts, D., and S. Vadas, Gravity wave penetration into the thermosphere: sensitivity to solar cycle variations and mean winds, in *Annales Geophysicae*, vol. 26, pp. 3841–3861, Copernicus GmbH, 2008. [Cited on page 80.]
- Fritts, D. C., Shear excitation of atmospheric gravity waves, *Journal of the Atmospheric Sciences*, 39, 1936–1952, 1982. [Cited on pages 22 and 27.]
- Fritts, D. C., Shear excitation of atmospheric gravity waves. part ii: Nonlinear radiation from a free shear layer, *Journal of the Atmospheric Sciences*, 41, 524–537, 1984. [Cited on pages 22 and 27.]
- Fritts, D. C., and M. J. Alexander, Gravity wave dynamics and effects in the middle atmosphere, *Rev. Geophys.*, 41, 2003. [Cited on pages 20, 22, 73, and 121.]
- Fuller-Rowell, T., G. Millward, A. Richmond, and M. Codrescu, Storm-time changes in the upper atmosphere at low latitudes, *Journal of atmospheric and solar-terrestrial physics*, 64, 1383–1391, 2002. [Cited on page 98.]
- Gavrilov, N., S. Kshevetskii, and A. Koval, Propagation of non-stationary acoustic-gravity waves at thermospheric temperatures corresponding to different solar activity, *Journal of Atmospheric and Solar-Terrestrial Physics*, 172, 100–106, 2018. [Cited on page 122.]
- Goel, M., S. Singh, and B. Rao, Postsunset rise of f layer height in the equatorial region and its relation to the f layer dynamo polarization fields, *Journal of Geophysical Research: Space Physics*, 95, 6237–6246, 1990. [Cited on page 9.]
- Goncharenko, L., J. L. Chau, P. Condor, A. Coster, and L. Benkevitch, Ionospheric effects of sudden stratospheric warming during moderate-to-high solar activity: Case study of january 2013, *Geophys. Res. Lett.*, 40, 4982–4986, 2013. [Cited on page 18.]
- Gouin, P., and P. N. Mayaud, A propos de l'existence possible d'un contre electrojet aux latitudes magnetiques equatoriales, *Ann. Geophys.*, 23, 41–47, 1967. [Cited on page 16.]
- Goupillaud, P., A. Grossmann, and J. Morlet, Cycle-octave and related transforms in seismic signal analysis, *Geoexploration*, 23, 85–102, 1984. [Cited on page 53.]

- Graham, M. J., A. J. Drake, S. Djorgovski, A. A. Mahabal, and C. Donalek, Using conditional entropy to identify periodicity, *Monthly Notices of the Royal Astronomical Society*, *434*, 2629–2635, 2013. [Cited on page 46.]
- Grainger, J. F., and J. Ring, Anomalous Fraunhofer line profiles, *Nature*, *193*, 762, 1962. [Cited on page 41.]
- Gregory, P., and T. J. Lored, A new method for the detection of a periodic signal of unknown shape and period, *The Astrophysical Journal*, *398*, 146–168, 1992. [Cited on page 46.]
- Grossmann, A., and J. Morlet, Decomposition of Hardy functions into square integrable wavelets of constant shape, *SIAM J. Math. Anal.*, *15*, 723–736, 1984. [Cited on page 53.]
- Guharay, A., and R. Sekar, Signature of latitudinal coupling during a major sudden stratospheric warming in the tropics, *J. Atmos. Sol. Terr. Phys.*, *75*, 122–126, 2012. [Cited on pages 18 and 27.]
- Guharay, A., P. Batista, and B. Clemesha, On the variability of the seasonal scale oscillations over Cachoeira Paulista (22.7°S, 45°W), Brazil, *Earth Planets Space*, *66*, 45, 2014. [Cited on pages 18 and 27.]
- Guharay, A., P. Batista, and B. Clemesha, Variability of the quasi-2-day wave and interaction with longer period planetary waves in the mlt at cachoeira paulista (22.7° s, 45° w), *Journal of Atmospheric and Solar-Terrestrial Physics*, *130*, 57–67, 2015. [Cited on page 27.]
- Guharay, A., P. P. Batista, R. A. Buriti, and N. J. Schuch, On the variability of the quarter-diurnal tide in the mlt over brazilian low-latitude stations, *Earth, Planets and Space*, *70*, 140, 2018. [Cited on page 27.]
- Guharay, A., P. P. Batista, R. A. Buriti, and N. J. Schuch, Signature of the 27-day oscillation in the mlt tides and its relation with solar radiation at low latitudes, *Earth, Planets and Space*, *72*, 1–10, 2020. [Cited on page 27.]
- Gurubaran, S., The equatorial counter electrojet: Part of a worldwide current system?, *Geophys. Res. Lett.*, *29*, 511–514, 2002. [Cited on page 6.]

- Gurubaran, S., R. Sridharan, R. Suhasisni, and K. G. Jani, Variabilities in the thermospheric temperatures in the region of the crest of the equatorial ionization anomaly - A case study, *J. Atmos. Sol. Terr. Phys.*, *57*, 695–703, 1995. [Cited on page 16.]
- Gurubaran, S., S. Sridharan, T. Ramkumar, and R. Rajaram, The mesospheric quasi-2-day wave over Tirunelveli (8.7°N), *J. Atmos. Sol. Terr. Phys.*, *63*, 975–985, 2001. [Cited on pages 18 and 27.]
- Haerendel, G., Theory of equatorial spread f, *Max-Planck inst. fur Phys. and Astrophys.*, 1973. [Cited on page 78.]
- Haerendel, G., and J. Eccles, The role of the equatorial electrojet in the evening ionosphere, *Journal of Geophysical Research: Space Physics*, *97*, 1181–1192, 1992. [Cited on page 82.]
- Hagan, M., and J. Forbes, Migrating and nonmigrating diurnal tides in the middle and upper atmosphere excited by tropospheric latent heat release, *Journal of Geophysical Research: Atmospheres*, *107*, ACL-6, 2002. [Cited on page 27.]
- Hagan, M., A. Maute, R. Roble, A. Richmond, T. Immel, and S. England, Connections between deep tropical clouds and the earth's ionosphere, *Geophysical Research Letters*, *34*, 2007. [Cited on page 19.]
- Hanson, W. B., and R. J. Moffett, Ionization transport effects in the equatorial F region, *J. Geophys. Res.*, *71*, 5559–5572, 1966. [Cited on pages 7 and 8.]
- Hargreaves, J. K., *The Solar-Terrestrial Environment*, Cambridge University Press, 1992. [Cited on pages 4, 20, and 33.]
- Hedin, A. E., and H. G. Mayr, Magnetic control of the near equatorial neutral thermosphere, *J. Geophys. Res.*, *78*, 1688–1691, 1973. [Cited on page 10.]
- Hedin, A. E., P. Bauer, H. G. Mayr, G. R. Carignan, L. H. Brace, H. C. Brinton, A. D. Parks, and D. T. Pelz, Observations of neutral composition and related ionospheric variations during a magnetic storm in February 1974, *J. Geophys. Res.*, *82*, 3183–3189, 1977. [Cited on page 25.]

- Hedin, A. E., N. W. Spencer, and T. L. Killeen, Empirical global model of upper thermosphere winds based on Atmosphere and Dynamics Explorer satellite data, *J. Geophys. Res.*, *93*, 9959–9978, 1988. [Cited on page 16.]
- Hedin, A. E., et al., Empirical wind model for the upper, middle and lower atmosphere, *J. Atmos. Terr. Phys.*, *58*, 1421 – 1447, 1996. [Cited on page 16.]
- Heelis, R. A., P. C. Kendall, R. J. Moffett, D. W. Windle, and H. Rishbeth, Electrical coupling of the E- and F-regions and its effect on F-region drifts and winds, *Planet. Space Sci.*, *22*, 743–756, 1974. [Cited on page 8.]
- Hernandez, G., and R. G. Roble, Direct measurements of nighttime thermospheric winds and temperatures, 2. Geomagnetic storms, *J. Geophys. Res.*, *81*, 5173–5181, 1976. [Cited on page 16.]
- Herrero, F., and J. Meriwether Jr, The 630 nm mig and the vertical neutral wind in the low latitude nighttime thermosphere, *Geophysical research letters*, *21*, 97–100, 1994. [Cited on page 17.]
- Herrero, F., H. Mayr, and N. Spencer, Low latitude thermospheric meridional winds between 250 and 450 km altitude: AE-E satellite data, *J. Atmos. Terr. Phys.*, *50*, 1001 – 1006, 1988. [Cited on page 16.]
- Hines, C. O., Internal atmospheric gravity waves at ionospheric heights, *Canadian Journal of Physics*, *38*, 1441–1481, 1960. [Cited on pages 19, 21, 27, 58, 64, 67, and 87.]
- Hines, C. O., et al., *The upper atmosphere in motion: A selection of papers with annotation*, vol. 18, American Geophysical Union, 1974. [Cited on page 21.]
- Hinteregger, H. E., EUV Fluxes in the solar spectrum below 2000 Å, *J. Atmos. Terr. Phys.*, *38*, 791 – 806, 1976. [Cited on page 4.]
- Hocke, K., and N. Kämpfer, Gap filling and noise reduction of unevenly sampled data by means of the Lomb-Scargle periodogram, *Atmos. Chem. Phys.*, *9*, 4197–4206, 2009. [Cited on page 67.]
- Hocke, K. K. S., A review of atmospheric gravity waves and travelling ionospheric disturbances: 1982-1995, *Ann. Geophys.*, *14*, 917–940, 1996. [Cited on pages 22, 75, and 98.]

- Holton, J. R., The Dynamics of Sudden Stratospheric Warmings, *Annu. Rev. Earth Planet. Sci.*, *8*, 169–190, 1980. [Cited on pages 18 and 19.]
- Horne, J. H., and S. L. Baliunas, A prescription for period analysis of unevenly sampled time series, *Astrophys. J.*, *302*, 757–763, 1986. [Cited on page 50.]
- Huang, C.-S., and M. C. Kelley, Nonlinear evolution of equatorial spread f: 2. gravity wave seeding of rayleigh-taylor instability, *Journal of Geophysical Research: Space Physics*, *101*, 293–302, 1996. [Cited on page 80.]
- Huang, X., and B. Reinisch, Vertical electron density profiles from the digisonde network, *Advances in Space Research*, *18*, 121–129, 1996. [Cited on page 36.]
- Huang, X., and B. W. Reinisch, Vertical electron content from ionograms in real time, *Radio Science*, *36*, 335–342, 2001. [Cited on pages 62 and 123.]
- Huba, J. D., G. Joyce, S. Sazykin, R. Wolf, and R. Spiro, Simulation study of penetration electric field effects on the low- to mid-latitude ionosphere, *Geophysical Research Letters*, *32*, 2005, <https://doi.org/10.1029/2005GL024162>. [Cited on page 23.]
- Hunsucker, R. D., Atmospheric gravity waves generated in the high-latitude ionosphere: A review, *Rev. Geophys.*, *20*, 293–315, 1982. [Cited on pages 58 and 98.]
- Hysell, D., and J. Burcham, Long term studies of equatorial spread f using the julia radar at jicamarca, *Journal of Atmospheric and Solar-Terrestrial Physics*, *64*, 1531–1543, 2002. [Cited on page 79.]
- Hysell, D., M. Kelley, W. Swartz, and R. Woodman, Seeding and layering of equatorial spread f by gravity waves, *Journal of Geophysical Research: Space Physics*, *95*, 17,253–17,260, 1990. [Cited on page 80.]
- Hysell, D., R. Jafari, D. Fritts, and B. Laughman, Gravity wave effects on postsunset equatorial f region stability, *Journal of Geophysical Research: Space Physics*, *119*, 5847–5860, 2014. [Cited on page 80.]
- Immel, T. J., S. B. Mende, H. U. Frey, N. Østgaard, and G. R. Gladstone, Effect of the 14 July 2000 solar flare on Earth’s FUV emissions, *J. Geophys. Res.*, *108*, 2003. [Cited on page 15.]

- Immel, T. J., E. Sagawa, S. L. England, S. B. Henderson, M. E. Hagan, S. B. Mende, H. U. Frey, C. M. Swenson, and L. J. Paxton, Control of equatorial ionospheric morphology by atmospheric tides, *Geophys. Res. Lett.*, *33*, 2006. [Cited on pages 19 and 27.]
- Jayachandran, P., P. S. Ram, V. Somayajulu, and P. R. Rao, Effect of equatorial ionization anomaly on the occurrence of spread-f, in *Annales Geophysicae*, vol. 15, pp. 255–262, Springer, 1997. [Cited on pages 14 and 80.]
- Jaynes, E., Probability theory: The logic of science, cambridge: Cambridge u, 2003. [Cited on page 52.]
- Jin, H., Y. Miyoshi, H. Fujiwara, and H. Shinagawa, Electrodynamics of the formation of ionospheric wave number 4 longitudinal structure, *Journal of Geophysical Research: Space Physics*, *113*, 2008. [Cited on page 19.]
- Jyoti, N., C. Devasia, R. Sridharan, and D. Tiwari, Threshold height (h_f) c for the meridional wind to play a deterministic role in the bottom side equatorial spread f and its dependence on solar activity, *Geophysical research letters*, *31*, 2004. [Cited on page 79.]
- Kakad, B., D. Tiwari, and T. Pant, Study of disturbance dynamo effects at nighttime equatorial f region in indian longitude, *Journal of Geophysical Research: Space Physics*, *116*, 2011. [Cited on page 98.]
- Karan, D. K., and D. Pallamraju, Small-scale longitudinal variations in the daytime equatorial thermospheric wave dynamics as inferred from oxygen dayglow emissions, *J. Geophys. Res.*, pp. 6528–6542, 2017. [Cited on pages 27, 58, and 63.]
- Karan, D. K., and D. Pallamraju, Effect of geomagnetic storms on the daytime low-latitude thermospheric wave dynamics, *Journal of Atmospheric and Solar-Terrestrial Physics*, *170*, 35–47, 2018. [Cited on pages 16, 24, 27, 63, 99, and 116.]
- Karan, D. K., and D. Pallamraju, On estimation of daytime equatorial vertical ($e \times b$) plasma drifts using optical neutral dayglow emission measurements, *Journal of Geophysical Research: Space Physics*, *125*, e2019JA026775, 2020. [Cited on page 27.]

- Karan, D. K., D. Pallamraju, K. A. Phadke, T. Vijayalakshmi, T. K. Pant, and S. Mukherjee, Electrodynamic influence on the diurnal behaviour of neutral daytime airglow emissions, *Ann. Geophys.*, *34*, 1019–1030, 2016. [Cited on pages 27 and 82.]
- Kato, S., T. Tsuda, and F. Watanabe, Thermal excitation of non-migrating tides, *Journal of Atmospheric and Terrestrial Physics*, *44*, 131–146, 1982. [Cited on page 18.]
- Kelley, M., et al., The condor equatorial spread f campaign: Overview and results of the large-scale measurements, *Journal of Geophysical Research: Space Physics*, *91*, 5487–5503, 1986. [Cited on page 80.]
- Kelley, M. C., and J. McClure, Equatorial spread-f: a review of recent experimental results, *Journal of Atmospheric and Terrestrial Physics*, *43*, 427–435, 1981. [Cited on page 80.]
- Kelley, M. C., J. J. Makela, J. L. Chau, and M. J. Nicolls, Penetration of the solar wind electric field into the magnetosphere/ionosphere system, *Geophysical Research Letters*, *30*, 2003, <https://doi.org/10.1029/2002GL016321>. [Cited on page 23.]
- Kikuchi, T., H. Lühr, T. Kitamura, O. Saka, and K. Schlegel, Direct penetration of the polar electric field to the equator during a dp 2 event as detected by the auroral and equatorial magnetometer chains and the eiscat radar, *Journal of Geophysical Research: Space Physics*, *101*, 17,161–17,173, 1996. [Cited on page 98.]
- Kikuchi, T., K. K. Hashimoto, T.-I. Kitamura, H. Tachihara, and B. Fejer, Equatorial counter-electrojets during substorms, *Journal of Geophysical Research*, *108*, 2003, <http://dx.doi.org/10.1029/2003JA009915>. [Cited on page 6.]
- Klausner, V., P. Fagundes, Y. Sahai, C. Wrasse, V. Pillat, and F. Becker-Guedes, Observations of gw/tid oscillations in the f2 layer at low latitude during high and low solar activity, geomagnetic quiet and disturbed periods, *Journal of Geophysical Research: Space Physics*, *114*, 2009. [Cited on page 59.]
- Klostermeyer, J., Nonlinear investigation of the spatial resonance effect in the nighttime equatorial f region, *Journal of Geophysical Research: Space Physics*, *83*, 3753–3760, 1978. [Cited on page 80.]

- Krall, J., J. Huba, and D. Fritts, On the seeding of equatorial spread f by gravity waves, *Geophysical research letters*, *40*, 661–664, 2013. [Cited on page 80.]
- Kutiev, I., Y. Otsuka, D. Pancheva, and R. Heelis, Response of low-latitude ionosphere to medium-term changes of solar and geomagnetic activity, *Journal of Geophysical Research: Space Physics*, *117*, 2012. [Cited on page 14.]
- Lakshmi Narayanan, V., S. Gurubaran, and K. Emperumal, Airglow imaging observations of small-scale structures driven by convective instability in the upper mesosphere over Tirunelveli (8.7°N), *J. Geophys. Res.*, *115*, 2010. [Cited on pages 27 and 58.]
- Laskar, F. I., and D. Pallamraju, Does sudden stratospheric warming induce meridional circulation in the mesosphere thermosphere system?, *J. Geophys. Res.*, *119*, 10,133–10,143, 2014. [Cited on pages 18 and 27.]
- Laskar, F. I., D. Pallamraju, T. V. Lakshmi, M. A. Reddy, B. M. Pathan, and S. Chakrabarti, Investigations on vertical coupling of atmospheric regions using combined multiwavelength optical dayglow, magnetic, and radio measurements, *J. Geophys. Res.*, *118*, 4618–4627, 2013. [Cited on pages 18, 27, and 121.]
- Laskar, F. I., D. Pallamraju, and B. Veenadhari, Vertical coupling of atmospheres: dependence on strength of sudden stratospheric warming and solar activity, *Earth, Planets and Space*, *66*, 94, 2014. [Cited on pages 18, 27, 28, and 121.]
- Laskar, F. I., D. Pallamraju, B. Veenadhari, T. V. Lakshmi, M. A. Reddy, and S. Chakrabarti, Gravity waves in the thermosphere: Solar activity dependence, *Adv. Space Res.*, *55*, 1651 – 1659, 2015. [Cited on pages 27, 28, 58, 62, 63, 122, and 138.]
- Laskar, F. I., J. P. McCormack, J. L. Chau, D. Pallamraju, P. Hoffmann, and R. P. Singh, Interhemispheric meridional circulation during sudden stratospheric warming, *Journal of Geophysical Research: Space Physics*, *124*, 7112–7122, 2019. [Cited on page 18.]
- Lau, K.-M., and H. Weng, Climate signal detection using wavelet transform: How to make a time series sing, *Bulletin of the American meteorological society*, *76*, 2391–2402, 1995. [Cited on page 53.]

- Le, H., L. Liu, and W. Wan, An analysis of thermospheric density response to solar flares during 2001–2006, *Journal of Geophysical Research: Space Physics*, 117, 2012. [Cited on page 15.]
- Le, H., L. Liu, Y. Chen, and W. Wan, Statistical analysis of ionospheric responses to solar flares in the solar cycle 23, *Journal of Geophysical Research: Space Physics*, 118, 576–582, 2013. [Cited on page 15.]
- Le, H., Z. Ren, L. Liu, Y. Chen, and H. Zhang, Global thermospheric disturbances induced by a solar flare: a modeling study, *Earth, Planets and Space*, 67, 1–14, 2015. [Cited on page 15.]
- Lean, J., The Sun's variable radiation and its relevance for Earth, *Annu. Rev. Astron. Astrophys.*, 35, 33–67, 1997. [Cited on pages 14 and 15.]
- Lei, J., L. Liu, W. Wan, and S.-R. Zhang, Variations of electron density based on long-term incoherent scatter radar and ionosonde measurements over millstone hill, *Radio science*, 40, 1–10, 2005. [Cited on pages 124 and 125.]
- Lindzen, R. S., *Dynamics in atmospheric physics*, Cambridge University Press, 1990. [Cited on pages 19 and 21.]
- Liu, H. L., and R. G. Roble, Dynamical coupling of the stratosphere and mesosphere in the 2002 southern hemisphere major stratospheric sudden warming, *Geophys. Res. Lett.*, 32, L13,804, 2005. [Cited on page 18.]
- Liu, P. C., Wavelet spectrum analysis and ocean wind waves, in *Wavelet Analysis and Its Applications*, vol. 4, pp. 151–166, Elsevier, 1994. [Cited on page 53.]
- Lomb, N. R., Least-squares frequency analysis of unequally spaced data, *Astrophys. Space Sci.*, 39, 447–462, 1976. [Cited on pages 46, 50, 52, and 61.]
- Long, R. R., Some aspects of the flow of stratified fluids: Iii. continuous density gradients, *Tellus*, 7, 341–357, 1955. [Cited on page 22.]
- Lott, F., and M. J. Miller, A new subgrid-scale orographic drag parametrization: Its formulation and testing, *Quarterly Journal of the Royal Meteorological Society*, 123, 101–127, 1997. [Cited on page 22.]

- Madhav Haridas, M., G. Manju, and T. K. Pant, On the solar activity variations of nocturnal f region vertical drifts covering two solar cycles in the indian longitude sector, *Journal of Geophysical Research: Space Physics*, 120, 1445–1451, 2015. [Cited on page 86.]
- Mandal, S., and D. Pallamraju, Thermospheric gravity wave characteristics in the daytime over low-latitudes during geomagnetic quiet and disturbed conditions, *Journal of Atmospheric and Solar-Terrestrial Physics*, 211, 105,470, 2020. [Cited on pages 24, 88, 143, and 144.]
- Mandal, S., D. Pallamraju, D. K. Karan, K. A. Phadke, R. P. Singh, and P. Suryawanshi, On deriving gravity wave characteristics in the daytime upper atmosphere using radio technique, *Journal of Geophysical Research: Space Physics*, 124, 6985–6997, 2019. [Cited on pages 88, 100, 106, and 142.]
- Mandal, S., D. Pallamraju, and P. Suryawanshi, Changes in the daytime thermospheric gravity wave propagation characteristics over low-latitudes in response to the variation in solar flux, *Journal of Atmospheric and Solar-Terrestrial Physics*, 209, 105,414, 2020. [Cited on pages 14, 88, 91, 100, 132, 143, and 144.]
- Manju, G., M. M. Haridas, and R. Aswathy, Role of gravity wave seed perturbations in esf day-to-day variability: A quantitative approach, *Advances in Space Research*, 57, 1021–1028, 2016. [Cited on pages 82 and 88.]
- Maruyama, T., and N. Matuura, Longitudinal variability of annual changes in activity of equatorial spread f and plasma bubbles, *Journal Of Geophysical Research: Space Physics*, 89, 10,903–10,912, 1984. [Cited on pages 13, 16, and 79.]
- Matsuno, T., A dynamical model of the stratospheric sudden warming, *J. Atmos. Sci.*, 28, 1479–1494, 1971. [Cited on page 18.]
- Mayr, H. G., I. Harris, and N. W. Spencer, Some properties of upper atmosphere dynamics, *Rev. Geophys.*, 16, 539–565, 1978. [Cited on pages 16, 24, 25, 98, and 112.]
- Mazaudier, C., and S. Venkateswaran, Delayed ionospheric effects of the geomagnetic storms of march 22, 1979 studied by the sixth co-ordinated data analysis

- workshop(cdaw-6), in *Annales Geophysicae*, vol. 8, p. 511, Toulouse, 1990. [Cited on page 98.]
- McLandress, C., M. J. Alexander, and D. L. Wu, Microwave limb sounder observations of gravity waves in the stratosphere: A climatology and interpretation, *Journal of Geophysical Research: Atmospheres*, 105, 11,947–11,967, 2000. [Cited on page 22.]
- Medvedev, A., and G. Klaassen, Parameterization of gravity wave momentum deposition based on nonlinear wave interactions: Basic formulation and sensitivity tests, *Journal of Atmospheric and Solar-Terrestrial Physics*, 62, 1015–1033, 2000. [Cited on pages 22 and 122.]
- Mendillo, M., Storms in the ionosphere: Patterns and processes for total electron content, *Reviews of Geophysics*, 44, 2006. [Cited on page 58.]
- Mendillo, M., and J. V. Evans, Incoherent scatter observations of the ionospheric response to a large solar flare, *Radio Science*, 9, 197–203, 1974. [Cited on page 15.]
- Mendillo, M., J. Baumgardner, X. Pi, P. J. Sultan, and R. Tsunoda, Onset conditions for equatorial spread f, *Journal of Geophysical Research: Space Physics*, 97, 13,865–13,876, 1992. [Cited on page 13.]
- Mendillo, M., J. Meriwether, and M. Biondi, Testing the thermospheric neutral wind suppression mechanism for day-to-day variability of equatorial spread f, *Journal of Geophysical Research: Space Physics*, 106, 3655–3663, 2001. [Cited on pages 14, 16, and 79.]
- Mendillo, M., et al., Behavior of the ionospheric f region during the great solar flare of august 7, 1972, *Journal of Geophysical Research*, 79, 665–672, 1974. [Cited on page 15.]
- Meriwether, J. W., P. Shih, T. L. Killeen, V. B. Wickwar, and R. G. Roble, Nighttime thermospheric winds over Sondre Stromfjord, Greenland, *Geophys. Res. Lett.*, 11, 931–934, 1984. [Cited on page 16.]
- Meriwether, J. W., J. W. Moody, M. A. Biondi, and R. G. Roble, Optical interferometric measurements of nighttime equatorial thermospheric winds at Arequipa, Peru, *J. Geophys. Res.*, 91, 5557–5566, 1986. [Cited on page 16.]

- Meyers, S. D., B. G. Kelly, and J. J. O'Brien, An introduction to wavelet analysis in oceanography and meteorology: With application to the dispersion of yanai waves, *Monthly weather review*, *121*, 2858–2866, 1993. [Cited on page 53.]
- Mitra, A. P., *Ionospheric Effects of Solar Flares*, D. Reidel Publishing Company, 1974. [Cited on page 15.]
- Mitra, S., Geomagnetic control of region f 2 of the ionosphere, *Nature*, *158*, 668–669, 1946. [Cited on page 7.]
- Miyoshi, Y., H. Fujiwara, H. Jin, and H. Shinagawa, A global view of gravity waves in the thermosphere simulated by a general circulation model, *Journal of Geophysical Research: Space Physics*, *119*, 5807–5820, 2014. [Cited on page 122.]
- Miyoshi, Y., D. Pancheva, P. Mukhtarov, H. Jin, H. Fujiwara, and H. Shinagawa, Excitation mechanism of non-migrating tides, *Journal of Atmospheric and Solar-Terrestrial Physics*, *156*, 24–36, 2017. [Cited on page 18.]
- Morlet, J., G. Arens, E. Fourgeau, and D. Glard, Wave propagation and sampling theory—Part I: Complex signal and scattering in multilayered media, *Geophysics*, *47*, 203–221, 1982. [Cited on page 53.]
- Namba, S., and K.-I. Maeda, Radio wave propagation, *Corona, Tokyo*, p. 86, 1939. [Cited on page 7.]
- Nance, L. B., and D. R. Durran, A modeling study of nonstationary trapped mountain lee waves. part ii: Nonlinearity, *Journal of the atmospheric sciences*, *55*, 1429–1445, 1998. [Cited on page 22.]
- Narayanan, R., J. N. Desai, N. K. Modi, R. Raghavarao, and R. Sridharan, Dayglow photometry: a new approach, *Appl. Opt.*, *28*, 2138–2142, 1989. [Cited on pages 27 and 39.]
- Navarro, L., B. G. Fejer, and L. Scherliess, Equatorial disturbance dynamo vertical plasma drifts over jicamarca: Bimonthly and solar cycle dependence, *Journal of Geophysical Research: Space Physics*, *124*, 4833–4841, 2019. [Cited on page 113.]

- Nicolls, M. J., and M. C. Kelley, Strong evidence for gravity wave seeding of an ionospheric plasma instability, *Geophysical research letters*, *32*, 2005. [Cited on page 80.]
- Nishida, A., Coherence of geomagnetic DP 2 fluctuations with interplanetary magnetic variations, *J. Geophys. Res.*, *73*, 5549–5559, 1968. [Cited on page 23.]
- Oberheide, J., and O. Gusev, Observation of migrating and nonmigrating diurnal tides in the equatorial lower thermosphere, *Geophysical research letters*, *29*, 20–1, 2002. [Cited on pages 19 and 27.]
- Oberheide, J., J. Forbes, K. Häusler, Q. Wu, and S. Bruinsma, Tropospheric tides from 80 to 400 km: Propagation, interannual variability, and solar cycle effects, *Journal of Geophysical Research: Atmospheres*, *114*, 2009. [Cited on page 19.]
- Oliver, W., Y. Otsuka, M. Sato, T. Takami, and S. Fukao, A climatology of f region gravity wave propagation over the middle and upper atmosphere radar, *Journal of Geophysical Research: Space Physics*, *102*, 14,499–14,512, 1997. [Cited on pages 58, 68, 69, 70, and 143.]
- Onwumechilli, A., Geomagnetic variations in the equatorial zone, in *Phys. of Geomagnetic Phenomena*, p. 426, 1967. [Cited on pages 6 and 16.]
- Ossakow, S., S. Zalesak, B. McDonald, and P. Chaturvedi, Nonlinear equatorial spread f: Dependence on altitude of the f peak and bottomside background electron density gradient scale length, *Journal of Geophysical Research: Space Physics*, *84*, 17–29, 1979. [Cited on page 78.]
- Pallam Raju, D., R. Sridharan, R. Narayanan, N. K. Modi, R. Raghavarao, and B. H. Subbaraya, Ground-based optical observations of daytime auroral emissions from Antarctica, *J. Atmos. Terr. Phys.*, *57*, 1591–1597, 1995. [Cited on page 27.]
- Pallam Raju, D., R. Sridharan, S. Gurubaran, and R. Raghavarao, First results from ground-based daytime optical investigation of the development of the equatorial ionization anomaly, *Ann. Geophys.*, *14*, 238–245, 1996. [Cited on pages 8, 27, 39, 40, and 58.]

- Pallamraju, D., and S. Chakrabarti, First ground-based measurements of OI 6300 Å daytime aurora over Boston in response to the 30 October 2003 geomagnetic storm, *Geophys. Res. Lett.*, *32*, 2005. [Cited on page 27.]
- Pallamraju, D., and S. Chakrabarti, Contributions of imaging Echelle spectrographs to daytime optical aeronomy, *J. Atmos. Sol. Terr. Phys.*, *68*, 1459 – 1471, 2006. [Cited on pages 27 and 39.]
- Pallamraju, D., and R. Sridharan, Ground-based optical measurements of daytime auroral emissions: A new means of investigating space-weather related processes, *Proceedings of the Indian Academy of Sciences - Earth and Planetary Sciences*, *107*, 203–211, 1998. [Cited on page 27.]
- Pallamraju, D., J. Baumgardner, and S. Chakrabarti, A multiwavelength investigation of the ring effect in the day sky spectrum, *Geophys. Res. Lett.*, *27*, 1875–1878, 2000. [Cited on pages 27 and 41.]
- Pallamraju, D., J. Baumgardner, S. Chakrabarti, and T. R. Pedersen, Simultaneous ground based observations of an auroral arc in daytime/twilighttime OI 630.0 nm emission and by incoherent scatter radar, *J. Geophys. Res.*, *106*, 5543–5549, 2001. [Cited on pages 22 and 147.]
- Pallamraju, D., J. Baumgardner, and S. Chakrabarti, HIRISE: A ground-based high-resolution imaging spectrograph using echelle grating for measuring daytime airglow/auroral emissions, *J. Atmos. Sol. Terr. Phys.*, *64*, 1581–1587, 2002. [Cited on pages 27, 39, and 42.]
- Pallamraju, D., S. Chakrabarti, and C. E. Valladares, Magnetic storm-induced enhancement in neutral composition at low latitudes as inferred by O(¹D) dayglow measurements from Chile, *Ann. Geophys.*, *22*, 3241–3250, 2004b. [Cited on pages 14, 16, 24, 27, 60, 77, 80, and 98.]
- Pallamraju, D., U. Das, and S. Chakrabarti, Short- and long-timescale thermospheric variability as observed from OI 630.0 nm dayglow emissions from low latitudes, *J. Geophys. Res.*, *115*, 2010. [Cited on pages 14, 15, 22, 27, 62, and 63.]

- Pallamraju, D., S. Chakrabarti, and S. C. Solomon, On deriving incident auroral particle fluxes in the daytime using combined ground-based optical and radar measurements, *J. Geophys. Res.*, *116*, 2011. [Cited on pages [24](#) and [27](#).]
- Pallamraju, D., F. I. Laskar, R. P. Singh, J. Baumgardner, and S. Chakrabarti, MISE: A multiwavelength imaging spectrograph using echelle grating for daytime optical aeronomy investigations, *J. Atmos. Sol. Terr. Phys.*, *103*, 176 – 183, 2013. [Cited on pages [27](#), [39](#), [40](#), [41](#), [42](#), and [58](#).]
- Pallamraju, D., D. K. Karan, and K. A. Phadke, First three dimensional wave characteristics in the daytime upper atmosphere derived from ground-based multiwavelength oxygen dayglow emission measurements, *Geophys. Res. Lett.*, *43*, 5545–5553, 2016. [Cited on pages [28](#), [58](#), [63](#), [67](#), [100](#), [106](#), [108](#), [110](#), and [132](#).]
- Pallamraju, D., D. K. Karan, F. I. Laskar, T. V. Lakshmi, and S. Chakrabarti, Effect of solar flux versus compositional variations on the variability of daytime oxygen optical emission rates over low-and mid-latitudes, *Journal of Atmospheric and Solar-Terrestrial Physics*, p. 105293, 2020. [Cited on pages [14](#) and [27](#).]
- Pallamraju, D., et al., Daytime wave characteristics in the mesosphere lower thermosphere region: Results from the balloon-borne investigations of regional-atmospheric dynamics experiment, *Journal of Geophysical Research: Space Physics*, *119*, 2229–2242, 2014. [Cited on pages [22](#), [28](#), [39](#), [58](#), [63](#), [77](#), [81](#), and [106](#).]
- Pancheva, D., and P. Mukhtarov, Stratospheric warmings: The atmosphere-ionosphere coupling paradigm, *J. Atmos. Sol. Terr. Phys.*, *73*, 1697–1702, 2011a. [Cited on page [27](#).]
- Pancheva, D., and P. Mukhtarov, Stratospheric warmings: The atmosphere-ionosphere coupling paradigm, *J. Atmos. Sol. Terr. Phys.*, *73*, 1697 – 1702, 2011b. [Cited on page [18](#).]
- Pancheva, D., N. Mitchell, R. Clark, J. Drobjeva, and J. Lastovicka, Variability in the maximum height of the ionospheric f2-layer over millstone hill (september 1998? march 2000); influence from below and above, 2002. [Cited on page [14](#).]

- Pancheva, D., P. Mukhtarov, B. Andonov, N. J. Mitchell, and J. M. Forbes, Planetary waves observed by TIMED/SABER in coupling the stratosphere–mesosphere–lower thermosphere during the winter of 2003/2004: Part 2 - Altitude and latitude planetary wave structure, *J. Atmos. Sol. Terr. Phys.*, *71*, 75–87, 2009. [Cited on page 27.]
- Pancheva, D., et al., Planetary waves in coupling the stratosphere and mesosphere during the major stratospheric warming in 2003/2004, *J. Geophys. Res.*, *113*, D12,105, 2008. [Cited on pages 18 and 27.]
- Pandey, K., R. Sekar, B. Anandarao, S. Gupta, and D. Chakrabarty, Estimation of nighttime dip-equatorial E-region current density using measurements and models, *J. Atmos. Sol. Terr. Phys.*, *146*, 160–170, 2016. [Cited on page 6.]
- Pandey, K., D. Chakrabarty, and R. Sekar, Critical evaluation of the impact of disturbance dynamo on equatorial ionosphere during daytime, *Journal of Geophysical Research: Space Physics*, *123*, 9762–9774, 2018. [Cited on page 98.]
- Pandey, K., R. Sekar, B. G. Anandarao, S. P. Gupta, and D. Chakrabarty, On the occurrence of afternoon counter electrojet over Indian longitudes during June solstice in solar minimum, *Journal of Geophysical Research: Space Physics*, *123*, 2204–2214, 2018, <http://dx.doi.org/10.1002/2017JA024725>. [Cited on pages 6, 23, and 82.]
- Pant, T. K., and R. Sridharan, A case-study of the low-latitude thermosphere during geomagnetic storms and its new representation by improved MSIS model, *Ann. Geophys.*, *16*, 1513–1518, 1998. [Cited on page 16.]
- Parish, H. F., J. M. Forbes, and F. Kamalabadi, Planetary wave and solar emission signatures in the equatorial electrojet, *J. Geophys. Res.*, *99*, 355–368, 1994. [Cited on page 18.]
- Park, J., H. Lühr, C. Lee, Y. H. Kim, G. Jee, and J.-H. Kim, A climatology of medium-scale gravity wave activity in the midlatitude/low-latitude daytime upper thermosphere as observed by champ, *Journal of Geophysical Research: Space Physics*, *119*, 2187–2196, 2014. [Cited on pages 58 and 122.]
- Pedatella, N. M., and J. M. Forbes, Evidence for stratosphere sudden warming-ionosphere

- coupling due to vertically propagating tides, *Geophys. Res. Lett.*, *37*, L11,104, 2010. [Cited on pages [18](#) and [27](#).]
- Picone, J., A. Hedin, D. P. Drob, and A. Aikin, Nrlmsise-00 empirical model of the atmosphere: Statistical comparisons and scientific issues, *Journal of Geophysical Research: Space Physics*, *107*, SIA-15, 2002. [Cited on pages [46](#), [74](#), [99](#), and [133](#).]
- Pitteway, M. L. V., and C. O. Hines, The viscous damping of atmospheric gravity waves, *Can. J. Phys.*, *41*, 1935–1948, 1963. [Cited on page [27](#).]
- Pogoreltsev, A. I., A. A. Vlasov, K. Fröhlich, and C. Jacobi, Planetary waves in coupling the lower and upper atmosphere, *J. Atmos. Sol. Terr. Phys.*, *69*, 2083 – 2101, 2007. [Cited on page [18](#).]
- Prakash, S., D. Pallamraju, and H. Sinha, Role of the equatorial ionization anomaly in the development of the evening prereversal enhancement of the equatorial zonal electric field, *Journal of Geophysical Research: Space Physics*, *114*, 2009. [Cited on pages [13](#), [14](#), [79](#), and [82](#).]
- Pramitha, M., M. V. Ratnam, A. Taori, B. Murthy, D. Pallamraju, and S. V. Bhaskar Rao, Evidence for tropospheric wind shear excitation of high-phase-speed gravity waves reaching the mesosphere using the ray-tracing technique., *Atmospheric Chemistry & Physics*, *15*, 2015. [Cited on page [22](#).]
- Prölss, G., Common origin of positive ionospheric storms at middle latitudes and the geomagnetic activity effect at low latitudes, *Journal of Geophysical Research: Space Physics*, *98*, 5981–5991, 1993. [Cited on pages [98](#) and [112](#).]
- Prolss, G. W., Magnetic storm associated perturbations of the upper atmosphere: Recent results obtained by satellite-borne gas analyzers, *Rev. Geophys.*, *18*, 183–202, 1980. [Cited on pages [25](#) and [98](#).]
- Prolss, G. W., M. Roemer, and J. W. Slowey, Dissipation of solar wind energy in the earth's upper atmosphere: The geomagnetic activity effect, *Adv. Space Res.*, *8*, 215 – 261, 1988. [Cited on page [25](#).]
- Raghavarao, R., and B. G. Anandarao, Vertical winds as a plausible cause for equatorial counter electrojet, *Geophys. Res. Lett.*, *7*, 357–360, 1980. [Cited on page [6](#).]

- Raghavarao, R., P. Sharma, and M. R. Sivaraman, Correlation of ionization anomaly with the intensity of the electrojet, *Space Res.*, *18*, 277–280, 1978. [Cited on pages 8 and 82.]
- Raghavarao, R., S. Gupta, R. Sekar, R. Narayanan, J. Desai, R. Sridharan, V. Babu, and V. Sudhakar, In situ measurements of winds, electric fields and electron densities at the onset of equatorial spread-F, *J. Atmos. Terr. Phys.*, *49*, 485 – 492, 1987. [Cited on page 17.]
- Raghavarao, R., M. Nageswararao, J. H. Sastri, G. Vyas, and M. Sriramarao, Role of equatorial ionization anomaly in the initiation of equatorial spread f, *Journal of Geophysical Research: Space Physics*, *93*, 5959–5964, 1988a. [Cited on pages 13, 14, 77, and 79.]
- Raghavarao, R., R. Sridharan, J. H. Sastri, V. V. Agashe, B. C. N. Rao, P. B. Rao, and V. V. Somayajulu, *The equatorial ionosphere; WITS handbook. World Ionosphere/Thermosphere Study, vol 1.*, SCOSTEP Secretariat, University of Illinois, Urbana, 1988b. [Cited on pages 8, 22, 36, and 126.]
- Raghavarao, R., L. E. Wharton, N. W. Spencer, H. G. Mayr, and L. H. Brace, An equatorial temperature and wind anomaly (ETWA), *Geophys. Res. Lett.*, *18*, 1193–1196, 1991. [Cited on pages 11 and 36.]
- Raghavarao, R., W. R. Hoegy, N. W. Spencer, and L. E. Wharton, Neutral temperature anomaly in the equatorial thermosphere- A source of vertical winds, *Geophys. Res. Lett.*, *20*, 1023–1026, 1993. [Cited on pages 11, 14, and 17.]
- Ram, S. T., P. R. Rao, K. Niranjana, D. Prasad, R. Sridharan, C. Devasia, and S. Ravindran, The role of post-sunset vertical drifts at the equator in predicting the onset of vhf scintillations during high and low sunspot activity years, 2006. [Cited on pages 13, 79, and 80.]
- Ram, S. T., M. Yamamoto, R. Tsunoda, S. Thampi, and S. Gurubaran, On the application of differential phase measurements to study the zonal large scale wave structure (lsws) in the ionospheric electron content, *Radio Science*, *47*, 1–10, 2012. [Cited on page 64.]
- Rao, P. R., S. G. Krishna, K. Niranjana, and D. Prasad, Temporal and spatial variations in

- tec using simultaneous measurements from the indian gps network of receivers during the low solar activity period of 2004? 2005, 2006. [Cited on pages 58 and 64.]
- Rastogi, R., Seasonal and solar cycle variations of equatorial spread-f in the american zone, *Journal of Atmospheric and Terrestrial Physics*, 42, 593–597, 1980. [Cited on pages 13 and 79.]
- Rastogi, R. G., and K. N. Iyer, Quiet day variation of geomagnetic H-field at low latitudes, *Journal of Geomagnetism and Geoelectricity*, 28, 461–479, 1976, <http://dx.doi.org/10.5636/jgg.28.461>. [Cited on page 42.]
- Rastogi, R. G., and J. A. Klobuchar, Ionospheric electron content within the equatorial F2 layer anomaly belt, *J. Geophys. Res.*, 95, 19,045–19,052, 1990. [Cited on page 58.]
- Rastogi, R. G., and A. Patil, Complex structure of equatorial electrojet current, *Current Science*, 55, 433–436, 1986. [Cited on page 42.]
- Ratcliffe, J. A., *The magneto-ionic theory and its applications to the ionosphere*, University Press, 1959. [Cited on page 33.]
- Reimann, J. D., Frequency estimation using unequally-spaced astronomical data, Ph.D. thesis, Citeseer, 1994. [Cited on page 46.]
- Reinisch, B. W., et al., New digisonde for research and monitoring applications, *Radio Science*, 44, 2009. [Cited on page 36.]
- Richards, P., J. Fennelly, and D. Torr, Euvac: A solar euv flux model for aeronomic calculations, *Journal of Geophysical Research: Space Physics*, 99, 8981–8992, 1994. [Cited on page 124.]
- Richmond, A., Gravity wave generation, propagation, and dissipation in the thermosphere, *Journal of Geophysical Research: Space Physics*, 83, 4131–4145, 1978. [Cited on pages 16, 24, 75, and 98.]
- Richmond, A., Thermospheric heating in a magnetic storm: Dynamic transport of energy from high to low latitudes, *Journal of Geophysical Research: Space Physics*, 84, 5259–5266, 1979. [Cited on pages 16, 24, and 98.]

- Richmond, A. D., and S. Matsushita, Thermospheric response to a magnetic substorm, *J. Geophys. Res.*, *80*, 2839–2850, 1975. [Cited on pages [16](#), [24](#), [98](#), and [112](#).]
- Rishbeth, H., Ion-drag effects in the thermosphere, *J. Atmos. Terr. Phys.*, *41*, 885–894, 1979. [Cited on page [16](#).]
- Rishbeth, H., The F-region dynamo, *Journal of Atmospheric and Terrestrial Physics*, *43*, 387–392, 1981, [https://doi.org/10.1016/0021-9169\(81\)90102-1](https://doi.org/10.1016/0021-9169(81)90102-1). [Cited on page [84](#).]
- Rishbeth, H., and O. K. Garriott, *Introduction to Ionospheric Physics*, Academic Press, 1969. [Cited on page [16](#).]
- Rishbeth, H., I. Müller-Wodarg, L. Zou, T. Fuller-Rowell, G. Millward, R. Moffett, D. Idenden, and A. Aylward, Annual and semiannual variations in the ionospheric f2-layer: Ii. physical discussion, in *Annales Geophysicae*, vol. 18, pp. 945–956, Springer, 2000a. [Cited on pages [126](#) and [129](#).]
- Rishbeth, H., K. Sedgemore-Schulthess, and T. Ulich, Semiannual and annual variations in the height of the ionospheric f2-peak, in *Annales Geophysicae*, vol. 18, pp. 285–299, Springer, 2000b. [Cited on page [125](#).]
- Roble, R., The upper atmosphere and magnetosphere, *National Academy of Science, Washington, DC*, p. 57, 1977. [Cited on page [25](#).]
- Roble, R., and S. Matsushita, An estimate of the global-scale joule heating rates in the thermosphere due to time mean currents, *Radio Science*, *10*, 389–399, 1975. [Cited on page [26](#).]
- Roble, R. G., and R. E. Dickinson, Is there enough solar extreme ultraviolet radiation to maintain the global mean thermospheric temperature?, *J. Geophys. Res.*, *78*, 249–257, 1973. [Cited on page [4](#).]
- Saito, S., and T. Maruyama, Ionospheric height variations observed by ionosondes along magnetic meridian and plasma bubble onsets, 2006. [Cited on page [82](#).]
- Salah, J. E., and J. M. Holt, Midlatitude thermospheric winds from incoherent scatter radar and theory, *Radio Science*, *9*, 301–313, 1974. [Cited on page [16](#).]

- Salby, M. L., Survey of planetary-scale traveling waves: The state of theory and observations, *Rev. Geophys.*, *22*, 209–236, 1984. [Cited on page 18.]
- Salby, M. L., *Fundamentals of Atmospheric Physics*, vol. 61, Academic press, 1996. [Cited on page 20.]
- Sampath, S., and T. S. G. Sastry, AC electric fields associated with the plasma instabilities in the equatorial electrojet-III, *Journal of Geomagnetism and Geoelectricity*, *31*, 391–400, 1979, <http://doi.org/10.5636/jgg.31.391>. [Cited on page 6.]
- Sassi, F., R. Garcia, and K. Hoppel, Large-scale rossby normal modes during some recent northern hemisphere winters, *J. Atmos. Sci.*, *69*, 820–839, 2012. [Cited on pages 18 and 27.]
- Sastri, J., M. Abdu, I. Batista, and J. Sobral, Onset conditions of equatorial (range) spread f at fortaleza, brazil, during the june solstice, *Journal of Geophysical Research: Space Physics*, *102*, 24,013–24,021, 1997. [Cited on page 79.]
- Sastri, J. H., Equatorial anomaly in F-region - A Review, *Indian Journal of Radio & Space Physics*, *19*, 225–240, 1990, <http://nopr.niscair.res.in/handle/123456789/36285>. [Cited on page 126.]
- Sastri, J. H., Equatorial anomaly in F region- A review, *Indian. J. Radio Space Phys*, *19*, 225–240, 1990. [Cited on pages 8 and 36.]
- Sastri, J. H., Longitudinal dependence of equatorial F region vertical plasma drifts in the dusk sector, *Journal of Geophysical Research*, *101*, 2445–2452, 1996, <http://dx.doi.org/10.1029/95JA02759>. [Cited on page 13.]
- Sastri, J. H., H. Lühr, H. Tachihara, T.-I. Kitamura, and J. V. S. V. Rao, Electric field fluctuations (25-35 min) in the midnight dip equatorial ionosphere, *Annales Geophysicae*, *18*, 252–256, 2000, <https://doi.org/10.1007/s00585-000-0252-2>. [Cited on page 23.]
- Sato, K., Small-scale wind disturbances observed by the mu radar during the passage of typhoon kelly, *Journal of the Atmospheric Sciences*, *50*, 518–537, 1993. [Cited on page 22.]

- Sato, K., H. Hashiguchi, and S. Fukao, Gravity waves and turbulence associated with cumulus convection observed with the uhf/vhf clear-air doppler radars, *Journal of Geophysical Research: Atmospheres*, *100*, 7111–7119, 1995. [Cited on page 22.]
- Scargle, J. D., Studies in astronomical time series analysis. II - Statistical aspects of spectral analysis of unevenly spaced data, *Astrophys. J.*, *263*, 835–853, 1982. [Cited on pages 46, 50, 52, 61, and 123.]
- Scherliess, L., and B. G. Fejer, Storm time dependence of equatorial disturbance dynamo zonal electric fields, *Journal of Geophysical Research: Space Physics*, *102*, 24,037–24,046, 1997, <http://dx.doi.org/10.1029/97JA02165>. [Cited on page 23.]
- Schunk, R., and A. Nagy, *Ionospheres: physics, plasma physics, and chemistry*, Cambridge university press, 2009. [Cited on page 7.]
- Schuster, A., On the investigation of hidden periodicities with application to a supposed 26 day period of meteorological phenomena, *Terrestrial Magnetism*, *3*, 13–41, 1898. [Cited on pages 46 and 47.]
- Scinocca, J., and R. Ford, The nonlinear forcing of large-scale internal gravity waves by stratified shear instability, *Journal of the atmospheric sciences*, *57*, 653–672, 2000. [Cited on page 22.]
- Sekar, R., and M. Kelley, On the combined effects of vertical shear and zonal electric field patterns on nonlinear equatorial spread f evolution, *Journal of Geophysical Research: Space Physics*, *103*, 20,735–20,747, 1998. [Cited on pages 13 and 79.]
- Sekar, R., and R. Raghavarao, Role of vertical winds on the Rayleigh-Taylor mode instabilities of the night-time equatorial ionosphere, *J. Atmos. Terr. Phys.*, *49*, 981 – 985, 1987. [Cited on pages 14, 16, and 78.]
- Sekar, R., R. Suhasini, and R. Raghavarao, Effects of vertical winds and electric fields in the nonlinear evolution of equatorial spread f, *Journal of Geophysical Research: Space Physics*, *99*, 2205–2213, 1994. [Cited on page 16.]
- Senior, C., and M. Blanc, On the control of magnetospheric convection by the spatial distribution of ionospheric conductivities, *Journal of Geophysical Research*, *89*, 261–284, 1984, <https://doi.org/10.1029/JA089iA01p00261>. [Cited on page 23.]

- Shepherd, G. G., and Y.-M. Cho, On the relationship of the o (1d) 630.0 nm dayglow emission to the f10.7 cm solar flux and the solar zenith angle, *Journal of Geophysical Research: Space Physics*, *126*, e2020JA028715, 2021. [Cited on page 40.]
- Shepherd, G. G., et al., The Wind Imaging Interferometer (WINDII) on the Upper Atmosphere Research Satellite: A 20 year perspective, *Rev. Geophys.*, *50*, 2012. [Cited on page 16.]
- Shiokawa, K., Y. Otsuka, and T. Ogawa, Propagation characteristics of nighttime mesospheric and thermospheric waves observed by optical mesosphere thermosphere imagers at middle and low latitudes, *Earth, Planets and Space*, *61*, 479–491, 2009. [Cited on pages 27, 58, and 67.]
- Shiokawa, K., et al., Thermospheric wind during a storm-time large-scale traveling ionospheric disturbance, *J. Geophys. Res.*, *108*, 2003. [Cited on page 16.]
- Singh, R. P., and D. Pallamraju, On the latitudinal distribution of mesospheric temperatures during sudden stratospheric warming events, *J. Geophys. Res.*, *120*, 2926–2939, 2015. [Cited on pages 18 and 27.]
- Singh, R. P., and D. Pallamraju, Effect of cyclone Nilofar on mesospheric wave dynamics as inferred from optical nightglow observations from Mount Abu, India, *J. Geophys. Res.*, *121*, 5856–5867, 2016. [Cited on pages 22, 27, 65, 69, and 88.]
- Singh, R. P., and D. Pallamraju, Large-and small-scale periodicities in the mesosphere as obtained from variations in o 2 and oh nightglow emissions, in *Annales Geophysicae*, vol. 35, pp. 227–237, Copernicus GmbH, 2017. [Cited on page 27.]
- Singh, R. P., and D. Pallamraju, Mesospheric temperature inversions observed in oh and o2 rotational temperatures from mount abu (24.6° n, 72.8° e), india, *Journal of Geophysical Research: Space Physics*, *123*, 8823–8834, 2018. [Cited on page 27.]
- Sivakandan, M., I. Paulino, T. Ramkumar, A. Taori, A. Patra, S. Sripathi, K. Niranjana, and A. Bilibio, Multi-instrument investigation of troposphere-ionosphere coupling and the role of gravity waves in the formation of equatorial plasma bubble, *Journal of Atmospheric and Solar-Terrestrial Physics*, *189*, 65–79, 2019. [Cited on page 80.]

- Smith, A. K., and L. V. Lyjak, An observational estimate of gravity wave drag from the momentum balance in the middle atmosphere, *Journal of Geophysical Research: Atmospheres*, *90*, 2233–2241, 1985. [Cited on page [22](#).]
- Smith, C. R., and G. Erickson, *Maximum-Entropy and Bayesian Spectral Analysis and Estimation Problems: Proceedings of the Third Workshop on Maximum Entropy and Bayesian Methods in Applied Statistics, Wyoming, USA, August 1–4, 1983*, vol. 21, Springer Science & Business Media, 2012. [Cited on page [52](#).]
- Smith, R. W., Vertical winds: A tutorial, *Journal of atmospheric and solar-terrestrial physics*, *60*, 1425–1434, 1998. [Cited on page [17](#).]
- Solomon, S. C., and V. J. Abreu, The 630 nm dayglow, *J. Geophys. Res.*, *94*, 6817–6824, 1989. [Cited on pages [40](#) and [60](#).]
- Somayajulu, V. V., L. Cherian, K. Rajeev, G. Ramkumar, and C. R. Reddi, Mean winds and tidal components during counter electrojet events, *Geophys. Res. Lett.*, *20*, 1443–1446, 1993. [Cited on page [6](#).]
- Spencer, N. W., L. Wharton, H. Niemann, A. Hedin, G. Carignan, and J. Maurer, The Dynamics Explorer wind and the temperature spectrometer, *Space Science Instrumentation*, *5*, 417–428, 1981. [Cited on page [16](#).]
- Sreeja, V., C. Vineeth, T. K. Pant, S. Ravindran, and R. Sridharan, Role of gravity wavelike seed perturbations on the triggering of esf—a case study from unique dayglow observations, in *Annales Geophysicae*, vol. 27, pp. 313–318, Copernicus GmbH, 2009. [Cited on page [88](#).]
- Sridharan, R., S. Gurubaran, R. Raghavarao, and R. Suhasini, Co-ordinated thermospheric and F-region measurements from low latitudes, *J. Atmos. Terr. Phys.*, *53*, 515–519, 1991a. [Cited on page [27](#).]
- Sridharan, R., R. Raghavarao, S. Gurubaran, and R. Narayanan, First results of OI 630.0 nm dayglow measurements from equatorial latitudes, *J. Atmos. Sol.-Terr. Phy.*, *53*, 521–528, 1991b. [Cited on page [27](#).]

- Sridharan, R., S. A. Haider, S. Gurubaran, R. Sekar, and R. Narayanan, OI 630.0-nm dayglow in the region of equatorial ionization anomaly: Temporal variability and its causative mechanism, *J. Geophys. Res.*, *97*, 13,715–13,721, 1992a. [Cited on pages 27 and 40.]
- Sridharan, R., R. Narayanan, and N. K. Modi, Improved chopper mask for the dayglow photometer, *Appl. Opt.*, *31*, 425–426, 1992b. [Cited on page 27.]
- Sridharan, R., R. Narayanan, N. K. Modi, and D. P. Raju, A Novel mask design for multiwavelength dayglow photometry, *Appl. Opt.*, *32*, 4178–80, 1993a. [Cited on pages 27 and 39.]
- Sridharan, R., R. Sekar, and S. Gurubaran, Two-dimensional high-resolution imaging of the equatorial plasma fountain, *J. Atmos. Terr. Phys.*, *55*, 1661 – 1665, 1993b. [Cited on page 27.]
- Sridharan, R., D. P. Raju, R. Raghavarao, and P. V. S. Ramarao, Precursor to equatorial spread-F in OI 630.0 nm dayglow, *Geophys. Res. Lett.*, *21*, 2797–2800, 1994. [Cited on pages 14, 27, 77, and 80.]
- Sridharan, R., D. Pallam Raju, R. Narayanan, N. K. Modi, B. H. Subbaraya, and R. Raghavarao, Daytime measurements of optical auroral emissions from Antarctica, *Current science*, *68*, 830–834, 1995. [Cited on page 27.]
- Sridharan, R., N. K. Modi, D. P. Raju, R. Narayanan, T. K. Pant, A. Taori, and D. Chakrabarty, A multiwavelength daytime photometer - a new tool for the investigation of atmospheric processes, *Meas. Sci. Technol.*, *9*, 585, 1998. [Cited on pages 27 and 39.]
- Sridharan, R., D. P. Raju, V. Somayajulu, A. Taori, D. Chakrabarty, and R. Raghavarao, Imprint of equatorial electrodynamic processes in the OI 630.0 nm dayglow, *J. Atmos. Sol. Terr. Phys.*, *61*, 1143 – 1155, 1999. [Cited on page 27.]
- Sridharan, S., Variabilities of low-latitude migrating and nonmigrating tides in gps-tec and timed-saber temperature during the sudden stratospheric warming event of 2013, *Journal of Geophysical Research: Space Physics*, *122*, 10–748, 2017. [Cited on page 27.]

- Sridharan, S., and S. Meenakshi, Semidiurnal tidal influence on the occurrence of post-midnight f region fair radar echoes, *Journal of Geophysical Research: Space Physics*, *125*, e2019JA027,700, 2020. [Cited on page 27.]
- Sridharan, S., S. Sathishkumar, and S. Gurubaran, Variabilities of mesospheric tides and equatorial electrojet strength during major stratospheric warming events, *Annales Geophysicae*, *27*, 4125–4130, 2009, <https://doi.org/10.5194/angeo-27-4125-2009>. [Cited on pages 6, 18, and 27.]
- Stellingwerf, R. F., Period determination using phase dispersion minimization, *The Astrophysical Journal*, *224*, 953–960, 1978. [Cited on page 46.]
- Stening, R. J., C. E. Meek, and A. H. Manson, Upper atmosphere wind systems during reverse equatorial electrojet events, *Geophys. Res. Lett.*, *23*, 3243–3246, 1996. [Cited on page 6.]
- Stolarski, R. S., P. B. Hays, and R. G. Roble, Atmospheric heating by solar EUV radiation, *J. Geophys. Res.*, *80*, 2266–2276, 1975. [Cited on page 4.]
- Sugiura, M., and J. C. Cain, A model equatorial electrojet, *Journal of Geophysical Research*, *71*, 1869–1877, 1966, <http://dx.doi.org/10.1029/JZ071i007p01869>. [Cited on page 6.]
- Sumod, S. G., T. K. Pant, C. Vineeth, and M. M. Hossain, On the ionospheric and thermospheric response of solar flare events of 19 January 2005: An investigation using radio and optical techniques, *J. Geophys. Res.*, *119*, 5049–5059, 2014. [Cited on page 15.]
- Takahashi, H., C. M. Wrasse, C. A. O. B. Figueiredo, D. Barros, M. A. Abdu, Y. Otsuka, and K. Shiokawa, Equatorial plasma bubble seeding by mstids in the ionosphere, *Progress in Earth and Planetary Science*, *5*, 1–13, 2018. [Cited on page 80.]
- Takahashi, H., et al., Simultaneous observation of ionospheric plasma bubbles and mesospheric gravity waves during the spreadfex campaign, in *Annales Geophysicae*, vol. 27, p. 1477, European Geosciences Union, 2009. [Cited on page 80.]
- Talaat, E. R., and R. S. Lieberman, Nonmigrating diurnal tides in mesospheric and lower-thermospheric winds and temperatures, *Journal of the atmospheric sciences*, *56*, 4073–4087, 1999. [Cited on page 27.]

- Taori, A., N. Parihar, R. Ghodpage, N. Dashora, S. Sripathi, E. Kherani, and P. Patil, Probing the possible trigger mechanisms of an equatorial plasma bubble event based on multistation optical data, *Journal of Geophysical Research: Space Physics*, *120*, 8835–8847, 2015. [Cited on page 80.]
- Tapping, K., The 10.7 cm solar radio flux (f10.7), *Space Weather*, *11*, 394–406, 2013. [Cited on page 15.]
- Taylor, M. J., M. B. Bishop, and V. Taylor, All-sky measurements of short period waves imaged in the OI(557.7 nm), Na(589.2 nm) and near infrared OH and O₂(0,1) nightglow emissions during the ALOHA-93 Campaign, *Geophys. Res. Lett.*, *22*, 2833–2836, 1995. [Cited on page 27.]
- Taylor, M. J., J.-M. Jahn, S. Fukao, and A. Saito, Possible evidence of gravity wave coupling into the mid-latitude F region ionosphere during the SEEK Campaign, *Geophys. Res. Lett.*, *25*, 1801–1804, 1998. [Cited on page 27.]
- Taylor, M. J., W. R. Pendleton Jr, P.-D. Pautet, Y. Zhao, C. Olsen, H. K. S. Babu, A. F. Medeiros, and H. Takahashi, Recent progress in mesospheric gravity wave studies using nightglow imaging system, *Rev. Bras. Geofísica*, *25*, 49–58, 2007. [Cited on page 27.]
- Thompson, R. O., Spectral estimation from irregularly spaced data, *IEEE Transactions on Geoscience electronics*, *9*, 107–110, 1971. [Cited on page 48.]
- Torrence, C., and G. P. Compo, A practical guide to wavelet analysis, *Bull. Amer. Meteor. Soc.*, *79*, 61–78, 1998. [Cited on pages 53, 54, and 55.]
- Tsunoda, R. T., Control of the seasonal and longitudinal occurrence of equatorial scintillations by the longitudinal gradient in integrated e region pedersen conductivity, *J. Geophys. Res.*, *90*, 447–456, 1985. [Cited on pages 13 and 79.]
- Tsunoda, R. T., and B. R. White, On the generation and growth of equatorial backscatter plumes 1. wave structure in the bottomside f layer, *Journal of Geophysical Research: Space Physics*, *86*, 3610–3616, 1981. [Cited on page 80.]
- Tsurutani, B. T., et al., The October 28, 2003 extreme EUV solar flare and resultant extreme ionospheric effects: Comparison to other Halloween events and the Bastille Day event, *Geophys. Res. Lett.*, *32*, 2005. [Cited on page 15.]

- Tulasi Ram, S., P. Rama Rao, D. Prasad, K. Niranjana, A. Raja Babu, R. Sridharan, C. Devasia, and S. Ravindran, The combined effects of electrojet strength and the geomagnetic activity (k p-index) on the post sunset height rise of the f-layer and its role in the generation of esf during high and low solar activity periods, in *Annales Geophysicae*, vol. 25, Copernicus GmbH, 2007. [Cited on pages 84 and 85.]
- Uemoto, J., T. Maruyama, S. Saito, M. Ishii, and R. Yoshimura, Relationships between pre-sunset electrojet strength, pre-reversal enhancement and equatorial spread-f onset, in *Annales Geophysicae*, vol. 28, pp. 449–454, Copernicus GmbH, 2010. [Cited on page 82.]
- Vadas, S. L., Horizontal and vertical propagation and dissipation of gravity waves in the thermosphere from lower atmospheric and thermospheric sources, *Journal of Geophysical Research: Space Physics*, 112, 2007. [Cited on pages 75 and 122.]
- Vadas, S. L., and D. C. Fritts, Thermospheric responses to gravity waves: Influences of increasing viscosity and thermal diffusivity, *J. Geophys. Res.*, 110, D15,103, 2005. [Cited on pages 27, 100, 122, 131, 132, and 138.]
- Vadas, S. L., and H.-l. Liu, Generation of large-scale gravity waves and neutral winds in the thermosphere from the dissipation of convectively generated gravity waves, *Journal of Geophysical Research: Space Physics*, 114, 2009. [Cited on page 122.]
- Vadas, S. L., D. C. Fritts, and M. J. Alexander, Mechanism for the generation of secondary waves in wave breaking regions, *Journal of the Atmospheric Sciences*, 60, 194–214, 2003. [Cited on page 122.]
- Valladares, C., S. Basu, K. Groves, M. Hagan, D. Hysell, A. Mazzella Jr, and R. Sheehan, Measurement of the latitudinal distributions of total electron content during equatorial spread f events, *Journal of Geophysical Research: Space Physics*, 106, 29,133–29,152, 2001. [Cited on pages 14 and 80.]
- VanderPlas, J. T., Understanding the lomb–scargle periodogram, *The Astrophysical Journal Supplement Series*, 236, 16, 2018. [Cited on pages 46 and 48.]
- Varney, R. H., M. C. Kelley, and E. Kudeki, Observations of electric fields associated

- with internal gravity waves, *Journal of Geophysical Research: Space Physics*, *114*, 2009. [Cited on page 80.]
- Volland, H., and H. G. Mayr, A theory of the diurnal variations of the thermosphere., *AnG*, *26*, 907–919, 1970. [Cited on page 26.]
- Willson, R. C., Solar irradiance variations and solar activity, *Journal of Geophysical Research: Space Physics*, *87*, 4319–4326, 1982. [Cited on page 14.]
- Witasse, O., J. Lilensten, C. Lathuillère, and P.-L. Blelly, Modeling the OI 630.0 and 557.7 nm thermospheric dayglow during EISCAT-WINDII coordinated measurements, *J. Geophys. Res.*, *104*, 24,639–24,655, 1999. [Cited on page 40.]
- Wolf, R. A., Effects of ionospheric conductivity on convective flow of plasma in the magnetosphere, *Journal of Geophysical Research*, *75*, 4677–4698, 1970, <https://doi.org/10.1029/JA075i025p04677>. [Cited on page 23.]
- Woodman, R. F., and C. La Hoz, Radar observations of f region equatorial irregularities, *Journal of Geophysical Research*, *81*, 5447–5466, 1976. [Cited on page 79.]
- Wu, D. L., P. Preusse, S. D. Eckermann, J. H. Jiang, M. de la Torre Juarez, L. Coy, and D. Y. Wang, Remote sounding of atmospheric gravity waves with satellite limb and nadir techniques, *Advances in Space Research*, *37*, 2269–2277, 2006. [Cited on page 58.]
- Yadav, S., and D. Pallamraju, On the coupled interactions between ring current intensity and high-latitude ionospheric electron density variations, *J. Atmos. Sol. Terr. Phys.*, *125-126*, 50–58, 2015. [Cited on pages 23 and 99.]
- Yamanaka, M. D., and S. Fukao, A simple model of gravity-wave momentum and energy fluxes transferred through the middle atmosphere to the upper atmosphere, *Journal of Atmospheric and Terrestrial Physics*, *56*, 1375–1385, 1994. [Cited on pages 68, 69, and 70.]
- Yamazaki, Y., and M. J. Kosch, The equatorial electrojet during geomagnetic storms and substorms, *Journal of Geophysical Research: Space Physics*, *120*, 2276–2287, 2015. [Cited on pages 23 and 98.]

- Yiğit, E., and A. S. Medvedev, Heating and cooling of the thermosphere by internal gravity waves, *Geophysical Research Letters*, *36*, 2009. [Cited on page 122.]
- Yiğit, E., and A. S. Medvedev, Internal gravity waves in the thermosphere during low and high solar activity: Simulation study, *Journal of Geophysical Research: Space Physics*, *115*, 2010. [Cited on pages 131, 137, and 138.]
- Yigit, E., A. D. Aylward, and A. S. Medvedev, Parameterization of the effects of vertically propagating gravity waves for thermosphere general circulation models: Sensitivity study, *J. Geophys. Res.*, *113*, D19,106, 2008. [Cited on pages 22 and 122.]
- Yiğit, E., A. D. Aylward, and A. S. Medvedev, Parameterization of the effects of vertically propagating gravity waves for thermosphere general circulation models: Sensitivity study, *Journal of Geophysical Research: Atmospheres*, *113*, 2008. [Cited on page 122.]
- Yokoyama, T., H. Jin, H. Shinagawa, and H. Liu, Seeding of equatorial plasma bubbles by vertical neutral wind, *Geophysical Research Letters*, *46*, 7088–7095, 2019. [Cited on page 80.]
- Yue, X., W. S. Schreiner, J. Lei, C. Rocken, D. C. Hunt, Y.-H. Kuo, and W. Wan, Global ionospheric response observed by cosmic satellites during the january 2009 stratospheric sudden warming event, *J. Geophys. Res.*, *115*, 2010. [Cited on page 18.]
- Zhang, S. P., and G. G. Shepherd, Neutral winds in the lower thermosphere observed by WINDII during the April 4–5th, 1993 storm, *Geophys. Res. Lett.*, *27*, 1855–1858, 2000. [Cited on page 25.]
- Zhang, S. P., and G. G. Shepherd, Solar influence on the O(¹D) dayglow emission rate: Global-scale measurements by WINDII on UARS, *Geophys. Res. Lett.*, *31*, L07,804, 2004. [Cited on page 40.]
- Zhang, Y., L. J. Paxton, D. Morrison, B. Wolven, H. Kil, C.-I. Meng, S. B. Mende, and T. J. Immel, O/N₂ changes during 1–4 October 2002 storms: IMAGE SI-13 and TIMED/GUVI observations, *J. Geophys. Res.*, *109*, 2004. [Cited on page 25.]
- Zhang, Y., L. Paxton, D. Morrison, D. Marsh, and H. Kil, Storm-time behaviors of O/N₂ and NO variations, *J. Atmos. Sol. Terr. Phys.*, *114*, 42–49, 2014. [Cited on page 25.]

List of Publications

Publications in Journals

1. Mandal, S., Pallamraju, D., Karan, D.K., Phadke, K.A., Singh, R.P., Suryawanshi, P. (2019). On deriving gravity wave characteristics in the daytime upper atmosphere using radio technique. *J. Geophys. Res.: Space Phys.* 124, 6985–6997. <https://doi.org/10.1029/2019JA026723>
2. Mandal, S., Pallamraju, D., Suryawanshi, P. (2020). Changes in the daytime thermospheric gravity wave propagation characteristics over low-latitudes in response to the variation in solar flux. *J. Atmos. Sol. Terr. Phys.* <https://doi.org/10.1016/j.jastp.2020.105414>
3. Mandal, S., and Pallamraju, D. (2020). Thermospheric gravity wave characteristics in the daytime over low-latitudes during geomagnetic quiet and disturbed conditions. *J. Atmos. Sol. Terr. Phys.* 211, 105,470. <https://doi.org/10.1016/j.jastp.2020.105470>.
4. Mandal, S., Pallamraju, D., et al., (to be submitted soon). Vertical propagation speeds of gravity waves in the daytime as precursors to the occurrence of ESF.

Presentations at Conferences

1. Duggirala Pallamraju, **Subir Mandal**, Kedar A Phadke, Deepak K Karan, and Ravindra P Singh, “Gravity waves in the ionosphere as derived from digisonde measurements at Ahmedabad, India”. Presented at 3rd URSI Regional Conference on Radio Science 2017, held at National Atmospheric Research Laboratory, Tirupati, India, during 01-04 March 2017. [Invited Oral by DP]
2. Duggirala Pallamraju, Deepak K. Karan, **Subir Mandal**, and Ravindra P Singh., “Results from the first three dimensional waves in the daytime obtained from day-glow emissions and their comparison with those derived from ionospheric measurements”. Presented at 14th Annual Meeting of AOGS held in Singapore during 06–11 August 2017. [Oral by DP]
3. **Subir Mandal**, Duggirala Pallamraju, and Deepak K Karan, “Gravity wave characteristics over low latitude upper atmospheric region obtained by radio technique”. Presented at the 15th International Symposium on Equatorial Aeronomy (ISEA) held during 22-26 October 2018 at Physical Research Laboratory, Ahmedabad, India. [Poster]
4. **Subir Mandal**, Duggirala Pallamraju, Deepak K Karan, Ravindra P Singh, Pradip Suryawanshi, and Sovan Saha, “Gravity wave characteristics over low latitude upper atmospheric region obtained by Digisonde”. Presented at the National Space Science Symposium-2019 (NSSS-2019)”, held at Savitribai Phule Pune University, Pune, India during 29-31 January 2019. [Poster]
5. **Subir Mandal**, Duggirala Pallamraju, Deepak K. Karan, Kedar A Phadke, Ravindra P Singh, and Pradip Suryawanshi, “Information on gravity wave propagation characteristics over a long duration in the upper atmosphere as obtained using digisonde measurements”. Presented at SuperDARN Workshop 2019, held in Fujiyoshida, Japan, during 02-04 June 2019. [Oral by SM]
6. **Subir Mandal**, Duggirala Pallamraju, and Tarun K Pant, “Study of thermospheric

- gravity wave characteristics and their behavior in relation to the occurrence of equatorial plasma irregularities in the post-sunset time using radio, and optical measurements”. Presented at Beacon Satellite Symposium 2019, held at University and Mazury, Olsztyn, Poland, during 19-23 August 2019. [Poster]
7. Duggirala Pallamraju and **Subir Mandal**, “New insights into the daytime thermospheric wave dynamics over low-latitudes obtained using radio technique: response to the solar flux and seasonal variations”. Presented at AGU Fall Meeting during 01-17 December 2020. [Poster]
 8. Duggirala Pallamraju and **Subir Mandal**, “Recent results on the low- latitudinal gravity wave behavior obtained through an innovative approach using digisonde technique”. Presented at 43rd COSPAR Scientific Assembly held during 28 Jan–04 Feb 2021. [Oral by DP]
 9. Duggirala Pallamraju, **Subir Mandal**, and Deepak K Karan, “New developments in the understanding of the daytime low-and equatorial-latitudinal electrodynamic and wave dynamics obtained using optical and radio techniques”. Presented at 43rd COSPAR Scientific Assembly held during 28 Jan–04 Feb 2021. [Oral by DP]
 10. **Subir Mandal**, and Duggirala Pallamraju, “Understanding the neutral wave characteristics in the daytime thermosphere using radio technique”. To be presented at CEDAR Workshop 2021 to be held during 20-25 June 2021. [Poster]
 11. Duggirala Pallamraju, Sovan Saha, Sunil Kumar, **Subir Mandal**, Pradip Suryawan-shi, Tatiparti Vijayalakshmi, and Seemala Gopi, “New results on the latitudinal variations in equatorial phenomena over Indian longitudes as obtained using night and daytime optical airglow emissions”. To be presented at 18th AOGS Annual Meeting during 01-06 August 2021. [Oral by DP]

Publications attached with the thesis

1. Mandal, S., Pallamraju, D., Karan, D.K., Phadke, K.A., Singh, R.P., Suryawanshi, P. (2019). On deriving gravity wave characteristics in the daytime upper atmosphere using radio technique. *J. Geophys. Res.: Space Phys.* 124, 6985–6997. <https://doi.org/10.1029/2019JA026723>
2. Mandal, S., Pallamraju, D., Suryawanshi, P. (2020). Changes in the daytime thermospheric gravity wave propagation characteristics over low-latitudes in response to the variation in solar flux. *J. Atmos. Sol. Terr. Phys.* <https://doi.org/10.1016/j.jastp.2020.105414>
3. Mandal, S., and Pallamraju, D. (2020). Thermospheric gravity wave characteristics in the daytime over low-latitudes during geomagnetic quiet and disturbed conditions. *J. Atmos. Sol. Terr. Phys.* 211, 105,470. <https://doi.org/10.1016/j.jastp.2020.105470>.